Virginia Commonwealth University
VCU Scholars Compass

Electrical and Computer Engineering Publications | Dept. of Electrical and Computer Engineering

2005

A comprehensive review of ZnO materials and devices

Ü. Özgür
Virginia Commonwealth University, uozgur@vcu.edu

Ya. I. Alivov
Virginia Commonwealth University

C. Liu
Virginia Commonwealth University

See next page for additional authors

Follow this and additional works at: http://scholarscompass.vcu.edu/egre_pubs

Part of the Electrical and Computer Engineering Commons

Ozgur, U., Alivov, Y. I., Liu, C., et al. A comprehensive review of ZnO materials and devices. Journal of Applied Physics 98, 041301 (2005). Copyright © 2005 AIP Publishing LLC.

Downloaded from

http://scholarscompass.vcu.edu/egre_pubs/174

This Article is brought to you for free and open access by the Dept. of Electrical and Computer Engineering at VCU Scholars Compass. It has been accepted for inclusion in Electrical and Computer Engineering Publications by an authorized administrator of VCU Scholars Compass. For more information, please contact libcompass@vcu.edu.

Authors
Ü. Özgür, Ya. I. Alivov, C. Liu, A. Teke, M. A. Reshchikov, S. Doğan, Vitaliy Avrutin, S.-J. Cho, and H. Morkoç

This article is available at VCU Scholars Compass: http://scholarscompass.vcu.edu/egre_pubs/174

HTML ABSTRACT + LINKS

JOURNAL OF APPLIED PHYSICS **98**, 041301 (2005)

APPLIED PHYSICS REVIEWS

A comprehensive review of ZnO materials and devices

Ü. Özgür,[a] Ya. I. Alivov, C. Liu, A. Teke,[b] M. A. Reshchikov, S. Doğan,[c] V. Avrutin, S.-J. Cho, and H. Morkoç[d]
Department of Electrical Engineering and Physics Department, Virginia Commonwealth University, Richmond, Virginia 23284-3072

(Received 2 February 2005; accepted 13 June 2005; published online 30 August 2005)

The semiconductor ZnO has gained substantial interest in the research community in part because of its large exciton binding energy (60 meV) which could lead to lasing action based on exciton recombination even above room temperature. Even though research focusing on ZnO goes back many decades, the renewed interest is fueled by availability of high-quality substrates and reports of *p*-type conduction and ferromagnetic behavior when doped with transitions metals, both of which remain controversial. It is this renewed interest in ZnO which forms the basis of this review. As mentioned already, ZnO is not new to the semiconductor field, with studies of its lattice parameter dating back to 1935 by Bunn [Proc. Phys. Soc. London **47**, 836 (1935)], studies of its vibrational properties with Raman scattering in 1966 by Damen *et al.* [Phys. Rev. **142**, 570 (1966)], detailed optical studies in 1954 by Mollwo [Z. Angew. Phys. **6**, 257 (1954)], and its growth by chemical-vapor transport in 1970 by Galli and Coker [Appl. Phys. Lett. **16**, 439 (1970)]. In terms of devices, Au Schottky barriers in 1965 by Mead [Phys. Lett. **18**, 218 (1965)], demonstration of light-emitting diodes (1967) by Drapak [Semiconductors **2**, 624 (1968)], in which Cu_2O was used as the *p*-type material, metal-insulator-semiconductor structures (1974) by Minami *et al.* [Jpn. J. Appl. Phys. **13**, 1475 (1974)], ZnO/ZnSe *n-p* junctions (1975) by Tsurkan *et al.* [Semiconductors **6**, 1183 (1975)], and Al/Au Ohmic contacts by Brillson [J. Vac. Sci. Technol. **15**, 1378 (1978)] were attained. The main obstacle to the development of ZnO has been the lack of reproducible and low-resistivity *p*-type ZnO, as recently discussed by Look and Claflin [Phys. Status Solidi B **241**, 624 (2004)]. While ZnO already has many industrial applications owing to its piezoelectric properties and band gap in the near ultraviolet, its applications to optoelectronic devices has not yet materialized due chiefly to the lack of *p*-type epitaxial layers. Very high quality what used to be called whiskers and platelets, the nomenclature for which gave way to nanostructures of late, have been prepared early on and used to deduce much of the principal properties of this material, particularly in terms of optical processes. The suggestion of attainment of *p*-type conductivity in the last few years has rekindled the long-time, albeit dormant, fervor of exploiting this material for optoelectronic applications. The attraction can simply be attributed to the large exciton binding energy of 60 meV of ZnO potentially paving the way for efficient room-temperature exciton-based emitters, and sharp transitions facilitating very low threshold semiconductor lasers. The field is also fueled by theoretical predictions and perhaps experimental confirmation of ferromagnetism at room temperature for potential spintronics applications. This review gives an in-depth discussion of the mechanical, chemical, electrical, and optical properties of ZnO in addition to the technological issues such as growth, defects, *p*-type doping, band-gap engineering, devices, and nanostructures.
© *2005 American Institute of Physics*. [DOI: 10.1063/1.1992666]

TABLE OF CONTENTS

I. INTRODUCTION 2
II. PROPERTIES OF ZnO 3
A. Crystal structures 3
B. Lattice parameters 6
C. Electronic band structure 7
D. Mechanical properties 12
E. Lattice dynamics 15
F. Thermal properties 18
1. Thermal-expansion coefficients 18
2. Thermal conductivity 19
3. Specific heat 21
G. Electrical properties of undoped ZnO 22
1. Low-field transport 23

[a]Electronic mail: uozgur@vcu.edu
[b]Present address: Balikesir University, Faculty of Art and Science, Department of Physics, 10100 Balikesir, Turkey.
[c]Present address: Atatürk University, Faculty of Art and Science, Department of Physics, 25240 Erzurum, Turkey.
[d]Electronic mail: hmorkoc@vcu.edu

[This article is copyrighted as indicated in the article. Reuse of AIP content is subject to the terms at: http://scitation.aip.org/termsconditions. Downloaded to] IP: 128.172.48.58 On: Mon, 19 Oct 2015 20:45:44

2. High-field transport 25
III. ZnO GROWTH 26
A. Bulk growth 26
B. Substrates 28
C. rf magnetron sputtering 29
D. Molecular-beam epitaxy 30
E. Pulsed-laser deposition 34
F. Chemical-vapor deposition 36
IV. OPTICAL PROPERTIES OF ZnO 39
A. Prelude 39
B. Optical transitions in ZnO 39
1. Free excitons and polaritons 39
2. Bound excitons 42
3. Two-electron satellites in PL 44
4. DAP and LO-phonon replicas in PL 45
5. Temperature-dependent PL measurements. 45
C. Time-resolved PL on ZnO 47
D. Refractive index of ZnO 48
E. Stimulated emission in ZnO 51
1. Thin films 51
2. Polycrystalline ZnO films and "random lasers" 54
3. Multiple-quantum wells 56
4. Stimulated-emission dynamics 56
V. DEFECTS IN ZnO 57
A. Predictions from first principles 57
B. Experimental studies of native and unintentionally introduced defects 58
1. Shallow acceptor in ZnO 58
2. Green luminescence band 59
3. Yellow luminescence band 61
4. Red luminescence band 62
VI. DOPING OF ZnO 62
A. *n*-type doping 62
B. *p*-type doping 63
1. Nitrogen doping 63
2. Codoping method: Nitrogen+group III . . . 65
3. Other dopants in group V 67
VII. ZnO-BASED DILUTE MAGNETIC SEMICONDUCTORS 68
A. Theory of ZnO-based magnetic semiconductors 69
B. Experimental results on ZnO-based magnetic semiconductors 72
VIII. BAND-GAP ENGINEERING 76
A. $Mg_xZn_{1-x}O$ alloy 77
B. $Cd_yZn_{1-y}O$ alloy 78
IX. PROCESSING, DEVICES, AND HETEROSTRUCTURES 79
A. Ohmic contacts to ZnO 79
B. Schottky contacts to ZnO 80
C. Heterostructure devices 82
1. Light-emitting devices 83
2. Photodiodes 85
D. Metal-insulator-semiconductor diodes 86
E. Transparent thin-film transistors 87
X. ZnO NANOSTRUCTURES 88
XI. SUMMARY 95

I. INTRODUCTION

There has been a great deal of interest in zinc oxide (ZnO) semiconductor materials lately, as seen from a surge of a relevant number of publications. The interest in ZnO is fueled and fanned by its prospects in optoelectronics applications owing to its direct wide band gap ($E_g \sim 3.3$ eV at 300 K). Some optoelectronic applications of ZnO overlap with that of GaN, another wide-gap semiconductor ($E_g \sim 3.4$ eV at 300 K) which is widely used for production of green, blue-ultraviolet, and white light-emitting devices. However, ZnO has some advantages over GaN among which are the availability of fairly high-quality ZnO bulk single crystals and a large exciton binding energy (~60 meV). ZnO also has much simpler crystal-growth technology, resulting in a potentially lower cost for ZnO-based devices.

As indicated in the abstract, ZnO is not really a newly discovered material. Research on ZnO has continued for many decades with interest following a roller-coaster pattern. Interest in this material at the time of this writing is again at a high point. In terms of its characterization, reports go back to 1935 or even earlier. For example, lattice parameters of ZnO were investigated for many decades.[1–9] Similarly, optical properties and processes in ZnO as well as its refractive index were extensively studied many decades ago.[10–25] Vibrational properties by techniques such as Raman scattering were also determined early on.[26–32] Investigations of ZnO properties presumes that ZnO samples were available. Growth methods not much different from what is employed lately have been explored, among which are chemical-vapor transport,[33] vapor-phase growth,[34] hydrothermal growth[35] which also had the additional motivation of doping with Li in an effort to obtain *p*-type material, high-quality platelets,[36] and so on.[37]

The ZnO bulk crystals have been grown by a number of methods, as has been reviewed recently,[38] and large-size ZnO substrates are available.[39–41] High-quality ZnO films can be grown at relatively low temperatures (less than 700 °C). The large exciton binding energy of ~60 meV paves the way for an intense near-band-edge excitonic emission at room and higher temperatures, because this value is 2.4 times that of the room-temperature (RT) thermal energy ($k_BT=25$ meV). There have also been a number of reports on laser emission from ZnO-based structures at RT and beyond. It should be noted that besides the above-mentioned properties of ZnO, there are additional properties which make it preferable over other wide-band-gap materials: its high-energy radiation stability and amenability to wet chemical etching.[38] Several experiments confirmed that ZnO is very resistive to high-energy radiation,[42–44] making it a very suitable candidate for space applications. ZnO is easily etched in all acids and alkalis, and this provides an opportunity for fabrication of small-size devices. In addition, ZnO has the same crystal structure and close lattice parameters to that of GaN and as a result can be used as a substrate for epitaxial growth of high-quality GaN films.[45,46]

ZnO has recently found other niche applications as well, such as fabrication of transparent thin-film transistors, where the protective covering preventing light exposure is elimi-

[This article is copyrighted as indicated in the article. Reuse of AIP content is subject to the terms at: http://scitation.aip.org/termsconditions. Downloaded to] IP: 128.172.48.58 On: Mon, 19 Oct 2015 20:45:44

nated since ZnO-based transistors are insensitive to visible light. Also up to 2×10^{21} cm^{-3} charge carriers can be introduced by heavy substitutional doping into ZnO. By controlling the doping level electrical properties can be changed from insulator through n-type semiconductor to metal while maintaining optical transparency that makes it useful for transparent electrodes in flat-panel displays and solar cells. ZnO is also a promising candidate for spintronics applications. Dietl *et al.*[47] predicted a Curie temperature of >300 K for Mn-doped ZnO. n-type doping in Fe-, Co-, or Ni-alloyed ZnO was predicted to stabilize high-Curie-temperature ferromagnetism. There have been a number of publications which appear to confirm these predictions, as has been reviewed recently,[48,49] albeit with a good deal of controversy, as will be discussed in Sec. VII.

However, one important problem should be overcome before ZnO could potentially make inroads into the world of optoelectronics devices: the growth of p-type-conductivity ZnO crystals. Despite all the progress that has been made and the reports of p-type conductivity in ZnO films using various growth methods and various group-V dopant elements (N, P, As, and Sb), a reliable and reproducible high-quality p-type conductivity has not yet been achieved for ZnO. Therefore, it remains to be the most pivotal topic in ZnO research today, and congruently most of the research efforts are directed just to solving this problem. In order to overcome this bottleneck and to control the material's properties, a clear understanding of physical processes in ZnO is necessary in addition to obtaining low n-type background. In spite of many decades of investigations, some of the basic properties of ZnO still remain unclear. For example, the nature of the residual n-type conductivity in undoped ZnO films, whether being due to impurities of some native defect or defects, is still under some degree of debate. Some authors ascribe the residual background to intrinsic defects [oxygen vacancies (V_O) and interstitial zinc atoms (Zn_i)], and others to noncontrollable hydrogen impurities introduced during growth. The well-known green band in ZnO luminescence spectra (manifesting itself as a broad peak around 500–530 nm), observed nearly in all samples regardless of growth conditions, is related to singly ionized oxygen vacancies by some and to residual copper impurities by others. Simply, a requisite consensus is lacking.

While p-type ZnO is difficult to attain, the advantages of ZnO are being explored and exploited by alternative methods such as heteroepitaxy in which p-n heterostructures can be obtained by depositing n-type ZnO films on other p-type materials while still utilizing ZnO as the active layer. Progress has been made in this arena with a number of heterostructures fabricated wherein one of the following, Si, NiO, GaN, AlGaN, SiC, ZnTe, CuO, CdTe, etc., plays the role of p-type layer. In particular, high-intensity UV emission has been observed from the n-ZnO/p-AlGaN heterojunction in which ZnO served as the active layer. These results are just harbingers of what can be expected of ZnO in an effort to position it for future device applications. As in the early developments of GaN predating the demonstration of p-type conductivity, metal-insulator-semiconductor device structures not requiring p-type ZnO have been introduced but lack the high efficiency.

In this paper we collate the properties of ZnO as well as review the recent progress in ZnO research. This present review is distinguishable from the other reviews[50–55] in that the previous ones focused mainly on material processing, doping, and transport properties, while the present one treats those topics in greater depth in addition to an in-depth discussion of the growth, optical properties, p-type doping, and device fabrication aspects. The organization of this review is as follows: First, structural, chemical, and electrical properties of undoped ZnO are discussed in Sec. II. This is followed by ZnO crystal growth, both bulk and film (Sec. III), and optical properties of ZnO (Sec. IV). Sections V–VII are devoted, respectively, to defects in ZnO, doping, and magnetic properties. Alloys of ZnO (band-gap engineering) are discussed in Sec. VIII, and this is followed by ZnO-based devices and their applications (Sec. IX). Finally, ZnO nanostructures are reviewed in Sec. X.

II. PROPERTIES OF ZnO

In this section crystal structures, inclusive of lattice parameters, electronic band structures, mechanical properties, inclusive of elastic contants and piezoelectric constants, lattice dynamics and vibrational processes, thermal properties, electrical properties, and low-field and high-field carrier transports are treated.

A. Crystal structures

Most of the group-II-VI binary compound semiconductors crystallize in either cubic zinc-blende or hexagonal wurtzite structure where each anion is surrounded by four cations at the corners of a tetrahedron, and vice versa. This tetrahedral coordination is typical of sp^3 covalent bonding, but these materials also have a substantial ionic character. ZnO is a II-VI compound semiconductor whose ionicity resides at the borderline between covalent and ionic semiconductor. The crystal structures shared by ZnO are wurtzite ($B4$), zinc blende ($B3$), and rocksalt ($B1$), as schematically shown in Fig. 1. At ambient conditions, the thermodynamically stable phase is wurtzite. The zinc-blende ZnO structure can be stabilized only by growth on cubic substrates, and the rocksalt (NaCl) structure may be obtained at relatively high pressures.

The ground-state total energy of ZnO in wurtzite, zinc-blende, and rocksalt structures has been calculated as a function of unit-cell volume using a first-principles periodic Hartree-Fock (HF) linear combination of atomic orbitals (LCAO) theory by Jaffee and Hess.[56] The total-energy data versus volume for the three phases are shown in Fig. 2 along with the fits to the empirical functional form of the third-order Murnaghan equation, which is used to calculate the derived structural properties,

[This article is copyrighted as indicated in the article. Reuse of AIP content is subject to the terms at: http://scitation.aip.org/termsconditions. Downloaded to] IP: 128.172.48.58 On: Mon, 19 Oct 2015 20:45:44

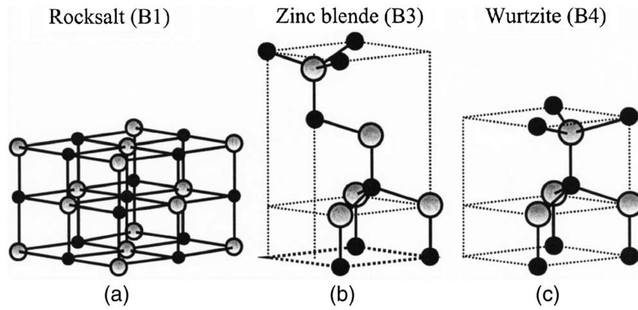

FIG. 1. Stick and ball representation of ZnO crystal structures: (a) cubic rocksalt ($B1$), (b) cubic zinc blende ($B3$), and (c) hexagonal wurtzite ($B4$). The shaded gray and black spheres denote Zn and O atoms, respectively.

$$E(V)=E_0-\frac{B_0V_0}{B'-1}+\frac{B_0V}{B'}\left[\frac{(V_0/V)^{B'}}{B'-1}+1\right], \quad (1)$$

where E_0, V_0, and B_0 are the total energy, volume per ZnO f.u., and bulk modulus at zero pressure (P), respectively, and $B'=dB/dP$ is assumed to be constant.

In this calculation, although E_0 represents the sum of the total energies of isolated neutral Zn and O atoms, the absolute value of the energy at the minimum of each curve was considered as a rough estimate of the equilibrium cohesive energy of the corresponding ZnO phases. The total energy (or roughly the cohesive energy per bond) in wurtzite variety was calculated to be −5.658 eV for wurtzite, −5.606 eV for zinc-blende, and −5.416 eV for rocksalt phases. Later, Jaffe *et al.*[57] employed the density-functional theory (DFT) using two different approximations, namely, the local-density approximation (LDA) and the generalized gradient approximation (GGA), in the exchange-correlation function to calculate the total energy and electronic structure of ZnO. In these calculations, cohesive energies were obtained by subtracting the total energy per ZnO f.u. of the solid at its equilibrium lattice constant from the energy of the corresponding isolated atoms. Using the LDA calculation technique, the equilibrium cohesive energy of ZnO was reported as −9.769, −9.754, and −9.611 eV for wurtzite, zinc-blende, and rocksalt structures, respectively. The best agreement with the experimental value of −7.52 eV, which is deduced from experimental Zn heat of vaporization, ZnO enthalpy of formation, and O_2 binding energy for the wurtzite phase,[58] was achieved using the GGA technique. It gives −7.692, −7.679, and −7.455 eV cohesive energies for wurtzite, zinc-blende, and rocksalt phases, respectively. In these two techniques, although the calculated energy difference $\Delta E_{\text{W-ZB}}$ between the wurtzite and zinc-blende lattices is small (about −15 and −13 meV/atom for LDA and GGA, respectively), whereas it is relatively large, ~50 meV/atom, for Hartree-Fock approximation, the wurtzite form is energetically preferable compared to zinc blende and rocksalt.

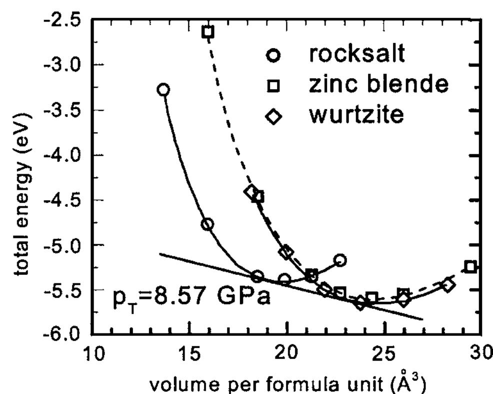

FIG. 2. Total energy vs volume (both per ZnO f.u.) for the three phases: zinc blende (squares), wurtzite (diamonds), and rocksalt (circles). The zero of energy is the sum of the total energy of an isolated Zn and an isolated O atom. [Reprinted with permission from J. E. Jaffe and A. C. Hess, Phys. Rev. B **48**, 7903 (1993). Copyright 1993 by the American Physical Society.]

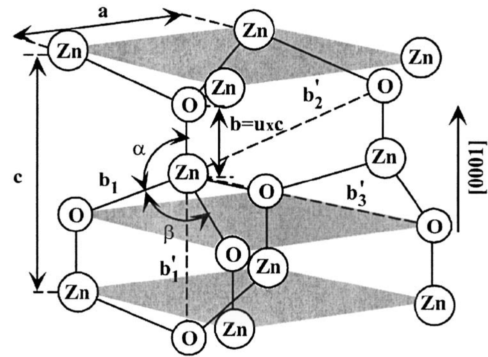

FIG. 3. Schematic representation of a wurtzitic ZnO structure having lattice constants a in the basal plane and c in the basal direction; u parameter is expressed as the bond length or the nearest-neighbor distance b divided by c (0.375 in ideal crystal), and α and β (109.47° in ideal crystal) are the bond angles.

The wurtzite structure has a hexagonal unit cell with two lattice parameters, a and c, in the ratio of $c/a=\sqrt{8/3}=1.633$ and belongs to the space group of C_{6v}^4 or $P6_3mc$. A schematic representation of the wurtzitic ZnO structure is shown in Fig. 3. The structure is composed of two interpenetrating hexagonal-close-packed (hcp) sublattices, each of which consists of one type of atom displaced with respect to each other along the threefold c-axis by the amount of $u=3/8=0.375$ (in an ideal wurtzite structure) in fractional coordinates (the u parameter is defined as the length of the bond parallel to the c axis, in units of c). Each sublattice includes four atoms per unit cell and every atom of one kind (group-II atom) is surrounded by four atoms of the other kind (group VI), or vice versa, which are coordinated at the edges of a tetrahedron. In a real ZnO crystal, the wurtzite structure deviates from the ideal arrangement, by changing the c/a ratio or the u value. It should be pointed out that a strong correlation exists between the c/a ratio and the u parameter in that when the c/a ratio decreases, the u parameter increases in such a way that those four tetrahedral distances remain nearly constant through a distortion of tetrahedral angles due to long-range polar interactions. These two slightly different bond lengths will be equal if the following relation holds:

$$u=\left(\frac{1}{3}\right)\left(\frac{a^2}{c^2}\right)+\frac{1}{4}. \quad (2)$$

Since the c/a ratio also correlates with the difference of the electronegativities of the two constituents, components with

[This article is copyrighted as indicated in the article. Reuse of AIP content is subject to the terms at: http://scitation.aip.org/termsconditions. Downloaded to] IP: 128.172.48.58 On: Mon, 19 Oct 2015 20:45:44

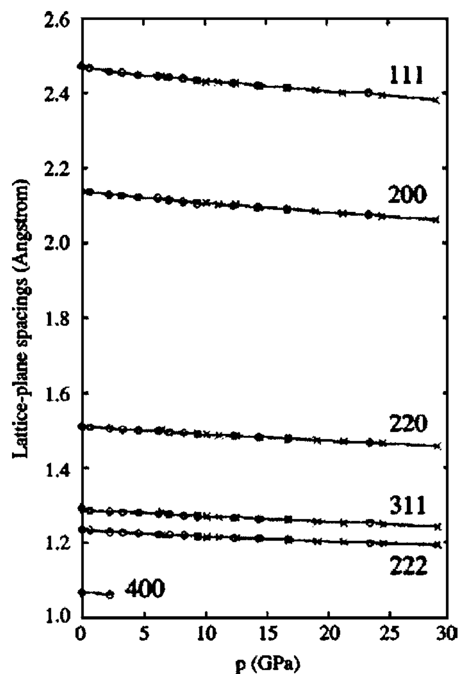

FIG. 4. Lattice-plane spacings as functions of pressure for the ZnO *B*1 phase. The crosses denote increasing pressure and the circles decreasing pressure. Miller indices *hkl* are indicated for each set of data. [Reprinted with permission from J. M. Recio, M. A. Blanco, V. Luaña, R. Pandey, L. Gerward, and J. Staun Olsen, Phys. Rev. B **58**, 8949 (1998). Copyright 1998 by the American Physical Society.]

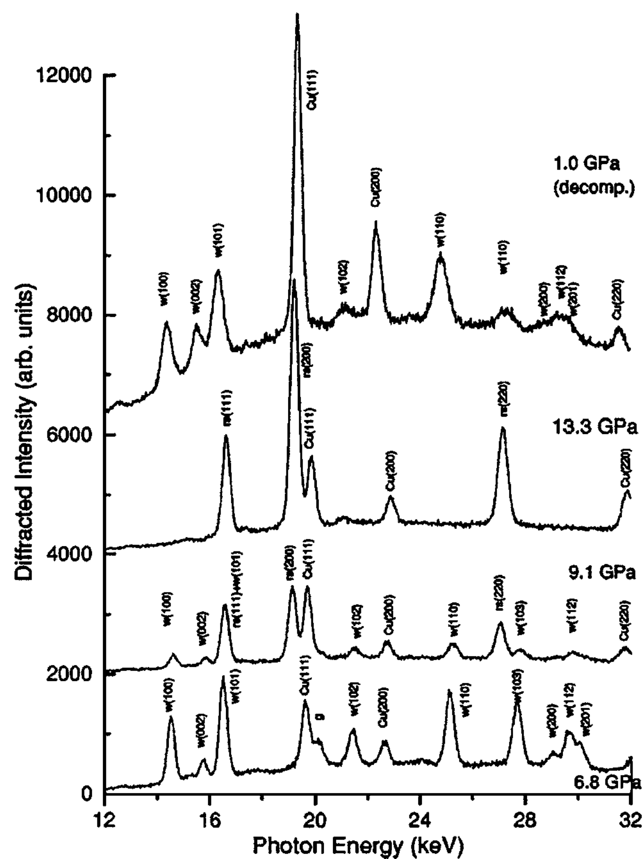

FIG. 5. Examples of EDXD spectra indicating the coexistence of the wurtzite and rocksalt phases around 9.1±0.2 GPa (increasing pressure) and the emergence of the wurtzite phase at $P < 1.9 \pm 0.2$ GPa upon decompression. The spectra are presented in cascade for clarity. The labels W and RS refer to wurtzite and rocksalt, respectively. The x-ray-diffraction lines from the Cu pressure gauge and the gasket material are labeled as Cu and g, respectively. [Reprinted with permission from S. Desgreniers, Phys. Rev. B **58**, 14102 (1998). Copyright 1998 by the American Physical Society.]

the greatest differences show the largest departure from the ideal c/a ratio.[59]

Like other II-VI semiconductors, wurtzite ZnO can be transformed to the rocksalt (NaCl) structure at relatively modest external hydrostatic pressures. The reason for this is that the reduction of the lattice dimensions causes the interionic Coulomb interaction to favor the ionicity more over the covalent nature. The space-group symmetry of the rocksalt-type of structure is *Fm*3*m*, and the structure is sixfold coordinated. However, the rocksalt structure cannot be stabilized by the epitaxial growth. In ZnO, the pressure-induced phase transition from the wurtzite (*B*4) to the rocksalt (*B*1) phase occurs at approximately 10 GPa and a large volume decrease of about 17%, as reported by Bates *et al.*[60] They found that high-pressure cubic phase is metastable for long periods of time even at ambient pressure and above 100 °C. More recently, energy-dispersive x-ray diffraction (EDXD) using synchrotron radiation has been employed to probe the phase transition in ZnO.[61,62] Gerward and Olsen[61] and Recio *et al.*[62] observed that the hexagonal wurtzite structure of ZnO undergoes a structural phase transformation with a transition pressure $p_{tr}=10$ GPa and completed at about 15 GPa. The measured lattice-plane spacings as a function of pressure for the *B*1 phase are shown in Fig. 4. Accordingly, a large fraction of the *B*1 phase is retained when the pressure is released, indicating the metastable state of the rocksalt phase of ZnO even at zero pressure.

In contrast, using *in situ* x-ray diffraction, Jamieson[63] and later, using EDXD, Desgreniers[64] reported that this transition is reversible at room temperature. A large number of EDXD spectra were recorded at pressures ranging from 0.1 MPa to 56±1 GPa at room temperature with increasing and decreasing pressures. A clear wurtzite-to-rocksalt transition was observed starting at 9.1±0.2 GPa with increasing pressure. The two phases coexist over a pressure range of 9.1–9.6 GPa, as shown in Fig. 5. The structural transition is completed at 9.6 GPa, resulting in a 16.7% change in the unit-cell volume. Upon decompression, it was observed that ZnO reverts to the wurtzite structure at 1.9±0.2 GPa, below which a single phase is present. The phase hysteresis is consequently substantial. Similar hysteresis was also reported by Karzel *et al.*[65] for this transition from x-ray and Zn-Mössbauer spectroscopy studies. The transition pressure was measured to be 8.7 GPa for increasing pressure, whereas it was 2.0 GPa for decreasing pressure.

On the theoretical side there have been several first-principles studies of compressive parameters of dense ZnO. Among them are the linear combination of Gaussian-type orbitals (LCGTO) HF method,[56] the full-potential linear muffin-tin orbital (FP-LMTO) approach to DFT within the LDA and GGA,[66] linear augmented plane-wave (LAPW) LDA,[65] HF,[67] correlated HF perturbed ion (HF-PI) models,[62] LCGTO-LDA and GGA methods,[62] and the extended ionic model.[68] A critical comparison between experimental and theoretical results can be made for ZnO as the structural and

[This article is copyrighted as indicated in the article. Reuse of AIP content is subject to the terms at: http://scitation.aip.org/termsconditions. Downloaded to] IP: 128.172.48.58 On: Mon, 19 Oct 2015 20:45:44

TABLE I. Theoretical and experimental pressure parameters of ZnO.

	Expt. results					Theor. calc.				
	Ref. 60	Ref. 63	Ref. 65	Ref. 61	Ref. 64	Ref. 57	Ref. 56	Ref. 66	Ref. 65	Ref. 70
Volume wurtzite (Å^3)	23.829		23.796	23.785	23.81	23.346	24.570	23.62		23.839
Volume rocksalt (Å^3)	19.60	19.40	19.484	19.60	19.60	19.515	19.799	19.08		19.041
Volume change, $\Delta V/V$ (%)	16.7		18.13	18.0	17.68	16.41	19.42	18.8	17.9	20.3
Transition pressure, p_{tr} (GPa)	9.5	9.0	8.7	10.0	9.1	9.32	8.57	8.0	14.5	10.45

compressive parameters are measured since the dense solid adopts simple structures. These calculations have mostly been limited to the same pressure range as the experiments, and reasonable agreements are realized. Both experimental and theoretical results are summarized in Table I for comparison.

In addition to the commonly observed and calculated phase transition of ZnO from $B4$ to $B1$ at moderate pressure (maximum pressure attained in any experiment on ZnO to date is 56 GPa where the $B1$ phase remained stable) it has been suggested[69] that at a sufficiently high pressure, ZnO should undergo a phase transformation from the sixfold-coordinated $B1$ (cubic NaCl) to the eightfold-coordinated $B2$ (cubic CsCl) structure, in analogy to the alkali halides and alkaline-earth oxides. Jaffe *et al.*[57] predicted the transition pressure from the $B1$ phase to the $B2$ phase at $p_{T2}=260$ and 256 GPa by employing LDA and GGA, respectively, whereas Zaoui and Sekkal[70] calculated the transition pressure at a higher value of $p_{T2}=352$ GPa by using atomistic calculations based on an interatomic pair potential within the shell-model approach. However, these theoretical predictions are still awaiting experimental observation for comparison.

The zinc-blende ZnO structure is metastable and can be stabilized only by heteroepitaxial growth on cubic substrates, such as ZnS,[71] GaAs/ZnS,[72] and Pt/Ti/SiO_2/Si,[73] reflecting topological compatibility to overcome the intrinsic tendency of forming a wurtzite phase. In the case of highly mismatched substrates, there is usually a certain amount of the zinc-blende phase of ZnO separated by crystallographic defects from the wurtzite phase. The symmetry of the zinc-blende structure is given by space group $F\bar{4}3m$ and composed of two interpenetrating face-centered-cubic (fcc) sublattices shifted along the body diagonal by one-quarter of a body diagonal. There are four atoms per unit cell and every atom of one type (group II) is tetrahedrally coordinated with four atoms of the other type (group VI), and vice versa.

Because of the tetrahedral coordination of wurtzite and zinc-blende structures, the four nearest neighbors and 12 next-nearest neighbors have the same bond distance in both structures. Stick and ball stacking models for $2H$ wurtzitic and $3C$ zinc-blende polytypes of ZnO crystals are shown in Fig. 1. The main difference between these two structures lies in the stacking sequence of closed-packed diatomic planes. The wurtzite structure consists of triangularly arranged alternating biatomic close-packed (0001) planes, for example, Zn and O pairs, thus the stacking sequence of the (0001) plane is $AaBbAaBb\cdots$ in the $\langle 0001\rangle$ direction. In contrast, the zinc-blende structure consists of triangularly arranged atoms in the closed-packed (111) planes along the $\langle 111\rangle$ direction that causes a stacking order of $AaBbCcAaBbCc\cdots$. The small and large letters stand for the two different kinds of constituents.

Since none of the three structures described above possess an inversion symmetry, the crystal exhibits crystallographic polarity, which indicates the direction of the bonds, i.e., closed-packed (111) planes in zinc-blende and rocksalt structures and corresponding (0001) basal planes in the wurtzite structure differ from $(\bar{1}\bar{1}\bar{1})$ and $(000\bar{1})$ planes, respectively. The convention is that the [0001] axis points from the face of the O plane to the Zn plane and is the positive z direction. In other words, when the bonds along the c direction are from cation (Zn) to anion (O), the polarity is referred to as Zn polarity. By the same argument, when the bonds along the c direction are from anion (O) to cation (Zn), the polarity is referred to as O polarity. Many properties of the material depend also on its polarity, for example, growth, etching, defect generation and plasticity, spontaneous polarization, and piezoelectricity. In wurtzite ZnO, besides the primary polar plane (0001) and associated direction $\langle 0001\rangle$, which are the most commonly used surface and direction for growth, many other secondary planes and directions exist in the crystal structure.

B. Lattice parameters

The lattice parameters of a semiconductor usually depend on the following factors: (i) free-electron concentration acting via deformation potential of a conduction-band minimum occupied by these electrons, (ii) concentration of foreign atoms and defects and their difference of ionic radii with respect to the substituted matrix ion, (iii) external strains (for example, those induced by substrate), and (iv) temperature. The lattice parameters of any crystalline material are commonly and most accurately measured by high-resolution x-ray diffraction (HRXRD) by using the Bond method[74] for a set of symmetrical and asymmetrical reflec-

[This article is copyrighted as indicated in the article. Reuse of AIP content is subject to the terms at: http://scitation.aip.org/termsconditions. Downloaded to] IP: 128.172.48.58 On: Mon, 19 Oct 2015 20:45:44

TABLE II. Measured and calculated lattice constants and u parameter of ZnO.

a (Å)	c (Å)	c/a	u	Ref.
		Wurtzite		
3.2496	5.2042	1.6018	0.3819	65[a]
3.2501	5.2071	1.6021	0.3817	59[b]
3.286	5.241	1.595	0.383	660[c]
3.2498	5.2066	1.6021		64[d]
3.2475	5.2075	1.6035		61[e]
3.2497	5.206	1.602		9[f]
		1.593	0.3856	56[g]
		1.600	0.383	661[h]
		Zinc blende		
		4.619,[c] 4.60,[g] 4.463,[i] 4.37,[i] 4.47[i]		
		Rocksalt		
		4.271,[a] 4.283,[d] 4.294,[e] 4.30,[g] 4.280,[j] 4.275,[k] 4.058,[k] 4.316,[k] 4.207,[k] 4.225[l]		

[a]Measured by using x-ray diffraction.
[b]Measured by using x-ray diffraction.
[c]Calculated by using *ab initio* periodic linear combination of atomic orbitals (LCAO) methods, based mainly on the Hartree-Fock Hamiltonian, with an all-electron Gaussian-type basis set.
[d]Measured by using EDXD.
[e]Measured by using x-ray diffraction.
[f]Measured by using x-ray powder diffraction.
[g]Calculated by using first-principles periodic Hartree-Fock (HF) linear combination of atomic orbitals (LCAO) program.
[h]Calculated by using *ab initio* quantum-mechanical level through the Berry-phase scheme applied to delocalized crystalline orbitals and through the definition of well-localized Wannier functions.
[i]Measured by using RHEED, XRD, and TEM (Ref. 72).
[j]Measured by using x-ray diffraction (Ref. 60).
[k]Measured by using EDXD, and calculated using Coulomb-Hartree-Fock pertubed ion, GGA, and LDA methods (Ref. 62).
[l]Calculated by using first-principles periodic Hartree-Fock (Ref. 67).

tions. Table II shows a comparison of measured and calculated lattice parameters, c/a ratio, and u parameter reported by several groups for ZnO crystallized in wurtzite, zinc-blende, and rocksalt structures.

For the wurtzite ZnO, lattice constants at room temperature determined by various experimental measurements and theoretical calculations are in good agreement. The lattice constants mostly range from 3.2475 to 3.2501 Å for the a parameter and from 5.2042 to 5.2075 Å for the c parameter. The data produced in earlier investigations reviewed by Reeber[9] are also consistent with the values given in Table II. The c/a ratio and u parameter vary in a slightly wider range, from 1.593 to 1.6035 and from 0.383 to 0.3856, respectively. The deviation from that of the ideal wurtzite crystal is probably due to lattice stability and ionicity. It has been reported that free charge is the dominant factor responsible for expanding the lattice proportional to the deformation potential of the conduction-band minimum and inversely proportional to the carrier density and bulk modulus. The point defects such as zinc antisites, oxygen vacancies, and extended defects, such as threading dislocations, also increase the lattice constant, albeit to a lesser extent in the heteroepitaxial layers.

For the zinc-blende polytype of ZnO, the calculated lattice constants based on a modern *ab initio* technique are predicted to be 4.60 and 4.619 Å. Ashrafi *et al.*[72] characterized the zinc-blende phase of ZnO films grown by plasma-assisted metal-organic molecular-beam epitaxy using reflection high-energy electron-diffraction (RHEED), x-ray-diffraction (XRD), transmission electron microscope (TEM), and atomic-force microscope (AFM) measurements. They have found that using a ZnS buffer layer led to the growth of the zinc-blende ZnO films. The lattice constants of the epilayer were estimated as 4.463, 4.37, and 4.47 Å by using the spacing of the RHEED pattern, albeit spotty, comparing the XRD peak position, and examining the TEM, respectively. These values are far from that of the wurtzite phase, indicating the formation of zinc-blende ZnO. The lattice constant measured with the RHEED technique is in very good agreement with the theoretical prediction.

A high-pressure phase transition from the wurtzite to the rocksalt structure decreases the lattice constant down to the range of 4.271–4.294 Å. The experimental values obtained by x-ray diffraction are in close agreement. The predicted lattice parameter of 4.058–4.316 Å using various calculation techniques, such as the HF-PI, GGA, and HF, are about 5% smaller or larger than the experimental values. The discrepancy in the calculated values is larger than the measured ones.

Desgreniers[64] has investigated whether the u parameter and the ideal correlation between u and c/a are affected by the compression of the ZnO wurtzite lattice. The change in c/a axial ratio was measured up to ~10 GPa, and a pressure coefficient of $d(c/a)/dP=-0.0005\pm0.0001\ \mathrm{GPa}^{-1}$ was obtained from a linear fit (giving $c/a=1.6021$ at atmospheric pressure) to the experimental data. Even though the variation with pressure seems within the experimental error, this pressure coefficient is in agreement with previously published experimental [$-0.0007\ \mathrm{GPa}^{-1}$ (Ref. 65)] and predicted [$-0.0005\ \mathrm{GPa}^{-1}$ (Ref. 56)] values. The effect of pressure-induced change of the axial ratio on the u parameter versus a possible breakdown of the ideal relationship between the axial ratio and u was isolated by recording the pressure-dependence variation of x-ray-diffraction intensity. It has been concluded that the ideal relationship between the c/a axial ratio and the u oxygen positional parameter is preserved as the wurtzite lattice becomes denser while approaching the structural transition pressure.

C. Electronic band structure

The band structure of a given semiconductor is pivotal in determining its potential utility. Consequently, an accurate knowledge of the band structure is critical if the semiconductor in question is to be incorporated in the family of materials considered for device applications. Several theoretical approaches of varying degrees of complexity have been employed to calculate the band structure of ZnO for its wurzite, zinc-blende, and rocksalt polytypes. Besides, a number of experimental data have been published regarding the band structure of the electronic states of wurtzite ZnO. X-ray- or UV reflection/absorption or emission techniques have conventionally been used to measure the electronic core levels in solids. These methods basically measure the energy difference by inducing transitions between electronic levels (for

[This article is copyrighted as indicated in the article. Reuse of AIP content is subject to the terms at: http://scitation.aip.org/termsconditions. Downloaded to] IP: 128.172.48.58 On: Mon, 19 Oct 2015 20:45:44

example, transitions from the upper valence-band states to the upper conduction-band states, and from the lower valence-band states) or by exciting collective modes (for example, the upper core states to the lower edge of the conduction band and to excitations of plasmons). Another important method for the investigation of the energy region is based on the photoelectric effect extended to the x-ray region, namely, photoelectron spectroscopy (PES). The peaks in emission spectrum correspond to electron emission from a core level without inelastic scattering, which is usually accompanied by a far-less-intense tail region in the spectrum. More recently, angle-resolved photoelectron spectroscopy (ARPES) technique has started to be used. This technique together with synchrotron radiation excitation has been recognized as a powerful tool that enables experimental bulk and surface electronic band-structure determinations under the assumptions of k conservation and single nearly-free-electron-like final band.[75] After the theoretical work on band-structure calculation of ZnO proposed by Rössler using Green's function [Korringa-Kohn-Rostoker (KKR) method][76] in 1969, there have been several experimental works[77–80] performed on the wurtzite ZnO which proved Rössler's predicted bulk electronic structure to be far from satisfactory. Langer and Vesely[77] have reported experimental data related to the energy levels of core electrons in ZnO using x-ray-induced photoemission spectroscopy. They have drawn two conclusions from their studies: (i) the location of the Zn 3d level in ZnO has been unambiguously determined and (ii) the discrepancy between the measured values and the theoretically determined energy values was angular momentum dependent. Powell *et al.*[78,79] have carried out UV photoemission measurements on hexagonal ZnO cleaved in vacuum. Those authors have placed the Zn 3d core level at about 7.5 eV below the valence-band maximum, which is 3 eV lower than the value predicted by Rössler's band calculation. This assignment also showed good agreement with x-ray photoemission results reported by Vesely *et al.*[81] (8.5 eV) and Ley *et al.*[80] (8.81 eV). In the following years, LDA and tight-binding methods were employed[82–85] by considering the Zn 3d states as core levels to ease calculations. Satisfactory agreement with qualitative valence-band dispersions was achieved with this assumption. However, quantitative disagreements remained and the location of the Zn 3d states could not be predicted. Most recently, with the advent of computer capabilities, theoretical works have taken to include the effect of the Zn 3d level in the calculations and thus to consider them as valence-band states.[86–89] These methods enable an estimation of the position of the Zn 3d states and also take into account their non-negligible influence on the s- and p-derived valence bands.

Recently, Girard *et al.*[90] have studied the electronic structure of the ZnO (0001) surface by angle-resolved photoelectron spectroscopy. They recorded both normal and off-normal-emission spectra, which give valuable information about bulk and surface states as well as the Zn 3d states. Figure 6 shows some of the normal-emission spectra recorded at photon energies ranging from 20 to 50 eV and the information extracted from these data for bulk-band structure. In these measurements, the binding energies were referred to the Fermi level and the intensities were normalized to the photon flux. Among all the spectra displayed, seven features were seen, labeled from A to G. The dispersions of the four valence bands observed in the (0001) direction were compared with theory based on LDA calculations, which consider the Zn 3d electrons as part of the valence band,[86] and good agreement was realized. It should also be noted that the Zn 3d states were observed to separate into two groups of four and six bands, which show dispersion with k, which is in agreement with theoretical results, but the location of these states (about 10.5 eV below Fermi level) were not accurately predicted.

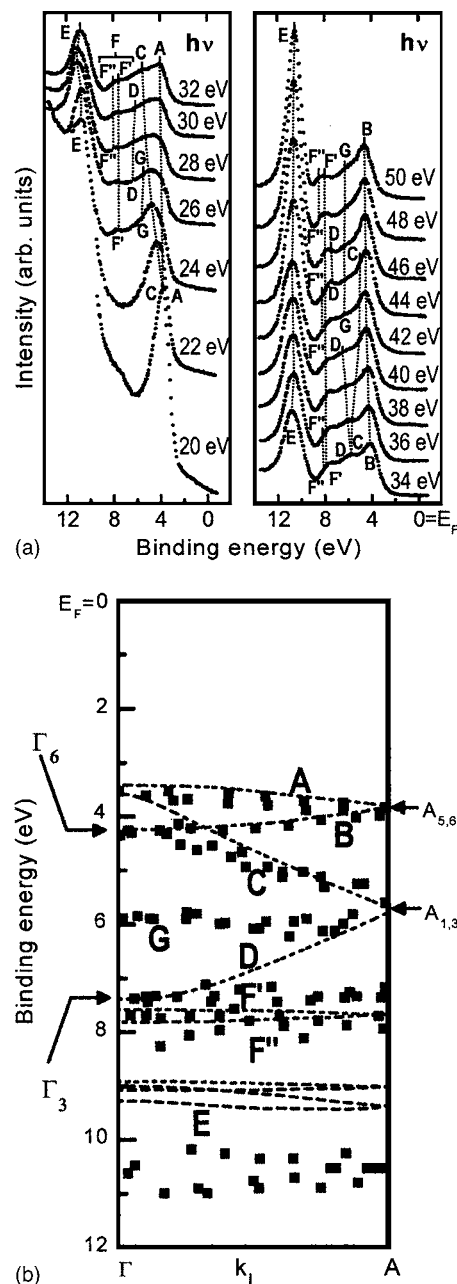

FIG. 6. (a) Normal-emission spectra for photon energies ranging from 20 to 50 eV. The spectra were normalized with respect to the photon flux. (b) The bulk-band structure of ZnO, ΓA corresponding to 0.6 Å^{-1}. [Reprinted from R. T. Girard, O. Tjernberg, G. Chiaia, S. Söderholm, U. O. Karlsson, C. Wigren, H. Nylèn, and I. Lindau, Surf. Sci. **373**, 409 (1997), Copyright 1997, with permission from Elsevier.] The dashed lines are the LDA calculation results reproduced from Schröer *et al.* (Ref. 86).

[This article is copyrighted as indicated in the article. Reuse of AIP content is subject to the terms at: http://scitation.aip.org/termsconditions. Downloaded to] IP: 128.172.48.58 On: Mon, 19 Oct 2015 20:45:44

The polar (0001)-Zn and (000$\bar{1}$)-O surfaces and the nonpolar (10$\bar{1}$0) surface (m plane) have also been the object of experimental and theoretical investigations. Of these surfaces, the nonpolar (10$\bar{1}$0) surface is of particular interest from the viewpoint of surface chemistry, because the surface is terminated with the same number of O and Zn atoms. The low-energy electron-diffraction (LEED) studies have revealed that the surface undergoes relaxation, which is characterized by downward shift (spatially) of both surface Zn and O atoms, with a greater shift for the Zn atom than the O atom, resulting in the Zn–O bond rotation by 6.2° (Ref. 91) or 11.5° (Ref. 92) with respect to the ideal surface plane. Such a surface relaxation should influence the energetic position as well as the dispersion width of the surface dangling-bond bands of the occupied O 2p and unoccupied Zn 4s states. Besides, several theoretical studies have indicated that, upon relaxation, the O 2p dangling-bond state is stabilized while the Zn 4s dangling-bond state shifts up in energy.[84,88,93] The theoretically determined position of these dangling-bond bands, especially the occupied O 2p dangling-bond band, relative to the bulk bands projected onto the (10$\bar{1}$0) surface varies depending on the method employed in the calculations.

A detailed experimental study applied to both polar and nonpolar surfaces of ZnO has been carried out by Göpel *et al.*[94] using ARPES. They have identified two surface-induced features at the Γ, M, and X points of the surface Brillouin zone (BZ) and have assigned these states to the O 2p-derived dangling-bond state and the Zn–O back-bond state. Zwicker and Jacobi[95] have also performed the ARPES study on the ZnO (10$\bar{1}$0) surface and have revealed the valence-band structure along the ΓM axis of the bulk BZ. In this experiment, however, a surface-related state was not identified and all the observed peaks were attributed to the bulk-band transitions. Recently, the off-normal ARPES spectra in the $\bar{\Gamma}\bar{M}$, $\bar{\Gamma}\bar{K}$, and $\bar{K}\bar{M}$ directions were recorded for 20, 34, and 44 eV photon energies at emission angles ranging between 0° and 30° by Girard *et al.*[90] From these measurements, two surface states were observed on the (0001) surface. One state, at 7.5 eV binding energy, which was also predicted by theory, was interpreted as arising from the "backbonding" of the Zn 4s-O 2p mixed bulk states. The other one, at 4.5 eV below Fermi level, which was not predicted by theoretical calculations, was related to Zn 4p-O 2p derived states.

More recently, detailed ARPES studies were performed to investigate the two-dimensional band structure of the O 2p dangling-bond state on the ZnO (10$\bar{1}$0) surface along the selected high-symmetry axes of the surface BZ, i.e., the $\bar{\Gamma}\bar{X}$ and $\bar{\Gamma}\bar{X}'$ axes.[96] The energetic position relative to the projected bulk bands and the dispersion width of the dangling-bond band were determined and compared with the calculated band structures by Wang and Duke[93] and by Schröer *et al.*[88] Figure 7 shows off-normal-emission spectra taken at various detection angles along the [1$\bar{2}$10] ($\bar{\Gamma}\bar{X}$) and [0001] ($\bar{\Gamma}\bar{X}'$) azimuths and measured dispersion of the O 2p

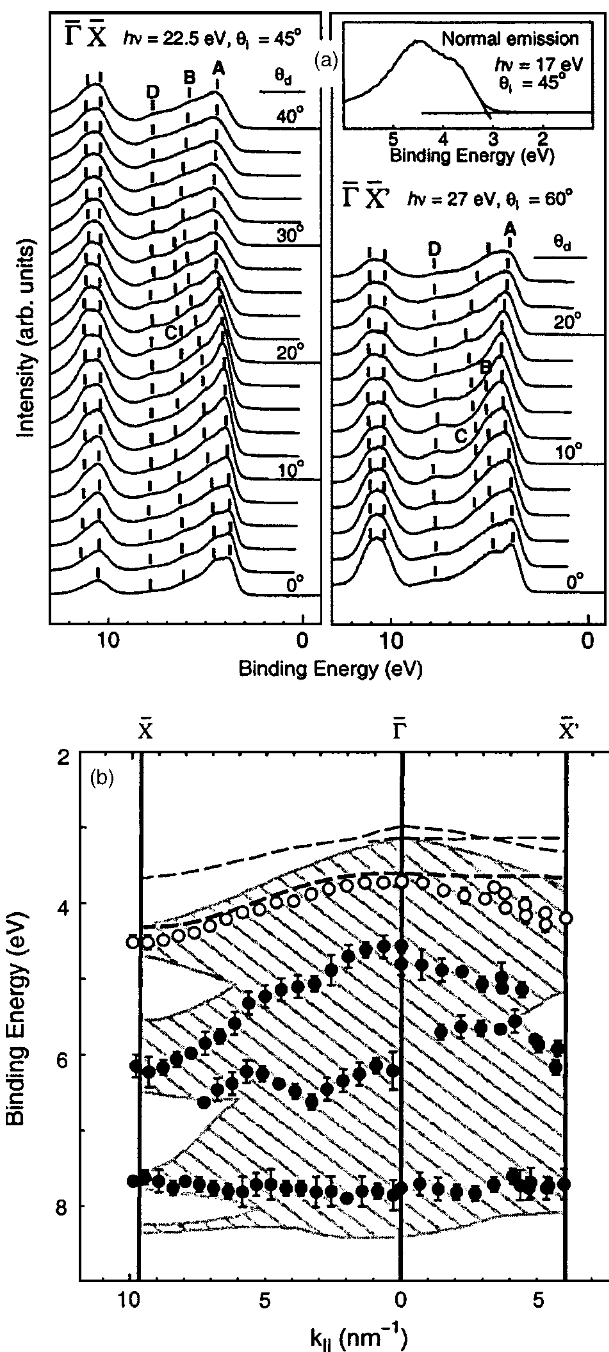

FIG. 7. (a) Off-normal-emission spectra of the clean surface recorded at $h\nu$=22.5 eV and θ_i=55° along the [1$\bar{2}$10] ($\bar{\Gamma}\bar{X}$) direction and at $h\nu$=27 eV and θ_i=55° along the [0001] ($\bar{\Gamma}\bar{X}'$) direction. The incidence plane of the light was parallel to the [1$\bar{2}$10] direction for both detection directions. The spectra are shown with 2° interval. The peak positions, indicated by the vertical bars, were determined from the second derivative of the spectra. The position of the valence-band maximum was determined from the normal-emission spectrum taken at $h\nu$=17 eV by extrapolating the onset of the valence-band emission as shown in the inset of the right panel. (b) The measured dispersion of the O 2p dangling-bond state (open circles) and the bulk-band-related states (filled circles) along the $\bar{\Gamma}\bar{X}$ and $\bar{\Gamma}\bar{X}'$ axes. The hatched area corresponds to the projected bulk-band region and the bold dashed line indicates the O 2p dangling-bond bands, both of which have been calculated using the sp^3 model by Wang and Duke (Ref. 93). The thin dashed lines which are located above the projected bulk bands are the dangling-bond bands obtained from the LDA calculations. [Reprinted with permission from K. Ozawa, K. Sawada, Y. Shirotori, K. Edamoto, and M. Nakatake, Phys. Rev. B **68**, 125417 (2003). Copyright 2003 by the American Physical Society.]

[This article is copyrighted as indicated in the article. Reuse of AIP content is subject to the terms at: http://scitation.aip.org/termsconditions. Downloaded to] IP: 128.172.48.58 On: Mon, 19 Oct 2015 20:45:44

dangling-bond state and the bulk-band-related states along the $\bar{\Gamma}\bar{X}$ and $\bar{\Gamma}\bar{X}'$ axes together with theoretical calculation for comparison.

From photon-energy-dependent measurements and K and O_2 adsorption studies it has been found that the surface-localized O 2*p* dangling-bond state exists at 3.7 eV below the Fermi level at the $\bar{\Gamma}$ point in the surface Brillouin zone and shifts to the higher-binding-energy side by 0.8 and 0.5 eV along the $\bar{\Gamma}\bar{X}$ and $\bar{\Gamma}\bar{X}'$ axes, respectively. Measurements on K- and O_2-exposed ZnO $(10\bar{1}0)$ surfaces helped to identify which peaks in the angle-resolved photoelectron spectra were associated with the states localized at the surface. The O 2*p* dangling-bond band was found to be located below the upper edge of the projected bulk bands along these two high-symmetry axes. The empirical tight-binding calculations performed by Ivanov and Pollmann[84] and by Wang and Duke,[93] which emphasize the ionic and covalent characters of the Zn–O bonds, respectively, predict that the gap state by the O 2*p* dangling bond is not formed at least along the $\bar{\Gamma}\bar{X}$ and $\bar{\Gamma}\bar{X}'$ axes. On the other hand, Schröer *et al.* have found in their LDA study that the dangling-bond band is formed within the gap above the upper edge of the projected bulk bands along the major high-symmetry axes of the surface BZ. Therefore, it has been concluded that the experimental study is consistent qualitatively with the band structure given by the two empirical tight-binding approaches.

The theoretical calculation of the band structure of ZnO mostly involve the LDA,[86,97–99] which is very demanding because of the cationic *d* electrons. If the *d* electrons are treated as core electrons, the calculated lattice constant underestimates the experimental values by as much as 18% for wurtzite ZnO, while inclusion of the *d* electrons in the valence band yields very accurate lattice constants. However, even if the *d* electrons are properly taken into account, the results of standard LDA calculations show distinct shortcomings, such as strongly underestimated band gap and overestimated occupied cationic *d* bands, which roughly reside 3 eV high in energy as compared to experiment. In addition, their interactions with the anion *p* valence bands are artificially enlarged, resulting in overestimated dispersion and bandwidth of the latter and shifting them unphysically close to the conduction bands. For example, the LDA underestimates the ZnO band gap to be as low as $E_g^{\mathrm{LDA}}=0.23$ eV, as opposed to $E_g^{\mathrm{exp}}=3.37$ eV. Zakharov *et al.*[100] have recently reported plane-wave *GW* method for a number of II-VI compounds. They simply treated the *d* electrons as core electrons and deliberately carried out their *GW* calculation at the experimental lattice constants. They obtained very good results for the anion *p* valence bands and for the band-gap energies but no assertion concerning the *d*-band positions could be made. Recently, Vogel *et al.*[89] suggested an alternative approach to treat the II-VI semiconductor compounds, which approximately incorporates dominant self-interaction corrections. It has been shown that self-interaction corrections to LDA can be very important for a quantitative description of a system with strongly localized states such as 3*d* electrons. Their results along with the previous LDA calculations and the O 2*p* valence bands are shown in Fig. 8 in more detail

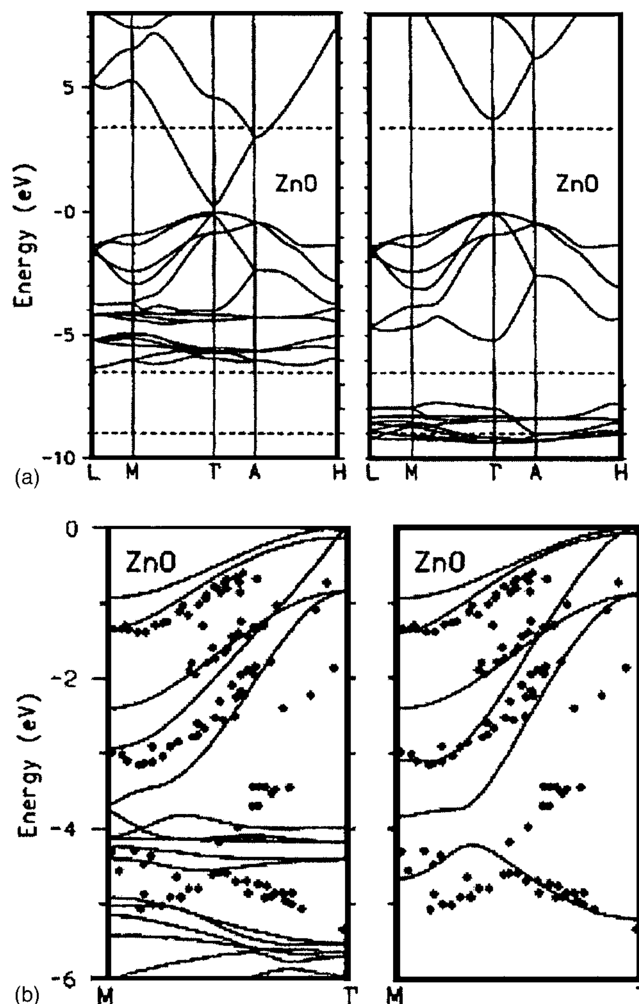

FIG. 8. (a) LDA bulk-band structure of ZnO as calculated using a standard pseudopotential (PP) (left panel) and using SIC-PP (right panel). The horizontal dashed lines indicate the measured gap energy and *d*-band width. (b) Comparison of the calculated and measured valence bands of ZnO. The left panel shows the standard LDA, while the right panel shows the SIC-PP results. [Reprinted with permission from D. Vogel, P. Krüger, and J. Pollmann, Phys. Rev. B **52**, R14316 (1995). Copyright 1995 by the American Physical Society.]

with the ARPES data for comparison. The left panel in (a) shows the standard LDA result, which reveals the above-mentioned shortcomings. The right panel shows the band structure as calculated with the self—interaction corrected pseudopotential (SIC-PP) approach included in the LDA. It has been observed that the *d* bands are shifted down in energy considerably and concomitantly the band gap is opened drastically. The dispersion and bandwidth of the O 2*p* are also changed. As compared to experimental data, the standard LDA result is obscured by the artificially high-lying bands leading to strong *p*-*d* interactions with the O 2*p* bands. The SIC-PP results are in better agreement with experiments. The calculated and measured energy gaps, the position of the cation *d* band, and anion valence bandwidths of ZnO are given in Table III. Based on this table, the LDA-SIC-PP approximation gives close agreement with the experimental results for band gap and bandwidth compared to the standard LDA method. However, the *d* bands result in energy roughly 1 eV too low as compared to the experimental value. This

[This article is copyrighted as indicated in the article. Reuse of AIP content is subject to the terms at: http://scitation.aip.org/termsconditions. Downloaded to] IP: 128.172.48.58 On: Mon, 19 Oct 2015 20:45:44

TABLE III. Calculated and measured energy gaps E_g, cation d-band positions E_d, and anion p valence bandwidths W_p (in eV) of ZnO [Vogel *et al.* (Ref. 89)]. LDA-PP, local-density approximation pseudopotential; LDA-SIC-PP, local-density approximation self-interaction-corrected pseudopotential.

	LDA-PP	LDA-SIC-PP	Expt.
E_g	0.23	3.77	3.4
E_d	−5.1	−8.9	−7.8
W_p	−3.99	−5.2	−5.3

deviation was attributed to the measured exciton energies influenced by electronic relaxations, which is expected to be mostly pronounced for the highly localized cationic semicore d states.

The electronic band structure of the other phases of ZnO has also been studied by a number of researchers.[56,57,101,102] For example, recently, Jaffe *et al.*[57] utilized both the LDA and the PBE96 form of the GGA together with optimized Gaussian basis sets to expand the crystal orbitals and periodic electron density in order to calculate the electronic structure for ZnO in the $B4$ (wurtzite), $B3$ (zinc blende), $B1$ (rocksalt), and $B2$ (CsCl) crystal structures over a range of unit-cell volumes. Figures 9 and 10 show the calculated band structure and the total density of states (DOS) of ZnO for different phases. When wurtzite ZnO is compressed, it has been observed that the peak at the top of the upper valence band is slightly reduced in height and shifted down in energy, the O 2s- and Zn 3d-derived peaks are slightly broadened and shifted up in energy, and a splitting appears in the Zn 3d states. While transforming to the $B1$ structure at the transition pressure p_{T1}, significant changes have been observed, in particular, the peak near the valence-band maximum is greatly reduced in height. The Zn 3d peak also becomes narrower, and the O 2s-derived states drop slightly in energy. Upon compression of the $B1$-phase ZnO through the wide pressure range from p_{T1} to p_{T2}, it has been observed that the upper valence band broadens greatly, the splitting of the Zn 3d peak in the DOS shows a large increase, and the O 2s-derived band moves down in energy and broadens. The fundamental band gap also increases with increasing pressure in this range. With the $B1 \rightarrow B2$ transition, the upper valence bandwidth remains almost unchanged but the peak near the valence-band maximum reappears. The structure of

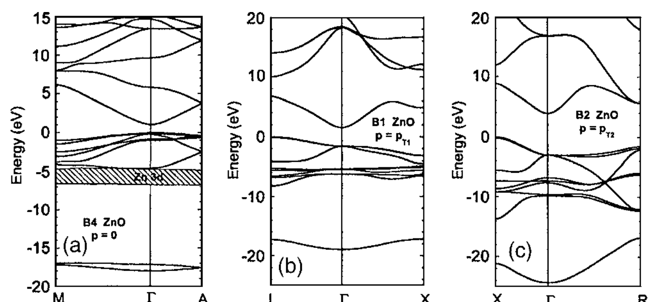

FIG. 9. Band structures for ZnO: (a) $B4$ structure at $p=0$, (b) $B1$ structure at $p=p_{T1}$, and (c) $B2$ structure at $p=p_{T2}$. [Reprinted with permission from J. E. Jaffe, J. A. Snyder, Z. Lin, and A. C. Hess, Phys. Rev. B **62**, 1660 (2000). Copyright 2000 by the American Physical Society.]

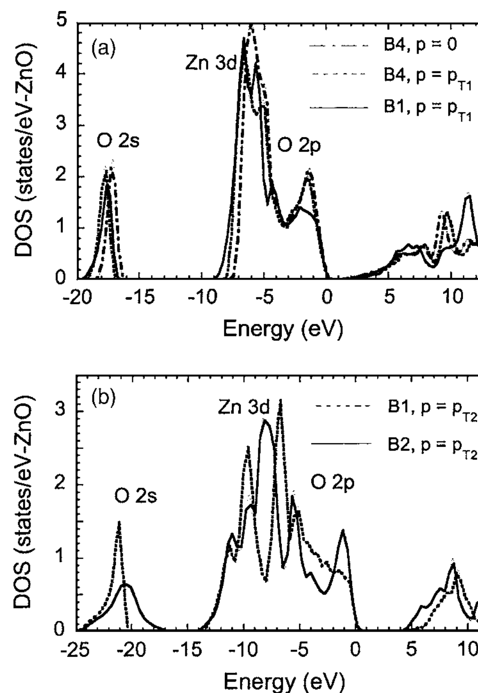

FIG. 10. Total density of states (DOS) for ZnO in the (a) $B4$ structure at $p=0$ and $p=p_{T1}$, $B1$ structure at $p=p_{T1}$, and (b) $B1$ and $B2$ structures at $p=p_{T2}$. [Reprinted with permission from J. E. Jaffe, J. A. Snyder, Z. Lin, and A. C. Hess, Phys. Rev. B **62**, 1660 (2000). Copyright 2000 by the American Physical Society].

the Zn 3d states changes radically with the O 2p-derived states because of heavy hybridization, and the O 2s-derived states broaden further and shift up in energy. From these observations of ZnO band structure with compression and changed atomic coordination it has been argued that the key features are (a) changes in nearest-neighbor bond lengths as they affect overlaps and bandwidths and (b) changes in symmetry as they affect p-d hybridization and band repulsion. As the neighboring atoms approach each other with compression of the solid, basis functions (and orbitals in a Hückel-like picture[103]) overlap more strongly, producing increased dispersion of the electron bands in k space and consequently increased bandwidths along the energy axis. However, it has also been considered that when there is a phase transition to a structure of increased coordination, the nearest-neighbor bonds lengthen even though the density is increased. The behavior of the bandwidths up to p_{T2} reflects these considerations. The band structures reveal further qualitative changes that occur with the change of symmetry at the structural transitions. Where the symmetry permits hybridization of O 2p- and Zn 3d-derived bands, there is an effective repulsion between them, which pushes the anion 2p states upwards. In the tetrahedrally coordinated $B4$ phase this repulsion is present throughout the Brillouin zone, but in the cubic $B1$ and $B2$ structures it is suppressed near the Γ point as a result of the inversion symmetry through the atomic center. Consequently, the highest valence bands are repelled upwards near the zone boundaries but not at the zone center, so that the valence-band maximum now occurs at the zone boundary. This accounts for the change in shape of the band edge seen in the total DOS plots. There is also a change in the form of

[This article is copyrighted as indicated in the article. Reuse of AIP content is subject to the terms at: http://scitation.aip.org/termsconditions. Downloaded to] IP: 128.172.48.58 On: Mon, 19 Oct 2015 20:45:44

the Zn 3d-derived bands, which are now narrowest near the Γ point as a result of the suppressed hybridization there. In the $B2$ structure the Zn 3d and O 2p states are completely hybridized and cannot be disentangled.

D. Mechanical properties

The mechanical properties of materials involve various concepts such as hardness, stiffness, and piezoelectric constants, Young's and bulk moduli, and yield strength. In hexagonal crystals, there exist five independent elastic constants: C_{11}, C_{33}, C_{12}, C_{13}, and C_{44}. Elastic constants C_{11} and C_{33} correspond to longitudinal modes along the [1000] and [0001] directions, respectively. Elastic constants C_{44} and $C_{66}=(C_{11}-C_{12})/2$ (owing to symmetry) can be determined from the sound velocity of transverse modes propagating along the [0001] and [1000] directions, respectively. The remaining constant C_{13} is present in combination with four other moduli in the velocity of modes propagating in less-symmetrical directions, such as [0011]. The bulk modulus is related to the elastic constants by[104]

$$B=\frac{(C_{11}+C_{12})C_{33}-2C_{13}^2}{C_{11}+C_{12}+2C_{33}-4C_{13}}. \quad (3)$$

Although the wurtzite ZnO crystal is acoustically anisotropic, there is only a very small difference between the shear sound velocities ν_{TA1} and ν_{TA2} propagating along the [001] and [100] directions, respectively ($\nu_{TA2}/\nu_{TA1}\cong 0.98$). In the isotropic approximation, the Young modulus E and shear modulus G can also be evaluated using the relations $E=3B(1-2\nu)$ and $G=E/2(1+\nu)$, respectively. The term ν is the Poisson ratio and is given by $\nu=C_{13}/(C_{11}+C_{12})$.

It has been argued that the most precise technique used to determine the elastic moduli of compound materials is ultrasonic measurement, which requires thick single-crystalline samples, about 1 cm thick, to enable precise measurement of the time required for the plane-wave acoustic pulses to propagate through the crystal.[105] The quasilongitudinal and quasishear wave velocities can be used in the following equation to calculate C_{13}:[105]

$$C_{13}=\frac{1}{\cos\alpha\sin\alpha}[(\lambda_{22}-\rho V)(\lambda_{33}-\rho V^2)]^{1/2}-C_{44}, \quad (4)$$

where, for hexagonal symmetry,

$$\lambda_{22}=C_{11}\cos^2\alpha+C_{44}\sin^2\alpha,$$
$$\lambda_{33}=C_{44}\cos^2\alpha+C_{33}\sin^2\alpha. \quad (5)$$

Here α is the angle between the propagation direction and the c axis, ρ is the mass per unit volume, and V is either the quasilongitudinal or the quasishear velocity.

As an optical technique, Brillouin scattering allows the determination of the elastic constants and hence of the bulk moduli through the interaction of light with thermal excitation in a material, in particular, acoustic phonons in a crystal. In this technique, the elastic constants C_{11} and C_{66} can be directly obtained from measurement of the phase velocity of the longitudinal mode and of the shear horizontal mode traveling parallel to the crystal surface. The remaining constants, C_{13}, C_{33}, and C_{44}, can be evaluated from measurement of the phase velocity of the Rayleigh surface wave and of the longitudinal bulk acoustic wave propagating at different angles from the surface normal. Various forms of x-ray diffraction, such as energy-dispersive x-ray diffraction (EDX), angular dispersive x-ray diffraction (ADX), and x-ray-absorption spectroscopy (XAS), can also be employed to determine the pressure dependence of the lattice parameters. From that, experimental equation of state (EOS), a widely used approach being the Murnaghan equation of state and hence directly the bulk modulus, which is based on the assumption that the bulk modulus has a linear dependence on pressure P, can be deduced as[106]

$$V=V_0\left(1+\frac{B'P}{B}\right)^{1/B'}, \quad (6)$$

where B and V_0 represent the bulk modulus and unit volume at ambient pressure, respectively, and B' is the derivative of B with respect to pressure. X-ray diffraction leads to the determination of the isothermal bulk modulus, whereas Brillouin scattering leads to the adiabatic one. Nevertheless in solids other than molecular solids there is no measurable difference between the two thermodynamic quantities. Besides the experimental investigations, many theoretical calculations have also been employed to determine the structural and mechanical properties of ZnO. Most of the calculations are based on density-functional theory within the LDA using various types of exchange-correlation functionals, and either plane-wave expansion for the pseudopotentials or the LMTO method.

Among the tetrahedrally bonded semiconductors, it has been stated that ZnO has the highest piezoelectric tensor or at least one comparable to that of GaN and AlN.[107] This property makes it a technologically important material for many applications, which require a large electromechanical coupling. The piezoelectric tensor has three independent components in hexagonal wurtzite phase and one (e_{14}) in the cubic zinc-blende phase, which characterize the full piezoelectric tensors of such crystals.[108] Two of these components in wurtzite phase measure the polarization induced along the c axis, at zero electric field, by a uniform strain either along the c axis or in the basal plane. The relevant relationship is[109]

$$P_z^{\text{piezo}}=e_{33}\varepsilon_z+e_{31}\varepsilon_\perp, \quad (7)$$

where ε_z and $\varepsilon_\perp$ are the strain along the c axis and in the basal plane, respectively. e_{33} and e_{31} are the piezoelectric coefficients. The third independent component of the piezoelectric tensor, e_{15}, describes the polarization induced by a shear strain which is usually neglected for simplicity. The sign of the piezoelectric tensor is generally fixed assuming that the positive direction along the c axis goes from the cation to the anion.

The natural structure of ZnO is wurtzite, which has a low symmetry, resulting in the existence of spontaneous polarization along the c direction. However, the absolute value of the spontaneous polarization in a nonferroelectric material has never been directly measured, while one invariably measures the polarization derivatives. In semiconductors, the

[This article is copyrighted as indicated in the article. Reuse of AIP content is subject to the terms at: http://scitation.aip.org/termsconditions. Downloaded to] IP: 128.172.48.58 On: Mon, 19 Oct 2015 20:45:44

spontaneous polarization may be deduced by investigating the two-dimensional electron gas and the redshift of the transitions in quantum wells albeit indirectly. From the theoretical point of view, there have been some efforts in determining the value of the spontaneous polarization in ZnO. One conventional approach is to define the spontaneous polarization of a low-symmetry crystal (wurtzite) as the polarization difference with respect to a high-symmetry structure (zinc blende) of the same material.

The micro- and nanoindentation methods are widely used in the determination of hardness of ZnO over a wide range of size scales and temperatures. Hardness measurements are usually carried out on the (0001) surface of the crystal using the conventional pyramidal or spherical diamond tip, or alternatively, with a sharp triangular indenter. The depth-sensing indentation measurements provide the complete information on the hardness and pressure-induced phase transformation of semiconductor materials. Table IV shows the measured and calculated mechanical parameters reported by several groups for ZnO crystallized in the form of wurtzite, zinc-blende, and rocksalt.

For ZnO, it seems that theoretical predictions are in good agreement with experimental findings for certain bulk material properties. The quality of the crystals and theoretical approximations are of primary importance for the precise determination of the physical properties. In regard to the elastic constants, theory and experiments seem capable of producing data which are quite consistent for wurtzite-phase ZnO. Bulk modulus and its rate of change with pressure for all phases are in good agreement within the various experimental findings as well as the theoretical predictions with a few exceptions. Any dispersion might be due to the sample quality, the accuracy of each experimental method, and phonon dispersion. Each calculation method also has its own limitations related to the basic material parameters, basis sets, and the precisions used in addition to the approximations of the method itself, leading to variations in the calculated parameters. As compared to group-III-nitrides (e.g., for GaN, $C_{11}=296$ GPa, $C_{12}=130$ GPa, $C_{13}=120$ GPa, $C_{33}=395$ GPa, $C_{44}=241$ GPa, and $B=190-245$ GPa),[110] the elastic and bulk moduli of ZnO are small. Recent ultrasonic experiments on single-crystal specimens of the wurtzite ($B4$) phase of ZnO have shown that, under pressure, this material becomes softer against shear-type acoustic distortions.

Decremps *et al.*[111] have studied the pressure behavior of both longitudinal (C_{11} and C_{33}) and transverse (C_{44} and C_{66}) elastic moduli for the wurtzite phase of single-crystal ZnO using ultrasonic wave velocity measurements up to 10 GPa at three different temperatures. As shown in Fig. 11, it has been observed that all the moduli exhibit a linear dependence on pressure up to the phase-transition pressures, with positive values for the room-temperature longitudinal moduli ($dC_{11}/dP=5.32$ and $dC_{33}/dP=3.78$) but negative values for the shear moduli ($dC_{44}/dP=-0.35$ and $dC_{66}/dP=-0.30$). At high temperatures, the pressure derivatives of the elastic shear modes become more negative. Thus, the elastic shear softening observed at room temperature is enhanced at elevated temperatures. The effect of phonons and the role of bond-bending forces as a function of pressure in causing the elastic softening were investigated. It has been observed that the pressure at which the phase transition ($B4-B1$) commences decreases to about 6 GPa at 600 °C as compared to 7.5 GPa at room temperature.

In an earlier study, similar pressure dependence was also reported by Soga and Anderson[112] who measured the pressure derivatives of the room-temperature longitudinal (L) and transverse (T) sound velocities of polycrystalline ZnO. They obtained $(\partial \nu_L/\partial P)_T=3.643\,310\,23$ km/s kbar and $(\partial \nu_T/\partial P)_T=23.193\,310\,23$ km/s kbar, corresponding to $(\partial B/\partial P)_T=4.8$ and $(\partial G/\partial P)T=-0.71$ (B is the bulk modulus and G is the shear modulus). On the theoretical side, a linear evolution under pressure was calculated for the two longitudinal modes, C_{11} and C_{33}, with pressure derivatives of 3.18 and 1.72, respectively, using atomistic calculations based on an interatomic pair potential within the shell-model approach.[70] The shear moduli C_{44} and C_{66} exhibited negative pressure dependence with pressure derivatives of −0.30 and −0.84, respectively. The experimental and calculated values slightly disagreed. The unusual negative values for both shear modes were attributed to two simultaneous effects:[111] (i) a major contribution of the second-nearest-neighbor interactions to the transverse-acoustic-phonon modes and (ii) an enhancement of the Coulomb forces screening between an atom and its second-nearest neighbor. Another explanation for the observed shear softening of ZnO was related to the decrease of bond-bending forces.

The deformation behavior of bulk ZnO single crystals was studied by a combination of spherical nanoindentation and atomic-force microscopy.[113] ZnO exhibited plastic deformation for relatively low loads ($>4-13$ mN with an ~4.2-mm radius spherical indenter). The average contact pressure hardness H and Young's modulus E as a function of indenter penetration were determined by analysis of partial load-unload data. The hardness value of ZnO is measured as 5.0 ± 0.1 GPa at a plastic penetration depth of 300 nm. The Young modulus remains essentially constant over the indenter penetration depth, with $E=111.2\pm4.7$ GPa. Previous indentation studies performed mostly on polycrystalline ZnO have reported a wide range of H (~1.5–12 GPa) and E (~40–120 GPa) values. However, it should be noted from these results that ZnO is significantly softer than GaN, where H (GaN)$=15.5\pm0.9$ GPa and E (GaN)$=210\pm23$ GPa.[113] The lower value of H for ZnO is, in fact, expected due to a lower melting point (1975 °C) and larger ionicity (0.616) as compared to that of GaN (2500 °C and 0.500).[114]

The spontaneous and piezoelectric polarization in ZnO have been studied theoretically by a number of groups and compared with a few available indirect experimental results. Dal Corso *et al.*[107] demonstrated the feasibility of *ab initio* studies of piezoelectricity within an all-electron scheme. A comparative analysis was performed in order to understand the microscopic origin of the peculiar behavior of ZnO. They have concluded that the piezoelectric effect results from two different contributions of opposite signs, which were referred to as the "clamped ion" and "internal strain." It has been shown that the large piezoelectric tensor of ZnO is due to the low value of its clamped-ion contribution (reducing the cancelation effect); besides, the piezoelectric tensor is domi-

[This article is copyrighted as indicated in the article. Reuse of AIP content is subject to the terms at: http://scitation.aip.org/termsconditions. Downloaded to] IP: 128.172.48.58 On: Mon, 19 Oct 2015 20:45:44

TABLE IV. Some mechanical properties of ZnO obtained by several experimental techniques and theoretical calculations.

Parameters	Wurtzite	Zinc blende	Rocksalt
C_{11} (GPa)	209.7,[a] 206,[b] 157,[c] 190,[d] 207,[e] 209,[f] 230,[g] 231,[h] 246[i]	193[i]	
C_{12} (GPa)	121.1,[a] 117,[b] 89,[c] 110,[d] 117.7,[e] 85,[f] 82,[g] 111,[h] 127[i]	139[i]	
C_{13} (GPa)	105.1,[a] 118,[b] 83,[c] 90,[d] 106.1,[e] 95,[f] 64,[g] 104,[h] 105[i]		
C_{33} (GPa)	210.9,[a] 211,[b] 208,[c] 196,[d] 209.5,[e] 270,[f] 247,[g] 183,[h] 246[i]		
C_{44} (GPa)	42.47,[a] 44.3,[b] 38,[c] 39,[d] 44.8,[e] 46,[f] 75,[g] 72,[h] 56[i]	96[i]	
C_{66} (GPa)	44.29,[a] 44.6,[b] 34,[c] 40,[d] 44.6,[e] 62,[f] 60,[h] 115[i]		
Bulk modulus, B (GPA)	142.4,[j] 183,[k] 170,[l] 160,[m] 162.3,[n] 133.7,[o] 156.8[k]	161.7,[n] 135.3,[o] 154.4[k]	202.5,[j] 228,[p] 205,[m] 205.7,[n] 172.7,[o] 203.3[k]
dB/dP	3.6,[j] 4.0,[p] 4.4,[m] 4.05,[n] 3.83,[o] 3.6[k]	3.95,[n] 3.72,[o] 3.6,[k]	3.54,[j] 4.0,[p] 4.88,[m] 3.90,[n] 3.77,[o] 3.6[k]
Young's modulus, E (GPa)	111.2±4.7[q]		
Hardness (GPa)	5.0±0.1[q]		
e_{31} (C/m^2)	−0.62,[r] −0.51,[c] −0.39,[s] −0.53,[t] −0.51,[u] −0.55,[i] −0.66[v]		
e_{33} (C/m^2)	0.96,[r] 1.22,[c] 0.92,[s] 1.19,[t] 1.21,[u] 1.19,[i] 1.30,[v]		
e_{15} (C/m^2)	−0.37,[r] −0.45,[c] −0.46[i]		
e_{14} (C/m^2)		0.69,[i] 0.64[w]	
Spontaneous polarization (C/m^2)	−0.057,[t] −0.047,[x] −0.057[u]		
Born effective charge, Z^*	2.06,[t] 2.11,[u] 2.10,[w] 2.1[x]		

[a]Ultrasonic measurement on single-crystal ZnO grown by chemical reaction in vapor state (Ref. 105).
[b]Surface Brillouin scattering on polycrystalline ZnO film deposited by rf sputtering on (100) Si substrate (Ref. 662).
[c]Acoustic investigation technique on ZnO film deposited by rf magnetron sputtering on sapphire substrate (Ref. 663).
[d]Polarized Brillouin scattering on bulk ZnO single crystal (Ref. 664).
[e]Ultrasonic resonance method on ZnO single crystal (Ref. 665).
[f]Calculated using LDA (Ref. 66).
[g]Calculated using GGA (Ref. 66).
[h]Atomistic calculations based on an interatomic pair potential within the shell-model approach (Ref. 70).
[i]Calculated using *ab initio* periodic linear combination of atomic orbitals (LCAO) method, based mainly on the Hartree-Fock Hamiltonian, with an all-electron Gaussian-type basis set (Ref. 660).
[j]X-ray diffraction using synchrotron radiation on polycrystalline ZnO (99.99% purity) (Ref. 64).
[k]Calculation based on *ab initio* all-electron periodic Hartree-Fock linear combination of atomic orbitals (Ref. 56).
[l]Calculation using molecular-dynamics simulation based on Tersoff's potential (Ref. 133).
[m]Calculation based on modern theoretical HF cluster and full-potential scaler-relativistic linearized-augmental plane wave (Ref. 65).
[n]Calculating using LDA (Ref. 57).
[o]Calculation using GGA (Ref. 57).
[p]X-ray diffraction and ^{67}Zn-Mössbauer spectroscopy on bulk ZnO (Ref. 65).
[q]Spherical nanoindentation on bulk ZnO (Ref. 113).
[r]Resonance-antiresonance method on ZnO single crystal (Ref. 665).
[s]Calculation using modern *ab initio* (Ref. 107).
[t]Calculation using *ab initio* quantum-mechanical level by using through the Berry-phase scheme applied to delocalized crystalline orbitals and through the definition of well-localized Wannier functions (Ref. 661).
[u]Calculation based on *ab initio* using the Berry-phase approach to polarization in solids (Ref. 109).
[v]Calculation using a plane-wave pseudopotential implementation of density-functional theory and density-functional linear response within the local-density approximation (Ref. 101).
[w]Reference 666.
[x]Calculation using the LDA, HF, and a model *GW* scheme (Ref. 87).

[This article is copyrighted as indicated in the article. Reuse of AIP content is subject to the terms at: http://scitation.aip.org/termsconditions. Downloaded to] IP: 128.172.48.58 On: Mon, 19 Oct 2015 20:45:44

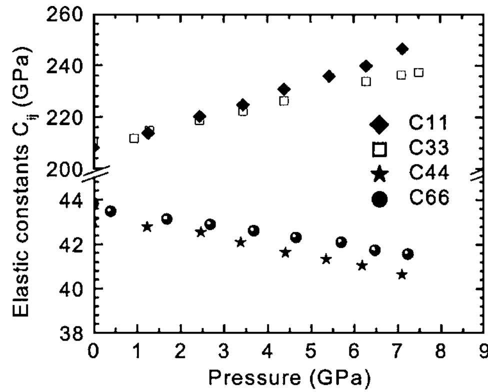

FIG. 11. Elastic moduli of ZnO vs pressure at ambient temperature. The slope of the C_{11} and C_{33} pressure dependences is positive ($dC_{11}/dP=5.32$ and $dC_{33}/dP=3.78$), whereas that for C_{44} and C_{66} is negative ($dC_{44}/dP=-20.35$ and $dC_{66}/dP=-20.30$. [Reprinted with permission from F. Decremps, J. Zhang, B. Li, and R. C. Liebermann, Phys. Rev. B **63**, 224105 (2001). Copyright 2001 by the American Physical Society.]

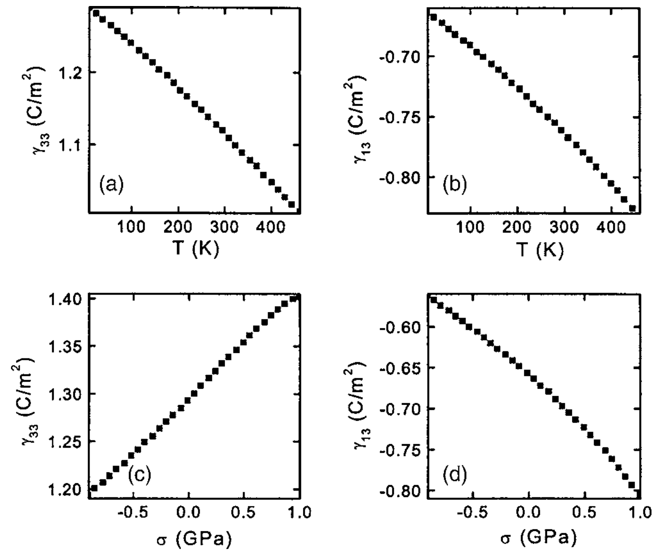

FIG. 12. Dependence of piezoelectric constants γ_{33} and γ_{13} of ZnO on temperature [(a) and (b)] and stress [(c) and (d)], respectively. γ_{ij} used by Hill and Waghmare correspond to e_{ij} used here. [Reprinted with permission from N. A. Hill and U. Waghmare, Phys. Rev. B **62**, 8802 (2000). Copyright 2000 by the American Physical Society.]

nated by the internal relaxation of anion and cation sublattices induced by the macroscopic strain. Later, the piezoelectric tensor in ZnO has been calculated by using various techniques such as plane-wave analysis, ultrasoft pseudopotentials, and a generalized-gradient-approximation Hamiltonian, an all-electron basis set and HF Hamiltonian. The values of e_{31} and e_{33} were reported in the range of 0.39–0.66 (mostly $\sim 0.52\ \mathrm{C/m^2}$) and $0.92-1.30\ \mathrm{C/m^2}$ (mostly $\sim 1.20\ \mathrm{C/m^2}$), respectively, which were in satisfactory agreement with the experimental data as given in Table IV.

Furthermore, the spontaneous polarization of ZnO has also been computed and compared with a very indirect experimental estimate of the same quantity. Massidda *et al.*[87] calculated *ab initio* the electronic states, spontaneous polarization, and Born dynamical charge of ZnO using the LDA, HF, and a model *GW* scheme. Among them the *GW* schemes give a spontaneous polarization value of $-0.047\ \mathrm{C/m^2}$, which is about 0.010 less than the other two reports [$-0.057\ \mathrm{C/m^2}$ (Refs. 107 and 109)]. Although there are no direct experimental data available, these theoretical predictions are in good agreement with an indirect experimental estimate value of $-0.07\pm0.02\ \mathrm{C/m^2}$ obtained from a model based on nonlinear optics. For Born dynamical charge, theoretical calculations and experimental data match quite well. From the value of the calculated Born dynamical charge, ~ 2.1, it has been suggested that rigid-ion-like behavior of ZnO is dominant and its band-by-band decomposition has anomalous contributions from O 2*s*, Zn 3*d*, and O 2*p* bands, indicating a substantial interaction between the corresponding occupied atomic orbitals.

Hill and Waghmare[101] have also performed a first-principles study of the piezoelectric ZnO, named after the application, as a function of stress and temperature using a plane-wave pseudopotential implementation of density-functional theory and density-functional linear response within the local-density approximation. The results are shown in Fig. 12. The piezoelectric constant is strongly sensitive to both temperature and stress, changing by about 20% and 15%–30%, respectively, over the range of parameters considered. By analyzing various physical contributions, these dependences were primarily attributed to the changes in structural parameters as manifested through the phonon and strain coupling. The strong bond-length-dependent hybridization between the O 2*p* and Zn 3*d* electrons were believed to be the cause of the large magnitude and sensitivity of this coupling.

E. Lattice dynamics

A fundamental understanding of the thermal as well as electrical properties in terms of low- and high-field carrier transports requires precise knowledge of the vibrational modes of the single crystal. In the wurtzite ZnO case,[115] the number of atoms per unit cell is $s=4$ and there are a total of 12 phonon modes, namely, one longitudinal-acoustic (LA), two transverse-acoustic (TA), three longitudinal-optical (LO), and six transverse-optical (TO) branches. In the zinc-blende polytypes with $s=2$, only six modes are present, three of which are acoustical (one LA and two TA) and the other three are optical (one LO and two TO) branches. Infrared reflection and Raman spectroscopies have been commonly employed to derive zone-center and some zone-boundary phonon modes in ZnO. Because the space group C_{6v} describes the crystalline structure of the wurtzite ZnO compound with 2 f.u. in the primitive cell, the optical phonons at the Γ point of the Brillouin zone belong to the following irreducible representation. The A_1 and E_1 branches are both Raman and infrared active, the two nonpolar E_2 branches are Raman active only, and the B_1 branches are inactive (silent modes). The A_1 and E_1 modes are each split into LO and TO components with different frequencies due to the macroscopic electric fields associated with the LO phonons. Because the electrostatic forces dominate the anisotropy in the short-range forces, the TO-LO splitting is larger than the A_1-E_1 splitting. For the lattice vibrations with A_1 and E_1 symmetries, the atoms move parallel and perpendicular to

[This article is copyrighted as indicated in the article. Reuse of AIP content is subject to the terms at: http://scitation.aip.org/termsconditions. Downloaded to] IP: 128.172.48.58 On: Mon, 19 Oct 2015 20:45:44

TABLE V. Phonon mode frequencies (in units of cm^{-1}) of wurtzite ZnO at the center of the Brillouin zone obtained from infrared spectroscopic ellipsometry (IRSE) and RS measurements in comparison with theoretical predictions.

Symmetry	Raman spectroscopy	Infrared spectroscopy	Theor. calc.
A_1-TO	380(2),[a] 379(2),[b] 380,[c] 380,[d] 378,[e] 380[f]	380[g]	382,[h] 386[i]
E_1-TO	409(2),[a]410(2),[b] 407,[c] 413,[d] 409.5[e]	409.1(0.9),[a] 408.2(0.3),[b] 412[g]	316,[h] 407[i]
A_1-LO	574,[d] 576,[e] 579,[d] 579[f]	574.5(0.3),[a] 577.1(0.4),[b] 570[g]	548[h]
E_1-LO	587(2),[a] 591(2),[b] 583,[c] 588,[e] 591[d]	588.3(0.7),[a] 592.1(0.2),[b] 591[g]	628[h]
E_2-low	102(1),[a] 102(1),[b] 101,[c] 101,[d] 98,[e] 99[f]		126,[h] 98[i]
E_2-high	438(1),[a] 437(1),[b] 437,[c] 444,[d] 437.5,[e] 438[f]		335,[h] 433[i]
B_1-low			240
B_2-high			540

[a]ZnO epilayer grown on sapphire. The error bars in parentheses represent the 90% confidence limits [Ashkenov *et al.*, 2003 (Ref. 118)].
[b]Bulk ZnO. The error bars in parentheses represent the 90% confidence limits. [Ashkenov *et al.*, 2003 (Ref. 118)].
[c]Raman scattering on ZnO single crystal [Damen *et al.*, 1966 (Ref. 26)].
[d]Raman spectra on ZnO [Arguello *et al.*, 1969 (Ref. 27)].
[e]Raman spectra [Bairamov *et al.*, 1983 (Ref. 116)].
[f]Raman spectra on ZnO film [Koyano *et al.*, 2002 (Ref. 667)].
[g]IR reflection [Venger *et al.*, 1995 (Ref. 668)].
[h]Atomistic calculations based on an interatomic pair potential within the shell-model approach [Zaoui and Sekkal, 2002 (Ref. 70)].
[i]Calculation [Tsuboi and Wada, 1968 (Ref. 30)].

the c axis, respectively. The low-frequency E_2 mode is associated with the vibration of the heavy Zn sublattice, while the high-frequency E_2 mode involves only the oxygen atoms. In the case of highly oriented ZnO films, if the incident light is exactly normal to the surface, only A_1(LO) and E_2 modes are observed, and the other modes are forbidden according to the Raman selection rules. Table V gives a list of observed zone-center optical-phonon wave numbers along with those calculated for wurtzite ZnO.

The complete set of phonon mode frequencies has been measured using either IR or Raman spectroscopy (RS) for both bulk and thin film ZnO. In early measurements, phonon modes of bulk ZnO were explored and discussed extensively by several groups using RS measurements.[26–29,116] Observation of the phonon modes in pulsed-laser deposition (PLD)-grown ZnO thin films was reported by Lu *et al.*[117] and Ashkenov *et al.*[118] No significant differences for the E_1(TO), A_1(TO), and E_2 mode frequencies were observed between the thin film and the bulk sample. The thin-film ZnO phonon mode frequencies are highly consistent with those of the bulk material. A small redshift of the longitudinal-optical-phonon mode frequencies of the ZnO films with respect to the bulk material was tentatively assigned to the existence of vacancy point defects within the films. The data obtained from IR and RS measurements are consistent with each other within the experimental accuracy. The predicted phonon frequencies reported by Tsuboi and Wada[30] are also in very good agreement with the experimental observations. The modes E_1(TO) and A_1(TO) reflect the strength of the polar lattice bonds. Accordingly, as discussed above no significant differences between the lattice constants of the film and bulk samples were observed.

Figure 13 shows typical Raman spectra of the bulk and thin-film ZnO sample.[118] In this particular study, the solid lines in both (a) and (b) indicate E_1, A_1, and E_2 phonon modes of ZnO. The dashed-dotted lines mark features observed at 332, 541, and 665 cm^{-1} which were assigned to possible multiple-phonon-scattering processes based on previous description.[26,29] The dotted lines are related to the sapphire phonon mode frequencies ($A1_g$ mode: 417 and 645 cm^{-1}; E_g mode: 379, 430, 450, 578, and 751 cm^{-1}).[31] For both samples A_1(LO) has not been observed and it was claimed that the scattering cross section for this mode is markedly smaller than that of the A_1(TO) mode due to the destructive interference between the Fröhlich interaction and the deformation-potential contributions to the LO-phonon scattering in ZnO.[28]

Rajalakshmi *et al.*[119] have reported additional Raman peaks at 205, 331, and 539 cm^{-1} in their ZnO nanoparticle

[This article is copyrighted as indicated in the article. Reuse of AIP content is subject to the terms at: http://scitation.aip.org/termsconditions. Downloaded to] IP: 128.172.48.58 On: Mon, 19 Oct 2015 20:45:44

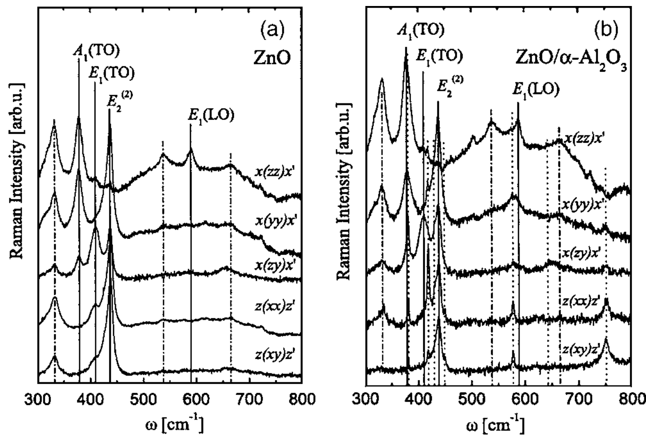

FIG. 13. (a) Raman spectra of the bulk ZnO sample. The first-order phonon modes of ZnO are indicated by the vertical solid lines. The vertical dashed-dotted lines mark the features due to multiple-phonon-scattering processes. (b) Raman spectra for the thin-film ZnO sample. The vertical dotted lines indicate the Raman-active sapphire substrate phonon mode frequencies. [Reprinted with permission from N. Ashkenov *et al.*, J. Appl. Phys. **93**, 126 (2003). Copyright 2003, American Institute of Physics.]

samples synthesized at ambient temperature using an electrochemical cell. Similar peaks (208, 332, and 541 cm^{-1}) that occur under resonance conditions were also reported for bulk ZnO.[29] In both studies, these peaks have been assigned to the second-order Raman spectrum arising from zone-boundary (M point) phonons 2-TA(M), 2-E_2(M), and 2-LA(M), respectively. However, the coupling to plasmons in highly doped material and stress-induced effects due to lattice mismatch with the substrate might play a role in the interpretation of the observed phonon frequencies.

The hydrostatic pressure dependence of the zone-center phonon modes has also been studied. In conjunction with previously reported results,[32,120] Decremps *et al.*[111] investigated, in detail, the pressure-induced Raman shift of a single-crystal ZnO sample at room temperature using Raman spectroscopy and *ab initio* calculations based on a plane-wave pseudopotential method within the density-functional theory. The pressure dependence of the zone-center phonons (E_2, A_1, and E_1) was measured for the wurtzite structure up to the hexagonal-cubic-phase-transition pressure (~8.7 GPa), above which all Raman peaks disappeared. The pressure dependences of the phonon frequencies for the two high-pressure experiments are shown in Fig. 14. Only the E_2-low mode exhibited a negative pressure dependence. The frequency shift of the E_2-high, A_1(TO), E_1(TO), and E_1(LO) modes was observed to increase with pressure. The pressure dependence of the optical-mode energies was also compared with the prediction of a model. No evidence of an anomaly in the E_2 and A_1 mode behaviors before the phase transition was detected. The corresponding perpendicular tensor component of the Born transverse dynamic charge e_T^* is experimentally found to increase under compression as $e_T^*(P) = (2.02-6.4)\times 10^{-3}P$, whereas calculations give $e_T^*(P) = (2.09-2.5)\times 10^{-3}P$ (in units of the elementary charge e and P in GPa). It has also been noted that the present observation of an optical phonon under pressure does not show any softening of the optic A_1- and E_2-high modes as theoretically expected.[121] Moreover, from the experimental observation as well as the theoretical calculations, the LO-TO splitting of the E_1 phonon mode, which depends on the long-range electrostatic forces, has unusually shown weak pressure dependence. This behavior has been attributed to a small variation of the chemical bond ionicity of wurtzite ZnO with pressure. Experimentally, the second-order process observation (via optical-phonon instabilities, for example) could not be performed because the wurtzite-to-rocksalt first-order transition limits the pressure range within which the wurtzite structure exists.

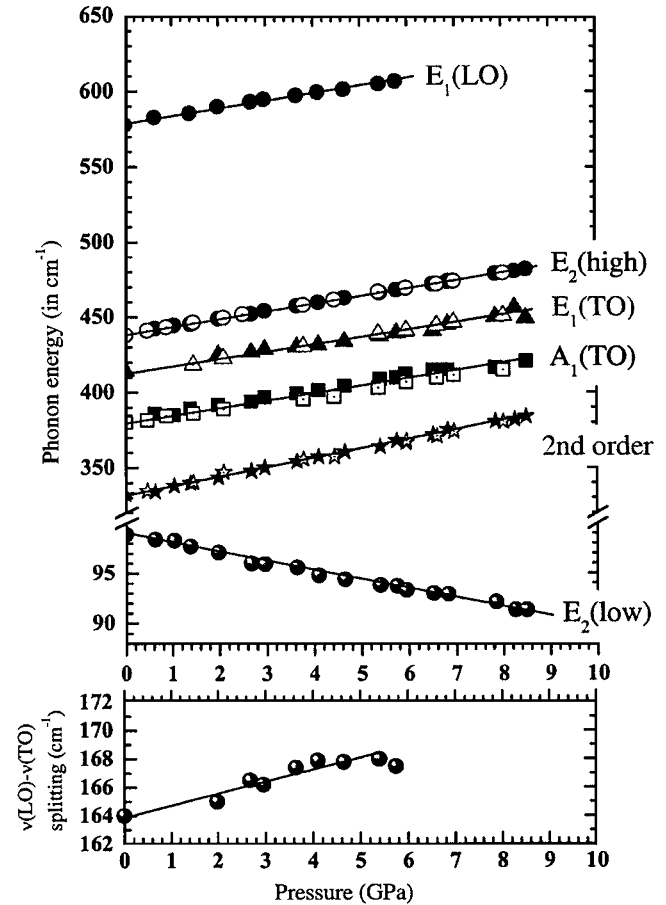

FIG. 14. Top: pressure dependence of the observed optical phonons. Open (full) symbols: propagation of light perpendicular (parallel) to c. Bottom: $(\nu_{\mathrm{LO}}-\nu_{\mathrm{TO}})$ E_1 phonon mode splitting vs pressure. The solid lines are the linear least-squares fits to the experimental points. [Reprinted with permission from F. Decremps, J. Pellicer-Porres, A. Marco Saitta, J.-C. Chervin, and A. Polian, Phys. Rev. B **65**, 092101 (2002). Copyright 2002 by the American Physical Society.]

The strong bond in ZnO and light O atoms result in high phonon frequencies and limit the range of possibly observable impurity-related local vibrational modes to even lighter elements at higher frequencies. So far, a number of reports has appeared for the infrared and Raman modes, which have been associated with local vibrational modes of impurities, dopants, and defect complexes. Kaschner *et al.*[122] have studied the influence of nitrogen, which is considered as a potential acceptor in ZnO, on the lattice dynamics of ZnO. They investigated a series of samples grown by chemical-vapor deposition (CVD) containing different nitrogen concentrations. The Raman spectra revealed vibrational modes at 275, 510, 582, 643, and 856 cm^{-1} in addition to the host phonons

[This article is copyrighted as indicated in the article. Reuse of AIP content is subject to the terms at: http://scitation.aip.org/termsconditions. Downloaded to] IP: 128.172.48.58 On: Mon, 19 Oct 2015 20:45:44

of ZnO as discussed above. It has been observed that the intensity of these additional modes correlates linearly with the nitrogen concentration. Therefore, these modes were interpreted as local vibrational modes due to the vibrating nitrogen-related complexes. The same group[123] later measured the phonon modes of Fe-, Sb-, Al-, Ga-, and Li-doped ZnO thin films, grown by pulsed-laser deposition on *c*-plane sapphire substrates using polarized micro-Raman measurements. Additional modes at about 277, 511, 583, and 644 cm^{-1}, which had been assigned to N incorporation in their previous work, were observed for intentionally doped Fe-, Sb-, and Al-doped films. The mode at 277 cm^{-1} was also observed for Ga-doped films. Based on these observations it has been stated that these modes cannot be related directly to N incorporation. Instead, they suggest intrinsic host lattice defects as their origin. Additional modes at 531, 631, and 720 cm^{-1} were attributed to the Sb, Ga, and Fe dopants.

First-principles calculations based on DFT within the LDA and the pseudopotential-plane-wave method by Van de Walle[124] suggest that hydrogen atoms might act as shallow donors in ZnO. It was argued that the incorporation of hydrogen accompanied by remarkably large relaxations of the surrounding atoms lead to an O–H bond, which in fact, can be regarded as a new type of dopant atom in ZnO. In order to determine the microscopic structure of hydrogen donors, the local vibrational modes (LVMs) arising from these complexes have been investigated using IR and Raman spectroscopies.[125,126] The hydrogen-related defects in ZnO samples, hydrogenated using a H or a D plasma, have been investigated by a combination of local vibrational mode spectroscopy and compared with the first-principles calculations. Three new infrared (IR)-absorption lines at 3611.3, 3349.6, and 3312.2 cm^{-1} have been observed at 10 K. Based on polarization studies and first-principles calculations, the line at 3611.3 cm^{-1} was assigned to a single interstitial hydrogen atom at the bond-center site oriented along the *c* axis of the crystal, although the possibility that this H atom is associated with an impurity cannot be excluded. The lines at 3349.6 and 3312.2 cm^{-1} were attributed to a zinc vacancy that contains two inequivalent hydrogen atoms, one in an O–H bond roughly aligned with the *c* axis, and the other in an O–H bond that forms an angle of 100° with the *c* axis.[126,127]

McCluskey *et al.*[125] have also used IR spectroscopy to measure local vibrational modes in ZnO annealed in hydrogen gas. An IR-absorption peak at 3326.3 cm^{-1} was observed at a temperature of 8 K and attributed to the O–H stretch mode based on comparison with the first-principles calculations of Van de Walle,[124] in which the calculated mode frequencies were 3726 and 3384 cm^{-1} for the bond-centered and antibonding configurations, respectively, after subtracting 166 cm^{-1} due to the anharmonic terms in the potential, causing the stretch-mode frequency to shift downward. However, because of the uncertainty in actual anharmonicity the bond-centered configuration was not ruled out. The IR spectrum of ZnO annealed in deuterium has revealed an additional stretch mode at 2470.3 cm^{-1} for the same temperature, which was tentatively assigned to the oxygen-deuterium (O–D) complexes. Using polarization measurements at room

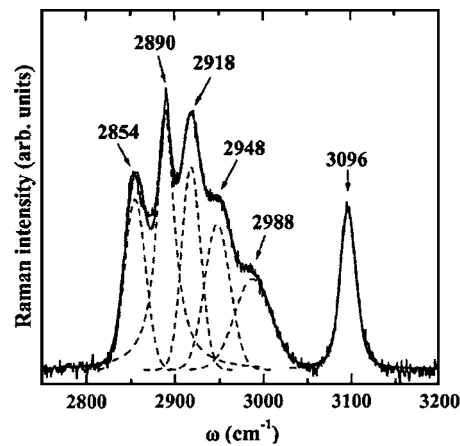

FIG. 15. Raman-backscattering spectrum of *as-grown* single-crystal ZnO after background subtraction. The sample was irradiated with the 488-nm line of an Ar laser and a power of 190 mW. The solid line represents a least-squares fit of six Gaussian lines to the data. The dashed lines indicate the individual local vibrational modes. The peak positions are indicated in the plot. [Reprinted with permission from N. H. Nickel and K. Fleischer, Phys. Rev. Lett. **90**, 197402 (2003). Copyright 2003 by the American Physical Society.]

temperature they also showed that the dipole of the O–H complex does not lie parallel to the *c* axis of wurtzite ZnO.[128,129]

More recently, using Raman-backscattering spectroscopy, Nickel and Fleischer[130] have detected six local vibrational modes at 2854, 2890, 2918, 2948, 2988, and 3096 cm^{-1}. A Raman-backscattering spectrum measured on an *as-grown* ZnO single crystal is shown in Fig. 15. The peak positions were obtained by deconvoluting the spectrum into six Gaussian lines. In order to elucidate the origin of the local vibrational modes Nickel and Fleischer performed hydrogen effusion experiments on ZnO single crystals. Upon annealing some samples up to 950 °C to remove hydrogen the subsequent measurement revealed that the local vibrational modes disappeared, from which the observed vibrational modes are attributed to the presence of hydrogen in the ZnO crystals. It has been found that the stretching vibration of the corresponding hydrogen complex is *not* parallel to the *c* axis. The vibrational modes located at 2854, 2890, 2918, 2948, and 2988 cm^{-1} were assumed to be due to the stretching modes of C–H, symmetric stretching modes of $C-H_3$, symmetric stretching modes of $C-H_2$, antisymmetric stretching modes of $C-H_3$, and antisymmetric stretching modes of $C-H_2$, respectively, based on the effusion data, where a significant concentration of hydrocarbons were detected. The local vibrational mode located at 3096 cm^{-1} was attributed to the N–H, assuming a considerable amount of hydrogen is bonded to nitrogen atoms based on the effusion experimental data. This observed mode frequency was also found to be consistent with that reported for ZnSe compound semiconductors.[131]

F. Thermal properties

1. Thermal-expansion coefficients

The lattice parameters of semiconductors are temperature dependent and quantified by thermal-expansion coeffi-

[This article is copyrighted as indicated in the article. Reuse of AIP content is subject to the terms at: http://scitation.aip.org/termsconditions. Downloaded to] IP: 128.172.48.58 On: Mon, 19 Oct 2015 20:45:44

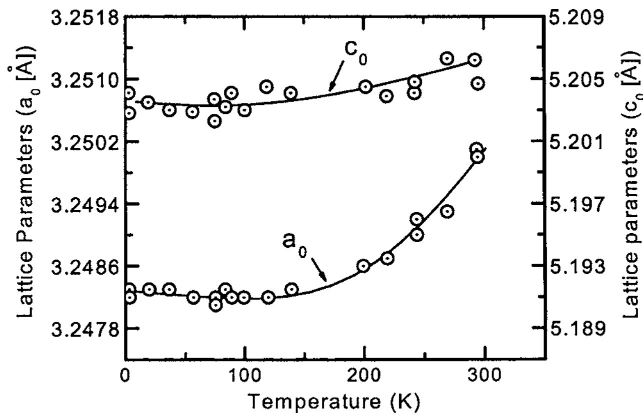

FIG. 16. Wurtzite ZnO lattice parameters as a function of temperature. [Reprinted with permission from R. R. Reeber, J. Appl. Phys. **41**, 5063 (1970). Copyright 1970, American Institute of Physics.]

cients, which are defined as $\Delta a/a$ or α_a and $\Delta c/c$ or α_c, for in-and out-of-plane cases, respectively. They are dependent on stoichiometry, presence of extended defects, and free-carrier concentration. The temperature dependence of the lattice constants a and c, and the thermal-expansion coefficients of hexagonal ZnO have been determined by the capacitive method.[132] Reeber[9] has employed x-ray powder-diffraction methods to measure the temperature dependence of the lattice parameters of ZnO in the range of 4.2–296 K. The results are shown in Fig. 16. When analyzing the dependence of the lattice parameters on temperature, fourth-order polynomials,

$$a_T = 3.248\,53 - 1.0811 \times 10^{-5}T + 6.820 \times 10^{-8}T^2 - 6.109 \times 10^{-11}T^3 + 2.143 \times 10^{-14}T^4, \quad (8)$$

were fitted using the least-squares method, which gives a minimum for the a_0 parameter at 93 K. The c_0 parameter did not give any minimum, most probably due to its less precision and uncertainty in the measurement.

Han and Jou[133] studied thermal properties of ZnO films prepared by rf magnetron sputtering on Si and GaAs substrates. Thermal stresses were determined by using the bending beam technique where the specimens were thermally cycled from 25 to 400 °C. They investigated the thermal-expansion coefficient as a function of some growth parameters, such as substrate temperature, sputtering power, etc. With a few exceptions, they found no significant changes with the variation of total gas pressure from 0.53 to 2.1 Pa, substrate temperature from 250 to 450 °C, Ar-to-O pressure ratio from 0.3 to 3, and power from 100 to 300 W. It has been observed that the thermal-expansion coefficient increases about 37% from 5×10^{-6} to 8×10^{-6} 1/°C within the temperature range of 25–400 °C. Aoumeur *et al.*[133] calculated the thermal-expansion coefficient for both the zinc-blende and rocksalt phases of ZnO using a molecular-dynamics simulation based on Tersoff's potential. They found that $\alpha=1.24\times10^{-5}$ K^{-1} for the zinc-blende and $\alpha=0.16\times10^{-5}$ K^{-1} for rocksalt structures.

2. Thermal conductivity

Thermal conductivity (κ), which is a kinetic property determined by the contributions from the vibrational, rotational, and electronic degrees of freedom, is an extremely important material property when high-power/high-temperature electronic and optoelectronic devices are considered. For pure crystals, phonon-phonon scattering, which is ideally proportional to T^{-1} above the Debye temperature, is the limiting process for thermal conductivity. The heat transport is predominantly determined by phonon-phonon umklapp scattering, and phonon scattering by point and extended defects, such as vacancies (inclusive of lattice distortions caused by them), impurities, and isotope fluctuations (mass fluctuation). As for other semiconductors, due to their imperfection, point defects play a significant role in the thermal conductivity of ZnO. The lattice contribution (phonon scattering) to the thermal conductivity κ is obtained from the kinetic theory as[134]

$$\kappa_{\rm lattice}(T) = \frac{1}{3}\nu_s C_{\rm lattice}(T)L(T), \quad (9)$$

where T is the temperature, ν_s is the velocity of sound (almost independent of temperature), $C_{\rm lattice}(T)$ is the lattice specific heat, and $L(T)$ is the phonon mean free path. In almost all materials $\kappa(T)$ first increases with temperature, reaches a maximum ($\kappa_{\max}$) at some characteristic temperature $T_{\rm ch}$, and then decreases. At low temperatures L is relatively long and is dominated by extrinsic effects such as "defects" and/or finite crystal size and $C_{\rm lattice}(T)\sim(T/\theta_D)^3$, where θ_D is the Debye temperature. As the temperature increases $C_{\rm lattice}(T)$ begins to saturate and intrinsic temperature-dependent umklapp processes become dominant, thus causing a decrease in L.

The electronic contribution to the thermal conductivity which is negligible for carrier concentrations $\leqslant 10^{19}$ cm^{-3} is[135]

$$\kappa_{\rm electr}(T) = \frac{\pi^2 n k_B^2 T \tau_{\rm electr}}{3m_c^*}, \quad (10)$$

where n is the carrier density, k_B is the Boltzman constant, $\tau_{\rm electr}$ is the scattering time of the electrons, and m_c^* is the conduction-band effective mass. The overall thermal conductivity generally decreases with increasing carrier concentration, because the decrease in the lattice component of κ due to increased phonon scattering from both the impurities and free electrons outweighs the increase in the electronic contribution to κ.[136]

Scanning thermal microscopy (SThM) has been applied to measure the room-temperature thermal conductivity on Zn and O face of high-quality ZnO (0001) single crystals, grown by a vapor-phase transport method.[137] The thermal investigation was performed in two ways: point-by-point (~2-μm resolution) and area scans. The point-by-point measurements on Zn-face samples produced $\kappa=1.16\pm0.08$ and 1.02 ± 0.07 W/cm K, while O-face samples showed $\kappa=1.10\pm0.09$ and 0.98 ± 0.08 W/cm K. The variations represent the standard deviation in the data, which was obtained by investigating approximately 15–20 points randomly dis-

[This article is copyrighted as indicated in the article. Reuse of AIP content is subject to the terms at: http://scitation.aip.org/termsconditions. Downloaded to] IP: 128.172.48.58 On: Mon, 19 Oct 2015 20:45:44

TABLE VI. Thermal conductivity, κ (W/cm K), at multiple positions of bulk ZnO samples with various surface treatments (Ref. 138).

Sample	Surface treatment	Thermal conductivity (W/cm K)
a	Forming-gas-annealed	(1) $\kappa=0.67\pm0.08$
		(2) $\kappa=0.46\pm0.05$
b	As-received (O face)	(1) $\kappa=1.00\pm0.08$
		(2) $\kappa=0.95\pm0.06$
c	Air-annealed	(1) $\kappa=1.35\pm0.08$
		(2) $\kappa=1.25\pm0.05$
d	Nitrogen plasma treated at 750 °C	(1) $\kappa=1.44\pm0.08$
		(2) $\kappa=1.47\pm0.08$
e	Oxygen plasma treated at 700 °C	(1) $\kappa=0.87\pm0.06$
		(2) $\kappa=0.75\pm0.06$
		(3) $\kappa=0.80\pm0.06$
		(4) $\kappa=1.24\pm0.05$
		(5) $\kappa=0.54\pm0.07$

tributed over a $6\times6\text{-mm}^2$ surface area. In this study, a correlation between the surface topography and thermal-conductivity variations was also studied by acquiring the AFM and SThM scans simultaneously during the area scan. The effects of surface roughness on effective κ values were treated in terms of tip-surface geometry. It was argued that when the experimental voltage variations (proportional to κ) correspond to only 6%–7% changes in the thermal conductivity, variations probably originate from the topography. Larger variations ($>12\%$) in the SThM voltage reading for AFM topographical features with heights <100 nm would be an indication of intrinsic thermal-conductivity variations across the area under investigation.

Pollak *et al.*[138] measured the thermal conductivity κ of several bulk ZnO (0001) samples grown by CERMET, Inc., and prepared by our group under different surface treatments. The measurements were made using SThM with a spatial/depth resolution of about 2–3 μm. The surface treatments of various samples are summarized in Table VI. The measurements were made at different points on each sample and the results are also shown in Table VI. On sample a in both positions, κ is considerably less than the previously reported values of about 1.0 W/cm K.[137] To be consistent with the earlier models, one would argue that forming-gas annealing has resulted in surface roughness, which has considerably reduced κ. The same is mostly true for sample e, which exhibits considerable inhomogeneity in the measured κ. At the present time we do not have an explanation for this result, although Florescu *et al.*[136] did find that in GaN, κ was a function of carrier concentration, i.e., it decreased with increasing carrier concentration due to scattering of phonons from the ionized impurities. We have no information about the carrier concentrations/doping levels, nor their distribution for this or any other of the samples. For sample b the measured results for κ are similar to those reported in Ref. 137, while for samples c and d they are actually somewhat higher and are the highest κ values reported for ZnO. Thus, air-annealing and nitrogen-plasma treatment both result in a good surface.

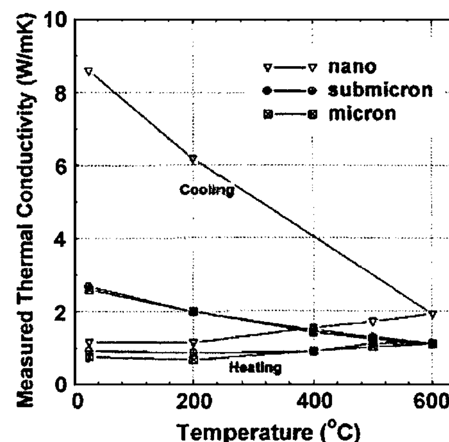

FIG. 17. Thermal conductivity of nanometer, submicrometer, and micrometer particle size ZnO heated from room temperature to 600 °C at 3 °C/min. [Reprinted with permission from T. Olorunyolemi, A. Birnboim, Y. Carmel, O. C. Wilson, Jr., and I. K. Lloyd, J. Am. Ceram. Soc. **85**, 1249 (2002). Copyright 2002, Blackwell Publishing.]

Olorunyolemi *et al.*[139] measured the thermal conductivity of ZnO powders with different particle sizes (micrometer, submicrometer, and nanometer) from the as-received powder state to the fully sintered state using a laser flash technique. Curves of thermal conductivity versus temperature for the three sets of ZnO samples (micrometer, submicrometer, and nanometer), measured as they were heated to 600 °C and cooled back to 25 °C, are shown in Fig. 17. The first surprising observation is that the thermal conductivity at room temperature and up to 200 °C is the reverse of what is expected for the different particle sizes, with the nanopowder having the highest thermal conductivity. The room-temperature thermal conductivities were measured as 0.745, 0.914, and 1.160 W/m K for micro-, submicro-, and nanosize samples having average particle diameters of 1.0 μm, 0.2 μm, and 20 nm, respectively. The initial higher thermal conductivity of the nanopowder ZnO samples were attributed to the adsorbed water including chemisorbed water (more than that adsorbed by the submicrometer, which in turn is more than that adsorbed by the micrometer powder). Above 400 °C the thermal conductivity of the nanoparticle size increases faster with increasing temperature than that of the submicrometer and the micrometer particle size samples. In this work, a model for interparticle neck growth was also developed based on mass transfer to the neck region of a powder as a result of a known temperature. The observed data were compared with the theoretical results obtained by the three-dimensional numerical code combined with this model.

Figure 18 shows the measured thermal conductivity of a fully sintered sample heated from room temperature to 1000 °C. The thermal conductivity decreases from 37 to 4 W/m K as the temperature is increased from room temperature to 1000 °C. This is the thermal conductivity curve for a fully dense ZnO crystal, where the resistive phonon-phonon interactions (umklapp processes) are the dominant scattering mechanism.

The thermal properties of ZnO doped with Al and Mg were also studied by a number of groups[140–144] for the evaluation of the thermoelectric performance. Tsubota *et al.*[143] in-

[This article is copyrighted as indicated in the article. Reuse of AIP content is subject to the terms at: http://scitation.aip.org/termsconditions. Downloaded to] IP: 128.172.48.58 On: Mon, 19 Oct 2015 20:45:44

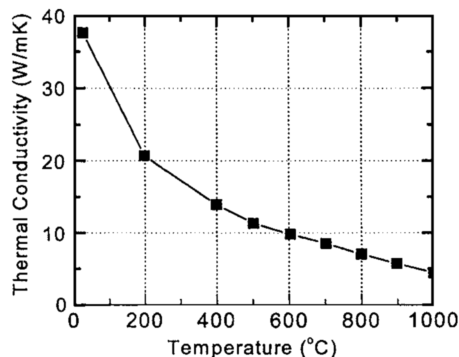

FIG. 18. Thermal conductivity of fully sintered ZnO heated from room temperature to 1000 °C. [Reprinted with permission from T. Olorunyolemi, A. Birnboim, Y. Carmel, O. C. Wilson, Jr., and I. K. Lloyd, J. Am. Ceram. Soc. **85**, 1249 (2002). Copyright 2002, Blackwell Publishing.]

vestigated the thermal conductivity of sintered $(Zn_{1-y}Mg_y)_{1-x}Al_xO$ ($x=0-0.1$ and $y=0-0.1$) samples determined from thermal diffusivity and specific-heat capacity measured by the laser flash technique and differential scanning calorimetry (DSC), respectively. The temperature dependences of the thermal conductivities of $(Zn_{1-y}Mg_y)_{0.98}Al_{0.02}O$ ($y=0,0.02,0.1$) are shown in Fig. 19 in comparison with that of ZnO. The reduction of κ from ZnO to $Zn_{0.98}Al_{0.02}O$ was almost negligible. Although addition of Al (using Al_2O_3) is considered to be ineffective in suppressing κ of ZnO-based materials, the difference in the κ values between the MgO-added samples and the $Zn_{0.98}Al_{0.02}O$ sample is significantly larger at low temperatures, indicating that the addition of MgO was very effective in reducing the thermal conductivity at low temperatures. From the temperature-dependence behavior ($1/T$ dependence above the Debye temperature) the authors have concluded that the decrease in phonon-phonon-scattering contribution is mainly responsible for the reduction of thermal conductivity upon addition of MgO as well as Al_2O_3. Formation of a solid solution of MgO and ZnO is thereby considered to be effective in introducing phonon-scattering centers in order to reduce the vibrational component, and thereby the overall value of κ.

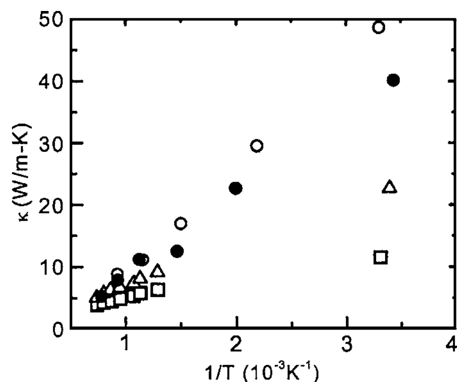

FIG. 19. The thermal conductivities of ZnO (○), $Zn_{0.98}Al_{0.02}O$ (●), and $(Zn_{1-y}Mg_y)_{0.98}Al_{0.02}O$ for $y=0.02$ (△) and 0.1 (□) as a function of inverse temperature. [Reproduced by permission of the Royal Society of Chemistry from T. Tsubota, M. Ohtaki, K. Eguchi, and H. Arai, J. Mater. Chem. **8**, 409 (1998).]

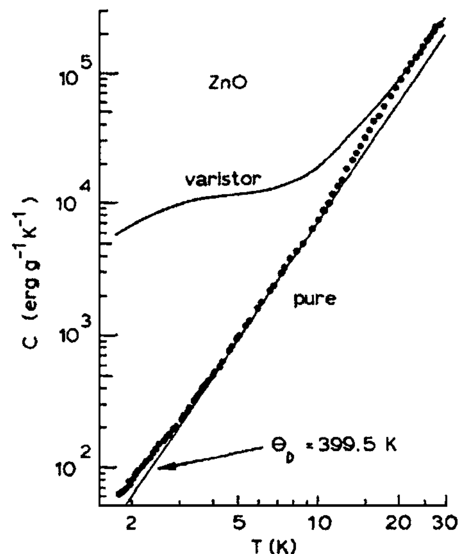

FIG. 20. Specific-heat data measured for pure ZnO compared to the data for varistor ZnO. [Reprinted with permission from W. N. Lawless and T. K. Gupta, J. Appl. Phys. **60**, 607 (1986). Copyright 1986, American Institute of Physics.]

Similarly, thermal properties of $(Zn_{1-y}Mg_y)_{1-x}Al_xO$ ($0<x<0.05$ and $0<y<0.16$) ceramics synthesized from a powder precursor prepared by a polymerized complex method has also been investigated by Katsuyama *et al.*[142] They observed similar dependence of thermal conductivity on temperature and doping constitutes as Tsubota *et al.*[143] The thermal conductivity decreased with increasing x, but further suppression of the thermal conductivity was attained by the additional substitution of the Zn sites by Mg atoms with the resultant lattice contribution, i.e., the point defects introduced by the addition of Mg enhanced the phonon scattering. However, in both studies, although the temperature dependence reveals $1/T$ behavior indicative of umklapp scattering, room-temperature thermal conductivity of sintered ZnO, which is about $40\ W\,m^{-1}\,K^{-1}$ and reduces to $\sim 7\ W\,m^{-1}\,K^{-1}$ with increasing MgO concentration, is much smaller than the values reported for the high-quality single crystal discussed above. This indicates the large contribution due to enhanced phonon-point defects or –extended defects and grain-boundary scattering.

3. Specific heat

The specific heat of a semiconductor has contributions from lattice vibrations, free carriers (very effective at low temperatures), and point and extended defects. For good-quality semi-insulating crystal, the specific heat is determined mostly by the lattice vibrations. The available specific-heat data for ZnO are very limited. Only Lawless and Gupta[145] investigated the specific heat for both pure and varistor types of ZnO samples between the temperature ranges of 1.7 and 25 K, where the latter has an average grain size of 10 μm. Specific-heat measurements were performed using the pulse method. As seen in Fig. 20, the specific heat of varistor ZnO diverges from that of pure ZnO below 20 K. This difference was attributed to the contribution by the large

[This article is copyrighted as indicated in the article. Reuse of AIP content is subject to the terms at: http://scitation.aip.org/termsconditions. Downloaded to] IP: 128.172.48.58 On: Mon, 19 Oct 2015 20:45:44

amount of impurities present in the region of the grain boundaries of varistor-type ZnO, giving rise to a very large excess specific heat below 20 K.

The specific-heat data for pure ZnO were further analyzed by considering two non-Debye features at different temperature regions according to

$$C = C_{\mathrm{Debye}} + C_{\mathrm{Schottky}} + C_{\mathrm{Einstein}}, \tag{11}$$

where C_{Debye}, C_{Schottky}, and C_{Einstein} represent the Debye, Schottky, and Einstein terms of the total specific heat of ZnO, respectively. In general, the Debye expression for the temperature dependence of specific heat in a solid at a constant pressure can be expressed as

$$C_{\mathrm{Debye}} = 18R\left(\frac{T}{\theta_D}\right)^3 \int_0^{x_D} \frac{x^4 e^x}{(e^x-1)^2}dx, \tag{12}$$

where $x_D \equiv \theta_D/T$, and $R=8.3144$ J/mol K is the molar gas constant. The coefficient in front of the term R has been multiplied by 2 to take into account the two constituents making up the binary compound. By fitting the measured temperature-dependent heat capacity to the Debye expression, one can obtain the Debye temperature θ_D specific to the heat capacity. It is often easier to extract a Debye temperature using data either near very low temperatures or well below the Debye temperature where the specific heat has a simple cubic dependence on temperature:

$$C_{\mathrm{Debye}} = 234R\left(\frac{T}{\theta_D}\right)^3. \tag{13}$$

Unfortunately for ZnO, the samples contain large densities of free carriers and defects, which make the Debye specific-heat expression unreliable. The Debye contribution to the specific heat of pure ZnO is also shown in Fig. 20 as the curve labeled with a calorimetric Debye temperature of θ_D $=399.5$ K, and the deviation of the data below ~5 K is due to the Schottky term, and above ~10 K due to the Einstein term. The latter has an exponential dependence and is given by

$$C_{\mathrm{Einstein}} = 3Rr_E\left(\frac{\theta_E}{T}\right)^2 \exp\left(-\frac{\theta_E}{T}\right) \quad \text{for } T \ll \theta_E, \tag{14}$$

where r_E is the number of Einstein oscillators per formula weight and θ_E is the Einstein temperature. The Schottky term has a T^{-2} dependence and is expressed by

$$C_{\mathrm{Schottky}} = bT^{-2}, \tag{15}$$

where $b=nR(\delta/2)^2$ ($n=r_E$ is assumed) is the Schottky coefficient.

The least-squares fit of these two expressions to the experimental data for the corresponding temperature range is shown in Fig. 21. Very good agreement with 2%–3% uncertainty was achieved for the values of $\theta_E=120.5$ K and r_E $=8.72\times10^{-2}$ for the case of the Einstein model, and b $=350.7$ ergs g^{-1} K^{-1} for the Schottky term. The Zn interstitials (3.6×10^{21} cm^{-3}) might be responsible for the dispersionless Einstein-type contribution to the specific heat above 10 K, whereas the Schottky contribution appearing below

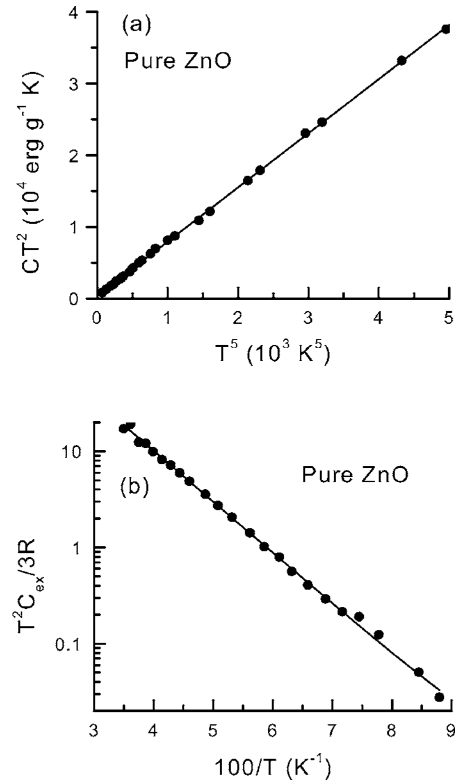

FIG. 21. Fit to the pure ZnO data (a) using the Schottky model (this fit yields a Debye temperature of 395.5 K) and (b) using the Einstein model. C_{ex} is obtained by removing the Debye and Schottky contributions. The Einstein oscillators are identified as the Zn interstitials. [Reprinted with permission from W. N. Lawless and T. K. Gupta, J. Appl. Phys. **60**, 607 (1986). Copyright 1986, American Institute of Physics.]

4 K is due to ordering of, possibly, Zn interstitials with a characteristic energy of $\delta=1.1\times10^5$ eV for such an ordering mechanism.

G. Electrical properties of undoped ZnO

As a direct and large-band-gap material, ZnO is attracting a lot of attention for a variety of electronic and optoelectronic applications. Advantages associated with a large band gap include higher breakdown voltages, ability to sustain large electric fields, lower noise generation, and high-temperature and high-power operation. The electron transport in semiconductors can be considered for low and high electric fields. (i) At sufficiently low electric fields, the energy gained by the electrons from the applied electric field is small compared to the thermal energy of electrons, and therefore, the energy distribution of electrons is unaffected by such a low electric field. Since the scattering rates determining the electron mobility depend on the electron distribution function, electron mobility remains independent of the applied electric field, and Ohm's law is obeyed. (ii) When the electric field is increased to a point where the energy gained by electrons from the external field is no longer negligible compared to the thermal energy of the electron, the electron distribution function changes significantly from its equilibrium value. These electrons become hot electrons characterized by an electron temperature larger than the lattice temperature. Furthermore, as the dimensions of the device are

[This article is copyrighted as indicated in the article. Reuse of AIP content is subject to the terms at: http://scitation.aip.org/termsconditions. Downloaded to] IP: 128.172.48.58 On: Mon, 19 Oct 2015 20:45:44

decreased to submicron range, transient transport occurs when there is minimal or no energy loss to the lattice during a short and critical period of time, such as during transport under the gate of a field-effect transistor or through the base of a bipolar transistor. The transient transport is characterized by the onset of ballistic or velocity overshoot phenomenon. Since the electron drift velocity is higher than its steady-state value, one can design a device operating at frequencies exceeding those expected from linear scaling of dimensions.

1. Low-field transport

Hall effect is the most widely used technique to measure the transport properties and assess the quality of epitaxial layers. For semiconductor materials, it yields the carrier concentration, its type, and carrier mobility. More specifically, experimental data on Hall measurements over a wide temperature range (4.2–300 K) provide quantitative information on impurities, imperfections, uniformity, scattering mechanisms, etc. The Hall coefficient and resistivity (ρ) are experimentally determined and then related to the electrical parameters through (for n-type conduction) $R_H = r_H / ne$ and $\mu_H = R_H / \rho$, where n is the free-electron concentration, e is the unit electronic charge, μ_H is the Hall mobility, and r_H is the Hall scattering factor which is dependent on the particular scattering mechanism. The drift mobility is the average velocity per unit electric field in the limit of zero electric field and is related to the Hall mobility through the Hall scattering factor by $\mu_H = r_H \mu$. As noted above, the Hall scattering factor depends on the details of the scattering mechanism, which limits the drift velocity. As the carriers travel through a semiconductor, they encounter various scattering mechanisms that govern the carrier mobility in the electronic system. The parameter for characterizing the various scattering mechanisms is the relaxation time τ, which determines the rate of change in electron momentum as it moves in the semiconductor crystal. Mobility is related to the scattering time by

$$\mu = \frac{q\langle \tau \rangle}{m^*}, \tag{16}$$

where m^* is the electron effective mass, q is the electronic charge, and $\langle \tau \rangle$ is the relaxation time averaged over the energy distribution of electrons. The total relaxation time τ_T when various scattering mechanisms are operative is given by Matthiessen's rule:

$$\frac{1}{\tau_T} = \sum_i \frac{1}{\tau_i}, \tag{17}$$

where i represents each scattering process, provided that the electron while undergoing one scattering event is not affected by another.

The major scattering mechanisms that generally govern the electron transport in III-V semiconductors are also valid for ZnO. They are briefly listed as follows.

(1) Ionized impurity scattering is due to deflection of free carriers by the long-range Coulomb potential of the charged centers caused by defects or intentionally doped impurities. This can be thought as a local perturbation of the band edge, which affects the electron motion.
(2) Polar LO-phonon scattering is caused by the interaction of a moving charge with an electric field induced by electric polarization associated with lattice vibration due to the ionic nature of the bonds in a polar semiconductor.
(3) Acoustic-phonon scattering through deformation potential arises from the energy change of the band edges induced by strain associated with acoustic phonons, where the scattering rate increases with the wave vectors of the phonons.
(4) Piezoelectric scattering arises from the electric fields that are produced by the strain associated with phonons in a crystal without inversion symmetry.
(5) If the density of dislocations and native defects are high in a semiconductor, dislocation scattering and scattering through defects are also considered as possible scattering mechanisms. Dislocation scattering is due to the fact that acceptor centers are introduced along the dislocation line, which capture electrons from the conduction band in an n-type semiconductor. The dislocation lines become negatively charged and a space-charge region is formed around it, which scatters electrons traveling across the dislocations, thus reducing the mobility.

Experimental investigation of the temperature-dependent carrier mobility and concentration can be used to determine the fundamental material parameters and understand the carrier scattering mechanisms along with an accurate comparison with theory. Table VII gives the selected best values of electron mobility and corresponding carrier concentration in bulk and thin-film ZnO grown by various techniques.

The transport properties reported in the literature are mostly based on Hall-effect measurements, assuming the Hall scattering factor to be unity. Using Monte Carlo simulations, Albrecht *et al.*[146] predicted the room-temperature electron mobility of ZnO as ~300 $cm^2/V\,s$. Nominally undoped ZnO with a wurtzite structure naturally becomes an n-type semiconductor due to the presence of intrinsic or extrinsic defects, which were generally attributed to native defects, such as the Zn-on-O antisite (ZnO), the Zn interstitial (Zn_I), and the O vacancy (V_O).[146] However, recently first-principles investigations based on density-functional theory suggest that hydrogen in ZnO occurs exclusively in the positive charge state and is responsible for the n-type conductivity of ZnO (Ref. 124) (discussed in detail in Sec. V). The highest room-temperature electron mobility for a bulk ZnO single crystal grown by vapor-phase transport method is reported to be about 205 $cm^2/V\,s$ with a carrier concentration of 6.0×10^{16} cm^{-3}.[146] This value is very close to the predicted mobility value. The Hall data obtained as a function of temperature is shown in Fig. 22. The mobility data were fitted using Rode's method of solving the Boltzmann transport equation by taking into consideration the major scattering mechanisms, such as polar-optical-phonon scattering, acoustic-phonon scattering through deformation and piezoelectric potentials, and Coulomb scattering from ionized impurities or defects. It was argued that the conduction was dominated by hopping at 8 K due to the carrier freeze-out

[This article is copyrighted as indicated in the article. Reuse of AIP content is subject to the terms at: http://scitation.aip.org/termsconditions. Downloaded to] IP: 128.172.48.58 On: Mon, 19 Oct 2015 20:45:44

TABLE VII. A compilation of XRD results, electron mobilities, and corresponding carrier concentration obtained in nominally undoped bulk and thin-film ZnO deposited on different substrates by various growth techniques.

Sample	FWHM of XRD rocking curves (arc sec)	Carrier concentration (cm^{-3})	Electron mobility ($cm^2 V^{-1} s^{-1}$)	Ref. (year)
Monte Carlo calculation	⋯	⋯	300	146 [Albrecht *et al.* (1999)]
Bulk ZnO grown by vapor-phase transport method	n/a	6.0×10^{16}	205	146 [Look *et al.* (1998)]
Bulk ZnO grown by pressurized melt method	49 (0002)	5.05×10^{17} (296 K) 3.64×10^{16} (77 K)	131 (296 K) 298 (77 K)	669 [Nause and Nemeth (2005)]
Bulk ZnO grown by hydrothermal method	18 (0002)	8×10^{13}	200	670 [Maeda *et al.* (2005)]
ZnO thin film on *c*-plane sapphire substrates grown by PLD	151 (0002)	2.0×10^{16}	155	147 [Kaidashev *et al.* (2003)]
ZnO thin films on *c*-plane sapphire grown by MBE	42 (0002)	1.2×10^{17}	130	148 [Kato *et al.* (2003)]
ZnO thin films grown on *a*-plane sapphire by MBE	n/a	7.0×10^{16}	120	148 [Iwata *et al.* (2000)]
$Zn_{0.9}Mn_{0.1}O/ZnO$ heterostructure grown on *c*-plane sapphire by PLD	n/a	8.8×10^{12} cm^{-2}	130	148 [Edahiro *et al.* (2003)]
ZnO thin film on *c*-plane sapphire with ZnO/MgO double-buffer layers grown by MBE	18 (0002) 1076 ($10\bar{1}1$)	1.2×10^{17}	145	148 [Miyamoto *et al.* (2004)] 671 [Cho *et al.* (2005)]
ZnO thin film grown on MgZnO-buffered $ScAlMgO_4$ substrates by PLD	<12 (0002) <12 ($10\bar{1}1$)	1×10^{16}	440	672 [Ohtomo and Tsukazaki (2005)]

effect, where the resistivity was measured to be 2.8×10^4 Ω cm. For 15 K$<T<$40 K, the transport was determined by a combination of mixed band and hopping conduction, whereas above 40 K, the data were well fitted by the usual statistical model (charge-balance equation) involving only the transport in the conduction band. The mobility showed a peak value of about 2000 cm^2/V s at 50 K.

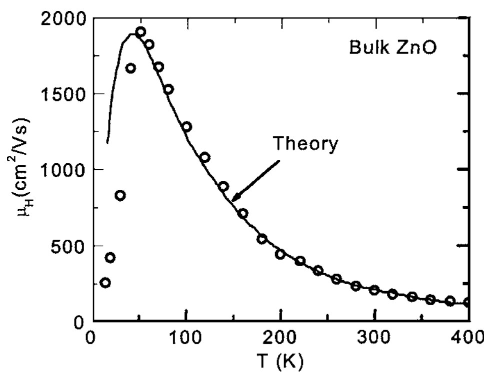

FIG. 22. Experimental (circles) and theoretical (solid line) Hall mobilities as a function of temperature in bulk ZnO. [Reprinted from D. C. Look, D. C. Reynolds, J. R. Sizelove, R. L. Jones, C. W. Litton, G. Cantwell, and W. C. Harsch, Solid State Commun. **105**, 399 (1998), Copyright 1998, with permission from Elsevier.]

For the carrier concentration data shown in Fig. 23 a two-donor charge-balance equation has been applied to fit the experimental data:

$$n + N_A = \sum_i \frac{N_{Di}}{1 + n/\phi_i}, \tag{18}$$

where $\phi_i=(g_{0i}/g_{1i})N_c' \exp(\alpha_i/k)T^{3/2}\exp(-E_{D0i}/kT)$, and g_{0i} (g_{1i}) is the unoccupied (occupied) state degeneracy of donor

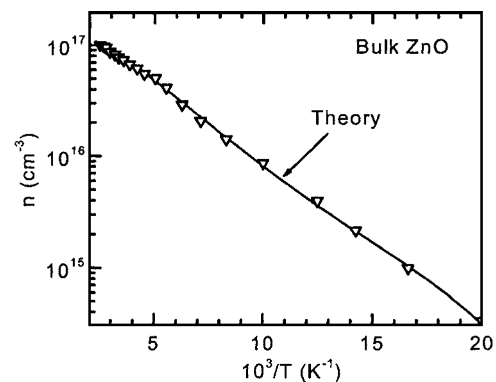

FIG. 23. Experimental carrier concentration (triangles) corrected for Hall *r* factor and theoretical fit (solid line) as a function of inverse temperature for bulk ZnO. [Reprinted from D. C. Look, D. C. Reynolds, J. R. Sizelove, R. L. Jones, C. W. Litton, G. Cantwell, and W. C. Harsch, Solid State Commun. **105**, 399 (1998), Copyright 1998, with permission from Elsevier.]

[This article is copyrighted as indicated in the article. Reuse of AIP content is subject to the terms at: http://scitation.aip.org/termsconditions. Downloaded to] IP: 128.172.48.58 On: Mon, 19 Oct 2015 20:45:44

i. The term N_c' is the effective conduction-band density of states at $T=1$ K and α_i is the temperature coefficient defined by $E_{Di}=E_{D0i}-\alpha_i T$, where E_{Di} is the activation energy of donor *i*. Although their origin was left unclear in this work it has been determined that the dominant hydrogenic shallow donor had a concentration of about 1×10^{17} cm^{-3} and an energy of about 60 meV, whereas the total acceptor concentration was much lower, about 2×10^{15} cm^{-3}, resulting in a lower compensation ratio of 0.02. However, the shallower donor that was ruled out in this work due to its smaller concentration (about one order of magnitude less than the deeper donor) at an energy of ~31 meV was further investigated later by the same group.[146] They reported that high-energy electron irradiation in ZnO produces shallow donors at about 30 meV. Because the process was found to be polarity dependent, where the production rate is much higher for Zn-face [0001] than O-face $[000\bar{1}]$ irradiation, it has been concluded that this native shallower donor is related to a Zn-sublattice defect, most likely the interstitial Zn_I or a Zn_I-related complex.

Regarding the ZnO epilayers grown by various growth techniques on different substrates, room-temperature mobilities are relatively poor[147] (typically below 100 cm^2/V s) compared to bulk ZnO, particularly the variety grown by the vapor-transport method. However, as listed in Table VII some room-temperature mobility values are comparable to the best reported value for bulk ZnO. Kaidashev *et al.*[147] reported the best reproducible electron mobilities from 115 up to 155 cm^2/V s at 300 K in a narrow carrier concentration range from 2×10^{16} to 5×10^{16} cm^{-3} for nominally undoped ZnO thin films of total thickness of 1–2 μm grown on *c*-plane sapphire substrates by a multistep PLD technique. They attributed this success to the multistep PLD process, which includes the insertion of 30-nm-thin ZnO relaxation layers deposited at a reduced substrate temperature. The topographical properties of the films were correlated with the corresponding electrical properties. The high-mobility samples showed atomically flat surface structure with a grain size of about 0.5–1 μm, whereas the surfaces of low-mobility films consist of clearly resolved hexagonally faceted columnar grains of only 200-nm size. The observation of the excitonic features at low-temperature photoluminescence spectra also reflects the quality of the samples, which is of primary importance to improve the electrical properties of ZnO.

Kato *et al.* and Iwata *et al.*[148] have performed similar and successful studies on heteroepitaxially grown ZnO epilayers using plasma-assisted molecular-beam epitaxy (MBE) and radical-source MBE techniques. Kato *et al.*[148] used $(11\bar{2}0)$ *a*-plane sapphire substrates and high-temperature growth with low-temperature buffer layers for high-quality undoped ZnO epitaxial films. They obtained electron mobilities as high as 120 cm^2/V s and residual carrier concentrations as low as 7×10^{16} cm^{-3}. With further optimization of the growth condition such as O/Zn flux ratio, a maximum mobility of 130 cm^2/V s with a residual carrier concentration of 1.2×10^{17} cm^{-3} was reported.[148] It has been suggested that stoichiometric ZnO films have the lowest dislocation density and the highest electron mobility compared to ZnO films grown under nonstoichiometric flux conditions. Iwata *et al.*[148] used ZnO/MgO double-buffer layers for high-electron-mobility ZnO epilayers grown on *c*-plane sapphire. It has been argued that the precisely controlled low growth rate of the double-buffer layers was crucial for the improvement of electrical properties. The highest electron mobility of 145 cm^2/V s in MBE-grown ZnO film was reported at room temperature. This improvement was attributed to a decrease in dislocation density, based on both x-ray-diffraction ω-rocking curve measurements and calculated electron mobilities.

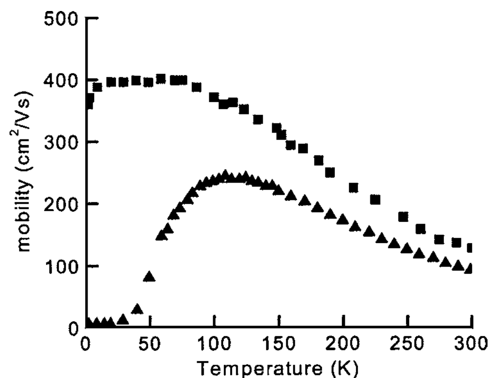

FIG. 24. Temperature dependence of the mobility of the ZnMnO/ZnO heterostructure (squares) and the 1-μm-thick ZnO single-layer (triangles) control sample. [Reprinted with permission from T. Edahiro, N. Fujimura, and T. Ito, J. Appl. Phys. **93**, 7673 (2003). Copyright 2003, American Institute of Physics.]

ZnO-based heterostructures, which contain magnetic impurities in the barrier layer, were grown on *c*-cut sapphire substrates by pulsed-laser deposition by Edahiro *et al.*[148] The temperature dependence of the mobility of the $Zn_{0.9}Mn_{0.1}O$/ZnO heterostructure exhibits the suppression of ionized impurity scattering below 100 K as shown in Fig. 24. The carrier concentration and the mobility measured at 1.85 K are 4.0×10^{12} cm^{-2} and 360 cm^2/V s, respectively. These transport properties revealed that two-dimensional electron gas is successfully formed at the $Zn_{0.9}Mn_{0.1}O$/ZnO interface.

2. High-field transport

Ensemble Monte Carlo (MC) simulations have been the popular tools to investigate the steady-state electron transport in semiconductors theoretically. In particular, the steady-state velocity-field characteristics have been determined using the Monte Carlo method for electric-field strengths up to 350 kV/cm in bulk, wurtzite-structure ZnO at lattice temperatures of 300, 450, and 600 K.[146] The conduction bands of wurtzite-phase ZnO structure were calculated using FP-LMTO-LDA method. For the MC transport simulation, the lowest Γ valley (Γ_1 symmetry) and the satellite valleys located at Γ (Γ_3 symmetry) and at *U* point, U_{min} (U_1 symmetry), which is located two-thirds of the way between the *M* and *L* symmetry points on the edge of the Brillouin zone, were considered.

The calculated electron drift velocity versus electric-field characteristics are plotted in Fig. 25 for wurtzite-phase ZnO

[This article is copyrighted as indicated in the article. Reuse of AIP content is subject to the terms at: http://scitation.aip.org/termsconditions. Downloaded to] IP: 128.172.48.58 On: Mon, 19 Oct 2015 20:45:44

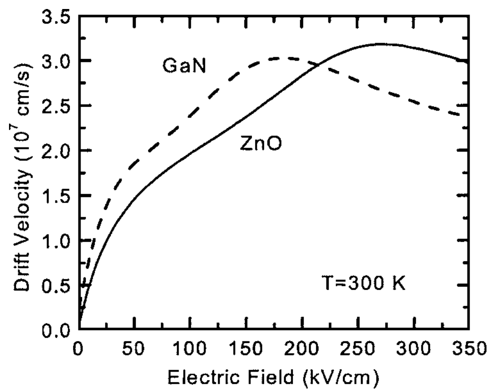

FIG. 25. Comparison of the calculated electron drift velocity vs electric field for the wurtzite-structure ZnO (solid) and GaN (dashed) at 300 K. [Reprinted with permission from J. D. Albrecht, P. P. Ruden, S. Limpijumnong, W. R. L. Lambrecht, and K. F. Brennan, J. Appl. Phys. **86**, 6864 (1999). Copyright 1999, American Institute of Physics.]

along with GaN for comparison. The first change in the differential mobility curve near 50 kV/cm was attributed to the onset of significant spontaneous polar-optical-phonon emission as the electrons are accelerated to energies greater than the longitudinal-optical-phonon energy of 72 meV. At higher temperatures, this effect reduces and becomes almost negligible at 600 K because the emission and absorption rates are of comparable magnitude at elevated lattice temperatures. With increasing electric field the drift velocity increases and reaches a peak value of 3×10^7 cm/s at 250 K. Further increase of electric field results in a negative differential effect. However, from examination of the electron energy distributions that showed only insignificant transfer of electrons to the higher valleys, the strong decrease of the differential mobility with increasing electric field was attributed to the pronounced nonparabolicity of the central valley. Although a comparison of the drift velocity of ZnO to the calculated drift velocity of wurtzite GaN shows comparable peak velocities, the peak fields differ considerably, with the peak field for GaN being at a field which is about 100 kV/cm lower than that of ZnO. It has been argued that this difference arises mainly from the lower satellite valleys in GaN, which have been demonstrated to exhibit a transferred electron effect, and from the stronger Fröhlich coupling in ZnO. If the hot phonon effects prevalant in GaN were to also take place in ZnO, which is very likely, much more refined work is needed on the theoretical side as well to get a good velocity figure in ZnO at high fields.

III. ZnO GROWTH

The growth of ZnO thin films has been studied for acoustical and optical devices because of their excellent piezoelectric properties and a tendency to grow with strong (0001) preferential orientation on various kinds of substrates, including glass,[149] sapphire,[150] and diamond.[151] The early reports dealt with deposition of ZnO utilizing growth techniques such as magnetron sputtering[151,152] and chemical-vapor deposition;[153–155] however, the films were mainly polycrystalline. Later attempts led to high-quality ZnO single-crystal films prepared by rf magnetron sputtering[156] and other growth techniques allowing a fine control over the deposition procedure, such as molecular-beam epitaxy (MBE),[157,158] pulsed-laser deposition (PLD),[159] metal-organic chemical-vapor deposition (MOCVD),[160] and hydride or halide vapor-phase epitaxy (HVPE).[161,162] Table VII compiles some of the structural and electrical properties from ZnO samples grown by different techniques. The improved quality of ZnO films allowed the observation of optically pumped lasing at room temperature.[163] Their potential application as ultraviolet light emitters brings considerable attention to research on ZnO growth.[163,164] Although high-quality ZnO substrates are available, making homoepitaxy possible, most of the growth until now has been done on sapphire (Al_2O_3) due to its low cost, availability as large-area wafers, and its wide energy-band gap despite its poor structural and thermal match to ZnO. It should be mentioned that availability of high-quality ZnO substrate does not automatically pave the way for high-quality epitaxial layers, and much work remains to be done to attain epitaxial layer matching the bulk in quality. In comparison with GaN/Al_2O_3, ZnO/Al_2O_3 has approximately equivalent x-ray-diffraction (XRD) and photoluminescence (PL) linewidths, and even lower dislocation densities.[165] Heteroepitaxial ZnO layers have been grown on several other substrates, such as CaF_2,[166] Si,[167] GaAs,[168,169] and $ScAlMgO_4$,[170] as well as on GaN/Al_2O_3 templates.[159]

A. Bulk growth

Growth of large-area and high-quality ZnO crystals is important not only for materials science but also for many device applications. Although sapphire has been conventionally used as the substrate for ZnO growth, high dislocation density caused by the large lattice mismatch (in-plane lattice mismatch: 18.4%) between the sapphire substrate and ZnO would deteriorate any device performance. High-quality large ZnO single crystals will be beneficial for the UV and blue light-emitting devices, due to the potential advantages of homoepitaxy. Homoepitaxy with its perfect lattice matching (in-plane and out-of-plane) has the potential for providing no strain induced by thermal- expansion mismatch, absence of highly defective substrate-layer interface, lower overall defect density, easy control over the material polarity by using Zn-face or O-face (0001) substrate, and simple device design (ZnO substrates can be made very conductive). In addition to homoepitaxy, ZnO single-crystal substrates could also be useful for heteroepitaxy of GaN-based active layers. The stacking order of ZnO is the same as that of GaN, with a lattice mismatch of only 1.8%.

Growth of bulk ZnO crystals is mainly carried out by three methods: hydrothermal,[171–173] vapor phase,[34,41,146,174] and melt growth.[175] Because of its high vapor pressure, growth of ZnO from the melt is difficult, and growth by vapor-phase deposition is difficult to control. The low supersaturation of the solution during hydrothermal reaction favors crystal growth. The hydrothermal growth of the quartz crystals has been well established. Therefore, its application to the large-sized single crystals is quite suitable. The growth rate has been reported to be anisotropic. The growth rate in

[This article is copyrighted as indicated in the article. Reuse of AIP content is subject to the terms at: http://scitation.aip.org/termsconditions. Downloaded to] IP: 128.172.48.58 On: Mon, 19 Oct 2015 20:45:44

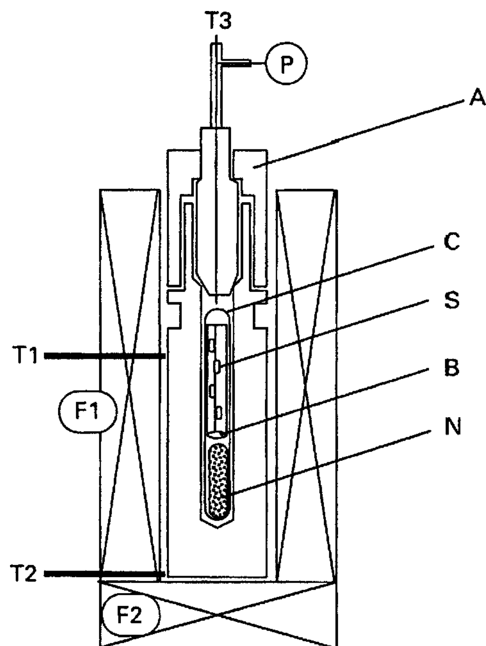

FIG. 26. Schematic drawing of a hydrothermal growth system. [Reprinted from T. Sekiguchi, K. Obara, T. Shishido, and N. Sakagami, J. Cryst. Growth **214/215**, 72 (2000), Copyright 2000, with permission from Elsevier.]

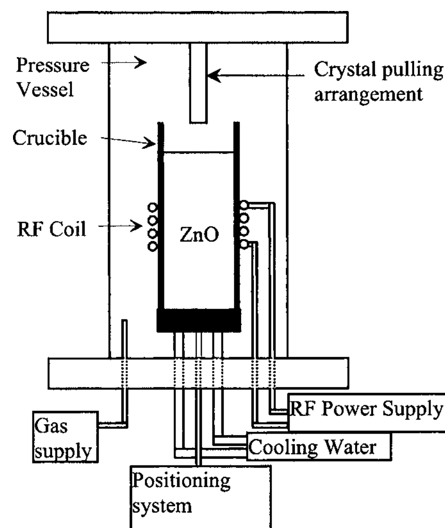

FIG. 27. Schematic sketch of the ZnO crystal melt growth apparatus [after Nause *et al.* (Ref. 175)].

the [0001] direction was ~0.25 mm/day, and the ratio of growth rates between the fast ([0001]) direction and slow ($[000\bar{1}]$) direction was 3:1.[176] However, the hydrothermal crystals inevitably incorporate alkali metals (K and Li) and small amounts of metallic impurities from the solution.

Figure 26 shows a schematic diagram of a hydrothermal growth system.[171] The hydrothermal method uses ZnO single-crystal seeds (suspended by Pt wire), and sintered ZnO strings together with a KOH (3 mol/l) and LiOH (1 mol/l) aqueous solution are used as a nutrient. The seeds and the nutrient are placed into a Pt crucible. This crucible is sealed by welding and placed in an autoclave. The autoclave is then placed into a two-zone vertical furnace. ZnO is transferred from the nutrient in the higher-temperature zone to the seeds in the lower-temperature zone. The seeds grow to bulk ingots about 10 mm in size after 2 weeks. The growth temperature is 300–400 °C at a pressure between 70 and 100 MPa. A Pt inner container is used for preventing impurity incorporation from the aqueous solution. Transparent ZnO crystals grown to a size of $50\times50\times15$ mm^3 showed a full width at half maximum (FWHM) of 8 arc sec for the (0002) XRD rocking curve. The ZnO crystals were surrounded by the (0001), $(10\bar{1}1)$, $(10\bar{1}0)$, $(10\bar{1}\bar{1})$, and $(000\bar{1})$ faces.[173] The crystal shapes were reported to depend on the precursor and the solution basicity, and on the shapes of seed crystals. The crystal color is nonuniform because of the anisotropic crystal growth in which the growth rate of each sector depends on orientation. When used as substrates for epitaxy, proper surface preparation is necessary to evaluate the quality of hydrothermally grown ZnO.[176] As confirmed by PL and XRD, improved polishing methods result in significantly improved surface quality. Properly polished hydrothermal ZnO exhibits optical properties similar to the vapor-phase-grown material.

A method which produces very high quality bulk ZnO wafers is based on vapor transport. In this method, the reaction takes place in a nearly closed horizontal tube.[146] Pure ZnO powder used as the ZnO source is placed at the hot end of the tube which is kept at about 1150 °C. The material is transported to the cooler end of the tube, maintained at about 1100 °C, by using H_2 as a carrier gas. A carrier gas is necessary because the vapor pressures of O and Zn are quite low over ZnO at these temperatures. The likely reaction in the hot zone is $ZnO(s)+H_2(g)\rightarrow Zn(g)+H_2O(g)$. At the cooler end, ZnO is formed by the reverse reaction, assisted by a single-crystal seed. To maintain the proper stoichiometry, a small amount of water vapor is added. Growth time of 150–175 h provided 2-in.-diameter crystals of about 1 cm in thickness. Hall carrier concentration and mobility at 300 K were about 6×10^{16} cm^{-3} and 205 cm^2 V^{-1} s^{-1}, respectively, and the peak mobility (at 50 K) was about 2000 cm^2 V^{-1} s^{-1}. Vapor transport using chlorine and carbon as transporting agents has been used to achieve ZnO crystal growth at moderate temperature of 950–1000 °C.[41] FWHMs of (0002) XRD rocking curves were around 30 arc sec, and room-temperature electron concentration in the crystals was as high as 3×10^{19} cm^{-3}.

Another method for producing bulk ZnO is that of melt growth which is employed at Cermet, Inc.[175] The Cermet, Inc. melt method is based on a pressurized induction melting apparatus (see Fig. 27). The melt is contained in a cooled crucible. Zinc oxide powder is used as the starting material. The heat source used during the melting operation is radio frequency (rf) energy, induction heating. The rf energy produces joule heating until the ZnO is molten at about 1900 °C. Once the molten state is attained, the crucible is slowly lowered away from the heated zone to allow crystallization of the melt. A FWHM of about 125 arc sec was reported for the (0004) x-ray rocking curve. The room-temperature electron concentration and mobility were 5.04×10^{17} cm^{-3} and 131 cm^2 V^{-1} s^{-1}, respectively.

[This article is copyrighted as indicated in the article. Reuse of AIP content is subject to the terms at: http://scitation.aip.org/termsconditions. Downloaded to] IP: 128.172.48.58 On: Mon, 19 Oct 2015 20:45:44

TABLE VIII. Lattice parameters of a number of the prospective substrate materials for ZnO.

Material	Crystal structure	Lattice parameters a (Å) c (Å)	Lattice mismatch (%)	Thermal-expansion coefficient, α (K^{-1}) α_a (10^{-6}) α_c (10^{-6})
ZnO	Hexagonal	3.252 5.213	⋯	2.9 4.75
GaN	Hexagonal	3.189 5.185	1.8	5.17 4.55
AlN	Hexagonal	3.112 4.980	4.5	5.3 4.2
α-Al_2O_3	Hexagonal	4.757 12.983	(18.4% after 30° in-plane rotation)	7.3 8.1
6H-SiC	Hexagonal	3.080 15.117	3.5	4.2 4.68
Si	Cubic	5.430	40.1	3.59
$ScAlMgO_4$	Hexagonal	3.246 25.195	0.09	
GaAs	Cubic	5.652	42.4	6.0

B. Substrates

In order to reduce the strains and dislocation density in epitaxial ZnO and related films, closely lattice-matched substrates are favored for growth. Sapphire substrates are commonly used for ZnO heteroepitaxial growth, primarily on the (0001) orientation (basal or c plane), and also on the $(11\bar{2}0)$ a plane. In addition, ZnO and related oxides have been grown on Si,[167] SiC,[177] GaAs,[168,169] CaF_2,[166] and $ScAlMgO_4$.[170] Lattice parameters of several substrate materials frequently used for ZnO growth and their mismatch to ZnO are listed in Table VIII.

Single-crystal ZnO films have been grown on sapphire with a high degree of surface flatness, which is essential for device fabrication. The ZnO layers have been grown on sapphire by using a variety of growth techniques, including PLD,[159] MOCVD,[178] and MBE.[157,179,180] Because of the large lattice mismatch between ZnO (a=0.3250 nm and c=0.5213 nm) and the underlying sapphire (a=0.4754 nm and c=1.299 nm), even after a 30° in-plane rotation to reduce the mismatch, as-grown ZnO films usually display large mosaicity, high residual (most likely due to defect-induced native centers) carrier concentrations (in the 10^{17}-cm^{-3} range), and low mobilities (less than 100 $cm^2\,V^{-1}\,s^{-1}$ at room temperature) as compared to an electron concentration of $\sim 10^{15}$ cm^{-3} and Hall mobility of $\sim$200 $cm^2\,V^{-1}\,s^{-1}$ typical for bulk single crystals,[157,170,181] making their use for optoelectronic applications a challenge.

The growth of ZnO films on sapphire (0001) (c plane) substrates usually results in the epitaxial relationship of $ZnO(0001)\parallel Al_2O_3(0001)$ and $ZnO[10\bar{1}0]\parallel Al_2O_3[11\bar{2}0]$ (basically the m-plane normal direction of ZnO aligns with the a-plane normal of sapphire).[157,158] The lattice mismatch decreased to 18.4% with the 30° in-plane rotation. The epitaxial relationship of ZnO grown on c-axis sapphire is shown in Fig. 28. ZnO layers were also successfully grown on sapphire $(11\bar{2}0)$ (a plane).[182] In order to eliminate the in-plane domain rotation, several lattice-matched substrates have been used for ZnO growth. Ohtomo *et al.*[170] selected hexagonal $ScAlMgO_4$ (0001) substrates to grow ZnO by laser-assisted MBE. The lattice constants of hexagonal $ScAlMgO_4$ are a=3.246 Å and c=25.195 Å, giving rise to an in-plane lattice mismatch with ZnO as small as 0.09%. ZnO layers were grown at temperatures ranging from 350 to 1000 °C, and the crystal perfection was drastically improved by using $ScAlMgO_4$ (0001) substrates. All the films showed an epitaxial relationship of $ZnO(0001)\parallel ScAlMgO_4(0001)$ and $ZnO[11\bar{2}0]\parallel ScAlMgO_4[11\bar{2}0]$ without any trace of the other in-plane orientation domains which were observed for ZnO/sapphire (0001). The residual carrier concentration and electron mobility were low 10^{16} cm^{-3} and 60–100 $cm^2\,V^{-1}\,s^{-1}$, respectively. The growth on CaF_2 (111) substrates (the lattice mismatch with ZnO is −15.8%) with the application of a low-temperature (LT) buffer layer have been performed to improve the ordering both in-plane and along the growth direction.[166] The epitaxial relationships between the ZnO films and CaF_2 (111) substrate are $ZnO(0001)\parallel CaF_2(111)$ and $ZnO[2\bar{1}\bar{1}0]\parallel CaF_2[\bar{1}10]$. For surface-acoustic wave (SAW) device applications, single-crystal ZnO films have been grown on $(01\bar{1}2)$ $LiTaO_3$ (Ref. 183) and (0001) $LiNbO_3$ substrates (Ref. 184) by electron-cyclotron-resonance-assisted MBE. The ZnO film orientation on $(01\bar{1}2)$ $LiTaO_3$ substrate was dependent on the oxygen-to-zinc ratio. Under high oxygen-to-zinc ratio condition, $(11\bar{2}0)$ ZnO with the c axis parallel to the $LiTaO_3$ substrate was grown, while under low oxygen-to-zinc ratio, (0001) ZnO with the c axis perpendicular to the $LiTaO_3$ substrate was grown. The epitaxial relationships between ZnO and $LiNbO_3$ are (0001) $ZnO\parallel(0001)LiNbO_3$ and $[\bar{1}2\bar{1}0]$ $ZnO\parallel[\bar{1}100]$ $LiNbO_3$. ZnO growth on GaN templates is discussed in detail in Sec. III D.

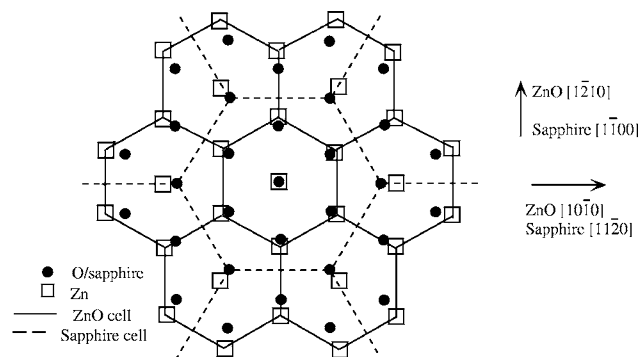

FIG. 28. Schematic diagram showing the epitaxial relationships of ZnO (0001) grown on Al_2O_3 (0001).

In addition to the heteroepitaxial growth on the abovementioned substrates, ZnO homoepitaxy has been studied by several groups.[185,186] Due to the nature of the wurtzite structure along the [0001] direction, i.e., alternating O and Zn layers, the (0001) ZnO wafer surfaces could be either Zn- or O-terminated, meaning, [0001] indicating Zn surface layer or $[000\bar{1}]$ indicating O surface layer. The chemical bonding of surface atoms for the aforementioned two polarities is differ-

[This article is copyrighted as indicated in the article. Reuse of AIP content is subject to the terms at: http://scitation.aip.org/termsconditions. Downloaded to] IP: 128.172.48.58 On: Mon, 19 Oct 2015 20:45:44

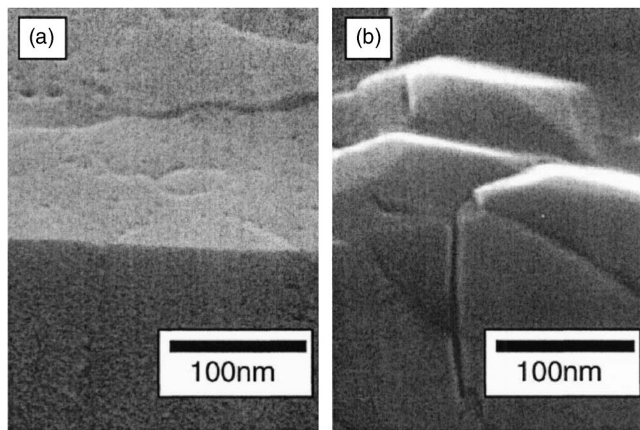

FIG. 29. SEM images of faceting ZnO films grown on bulk ZnO substrates (a) on $-c$ surface and (b) on $+c$ surface. [Reprinted from K. Sakurai, M. Kanehiro, T. Tanabe. S. Fujita, and S. Fujita, J. Cryst. Growth **209**, 522 (2000), Copyright 2000, with permission from Elsevier.]

ent, which has an impact on surface preparation due to the difference in surface hardness. Studies on the sublimation of ZnO basal surface showed that Zn atoms start to evaporate from the Zn-face substrate at temperatures as low as 380 °C, while the sublimation of O surface takes place above ~600 °C.[187] Homoepitaxial films were grown on the two polar surfaces of ZnO substrates.[185] Under excessive Zn supply, the surface was smooth on $-c$-oriented or $[000\bar{1}]$ (O surface) ZnO substrate but was completely covered with hillocks on $+c$-oriented or [0001] (Zn surface) ZnO substrate, as shown in Fig. 29. It was concluded that excessive Zn pressure from the initial growth stage is required for $-c$-direction growth, while excessive oxygen supply leads to $+c$-direction growth.[185] The O surface is better than the Zn surface for film growth because mechanical damage can easily occur on the softer Zn surface. The Zn-rich surface may also form different compositional domains in the oxygen environment. High-temperature annealing of single crystals in air improves the structure, morphology, and optical property of the O surface but there is only a slight effect on the Zn surface.

C. rf magnetron sputtering

One of the most popular growth techniques for early ZnO investigations was sputtering (dc sputtering, rf magnetron sputtering, and reactive sputtering). As compared to sol gel and chemical-vapor deposition,[153–155] the magnetron sputtering was a preferred method because of its low cost, simplicity, and low operating temperature.[188] ZnO films grow at a certain substrate temperature by sputtering from a high-purity ZnO target using a rf magnetron sputter system. The growth is usually carried out in the growth ambient with $O_2/Ar+O_2$ ratios ranging from 0 to 1 at a pressure of $10^{-3}-10^{-2}$ Torr. O_2 serves as the reactive gas and Ar acts as the sputtering enhancing gas. ZnO can also be grown by dc sputtering from a Zn target in an $Ar+O_2$ gas mixture. The rf power applied to the plasma is tuned to regulate the sputtering yield rate from the ZnO target. For these experiments, the target is presputtered for 5–15 min before the actual deposition begins to remove any contamination on the target surface, make the system stable, and reach optimum condition.

Although most of the earlier sputtered materials were polycrystalline or even amorphous, some important accomplishments were reported. Although, sapphire substrates are the most popular choice due to the similar lattice structure, other substrates have also been used for various device applications. For SAW devices and piezoelectric studies, ZnO films have been deposited on diamond (111),[151] glass,[189,190] GaAs,[168,169] and Si substrates.[167,191–194] The epitaxial relationship between ZnO thin film and the diamond was determined as $[11\bar{2}0]$ ZnO$\|[\bar{1}01]$ diamond.[151] The growth temperature used in these studies was ranged from room temperature to about 400 °C, and the ZnO thin films showed preferred (0001) orientation.[193,194] Jeong *et al.*[191] reported the effects of growth ambient on PL properties of ZnO films grown on Si (100) by rf magnetron sputtering. Upon increasing the $O_2/Ar+O_2$ ratio in the growth ambient, the visible emission in the RT PL spectra was drastically suppressed without sacrificing the band-edge emission intensity in the ultraviolet region. This tendency is attributed to the reduction of the oxygen vacancies and zinc interstitials in the film induced by the improvement of the stoichiometry, indicating that the visible emission in ZnO originates possibly from oxygen vacancy or zinc-interstitial-related defects. A MgO buffer layer has been used for sputtered ZnO on Si (100) substrates to accommodate the large lattice mismatch.[192] The MgO films used as buffers were deposited by electron-beam evaporation from MgO crystals, and ZnO films were formed by annealing the rf-sputtered Zn metallic films in O_2. At an annealing temperature above 800 °C, the ZnO film underwent a phase transformation from ZnO to $Mg_xZn_{1-x}O$ alloy, although the composition was not reported. Intense UV band-edge PL from the MgZnO alloy was observed at room temperature.

The ZnO films with (0001) orientation have been observed on both c- and a-plane sapphire substrates just as in the case of GaN on sapphire.[110] The effect of sputtering variables (substrate temperature, rf power, gas pressure, and composition) on the ZnO film structure and optical properties have been one of the major research topics. Kim *et al.*[156] reported high-quality single-crystal ZnO films prepared on sapphire (0001) by rf magnetron sputtering. They found that a high substrate temperature is essential to improve the crystal structure, but rf power had to be adjusted for the appropriate growth rate, as shown in Fig. 30.[156] The ZnO film deposited at 120 W and 600 °C exhibited the best FWHM of 0.13° for (0002) XRD rocking curve and the corresponding FWHM of RT PL was 76 meV. The cross-sectional transmission electron microscopy (TEM) revealed that the samples grown under the optimum temperature and rf power combination exhibited the largest grain size. A TEM study of crystallite structure and data from RT PL suggested that the origin of deep-level emission in the ZnO films could be due to the existence of oxygen vacancies, which is consistent with the result reported in Ref. 191. In the sputtering growth of oxide films, O^- ions are mainly responsible for the resputtering phenomenon.[195,196] The sputtering effect of O ions on the ZnO film surface was studied by applying a grid bias during

[This article is copyrighted as indicated in the article. Reuse of AIP content is subject to the terms at: http://scitation.aip.org/termsconditions. Downloaded to] IP: 128.172.48.58 On: Mon, 19 Oct 2015 20:45:44

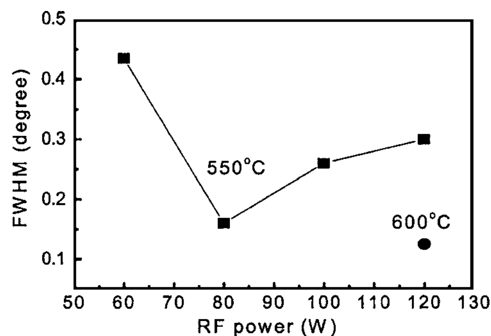

FIG. 30. The FWHM variation of the XRD θ-rocking curve of the ZnO film grown on the (0001) sapphire substrate at 550 and 600 °C. [Reprinted with permission from K.-K. Kim, J.-H. Song, H.-J. Jung, W.-K Choi, S.-J. Park, and J.-H. Song, J. Appl. Phys. **87**, 3573 (2000). Copyright 2000 American Institute of Physics.]

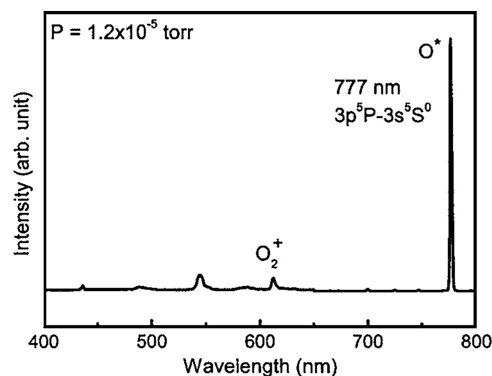

FIG. 31. Optical emission spectra of the oxygen plasma.

the deposition on sapphire (0001).[197] The improved epitaxial quality at an optimum bias was attributed to a reduction of the flux of energetic oxygen anions bombarding the film surface and, thereby, to significant suppressing of the resputtering phenomenon.

The stress in the sputtered ZnO was investigated as a function of the substrate temperature in the range of 250–450 °C, the sputtering pressure, and the type of substrate (Si or GaAs).[198–200] Postdeposition annealing also has been used to relieve the stress and improve the structure and optical properties of the sputtered ZnO films.[167,201,202] Liu *et al.*[203] deposited ZnO thin films by rf magnetron sputtering in $Ar+O_2$ plasma. The samples annealed at 950 and 1000 °C showed the sharpest (0002) XRD peak and the smallest root-mean-square (rms) surface roughness. During the annealing process, the atoms of ZnO gain energy to rearrange in the lattice. The (0002) XRD rocking curves were of the Gaussian shape and showed no tail caused by the deformed interfacial regions.[204] An atomic-force microscopy (AFM) study revealed the increase in grain size with increasing annealing temperature, with a grain-size distribution between 100 and 200 nm for the sample annealed at 1000 °C. Table IX summarizes the results of XRD, AFM, and PL measurements on ZnO films annealed at different temperatures.[203]

The attainment of *p*-type ZnO by rf magnetron sputtering method, albeit controversial, has also been reported. Phosphorus-doped *p*-type ZnO was obtained by sputtering a ZnO target with 1-wt % P_2O_5 and rapid thermal-annealing (RTA) in N_2.[205] It was also demonstrated that reactively sputtered ZnO thin films could be changed from *n*-type to moderate *p*-type by adjusting the O_2/Ar ratio in the sputtering plasma.[206] The ZnO films deposited on (100) Si substrates by reactive sputtering of a Zn target in O_2/Ar atmosphere produced *n*-type ZnO at low O_2/Ar ratios and moderately *p*-type ZnO at higher O_2/Ar ratios. In addition, when ZnO films were prepared on (001) GaAs substrates,[169] a *p*-type conductivity was observed in the film annealed in vacuum after the growth. The conduction-type conversion was attributed to As diffusion from the substrate.

TABLE IX. Structural and optical parameters for the ZnO samples obtained from AFM, XRD, and PL measurements.

Annealing temperature	rms surface roughness (nm)	XRD (0002) FWHM (arc min)	10-K PL FWHM (meV)
As grown	14.8	66.0	10
800 °C	13.5	25.1	3.8
950 °C	7.5	16.9	2.7
1000 °C	6.8	16.2	3.0

A more advanced sputtering technique utilizes electron-cyclotron-resonance (ECR) source to supply the power to the plasma. The advantage of the ECR sputtering system is that it enables the production of highly ionized plasma under low gas pressures. The ZnO films deposited by ECR sputtering exhibited a high electrical resistivity ($\rho > 10^{10}\ \Omega$ cm) and good piezoelectric and optical properties.[207,208]

D. Molecular-beam epitaxy

The main advantage of molecular-beam epitaxy (MBE) is its precise control over the deposition parameters and *in situ* diagnostic capabilities. With the feedback from reflection high-energy electron diffraction (RHEED), the growth mode of ZnO epilayers can be monitored in real time dynamically. For ZnO thin-film deposition by MBE, Zn metal and O_2 are usually used as the source materials. High-purity Zn metal is evaporated from an effusion cell, where the cell temperature can be varied to examine the effect of the Zn flux on the growth rate and material properties. The oxygen radical beam, which can be generated by an ECR (Ref. 209) or a rf plasma source,[210] is directed on the film surface to obtain high-oxidation efficiency. When the O plasma is used, the chamber pressure during growth is in the 10^{-5}-Torr range. Nitrogen dioxide (NO_2) was also utilized for MBE of ZnO on (0001) sapphire substrates to keep the chamber pressure low in an effort to protect sensitive filaments and heaters,[211] but the resultant crystal structures and the surface morphology were not satisfactory. Successful growth of ZnO films by using hydrogen peroxide (H_2O_2) vapor as a source of active oxygen has also been reported.[212] rf radical sources are employed by most groups nowadays because of the high reactivity of oxygen radicals produced and reasonable oxygen pressures [typically $(1-8)\times 10^{-5}$ Torr]. For the correct rf plasma mode, the emission at 777 nm due to the atomic oxygen transition of $3p^5P\text{-}3s^5S^0$ should dominate the optical emission spectrum (OES),[158,213] as shown in Fig. 31. The

[This article is copyrighted as indicated in the article. Reuse of AIP content is subject to the terms at: http://scitation.aip.org/termsconditions. Downloaded to] IP: 128.172.48.58 On: Mon, 19 Oct 2015 20:45:44

II/VI ratio can be tuned through the Zn cell temperature as well as rf power and O_2 flow rate of the plasma source. For high-quality ZnO films, the reported growth temperature is in the range of 350–650 °C with a growth rate of 0.3–0.7 μm/h.[157,158,214]

In 1997 and 1998 Chen *et al.* reported ZnO epitaxial growth on (0001) sapphire substrates by using an oxygen microwave plasma source.[158,180] The epitaxy process exhibited two-dimensional (2D) nucleation at the initial growth stage, which was followed by three-dimensional (3D) growth as indicated by RHEED. An *in situ* oxygen plasma preexposure of the sapphire substrate was found to be critical for the initial two-dimensional nucleation. The sapphire substrates were exposed to the oxygen plasma for 30 min at 600 °C before the growth. The preexposure produces an oxygen-terminated surface, which allows the first monolayer of ZnO to adjust itself to the oxygen sublattice of the Al_2O_3 substrate and thus to reduce the lattice mismatch. The XRD rocking curve of ZnO showed a narrow (0002) peak (FWHM ~0.005°) with a broad tail extending from the peak due to the in-plane mosaicity. The PL spectra exhibited dominant bound-exciton emission with a FWHM of 3 meV at low temperatures and a free-exciton emission combined with a very weak deep-level emission at RT.

The *c* plane of sapphire is composed of alternating layers of oxygen (sixfold symmetry) and Al atoms (threefold symmetry), while in the wurtzite structure of ZnO, both O and Zn are sixfold symmetric about the ZnO *c* axis, as shown in Fig. 28. For films grown on *c*-plane sapphire, the orientation relationship along the direction normal to the surface is ZnO (0001)‖sapphire (0001), but two types of in-plane rotational domains are observed as a result of the following alignments: ZnO $[1\bar{2}10]$‖sapphire $[1\bar{1}00]$ and ZnO $[10\bar{1}0]$‖sapphire $[11\bar{2}0]$.[157,158] This corresponds to a 30° rotation between the ZnO and sapphire *a* axes, presumably due to preferential bonding of Zn atoms with sapphire O atoms. The presence of these domains leads to increased carrier scattering as exemplified by the typical low mobilities of 10–40 $cm^2\,V^{-1}\,s^{-1}$.

In order to eliminate the orientational domains often observed in ZnO thin films grown on (0001) sapphire, $(11\bar{2}0)$ sapphire substrates have been used for ZnO epitaxy. The lattice parameter $a=0.3250$ nm of ZnO and parameter $c=1.299$ nm of sapphire are related almost exactly by a factor of 4, with a mismatch less than 0.08% at room temperature. Based on this fact and coining the term "uniaxial locked epitaxy," Fons *et al.*[210,215] conducted an investigation of ZnO epitaxy growth on *a*-plane $(11\bar{2}0)$ sapphire, including a detailed analysis of the initial stages of growth.[216] The out-of-plane and in-plane orientational relationships are ZnO [0001]‖sapphire $[11\bar{2}0]$ and ZnO $[11\bar{2}0]$‖sapphire [0001], respectively. The epitaxial relationship is shown in Fig. 32. As confirmed by the x-ray pole figure shown in Fig. 33, no rotational domains or twins were present in the films. The use of *a*-plane sapphire substrates showed a significant improvement compared to the *c*-plane sapphire substrates. The residual carrier concentration was decreased to $6\times10^{16}\,cm^{-3}$ with electron mobility over 120 $cm^2\,V^{-1}\,s^{-1}$. AFM revealed a rms roughness of less than 0.4 nm.

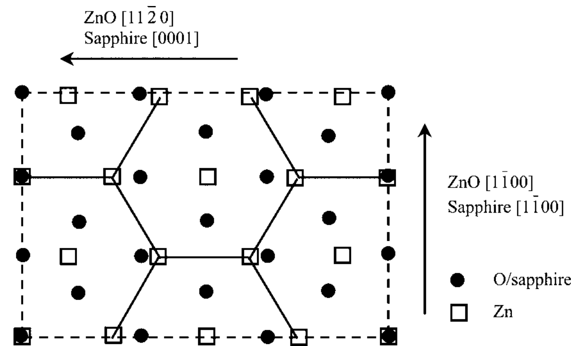

FIG. 32. Schematic diagram of the atom positions for basal ZnO grown on *a*-plane sapphire. The dots mark the O-atom positions and the dashed lines show the sapphire *a*-plane unit cells. The open squares mark the Zn-atom positions and the solid lines show the ZnO basal-plane unit cell.

The effects of substrate offset angle on MBE growth of ZnO on *c*-plane sapphire were investigated by Sakurai *et al.*[217] Twin-crystal RHEED patterns from both $(10\bar{1}0)$ and $(11\bar{2}0)$ planes and surface faceting observed with *c*-plane-oriented substrates were suppressed by enlarging the offset angles from near 0° to 2.87°, tilted from *c*-plane toward the *a*-axis direction. As a result, improvement in crystal structure and surface morphology was observed.

Different surface chemistries of sapphire substrates can lead to different growth modes. The surface chemistry of $(11\bar{2}0)$-oriented sapphire was alternated from O rich to Al rich by changing the pregrowth treatment from oxygen plasma to atomic hydrogen.[218] The two-dimensional growth was more favorable and continued longer on a hydrogen-treated surface, although the initial two-dimensional growth was eventually taken over by a three-dimensional growth for both types of pretreatments. Figure 34 shows different ZnO

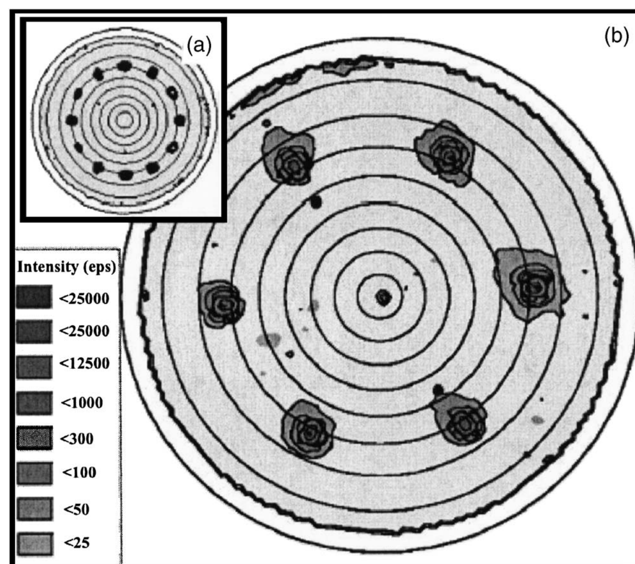

FIG. 33. Stereographic projections of the x-ray pole figure results for the ZnO $(10\bar{1}1)$ reflection for a ZnO film grown on (a) (inset) a *c*-plane sapphire substrate and (b) an *a*-plane sapphire substrate. The in-plane orientation of sapphire is indicated by a sapphire $\langle 11\bar{2}6\rangle$ measurement (filled circles). [Reprinted with permission from P. Fons, K. Iwata, A. Yamada, K. Matsubara, S. Niki, K. Nakahara, T. Tanabe, and H. Takasu, Appl. Phys. Lett. **77**, 1801 (2000). Copyright 2000 American Institute of Physics.]

[This article is copyrighted as indicated in the article. Reuse of AIP content is subject to the terms at: http://scitation.aip.org/termsconditions. Downloaded to] IP: 128.172.48.58 On: Mon, 19 Oct 2015 20:45:44

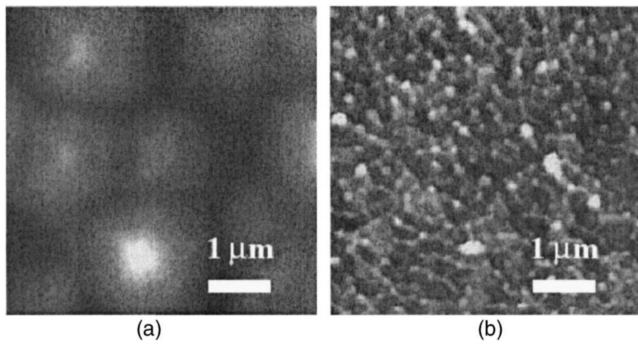

FIG. 34. AFM surface observation with a contact mode. (a) H-pretreated sample (grain size of 2.5 μm) and (b) O-pretreated sample (grain size of 0.2 μm). [Reprinted with permission from M. Sano, K. Miyamoto, H. Kato, and T. Yao, Jpn. J. Appl. Phys., Part 2 **42**, L1050 (2003). Copyright 2003, Institute of Pure and Applied Physics.]

film surface morphologies grown on H- and O-pretreated sapphire substrates. The ZnO epilayers with electron mobility as high as 130 $cm^2 V^{-1} s^{-1}$ and electron concentration of 1.4×10^{17} cm^{-3} were grown with good reproducibility by using the H pretreatment. A Ga preexposure after H and O pretreatments of the sapphire (0001) surface was adopted by Du *et al.* just before the ZnO growth in order to eliminate the rotational domain structures.[219] The ZnO (0002) XRD rocking curve had a FWHM of 67 arc sec, and the electron mobility was 109 $cm^2 V^{-1} s^{-1}$ with an electron concentration of 3.2×10^{17} cm^{-3}. Nitridation of (0001) sapphire substrate was also used to improve the quality of ZnO films grown by plasma-assisted MBE.[220] A very thin nitrogen-polar AlN layer formed by nitridation acted as a template for the following ZnO growth, resulting in the elimination of the rotational domains which were often observed in the films grown without nitridation. For the nitridized substrates, the FWHMs of (002) and (102) ω scans decreased substantially from 912 to 95 arc sec and from 2870 to 445 arc sec, respectively.

The buffer layer is another critical factor affecting the growth of ZnO layers besides substrates. Although Fons *et al.* reported sharp and streaky ZnO $[11\bar{2}0]$ RHEED patterns for both *c*-plane sapphire[157] (Fig. 35) and *a*-plane sapphire[215] without using any buffer layer, ZnO growth on sapphire without a buffer layer usually changed from the 2D growth mode to 3D island growth as confirmed by the appearance of a spotty RHEED pattern (Fig. 36).[158,180,218] LT buffer layers are usually grown at 250–350 °C, and the surface morphology of the buffer layer can be improved by thermal treatment at a temperature higher than 700 °C. This is followed by growth on the main ZnO layers at a temperature in the range of 600–650 °C.[213,221,222] By employing *a*-plane sapphire substrates and LT buffer layers, the electrical properties of undoped ZnO films have been somewhat improved; a carrier concentration of 7.6×10^{16} cm^{-3} and a mobility of 120 $cm^2 V^{-1} s^{-1}$ have been obtained.[213]

Layer-by-layer growth of ZnO epilayers by plasma-assisted MBE on *c*-plane sapphire (0001) substrates has been

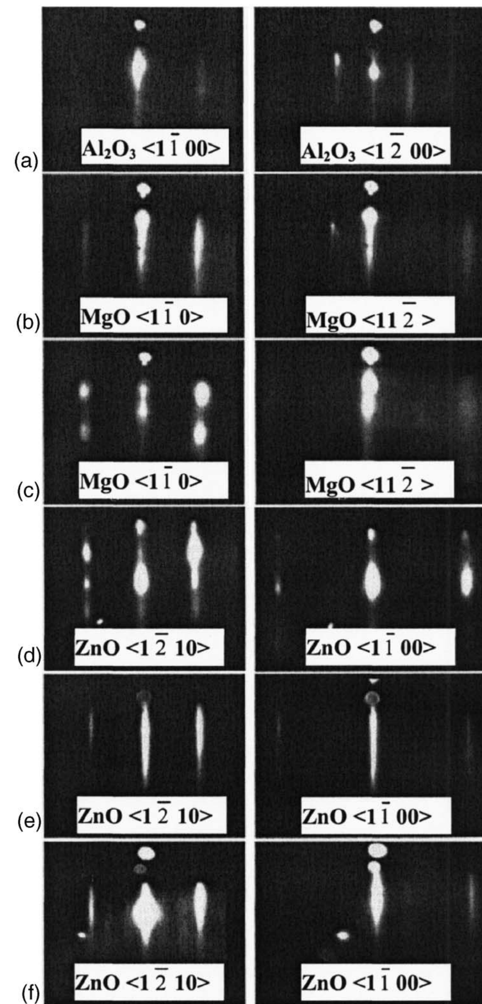

FIG. 36. RHEED patterns show the surface morphology evolution during initial growth stages. (a) The Al_2O_3 (0001) surface after oxygen plasma treatment. The MgO buffer layer (b) before and (c) after 2D-3D transition. The LT-grown ZnO layer on MgO buffer (d) before and (e) after annealing; (f) the ZnO epilayer after a few minutes of growth on the buffer layer. [Reprinted with permission from Y. Chen, H.-J. Koh, S.-K. Hong, and T. Yao, Appl. Phys. Lett. **76**, 559 (2000). Copyright 2000, American Institute of Physics.]

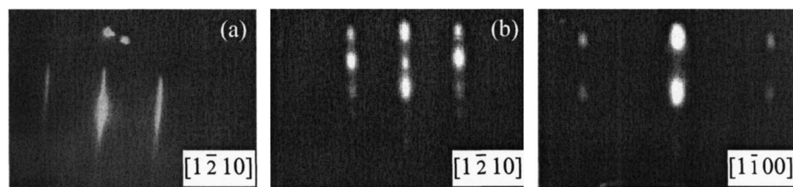

FIG. 35. (a) RHEED pattern taken along the $[1\bar{2}10]$ direction of ZnO after 1 h of growth. [Reprinted from P. Fons, K. Iwata, S. Niki, A. Yamada, and K. Matsubara, J. Cryst. Growth **201–202**, 627 (1999), Copyright 1999, with permission from Elsevier.] (b) RHEED patterns along ZnO $[1\bar{2}10]$ and ZnO $[1\bar{1}10]$ after deposition of about 300 nm. [Reprinted with permission from P. Y. Chen, D. M. Bagnall, H.-J. Koh, K.-T. Park, K. Hiraga, Z.-Q. Zhu, and T. Yao, J. Appl. Phys. **84**, 3912 (1998), Copyright 1998, American Institute of Physics.]

[This article is copyrighted as indicated in the article. Reuse of AIP content is subject to the terms at: http://scitation.aip.org/termsconditions. Downloaded to] IP: 128.172.48.58 On: Mon, 19 Oct 2015 20:45:44

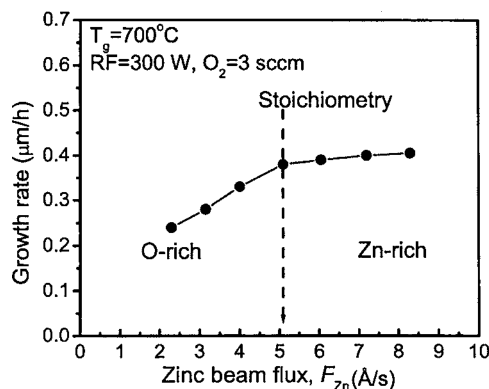

FIG. 37. Growth rate of ZnO layers against Zn beam flux. [Reprinted with permission from H. Kato, M. Sano, K. Miyamoto, and T. Yao, Jpn. J. Appl. Phys., Part 1 **42**, 2241 (2003). Copyright 2003, Institute of Pure and Applied Physics.]

achieved by introducing a thin MgO buffer.[181,223,224] The ionic radius of Mg^{2+} is close to that of Zn^{2+},[225] so the replacement of Zn by Mg is not expected to induce a significant change for the lattice constants of MgZnO alloys. The incorporation of MgO buffer is very effective in improving the surface morphology during the initial stages of growth and leads to an atomically flat surface. The 3×3 surface reconstruction of ZnO was observed from RHEED (see Fig. 36). The twin defects with a 30° in-plane crystal-orientation misalignment were completely eliminated and the total dislocation density was reduced as confirmed by small linewidths of 13 and 84 arc sec observed for (0002) and $(10\bar{1}5)$ ω-rocking curves, respectively.[181] The (111)-oriented rocksalt MgO grows on sapphire (0001) with the following epitaxial relationship: MgO $[1\bar{1}0]\|$sapphire $[2\bar{1}\bar{1}0]$ and MgO $[\bar{1}\bar{1}2]\|$sapphire $[01\bar{1}0]$.

When the effects of the substrate orientation and buffer layers are considered, homoepitaxy of ZnO seems to be the most efficient way to improve the overall properties.[186] ZnO films have been grown on Zn-polar ZnO substrates, and two-dimensional growth with a smooth surface has been obtained under the O-rich flux condition. In addition to the improvement in the structural and optical properties, due to the reduction in density of the edge-type threading dislocation, the residual carrier concentration in the homoepitaxial ZnO films was as low as 2.2×10^{16} cm^{-3}, and the electron mobility of 158 cm^2/V s was achieved.

The II/VI ratio has been studied for its effects on the surface morphology and electrical properties. Figure 37 shows the change of growth rate with Zn/O ratio.[226] ZnO thin films with a MgO buffer layer were grown on c-plane sapphire substrate. ZnO layers grown under stoichiometric and O-rich flux conditions show larger hexagonal islands of 3000-nm diameter, whereas those grown under Zn-rich flux conditions show smaller hexagonal islands of 200-nm diameter. The ZnO film was found to have O polarity. The observed surface morphology can be explained by the fact that for growth conducted on the O-polar surface, the surface diffusion length of Zn adatoms was smaller under the Zn-rich condition than under the stoichiometric or O-rich condition. ZnO layers grown under stoichiometric flux conditions had high crystalline quality, the lowest dislocation density, and the highest electron mobility ($\sim$130 cm^2 V^{-1} s^{-1}) when compared with ZnO films grown under nonstoichiometric flux conditions.

The control of the film polarity is an important issue in epitaxial growth of ZnO. When the film is grown in the [0001] direction, Zn polarity ($+c$) is obtained and the top surface is Zn terminated. Likewise when the growth is in the $[000\bar{1}]$ direction, O polarity ($-c$) is obtained and the top surface is O terminated. Much effort has been expended to determine the effects of polarity and to find a way of controlling the polarity during growth. The ZnO films grown by plasma-assisted MBE on as-polished (0001) sapphire substrates with or without a MgO buffer layer have O polarity[158,227,228] mainly due to the growth conditions. The sapphire surface should be O terminated, since sapphire substrates are treated at elevated temperatures (600–700 °C) by O plasma prior to the growth. MgO buffer under the oxygen ambient most likely has O-stabilized MgO surface. As demonstrated for atomically flat sapphire (0001) substrates, the polarity of ZnO grown by laser MBE is closely correlated with the in-plane orientation of ZnO, i.e., ZnO $[10\bar{1}0]\|Al_2O_3$ $[11\bar{2}0]$ in the case of O polarity and ZnO $[11\bar{2}0]\|Al_2O_3$ $[11\bar{2}0]$ in the case of Zn polarity.[229] ZnO films with Zn polarity are preferentially obtained at low growth temperature and high growth rate. The control over the ZnO surface polarity has also been achieved on GaN substrates by plasma-assisted MBE.[228,230] As confirmed by the coaxial impact collision ion scattering spectroscopy (CAICISS) (see Fig. 38), Zn- and O-polar ZnO films were successfully grown with Zn- and O-plasma preexposures on Ga-polar GaN templates prior to ZnO growth, respectively.

Although ZnO films grown on sapphire have shown promising electrical and optical properties as discussed above, the crystal quality still needs improvement, since high density of defects are present at the interface and throughout the films as a consequence of a large lattice mismatch (18%) between ZnO and sapphire. On the other hand, GaN is a closely lattice-matched material to ZnO with a lattice mismatch of 1.8%. In this vein, Ko *et al.*[231] studied the growth and characteristics of as-grown and annealed ZnO thin films with LT buffer layers on (0001) GaN templates grown by MOCVD on sapphire. The LT ZnO buffer layers were grown at 250–300 °C, and the surface was dramatically improved by a thermal treatment above 600 °C.[232] The growth temperature for the top ZnO layer was in the range from 500 to 700 °C. A 3×3 RHEED pattern was observed during cooling for the flat ZnO surface (see Fig. 39).[232]

Ko *et al.*[231] also studied the possibility of controlling the ZnO/GaN interface by employing different surface-treatment procedures prior to ZnO growth.[233] A treatment of the GaN surface by using Zn- or oxygen-plasma preexposures affects the subsequent ZnO growth in different ways. The Zn pretreatment provides a well-ordered GaN surface without any interface layer, while the oxygen-plasma pretreatment results in the formation of a disordered surface due to the formation of a Ga_2O_3 interface layer. Accordingly, the structural and optical properties of Zn-exposed samples are

[This article is copyrighted as indicated in the article. Reuse of AIP content is subject to the terms at: http://scitation.aip.org/termsconditions. Downloaded to] IP: 128.172.48.58 On: Mon, 19 Oct 2015 20:45:44

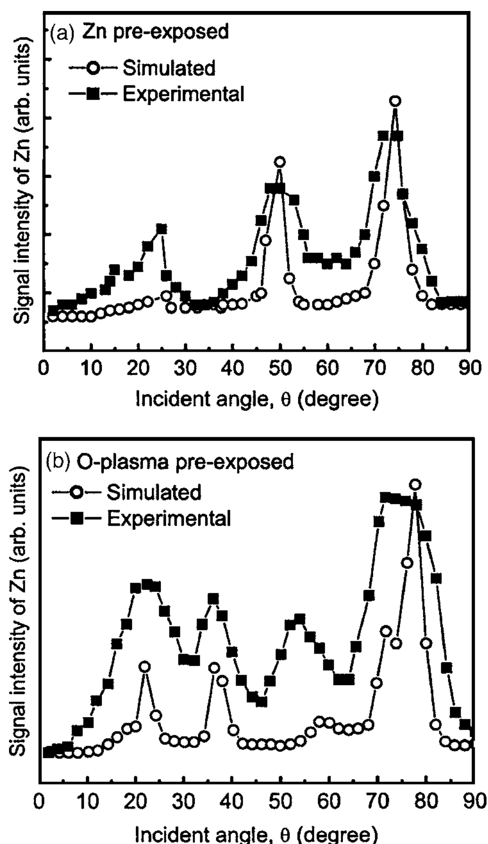

FIG. 38. Polar-angle-dependent CAICISS spectra from ZnO films with (a) Zn preexposure and (b) O-plasma preexposure. The solid squares and open circles indicate the experimental and simulated spectra [Zn polar for (a) and O polar for (b)], respectively. The spectra are plotted as a function of an incident angle, where 90° minus a polar angle is an incident angle. [Reprinted with permission from S. K. Hong, T. Hanada, H. J. Ko, Y. Chen, T. Yao, D. Imai, K. Araki, M. Shinohara, K. Saitoh, and M. Terauchi, Phys. Rev. B **65**, 115331 (2002). Copyright 2002 by the American Physical Society.]

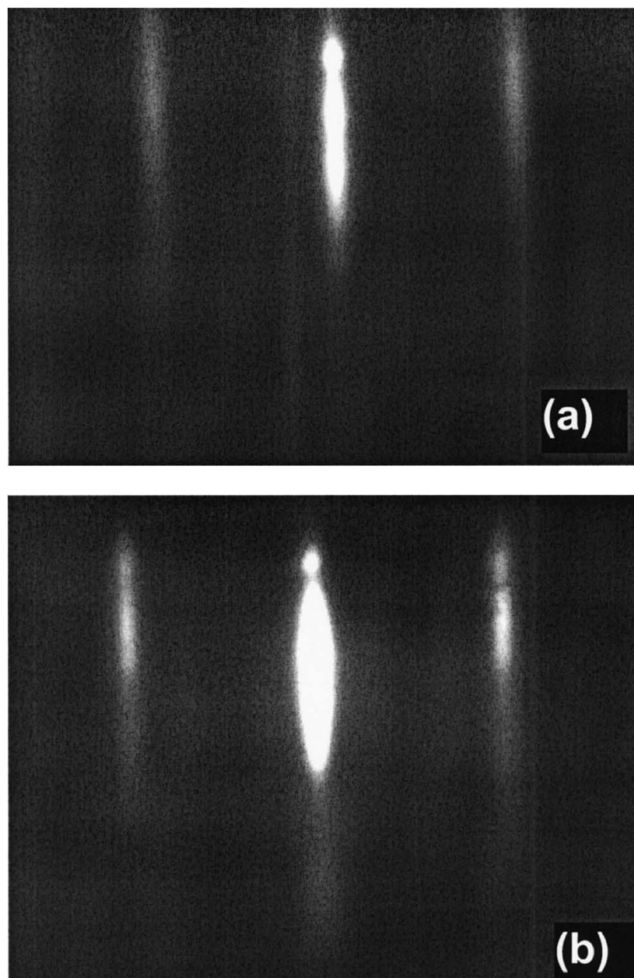

FIG. 39. RHEED pattern of ZnO layer along the $[11\bar{2}0]$ direction (a) at the end of growth and at a substrate temperature of 550 °C and (b) after cooling down to 300 °C.

better than those of the O-exposed samples. TEM and XRD studies of the structural properties of epitaxial ZnO/epi-GaN/Al_2O_3 heterostructures revealed that the majority of the threading dislocations are of screw type, and high density of edge dislocations exists at the interfacial region.[234] As discussed above a Zn- and a O-plasma preexposure of Ga-polar GaN templates prior to ZnO growth produced Zn- and O-polar ZnO films, respectively.[228,230]

The pregrowth treatment and LT buffer layers have also been applied to the growth of ZnO on Si substrates. An initial deposition of a Zn layer followed by its oxidation produces a superior template for the subsequent ZnO growth.[235] The RHEED pattern suggests that the initial Zn layer and ZnO film are rotated by 30° with respect to the orientation of Si (111) substrate. Although the linewidth of the donor-bound-exciton emission was as small as 6 meV at 10 K, the crystal quality of the ZnO films was not as good as those grown on sapphire.[236]

E. Pulsed-laser deposition

In the pulsed-laser deposition (PLD) method, high-power laser pulses are used to evaporate material from a target surface such that the stoichiometry of the material is preserved in the interaction. As a result, a supersonic jet of particles (plume) is directed normal to the target surface. The plume expands away from the target with a strong forward-directed velocity distribution of different particles. The ablated species condense on the substrate placed opposite to the target. A schematic diagram of the typical PLD system is shown in Fig. 40. The main advantages of PLD are its ability to create high-energy source particles, permitting high-quality film growth at low substrate temperatures, typically

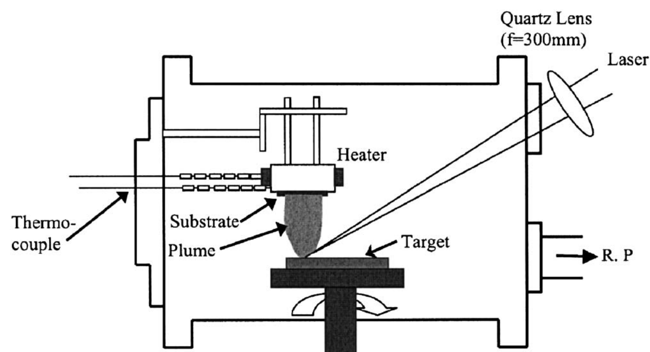

FIG. 40. Schematic diagram of a pulsed-laser-deposition system [after Singh *et al.* (Ref. 244)].

[This article is copyrighted as indicated in the article. Reuse of AIP content is subject to the terms at: http://scitation.aip.org/termsconditions. Downloaded to] IP: 128.172.48.58 On: Mon, 19 Oct 2015 20:45:44

ranging from 200 to 800 °C, its simple experimental setup, and operation in high ambient gas pressures in the $10^{-5}-10^{-1}$-Torr range. For the growth of ZnO by PLD technique, usually UV excimer lasers (KrF: $\lambda=248$ nm and ArF: $\lambda=193$ nm) and Nd: yttrium aluminum garnet (YAG) pulsed lasers ($\lambda=355$ nm) are used for ablation of the ZnO target in an oxygen environment. In some cases, Cu-vapor laser emitting at $\lambda=510-578$ nm (Ref. 237) was also used for the same purpose. Cylindrical ZnO tablets made from pressed ZnO powder are usually used as targets. Single-crystal ZnO has been used to grow high-quality ZnO thin films very recently.[238] A pure Zn metal is used only in rare cases.[239,240] The properties of the grown ZnO films depend mainly on the substrate temperature, ambient oxygen pressure, and laser intensity. Sankur and Cheung[241] and Nakayama[242] have reported on high-quality ZnO growth by PLD. However, the influence of the growth conditions on the ZnO properties was studied much later.[243–246]

Tsukazaki *et al.*[238] reported the high-quality ZnO thin-film deposition on close lattice-mismatched hexagonal $ScAlMgO_4$ substrates by laser MBE at high growth temperatures up to 1000 °C. The growth direction is identified as $[000\bar{1}]$ direction (oxygen face). The FWHM of (0002) XRD rocking curve is less than 18 arc sec for 1-μm-thick ZnO films. By using the high-quality undoped ZnO films, these authors also demonstrated ZnO *p-i-n* homojunctions for light-emitting diode (LED) application. Nitrogen was used as the p-type dopant by applying a "repeated temperature modulation epitaxy" method.

Choopun *et al.*[243] studied the influence of oxygen pressure on surface morphology and optoelectronic properties of ZnO films grown on sapphire (0001) by PLD. The films were grown at an optimized growth temperature of 750 °C. The growth was carried out under various oxygen background pressures ranging from 10^{-5} to 10^{-1} Torr. All the ZnO layers grown were found to be *c*-axis oriented. The films grown under lower oxygen pressure regimes ($10^{-5}-10^{-4}$ Torr) had a *c*-axis lattice parameter 0.25% larger than that of the bulk material. This effect was attributed to both oxygen deficiency and compressive strain induced by the sapphire substrate. However, for the films deposited under higher oxygen pressures ($10^{-2}-10^{-1}$ Torr), the *c* lattice constant was found to approach the bulk value. The FWHM of XRD ω-rocking curve was 0.069° for the film grown at an O_2 pressure of 10^{-4} Torr. The in-plane ordering, as determined from XRD ϕ scans of the ZnO $(10\bar{1}1)$ planes, however, was strongly influenced by the oxygen pressure. The FWHMs of $(10\bar{1}1)$ peaks were 0.43° and 0.78° for the ZnO films grown at 10^{-4} and 10^{-1} Torr, respectively.

Figure 41 shows the surface morphology of the ZnO films grown at various O_2 pressures.[243] The morphology of the films grown at $10^{-5}-10^{-4}$ Torr was dominated by a typical "honeycomblike" structure with 3D growth features as evidenced by the well-faceted hexagons [Fig. 41(a)]. The transition towards the growth of a smooth film was found at an O_2 pressure of 10^{-2} Torr. This change in the growth mode resulted in a substantial reduction of rms roughness to 10–20 Å for a flat surface. A further increase of the O_2 pressure to 10^{-1} Torr showed an adverse effect on the surface morphology [Fig. 41(c)] typically featured by high nucleation densities, irregular grains with different sizes, and the increase in surface roughness to about 400 Å.

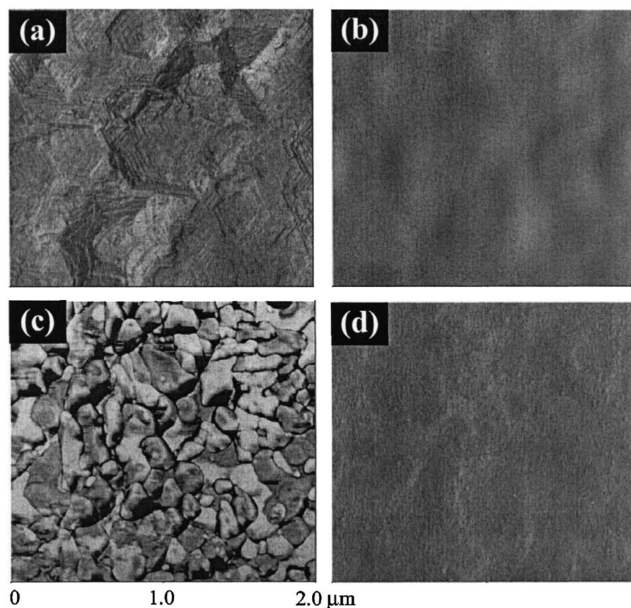

FIG. 41. AFM images of the ZnO films grown at various oxygen pressures: (a) 10^{-4} Torr, (b) 10^{-2} Torr, (c) 10^{-1} Torr, and (d) 10^{-1} Torr, with a nucleation layer of 100 Å grown at 10^{-4} Torr. [Reprinted with permission from S. Choopun, R. D. Vispute, W. Noch, A. Balsamo, R. P. Sharma, T. Venkatesan, A. Iliadis, and D. C. Look, Appl. Phys. lett. **75**, 3947 (1999). Copyright 1999, American Institute of Physics.]

The effect of oxygen pressure on the electrical properties (Hall mobility μ and carrier concentration n) of the ZnO films is shown in Fig. 42.[243] The highest electron mobility ($72\ cm^2/V\ s$) was obtained for the film grown at $10^{-4}-10^{-3}$ Torr, but this film also showed the highest carrier concentration ($7\times10^{17}\ cm^{-3}$). Further increase in O_2 pressure reduced the Hall mobility, possibly as a result of electron scattering by defects/ionized impurities. The optical quality of the ZnO epilayer grown at 10^{-4} Torr was much higher than those grown at 10^{-1} Torr, as evidenced by a much higher excitonic luminescence intensity (by two orders of magnitude). This indicates that a high concentration of defects in ZnO film affects the radiative processes.

As seen from the above results, the PLD growth of high-quality epitaxial ZnO films with smooth surfaces and desirable electrical and optical properties has different optimum oxygen pressure regimes. To overcome this problem, a two-step growth procedure has been developed.[243] In this process, the nucleation layer is grown at low oxygen pressure (10^{-4} Torr), which produces a high-quality template for the subsequent growth of ZnO at a high oxygen pressure (10^{-1} Torr).

The preparation of highly conducting and transparent aluminum-doped zinc oxide films was reported by Singh *et al.*[244] The films were deposited on quartz and Corning 7059 glass by focusing a XeCl ($\lambda=308$ nm and 20-ns pulse width) excimer laser onto a target rotating at 15 rpm. The ZnO target was 2 in. in diameter and doped with 2-wt % Al_2O_3. For all the experiments, a repetition rate of 5 Hz and an energy

[This article is copyrighted as indicated in the article. Reuse of AIP content is subject to the terms at: http://scitation.aip.org/termsconditions. Downloaded to] IP: 128.172.48.58 On: Mon, 19 Oct 2015 20:45:44

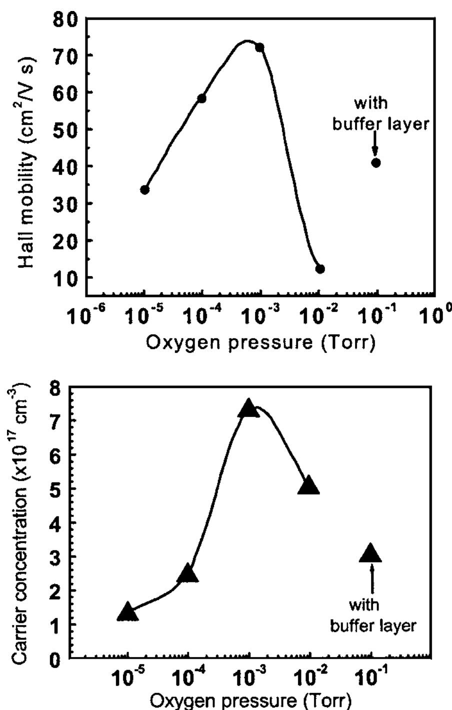

FIG. 42. Hall mobility and carrier concentration vs oxygen pressure for ZnO growth. For comparison, the data for the ZnO film grown at 10^{-1} Torr with the nucleation layer grown at 10^{-4} Torr are also shown. [Reprinted with permission from S. Choopun, R. D. Vispute, W. Noch, A. Balsamo, R. P. Sharma, T. Venkatesan, A. Iliadis, and D. C. Look, Appl. Phys. Lett. **75**, 3947 (1999). Copyright 1999, American Institute of Physics.]

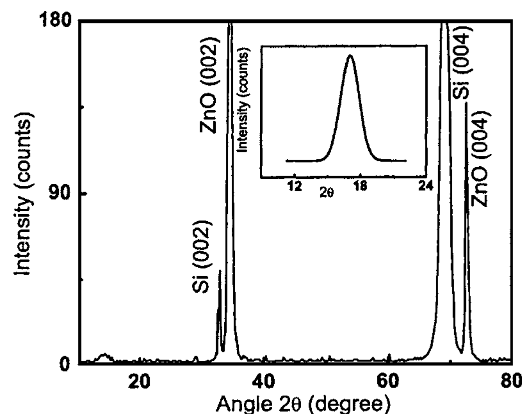

FIG. 43. XRD pattern of a ZnO thin film deposited under optimized conditions. The rocking curve recorded for the (002) line is shown in the inset. [Reprinted with permission from V. Craciun, J. G. E. Gardeniers, and I. W. Boyd, Appl. Phys. Lett. **65**, 2963 (1994). Copyright 1994, American Institute of Physics.]

density of 1.5 J/cm^2 were used. The distance between the target and the substrate was 30 mm, and the deposition time was kept at 30 min. The effects of substrate temperature (from room temperature to 400 °C) and oxygen pressure (from 0.1 to 5 mTorr) were investigated by analyzing the optical and electrical properties of the films. The average transmittance was found to be in the range of 86%–92%, and resistivity varied from 3.56×10^{-3} to 7.0×10^{-3} Ω cm. The lowest resistivity measured was 1.4×10^{-4} Ω cm for the films grown at 300 °C and 1 mTorr oxygen pressure.

Matsubara *et al.*[245] used oxygen radical-assisted PLD to grow highly transparent and low-resistivity Al-doped ZnO films at room temperature. A KrF excimer laser ($\lambda=248$ nm, 30-ns pulse width, and 10-Hz repetition rate) was used for ablation. The oxygen partial pressure during deposition was $(0.7-1.4)\times10^{-5}$ Torr, and the applied rf power was 150 W. The distance between the target and the substrate was approximately 6 cm. The minimum resistivity of the obtained transparent films was 5×10^{-4} Ω cm. The average transmittance in the visible wavelength region was over 86% for ~0.7-μm-thick films. The films grown in a low-pressure molecular-oxygen atmosphere (1.4×10^{-5} Torr) were slightly black and had low transmittance in the visible and near infrared regions of the optical spectrum, and had relatively lower resistivity. The radical source assisted the incorporation of oxygen into the films and made the films transparent.

Craciun *et al.*[246] deposited high-quality ZnO films on glass and silicon substrates by the PLD technique employing a KrF laser ($\lambda=248$ nm), and studied the influence of the deposition parameters, such as substrate temperature, oxygen pressure, and laser fluence, on the properties of the grown films. All the films grown over a rather wide range of deposition conditions were found to be optically transparent, electrically conductive, and *c*-axis oriented, with the FWHM of the (002) XRD line being very often less than 0.25°. Investigations of the effect of different oxygen partial pressures showed that the best-quality films could be obtained in the higher pressure range, i.e., between 1×10^{-3} and 4×10^{-3} Torr. This result is quite different from that obtained previously, and has been accounted for by the differences in the substrate-to-target distances employed. The electrical resistivity of the films was strongly affected by the oxygen pressure, increasing from $(7-9)\times10^{-3}$ Ω cm for the films deposited at 2×10^{-5} Torr to $(5-8)\times10^{-2}$ Ω cm for those deposited at 2×10^{-3} Torr. This behavior can be easily understood by taking into account that the electrical conductivity of ZnO is controlled by Zn interstitials or O vacancies. From these studies it was concluded that the best conditions for PLD of ZnO films center around substrate temperatures between 300 and 350 °C, oxygen partial pressures from 1×10^{-3} to 2×10^{-3} Torr, and a laser fluence of around 2 J/cm^2. Within this range, the FWHM of the (002) XRD line is always below 0.18° and the transparency is above 85% in the visible region of the spectrum. Figure 43 shows the XRD pattern recorded for a ZnO film grown with a fluence of 2.1 J/cm^2, substrate temperature of 350 °C, and oxygen pressure of 2×10^{-3} Torr.[246] Only the (002) and (004) XRD lines are present along with the Si (100) peak of the substrate. The FWHM of the (002) reflection was 0.13°, one of the lowest values yet reported in the literature for PLD-grown ZnO. The small peak at around 10° was attributed to the presence of a very thin amorphous transitional layer between the Si substrate and the grown ZnO film. The rocking curve measured for the (002) diffraction, as shown in the inset of Fig. 43, is at 16.99° with a FWHM of 2.07°.

F. Chemical-vapor deposition

Among other growth methods, chemical-vapor deposition (CVD) technology is particularly interesting not only

[This article is copyrighted as indicated in the article. Reuse of AIP content is subject to the terms at: http://scitation.aip.org/termsconditions. Downloaded to] IP: 128.172.48.58 On: Mon, 19 Oct 2015 20:45:44

because it gives rise to high-quality films but also because it is applicable to large-scale production. This technique is widely used in the fabrication of epitaxial films toward various GaN-based optoelectronic devices, and similar trend might be expected for future applications of ZnO. There are several modifications of this method depending on precursors used. When metal-organic precursors are used, the technique is called MOCVD,[160] metal-organic vapor-phase epitaxy (MOVPE), or organometallic vapor-phase epitaxy (OMVPE). In the case of hydride or halide precursors, the technique is named hydride or halide CVD or VPE.[161,162]

In the CVD method, ZnO deposition occurs as a result of chemical reactions of vapor-phase precursors on the substrate, which are delivered into the growth zone by the carrier gas. The reactions take place in a reactor where a necessary temperature profile is created in the gas flow direction.

For hydride VPE growth of ZnO, hydrogen (H_2) was employed as a carrier gas.[247–249] In these particular cases, the typical pressure was ≤133 Pa and the flow rate was about 40 ml/min. Targets made from ZnO powder were placed in the evaporation zone in which the temperature was around 770 °C. The following chemical reaction between the ZnO target and H_2 carrier gas takes place in the evaporation zone:

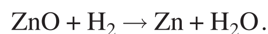

$$ZnO + H_2 \rightarrow Zn + H_2O.$$

On the substrate (the deposition zone), where the temperature was kept in the range of 590–610 °C, the reverse reaction occurs:

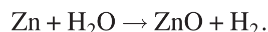

$$Zn + H_2O \rightarrow ZnO + H_2.$$

The ZnO films grown by this method show quite high crystal, electrical, and luminescence properties.[250,251]

ZnO films were also grown by halide VPE employing oxygen gas and Zn chloride ($ZnCl_2$) (Ref. 162) or Zn iodide (ZnI_2) (Ref. 252) as sources of Zn and O, respectively. It was demonstrated that the iodide system allows growing ZnO layers of higher optical and structural properties. The main advantage of this technique is its very high growth rate. The preparation of 100-μm ZnO films showing room-temperature ultraviolet emission with a PL FWHM as narrow as 10 meV was reported by Takashi *et al.*[253]

For ZnO growth, MOCVD/MOVPE technique typically involves the use of metal alkyls, usually dimethyl zinc [$(CH_3)_2Zn$] (DMZn) or diethyl zinc [$(C_2H_5)_2Zn$] (DEZn) in combination with a separate source of oxygen and argon or nitrogen as a carrier gas. In earlier investigations, O_2 or H_2O were used as oxygen precursors.[37,254,255] However, DEZn and DMZn are highly reactive with oxygen and water vapor so that severe premature reaction in the gas phase occurs in the cold zone of the reactor, resulting in the formation of white powder, that degrades the film quality. Nevertheless, great progress has been made in ZnO growth by MOCVD recently. The improvement of the material quality is related to improved reactor design[256] and/or the use of less-reactive precursors, allowing one to minimize parasitic prereactions in the gas phase. Stable metal-organic source of zinc acetylacetonate in combination with oxygen was successfully used for the growth of high-quality ZnO films on *r*-plane[257] as well as on *c*- and *a*-plane[258] sapphire substrates by atmospheric pressure MOCVD. For the group-VI precursor, a variety of oxygen compounds were employed: isopropanol (*i*-PrOH),[259–262] tertiary-butanol (*t*-BuOH),[263–266] acetone,[37] N_2O,[37,267–270] and NO_2.[258]

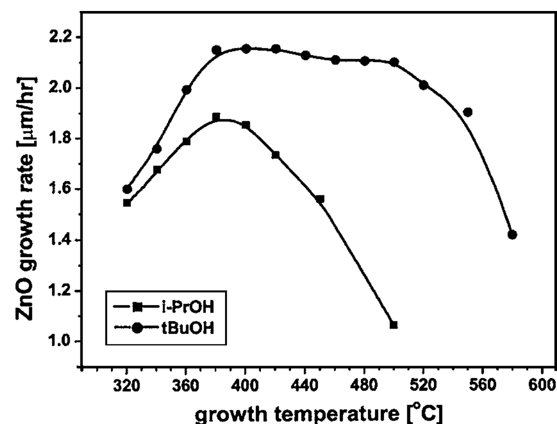

FIG. 44. Temperature dependence of the ZnO growth rate using isopropanol (black rectangles) or tertiary butanol (black circles) as the oxygen precursor. The DEZn flow rate is 100 μmol/min. The reactor pressure for both sets of samples is 400 mbars. [Reprinted from C. Kirchner, T. Gruber, F. Reuss, K. Thonke, A. Waag, C. Giessen, and M. Heuken, J. Cryst. Growth **248**, 20 (2003), Copyright 2003, with permission from Elsevier.]

High-quality ZnO layers have been prepared on GaN/sapphire[259,261] and *c*-plane sapphire[252,260] substrates by using DEZn and *i*-PrOH. FWHMs of the ω-2θ scans were 100 and 270 arc sec depending on the substrate, and the 5-K PL spectra showed strong near-band-edge emission with line widths of 5–12 meV with phonon replicas.[251,259] For the films grown on *c*-plane sapphire under optimized conditions, PL was dominated by strong near-band-edge lines with FWHM below 4 meV, and the excitonic signals were clearly visible in reflectivity measurements.[260] Hall-effect measurements indicated an *n*-type background doping in the 10^{17}-cm^{-3} range with carrier mobilities of more than 100 cm^2/V s.

Kirchner *et al.*[266] have reported direct comparison of MOVPE growth of ZnO layers on *c*-plane sapphire using *i*-PrOH and *t*-BuOH as oxygen precursors and DEZn as a zinc source. It has been demonstrated that the two oxygen precursors show similar pressure dependence of the ZnO growth rate but large differences in temperature-dependent growth rate (see Fig. 44). The growth rate was found to be almost constant over a wide temperature range from 380 to 510 °C in the case of *t*-BuOH, whereas for *i*-PrOH the maximum growth rate was achieved at 380 °C. The optical quality of the ZnO layers grown with *t*-BuOH were superior to those grown with *i*-PrOH. For ZnO grown under optimized conditions using *t*-BuOH, strong near-band-edge emission lines with half-widths of 1.1 meV dominated the PL spectra.

Great potential of nitrous oxide for MOVPE of ZnO was demonstrated by Ogata *et al.*[267] Low reactivity allows one to grow ZnO films at a high substrate temperature that results in high crystal perfection and good optical quality of the material. Oleynik *et al.*[262] reported superior characteristics of ZnO layers grown on GaN/Si substrates with the use of N_2O compared to those prepared with *i*-PrOH and acetone. The

[This article is copyrighted as indicated in the article. Reuse of AIP content is subject to the terms at: http://scitation.aip.org/termsconditions. Downloaded to] IP: 128.172.48.58 On: Mon, 19 Oct 2015 20:45:44

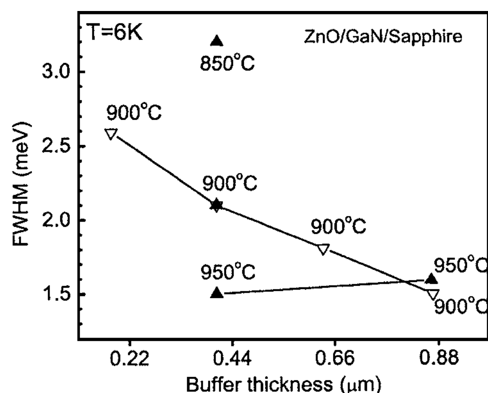

FIG. 45. CL linewidth of the ZnO near band-edge emission as a function of LT buffer layer thickness and growth temperature. The linewidth decreases with increasing growth temperature and with increasing layer thickness of the LT ZnO buffer. [Reprinted from A. Dadgar, N. Oleynik, D. Forster, S. Deiter, H. Witek, J. Blasing, F. Bertramm, A. Krtschil, A. Diez, J. Christen, and A. Frost, J. Cryst. Growth **267**, 140 (2004), Copyright 2004, with permission from Elsevier.]

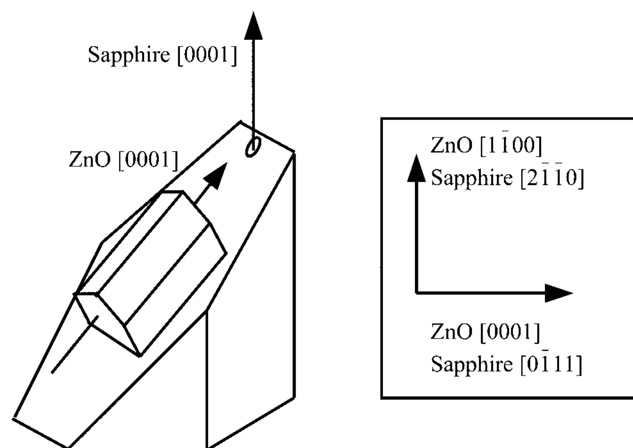

FIG. 46. Epitaxial relationships of a-plane ZnO grown on R-plane Al_2O_3.

growth of a LT- (500 °C) buffer layer of ZnO was demonstrated to be essential to enhance the initial nucleation process and to achieve high-quality ZnO overgrown layers at higher growth temperatures (600–700 °C).[267] Dadgar *et al.*[270] used *t*-BuOH and DEZn as precursors for the growth of LT (450 °C) ZnO buffers on GaN/sapphire substrates. At the second stage, ZnO layers were grown at a high temperature (900–950 °C) using N_2O. The layers showed smooth surface morphology and high crystalline quality as demonstrated by XRD [FWHM of (0002) ω scans for a 2.28-μm-thick layer was 160 arc sec]. The bright luminescence was dominated by narrow excitonic (FWHM <1.3 meV) emission lines. The effects of LT-buffer thickness as well as substrate temperature on the optical quality of ZnO layers were studied systematically (see Fig. 45).

High-quality homoepitaxial ZnO layers were grown on bulk ZnO substrates by using N_2O and DEZn.[271] Two conditions, proper thermal treatment of substrate prior to the growth to obtain a flat surface and high flow-rate ratios of source materials, were found to be important to obtain high-quality layers. Surface roughness below 1 nm as well as strong free-exciton emission at 15 K was reported for the films grown under optimal conditions.

The improvement of MOCVD technology also gave rise to great progress in the quality of ZnO layers grown with the use of DEZn and O_2. The pressure used for the growth was in the range of 5–250 Torr.[272,273] Lower-pressure effect was investigated and the results showed that the crystal quality was better for films grown at 6 Torr than those grown at 0.05 Torr.[274] *R*-plane sapphire substrate has been used in MOCVD growth of ZnO.[272] The epitaxial relationship between ZnO and *R*-plane sapphire was found to be $(11\bar{2}0)\text{ZnO}\parallel(01\bar{1}2)$ sapphire and $[0001]\text{ZnO}\parallel[0\bar{1}11]$ sapphire. Figure 46 shows the epitaxial relationship. High-crystallinity ZnO epilayers were grown on sapphire (0001) substrates with LT ZnO buffer layer.[273] The XRD rocking curve data of as-grown films exhibited FWHM values in the range of 0.04°–0.05°.

The in-plane orientation of ZnO epitaxial films grown on as-polished (0001) sapphire substrates by MOCVD has been reported to depend on the initial conditions when starting the flow of DEZn over the substrate.[275] The epitaxial orientation can easily be controlled to be either ZnO $[11\bar{2}0]\parallel$sapphire$[11\bar{2}0]$ (no in-plane rotation) or ZnO $[10\bar{1}0]\parallel$sapphire$[11\bar{2}0]$ (30° in-plane rotation), but all the films had Zn polarity regardless of the in-plane orientation, in contrast to the result obtained by MBE.[229]

The effect of oxygen partial pressure on the structural perfection as well as optical and electrical properties of ZnO films grown at 600 °C on Al_2O_3 (0001) was studied by Ma *et al.*[276] It was found that the conduction type in undoped ZnO layers could be controlled by adjusting the oxygen partial pressure during growth. The films grown under an oxygen partial pressure lower than 45 Pa showed *n*-type conductivity. With increasing oxygen pressure, the crystallinity of the ZnO layers degraded to polycrystalline with additional $(10\bar{1}2)$ orientation, and intrinsic *p*-type ZnO (which should be treated with some caution) was produced as the oxygen partial pressure became higher than 55 Pa. The hole concentration and mobility reached $1.59\times10^{16}\ \text{cm}^{-3}$ and $9.23\ \text{cm}^2/\text{V s}$, and the resistivity was 42.7 Ω cm. The near-band-edge and deep-level emissions in RT PL spectra were influenced strongly by the oxygen partial pressure. Temperature-dependent PL spectra in *n*-type ZnO films showed a dominant neutral-donor-bound-exciton emission, while the *p*-ZnO was dominated by the neutral-acceptor-bound-exciton line. With decreasing temperature, both peaks increased in intensity and blueshifted. The band that originated from zinc vacancies emerged for temperatures below 155 K only in the *p*-type films. The origin of intrinsic *p*-type conductivity in ZnO thin films was attributed to zinc vacancies, the premise of which should be treated with a great deal of caution.

Evolution and growth of ZnO films grown on GaN/AlN/SiC (0001) (Refs. 277 and 278) and ZnO (Ref. 279) from DEZn and O_2 have been reported by Smith *et al.* From a microscopic study of initial growth stages it was concluded that ZnO on GaN templates nucleated and grew via the Stranski-Krastanov mode.[277] At 500 °C, dense ZnO

[This article is copyrighted as indicated in the article. Reuse of AIP content is subject to the terms at: http://scitation.aip.org/termsconditions. Downloaded to] IP: 128.172.48.58 On: Mon, 19 Oct 2015 20:45:44

(0001) films formed via coalescence of islands either on GaN/AlN/SiC (0001) substrates or on initial, coherent ZnO layers.[278] To check the possible effect of interface oxide layer on the growth mode and film morphology, the GaN surface was preexposed to the reagents in different ways at the initiation of growth. Interfaces between ZnO and GaN exposed either simultaneously to diethylzinc and oxygen or only to diethylzinc were sharp and epitaxial. Interfaces formed after the exposure of the GaN to O_2 were less coherent, though an interfacial oxide was not observed by cross-sectional TEM.[278] A strong effect of the surface polarity was revealed for homoepitaxial growth of ZnO films on O- and Zn-terminated ZnO (0001) substrates.[279] The films, grown on O-terminated ZnO surfaces were initially dense. However, they changed to a textured polycrystalline microstructure after approximately 100 nm and exhibited a surface roughness of 7.3 nm. By contrast, the films grown on the Zn-terminated surface under the same conditions were fully dense, without texture, and appeared to be monocrystalline with a significantly improved surface roughness of 3.4 nm.

An important advantage of the MOCVD/MOVPE technique is the feasibility of catalyst-free growth of ZnO nanowires (nanorods). For DEZn and N_2O source materials, Ogata *et al.*[280] demonstrated a possibility to control the growth mode by tuning the growth parameters. At lower temperatures and/or lower VI/II ratio, the growth tended to be three-dimensional and nanorod structure could be grown on sapphire substrates. At higher temperatures two-dimensional growth was performed, and the flat and uniform epilayers could be formed both on sapphire and bulk ZnO substrates. The homoepitaxial ZnO layers exhibited a rms value of 3 nm and a FWHM of 0.5 meV in low-temperature (9 K) PL emission. With the use of different precursor systems, the MOCVD/MOVPE method was successfully applied to the catalyst-free growth of ZnO nanowires on various substrates, such as Si,[281,282] GaN/sapphire,[281] *c*-plane sapphire,[281,283,284] and GaAs (001).[285] In the case of GaAs substrate it was reported that, postgrowth heat treatment resulted in *p*-type doping of nanowires owing to As diffusion from GaAs substrate.[285] Yang and Zhang [286] used MOCVD to grow ZnO single-crystal whiskers on glass substrates. In order to investigate the possibility of a combination of bandgap engineering and nanopillar growth, Kling *et al.*[287] grew ZnMgO nanorods. The Mg incorporation was confirmed by PL measurements and a blueshift of the band gap of up to 170 meV could be achieved for the nanopillars with the highest Mg concentration. Park *et al.*[288] also demonstrated the growth of $ZnO/Zn_{0.8}Mg_{0.2}O$ nanorod single-quantum-well structures. Moreover, a fabrication of high-mobility field-effect transistors (FETs) using ZnO nanorods grown by MOVPE has been reported very recently.[289] A high transconductance of 1.9 μS and high electron mobility above 1000 cm^2/V s were achieved.

IV. OPTICAL PROPERTIES OF ZnO

A. Prelude

The optical properties of a semiconductor are connected with both intrinsic and extrinsic effects. Intrinsic optical transitions take place between the electrons in the conduction band and holes in the valence band, including excitonic effects due to the Coulomb interaction. Excitons are classified into free and bound excitons. In high-quality samples with low impurity concentrations, the free exciton can also exhibit excited states, in addition to their ground-state transitions. Extrinsic properties are related to dopants or defects, which usually create discrete electronic states in the band gap, and therefore influence both optical-absorption and emission processes. The electronic states of the bound excitons (BEs) depend strongly on the semiconductor material, in particular, the band structure. In theory, excitons could be bound to neutral or charged donors and acceptors. A basic assumption in the description of the principal bound-exciton states for neutral donors and acceptors is a dominant coupling of the like particles in the BE states. For a shallow neutral-donor-bound exciton (DBE), for example, the two electrons in the BE state are assumed to pair off into a two-electron state with zero spin. The additional hole is then weakly bound in the net hole-attractive Coulomb potential set up by this bound two-electron aggregate. Similarly, shallow-neutral acceptor-bound excitons (ABEs) are expected to have a two-hole state derived from the topmost valence band and one electron interaction. These two classes of bound excitons are by far the most important cases. Other defect-related transitions could be seen in optical spectra such as free to bound (electron-acceptor), bound to bound (donor-acceptor), and the so-called yellow/green luminescence.

B. Optical transitions in ZnO

Optical transitions in ZnO have been studied by a variety of experimental techniques such as optical absorption, transmission, reflection, photoreflection, spectroscopic ellipsometry, photoluminescence, cathodoluminescence, calorimetric spectroscopy, etc. In this section, a review on the intrinsic excitonic properties is given first. The donor- and acceptor-bound excitons are discussed next. This is followed by a discussion of two-electron satellites related to the donor-bound excitons. Finally, LO-phonon replicas of the main excitonic emissions and the donor-acceptor-pair (DAP) transition are reviewed. The temperature dependence of the full PL spectrum is also explored and necessary arguments are made to support the assignments for specific transitions. The defect-related transitions are discussed in detail in Sec. V.

1. Free excitons and polaritons

The wurtzite ZnO conduction band is mainly constructed from the *s*-like state having Γ_7^c symmetry, whereas the valence band is a *p*-like state, which is split into three bands due to the influence of crystal-field and spin-orbit interactions.[290] The near-band-gap intrinsic absorption and emission spectrum is therefore dominated by transition from these three valence bands. The related free-exciton transitions from the conduction band to these three valence bands or vice versa are usually denoted by *A* (also referred to as the heavy hole), *B* (also referred to as the light hole), and *C* (also referred to as crystal-field split band). However, the ordering of the crystal-field and spin-orbit coupling split states of the

[This article is copyrighted as indicated in the article. Reuse of AIP content is subject to the terms at: http://scitation.aip.org/termsconditions. Downloaded to] IP: 128.172.48.58 On: Mon, 19 Oct 2015 20:45:44

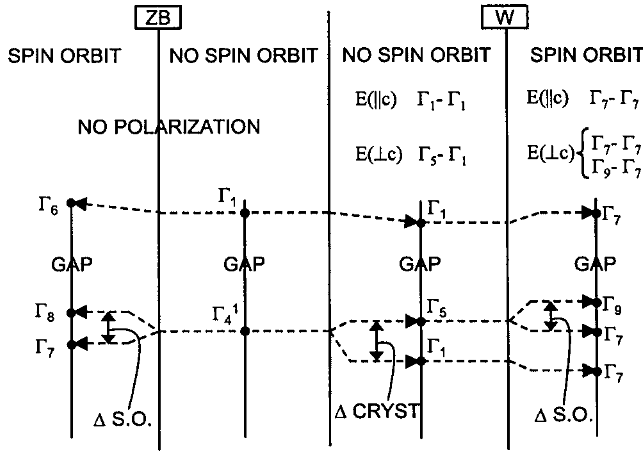

FIG. 47. Band structure and selection rules for the ZB and W structures. The crystal field and spin-orbit splittings are indicated schematically. The transitions which are allowed for various polarizations of photon electric-field vector with respect to the c axis are indicated [after Birman (Ref. 296)].

valence-band maximum in wurtzite ZnO has been a subject of controversy.[11,12,290–292] The essential difference has its genesis in the interpretation of the spectral line, which was initially assigned to the intrinsic ground-state A-exciton transition by Thomas,[11] and in contrast to extrinsic, ionized donor-bound-exciton complex transition, by Park *et al.*[12] Recent availability of high-quality ZnO single crystals has paved the way to observe intrinsic exciton transitions in low-temperature photoluminescence, magnetoluminescence, and reflectance measurements.[291,293,294] Reynolds *et al.*[291] addressed this issue using second-order photoluminescence spectra, which helped resolve the additional fine structure of the excitons. They concluded that the valence-band symmetry ordering (A-Γ_9, B-Γ_7, and C-Γ_7) in ZnO is not reversed but the same as that observed in most other wurtzitic II-VI structures and GaN. However, Lambrecht *et al.*[295] argued that the analysis of Reynolds *et al.* was incorrect due to their assumptions about the sign of the Lande g factor for holes and that the valence-band ordering is in fact A-Γ_7, B-Γ_9, and C-Γ_7. Figure 47 shows the band diagram for the zinc-blende and the wurtzite ZnO structures. (After Birman[296] for valence-band ordering A-Γ_9, B-Γ_7, and C-Γ_7.)

Group-theory arguments and the direct product of the group representations of the band symmetries (Γ_7 for the conduction band, Γ_9 for the A valence band, upper Γ_7 for B valence band, and lower Γ_7 for C valence band) will result in the following intrinsic exciton ground-state symmetries:

$$\Gamma_7 \times \Gamma_9 \rightarrow \Gamma_5 + \Gamma_6,$$

$$\Gamma_7 \times \Gamma_7 \rightarrow \Gamma_5 + \Gamma_1 + \Gamma_2.$$

The Γ_5 and Γ_6 exciton ground states are both doubly degenerate, whereas Γ_1 and Γ_2 are both singly degenerate. In ideal, i.e., strain-free, wurtzite crystals free excitons should obey the selection rules in optical one-photon processes; Γ_5 and Γ_1 are allowed transitions with $E \perp c$ and $E \| c$ polarizations, respectively, but the Γ_6 and Γ_2 are not allowed. Therefore, all three excitons are allowed in the σ polarization ($E \perp c$ and $k \perp c$), but the C exciton is quite weak. The C exciton is strongly allowed in the π polarization ($E \| c$ and $k \perp c$). However, the A exciton is forbidden and the B exciton is only weakly observable in this geometry. In the α polarization ($E \perp c$ and $k \| c$) all three transitions are clearly observable. Each of these fundamental excitonic states are expected to have a fine structure due both to exciton-polariton longitudinal-transverse splitting and the splitting caused by electron-hole exchange interaction, which are on the order of a few meV.[22,297]

The transition energies of the intrinsic excitons were measured by employing the low-temperature absorption,[18,298] reflection,[12,291,299] photoreflectance (PR),[300,301] and PL (Refs. 299, 291, 293, and 294) spectroscopy techniques. These measurements pave the way for the determination of exciton binding energies, exciton Bohr radii, the dielectric constant, and with the aid of the quasicubic model, spin-orbit and crystal-field parameters. In this section, these optical properties of the ZnO excitonic transitions will be discussed in detail.

In 1960, Thomas[11] studied the fundamental absorption edge and the exciton structure of ZnO. He measured the low-temperature absorption and reflectance spectra of polished and etched thin crystals grown from the vapor phase. Thomas analyzed the reflectance data by means of the Kramers-Kronig relation and three peaks arising from $n=1$ exciton transitions involving holes from each one of the *three* valence bands. At 4.2 K the $n=2$ exciton states were apparent in reflection, allowing estimates to be made of the exciton binding energy and reduced mass. An example of a reflectance spectra obtained in the σ and π polarizations are given in Fig. 48 for a single-crystal ZnO sample.

Park *et al.*[12] reported the fundamental spectra of ZnO and successfully explained the exciton spectrum on the basis of Birman's model[296] of the wurtzite structure analyzing the energy and polarization of the fine structure around the fundamental absorption region. Stimulated by these results, Hopfield and Thomas[22] studied the polariton absorption lines in ZnO using a magnetic field in appropriate geometry to

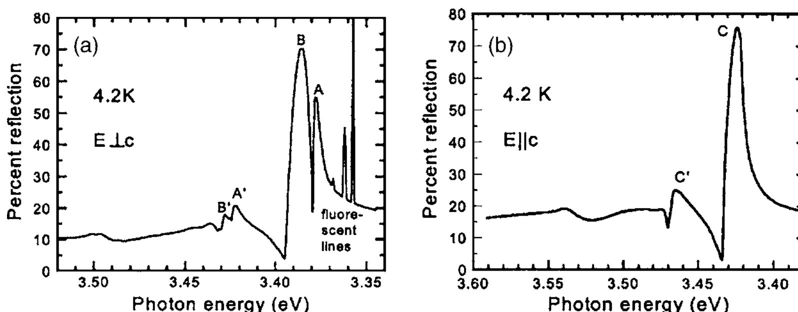

FIG. 48. Reflection from ZnO at 4.2 K for (a) $E \perp c$ and (b) $E \| c$. Notice the PL lines for the $E \perp c$ data. [Reprinted from D. G. Thomas, J. Phys. Chem. Solids]**15**, 86 (1960), Copyright 1960, with permission from Elsevier.]

[This article is copyrighted as indicated in the article. Reuse of AIP content is subject to the terms at: http://scitation.aip.org/termsconditions. Downloaded to] IP: 128.172.48.58 On: Mon, 19 Oct 2015 20:45:44

allow couplings at polariton crossings. A satisfactory agreement was attained when the crossing frequencies of the polariton dispersion and light with $E \parallel c$ and $E \perp c$ polarizations were compared with the measured absorption line energies. Depending on their results Hopfield and Thomas also argued that the B exciton in fact belongs to the Γ_9 symmetry group.

Among these publications, there exists a discrepancy in the quoted values for the spin-orbit interaction energy and the exciton binding energies, which most likely may have its genesis in the difficulty of interpreting the complex spectra near the band edge. The features associated with A-, B-, and C-exciton transitions, their excited states, and exciton-polariton and exciton-LO-phonon complexes are sometimes misinterpreted, resulting in reports of different energy values. To shed additional light, Liang and Yoffe[18] performed polarization-dependent transmission measurements on single-crystal ZnO thin platelets grown by the vapor transport method. In addition to the transitions associated with the ground, the first, and the second excited states of intrinsic excitons, the exciton-phonon complexes were also observed in the transmission spectrum. In the same vein but later on, Reynolds *et al.*[302] reported the shift in intrinsic exciton transitions analyzing the reflection data from strained ZnO single crystals grown by the vapor transport method. During growth, defect complexes (probably pairs) are preferentially incorporated in certain crystallographic orientations, producing compressive strain in the vicinity of the defect pairs with the strain being oriented in the direction of the pair. By observing the changes in emission from the defect pairs as the annealing temperature is increased, Reynolds *et al.*[302] investigated the relaxation of strain following an increase in the number of nearer pairs. Intrinsic energy bands were observed to adjust to these changes by moving to lower energies. For an annealing temperature of 800 °C, shifts as much as 0.4 meV for the A-exciton transition and 3 meV for the B-exciton transition were quoted for σ polarization at 2 K.

Chichibu *et al.*[301] studied the photoreflectance spectra of high-quality ZnO epitaxial layers grown on $ScAlMgO_4$ substrates by laser MBE and observed clear excitonic resonances due to the three excitons. A larger broadening was observed for the B and C excitons compared to the A exciton, which was interpreted to be due to a contribution by the exciton polaritons in terms of large longitudinal-transverse splitting of the respective excitons. Chichibu *et al.*[300] also used polarized photoreflectance spectroscopy to study excitonic polaritons in a ZnO single crystal. Following their observations of longitudinal-transverse splitting of ground-state exciton polaritons and resonances due to the first excited states of the respective excitons, they confirmed the valence-band ordering to be A-$\Gamma_{9\nu}$, B-$\Gamma_{7\nu}^{u}$, and C-$\Gamma_{7\nu}^{l}$. The observed longitudinal-transverse splitting energies (1.5, 11.1, and 13.9 meV for the A, B, and C excitons, respectively) were in good agreement with earlier results by Hümmer and Gebhardt[303] (2, 11, and 16 meV for A, B, and C excitons, respectively).

By transmission measurements Muth *et al.*[304] determined the absorption coefficient, band gap, and exciton binding energies in epitaxial zinc oxide thin films grown by pulsed-laser deposition on c-plane sapphire substrates. It was found that the excitonic absorption features were sharper in films annealed in oxygen. The absorption coefficient was consistent with the earlier report on thin ZnO platelets by Liang and Yoffe.[18] However, assignments by Muth *et al.* shown in Fig. 49 for the B- and C-exciton energies are very different from that in other reports most probably due to misinterpretation of the C exciton as the B exciton and the exciton-LO-phonon complex transitions[18,305] as the C exciton.

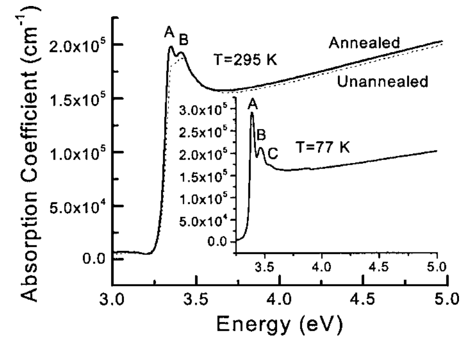

FIG. 49. Absorption coefficient and excitonic structure for an annealed (solid lines) and an unannealed (dotted line) sample at room temperature. The inset shows the absorption coefficient for the annealed samples at 77 K. [Reprinted with permission from J. F. Muth, R. M. Kolbas, A. K. Sharma, S. Oktyabrsky, and J. Narayan, J. Appl. Phys. **85**, 7884 (1999). Copyright 1999, American Institute of Physics.] The C exciton is misinterpreted as the B exciton and the exciton-LO-phonon complex transitions as the C exciton.

Another very powerful technique for studying exciton structure is photoluminescence (PL). The low-temperature PL spectrum of ZnO single crystal has been investigated in many aspects by many researchers.[291,293,294,299,302,306–310] Figure 50 shows the typical PL spectrum in the range of the fundamental excitonic region taken at 10 K by Teke *et al.*[299] in the $E \perp c$ polarization geometry for a high-quality ZnO crystal annealed under forming gas (5% H_2 and 95% N_2). The A free excitons and their first excited-state transitions are observed at $FX_A^{n=1}=3.3771$ eV and $FX_A^{n=2}=3.4220$ eV, respectively, for Γ_5- (3.3757 and 3.4202 eV for Γ_6) band symmetry. Although, at $k=0$, Γ_6 exciton is forbidden in the measurement mode of polarization, it is still observed, evidently

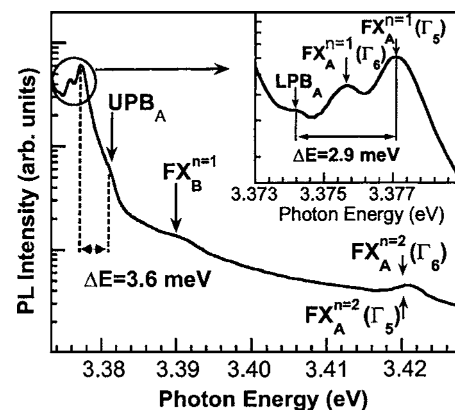

FIG. 50. Free-excitonic fine-structure region of the 10-K PL spectrum for a forming-gas-annealed ZnO substrate. [Reprinted with permission from A. Teke, Ü. Özgür, S. Doğan, X. Gu, H. Morkoç, B. Nemeth, J. Nause, and H. O. Everitt, Phys. Rev. B **70**, 195207 (2004). Copyright 2004 by the American Physical Society.]

[This article is copyrighted as indicated in the article. Reuse of AIP content is subject to the terms at: http://scitation.aip.org/termsconditions. Downloaded to] IP: 128.172.48.58 On: Mon, 19 Oct 2015 20:45:44

due to the fact that the photon has finite momentum. Geometrical effects such as not having the sample orientation exactly perpendicular to electric field can also be considered as a reason for the observed Γ_6 transition. Using the energy separations of ground-state and excited-state peak positions, and assuming that exciton has a hydrogenlike set of energy levels, the exciton binding energy and band-gap energy can be predicted. The energy differences of about 45 meV gives an *A*-free-exciton binding energy of 60 meV and a corresponding band-gap energy of 3.4371 eV at 10 K. Based on the reported energy separation of the *A* and *B* free excitons (in the range of $\Delta_{AB}=9-15$ meV),[11,291,294] the weak emission centered at 3.3898 eV, which is about 12.7 meV apart from the *A* exciton, is assigned to the *B*-exciton transition.

In strongly polar materials such as ZnO, transverse Γ_5 excitons couple with photons to form polaritons. In principle, although the polaritons can be formed anywhere along the dispersion curves, polariton lifetimes, which are higher at certain points, determine the observed peak positions. Therefore, as indicated in Fig. 50 the $FX_A^{n=1}(\Gamma_5)$ exciton line has two components. The higher energy component at 3.3810 eV, which is 3.6 meV apart from the *A* exciton, is assigned to the so-called longitudinal exciton (upper polariton branch, UPB_A). The lower energy component at 3.3742 eV, which is about 2.9 meV apart from the *A* exciton, corresponds to the recombination from the "bottleneck" region, in which the photon and free-exciton dispersion curves cross (lower polariton branch, LPB_A). These assignments are also consistent with the theory used to calculate the energy separation between the main exciton and polariton branches. The longitudinal-transverse splitting is given by $\Delta E = E(\Gamma_5)4\pi\alpha/2\varepsilon$, where $E(\Gamma_5)$ is the energy of the Γ_5 exciton, $4\pi\alpha$ is the polarizability, and ε is the optical dielectric constant. By using the reported values of 7.7×10^{-3} for polarizability[311] and 4.0–5.0 for optical dielectric constant[312,313] the calculated value will be in the range of 2.6–3.3 meV for $E(\Gamma_5)=3.3771$ eV. The measured energy splitting (2.9 meV for LPB_A and 3.6 meV for UPB_A) is comparable to the predicted values and also to the experimental values of Chichibu *et al.*[300] (1.5 meV) and Hümmer and Gebhardt[303] (2 meV), supporting the assignment of these two peaks. Since the Γ_6 excitons do not have transverse character, they do not interact with light to form polaritons, and thus have only normal free-exciton dispersion curves as seen in the PL spectra.

Low-temperature reflectivity measurements were also performed by Teke *et al.*[299] in order to validate the free-excitonic features and corresponding peak assignments depending on PL measurements. Figure 51 shows reflectivity measurements performed at 10 K for unpolarized and π-polarized light. The 10-K PL spectrum is also superimposed on the same graph to show the agreement in the peak positions. For unpolarized light, ground and first excited states of *A* and *B* excitons along with a weak *C*-exciton feature are observed. The reflection minima at $FX_A^{n=1} = 3.3772$ eV and $FX_{AB}^{n=1}=3.3901$ eV are in excellent agreement within the experimental resolution with the emission peaks for *A* and *B* free excitons in PL spectra. The position of the first excited state ($FX_A^{n=2}=3.421$ eV) and thereby binding energy of the *A* free exciton (~60 meV) were also confirmed by reflectivity measurements. Additionally, the reflection minima at 3.427 and 3.433 eV were assumed to be related to the second and first excited states of the *A* and *B* free excitons, respectively. As will be discussed later, the temperature evolutions of the *A*- and *B*-exciton PL peaks also reveal characteristic features related to these exciton transitions, supporting this premise.

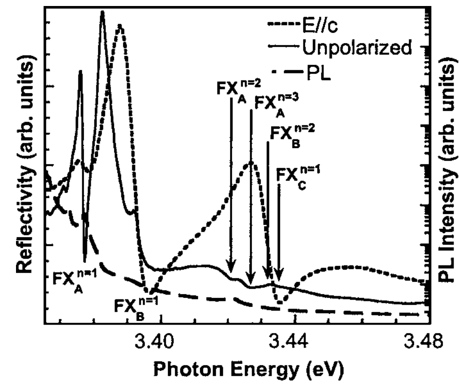

FIG. 51. Reflection spectra of a forming-gas-annealed ZnO substrate measured at 10 K with unpolarized light and with $E\parallel c$. The PL spectrum is also superimposed for comparison. [Reprinted with permission from A. Teke, Ü. Özgür, S. Doğan, X. Gu, H. Morkoç, B. Nemeth, J. Nause, and H. O. Everitt, Phys. Rev. B **70**, 195207 (2004). Copyright 2004 by the American Physical Society.]

Table X tabulates the observed excitonic peak energies reported by Teke *et al.*[299] along with some of the other reported results for high-quality ZnO single crystals from reflectance, photoreflectance, absorption, and PL measurements. The peak position of the *A* and *B* free excitons, and the first excited states of the *A* exciton are in very good agreement, within the experimental accuracy, with the results reported by Reynolds *et al.*[291] The observed polariton positions are also in reasonable agreement with the reported energies for bulk ZnO grown by Eagle-Picher using vapor-phase transport. It should be noted that experimental resolution and the wavelength calibration of the particular setup used must be considered carefully to identify the exact peak positions of the very narrow excitonic lines.

2. Bound excitons

Bound excitons are extrinsic transitions and are related to dopants or defects, which usually create discrete electronic states in the band gap, and therefore influence both optical-absorption and emission processes. The electronic states of the bound excitons depend strongly on the semiconductor material, in particular, the band structure. In theory, excitons could be bound to neutral or charged donors and acceptors. A basic assumption in the description of the bound exciton states for neutral donors and acceptors is a dominant coupling of the like particles in the bound-exciton states. These two classes of bound excitons are by far the most important cases for direct band-gap materials. In high-quality bulk ZnO substrates, the neutral shallow DBE often dominates because of the presence of donors due to unintentional (or doped) impurities and/or shallow donorlike defects. In samples containing acceptors, the ABE is observed. The recombination

[This article is copyrighted as indicated in the article. Reuse of AIP content is subject to the terms at: http://scitation.aip.org/termsconditions. Downloaded to] IP: 128.172.48.58 On: Mon, 19 Oct 2015 20:45:44

TABLE X. Excitonic peak energies (eV) in ZnO single crystals.

	$FX_A^{n=1}(\Gamma_5)$	$FX_A^{n=1}(\Gamma_6)$	$FX_A^{n=2}(\Gamma_5)$	$FX_A^{n=2}(\Gamma_6)$	LPB_A	UPB_A	$FX_B^{n=1}$	$FX_B^{n=2}$	$FX_C^{n=1}$	$FX_C^{n=2}$
Teke *et al.* (Ref. 299)	3.3771	3.3757	3.4220	3.4206	3.3740	3.3810	3.3898			
Reynolds *et al.* (Ref. 291)	3.3773	3.3756	3.4221	3.4209			3.3895			
Reynolds *et al.* (Ref. 297)	3.3793	3.3775			3.3743	3.3829				
Hamby *et al.* (Ref. 308)	3.378				3.374		3.385			
Muth *et al.* (Ref. 304)	3.40 (295 K) 3.455 (77 K)						3.45 (295 K) 3.516 (77 K)		3.55 (295 K) 3.60 (77 K)	
Chichibu *et al.* (Ref. 300)			3.4231		3.3768	3.3783		3.4290		3.4679
Park *et al.* (Ref. 12)	3.3931		3.4243				3.4331		3.4696	
Thomas (Ref. 11)	3.3768						3.3828		3.4208	
Liang andYoffe (Ref. 18)	3.3781		3.4282				3.3856	3.4324	3.4264	3.4722

of bound excitons typically gives rise to sharp lines with a photon energy characteristic to each defect. Many sharp donor- and acceptor-bound-exciton lines were reported in a narrow energy range from 3.348 to 3.374 eV in ZnO (see, for example, Ref. 314 and references therein). However, the chemical origin and binding energy of the most underlying donor and acceptor atoms remain unclear.

The low-temperature PL spectra are dominated by several bound excitons in the range from 3.348 to 3.374 eV, as seen in Fig. 52, for the bulk sample characterized by Teke *et al.*[299] The prominent lines are the A excitons bound to neutral donors that are positioned at $3.3598(D_1^0X_A)$, $3.3605(D_2^0X_A)$, $3.3618(D_3^0X_A)$, $3.3650(D_4^0X_A)$, and $3.3664(D_5^0X_A)$ eV. The most intense one at 3.3605 eV has a full width at half maximum of about 0.7 meV, indicating a good quality of the sample. Several small peaks and shoulders can also be seen between these prominent lines. Based on the energy separation between the $FX_A^{n=1}(\Gamma_5)$ and DBE peaks, it is concluded that the binding energies of the DBEs related to the different donors range from 10 to 20 meV.

On the high-energy side of the neutral DBE, transitions between 3.3664 and 3.3724 eV have been attributed to the

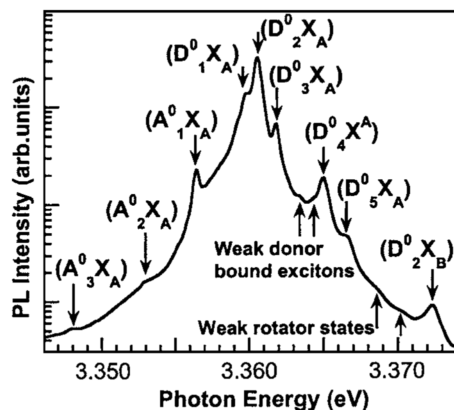

FIG. 52. Bound-excitonic region of the 10-K PL spectrum for a forming-gas-annealed ZnO substrate. [Reprinted with permission from A. Teke, Ü. Özgür, S. Doğan, X. Gu, H. Morkoç, B. Nemeth, J. Nause, and H. O. Everitt, Phys. Rev. B **70**, 195207 (2004). Copyright 2004 by the American Physical Society.]

excited states or excited rotator states of the ground-state neutral-donor-bound excitons. These excited states are analogous to the rotational states of the H_2 molecule. Several models have been proposed to explain the rotator states for different material systems. To identify these rotator states in bulk ZnO, Reynolds *et al.*[306] adopted the model which is originally proposed by Rorison *et al.*[315] to explain their high-magnetic-field results in InP. In this model, DBEs are considered to be free excitons rotating around neutral donors, where one electron of the DBE state is strongly correlated with the hole and the other with the donor. In Ref. 306, the transitions observed at 3.3662 (Γ_6) and 3.3670 (Γ_5) eV were attributed to the rotator states associated with the ground-state neutral-bound-exciton line at 3.3564 eV. The peaks at 3.702 (Γ_6) and 3.3714 (Γ_5) eV are assigned to the rotator state of the neutral-bound exciton at 3.3594 eV. In measurements by Teke *et al.*,[299] very weak emissions at 3.3686 (Γ_6) and 3.3702 (Γ_5) eV with an energy separation of about 1.6 meV has been attributed to the rotator states associated with the main neutral-bound-exciton emission at 3.3605 eV ($D_2^0X_A$). The splitting of these two peaks is consistent with the energy separation of the Γ_6- and Γ_5-band symmetries. Another relatively strong emission line at 3.3724 eV ($D_2^0X_B$) that is attributed to the transition due to the B free exciton bound to the same main neutral donor was also observed. The energy separation between this peak and the main peak at 3.3605 eV ($D_2^0X_A$) is about 12 meV, which is consistent with the energy splitting of the A- and B-free-exciton lines. Analysis of the temperature dependence of the PL spectrum also supports this assignment.

In the lower-energy part of the PL spectrum, ABEs at 3.3564 ($A_1^0X_A$), 3.3530 ($A_2^0X_A$), and 3.3481 ($A_3^0X_A$) eV are also observed. Some of the recently reported values for bound-exciton peak energies observed in low-temperature PL are given in Table XI for comparison. Reynolds *et al.*[306] have investigated the bound-exciton region in detail by using low-temperature PL measurements performed for different polarizations and applied magnetic fields. They resolved seven bound-exciton lines using the second-order grating configuration in the bound-exciton spectral region. However, in this particular paper there is almost a 2-meV shift between

[This article is copyrighted as indicated in the article. Reuse of AIP content is subject to the terms at: http://scitation.aip.org/termsconditions. Downloaded to] IP: 128.172.48.58 On: Mon, 19 Oct 2015 20:45:44

TABLE XI. Bound exciton peak energies (eV) in ZnO single crystals.

	Neutral-acceptor-bound excitons			*A* excitons bound to neutral or ionized donors						Rotator states		*B* excitons bound to neutral donor
Teke *et al.* (Ref. 299)	3.3481	3.3530	3.3564	3.3598	3.3605	3.3618	3.3634 3.3643	3.3650	3.3664	3.3686	3.302	3.3724
Reynolds *et al.* (Ref. 306)			3.3562	3.3594	3.3602	3.3610	3.3624 3.3634	3.3652		3.3670 3.3664	3.3702 3.3714	
Alves *et al.* (Ref. 309)			3.358		3.361	3.362		3.364				
Thonke *et al.* (Ref. 293)			3.3566	3.3597	3.3606	3.3620	3.3628	3.364				
Boemare *et al.* (Ref. 294)				3.3592			3.3622 3.3632	3.3653	3.3693	3.3693 3.3707	3.3741 3.3754	3.3707 3.3741 3.3754 3.3772

the first- and the second-order PL spectra that might be due to the experimental issues associated with the setup used. Nevertheless, the peak energies of the neutral-donor-bound excitons reported by Teke *et al.*[299] are almost at the same positions, within the experimental resolution, as those reported by Reynolds *et al.*[306] Relative peak intensities of the particular donor-related-exciton lines show some differences from sample to sample. For example, the most intense line was observed at 3.3628 eV by Thonke *et al.*,[293] at 3.3624 eV by Reynolds *et al.*,[306] at 3.3653 eV by Boemare *et al.*,[294] and at 3.364 eV by Alves *et al.*[309] and Hamby *et al.*,[308] whereas Teke *et al.*[299] observed the most intense neutral-donor-bound-exciton line at 3.3605 eV. This is because the concentration of the particular donor as well as its capture cross section could vary from sample to sample.

In the ABE region, the main peak at 3.3564 eV is commonly observed by all and is probably related to the Na or Li acceptors.[316] Two other weak emissions at 3.3481 and 3.3530 eV are also visible in Fig. 52, which indicate the presence of the deeper acceptor states. However, their chemical origin has not yet been identified.

3. Two-electron satellites in PL

Another characteristic of the neutral-donor-bound-exciton transition is the two-electron satellite (TES) transition in the spectral region of 3.32–3.34 eV. These transitions involve radiative recombination of an exciton bound to a neutral donor, leaving the donor in the excited state, thereby leading to a transition energy which is less than the DBE energy by an amount equal to the energy difference between the first excited and ground states of the donor. In the effective-mass approximation, the energy difference between the ground-state neutral-donor-bound excitons and their excited states (TES) can be used to determine the donor binding energies[293,309] (the donor excitation energy from the ground state to the first excited state is equal to 3/4 of the donor binding energy E_D) and catalog the different species present in the material. The spectral region for the expected two-electron satellite transitions is shown in Fig. 53 for a forming-gas-annealed ZnO sample. The main peak at 3.3224 eV $(D_2^0X_A)_{2e}$ is the excited state associated with the most intense neutral-donor-bound exciton at 3.3605 eV $(D_2^0X_A)$. The shoulder seen at about 3.3268 eV $(D_3^0X_A)_{2e}$ on the high-energy side of the main TES peak is related to the excited state of the donor whose ground-state emission is at 3.3618 eV $(D_3^0X_A)$. A weak emission at 3.3364 eV $(D_4^0X_A)_{2e}$ is also attributed to the TES transition of the neutral donor whose ground state is at 3.3650 eV $(D_4^0X_A)$. From the separation of the ground state and the corresponding excited states, the donor binding energies are calculated as 51 meV for the donor at 3.3606 eV, 47 meV for the donor at 3.3618 eV, and 38 meV for the donor at 3.3650 eV.

From the separation between the *A* free exciton and the ground-state neutral DBEs, Teke *et al.*[299] determined the binding energies of these excitons as 16.5 meV (for 3.3605 eV), 15.3 meV (for 3.3618 eV), and 12.1 meV (for 3.3560 eV). According to the empirical Haynes rule,[317] the binding or localization energy of the DBEs is proportional to the binding energy of the corresponding donor. Indeed, this relation is clearly seen in the inset of Fig. 53. The proportionality constant (α) is found to be 0.34, which is close to the 0.3 reported by Alves *et al.*,[309] who calculated the binding energies of the donors as 43, 52, and 55 meV for the

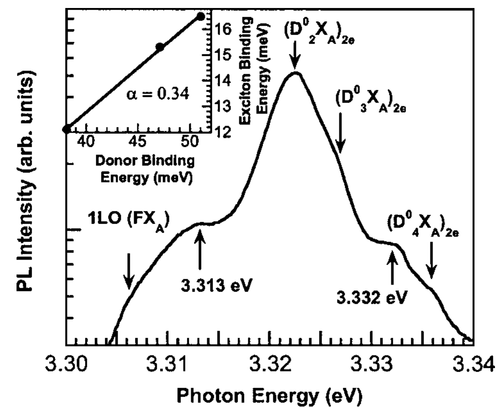

FIG. 53. 10-K PL spectrum for a forming-gas-annealed ZnO substrate in the TES region of the main bound-exciton lines. The inset shows the exciton binding energy vs donor binding energy. [Reprinted with permission from A. Teke, Ü. Özgür, S. Doğan, X. Gu, H. Morkoç, B. Nemeth, J. Nause, and H. O. Everitt, Phys. Rev. B **70**, 195207 (2004). Copyright 2004 by the American Physical Society.]

[This article is copyrighted as indicated in the article. Reuse of AIP content is subject to the terms at: http://scitation.aip.org/termsconditions. Downloaded to] IP: 128.172.48.58 On: Mon, 19 Oct 2015 20:45:44

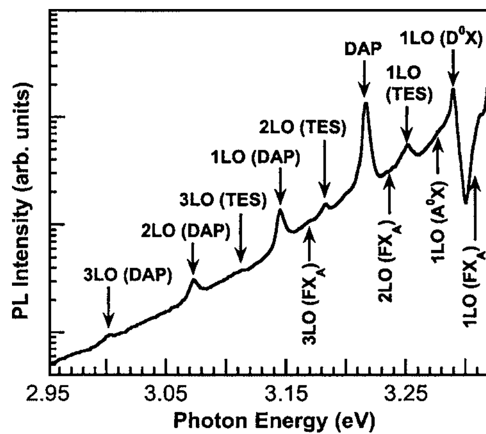

FIG. 54. 10-K PL spectrum for a forming-gas-annealed ZnO substrate in the region where the donor-acceptor-pair transition and LO-phonon replicas are expected to appear. [Reprinted with permission from A. Teke, Ü. Özgür, S. Doğan, X. Gu, H. Morkoç, B. Nemeth, J. Nause, and H. O. Everitt, Phys. Rev. B **70**, 195207 (2004). Copyright 2004 by the American Physical Society.]

donors whose ground-state bound-exciton lines were at 3.364, 3.362, and 3.361 eV, respectively. Thonke *et al.*[293] also studied the TES transitions and found the binding energies of two shallow donors to be 39.9 and 55.5 meV. Reynolds *et al.*[306] reported binding energies of 55.5 and 56.7 meV for two donors at 3.3636 and 3.3614 eV, respectively. The Haynes proportionality constant obtained from these binding energies is about 2, much higher than the values given above. There are two additional peaks at 3.332 and 3.312 eV on both sides of the main TES lines, which could not be identified at this point but they may be related to the excitons bound to structural defects.

4. DAP and LO-phonon replicas in PL

The spectral region containing the DAP transition and LO-phonon replicas of the main transitions has not been studied widely for single-crystal ZnO. Figure 54 shows the corresponding spectrum taken by Teke *et al.*[299] at 10 K for a forming-gas-treated sample. It should be noted that LO-phonon replicas occur with a separation of 71–73 meV, the LO-phonon energy in ZnO.[318] Since some of the peaks are either very weak or mixed with other closely spaced peaks, temperature evolution of these peaks should be tracked carefully in order to make sure that the corresponding assignments are correct. As indicated in Fig. 54, the bump at the higher-energy side of the spectrum labeled as 1LO (FX_A) has a peak around 3.306 eV, which is at the expected position for the 1LO-phonon replica of the free-exciton peak (about 71 meV apart from the $FX_A^{n=1}$ free-exciton peak). Although they are weak, second- and third-order LO-phonon replicas [labeled as 2LO (FX_A) and 3LO (FX_A)] are also observed in the PL spectrum.

The first-order LO-phonon replicas of the main neutral-bound excitons should fall between 3.290 and 3.295 eV. However, due to the line broadening, the peaks corresponding to each individual bound exciton could not be resolved very well. Indeed, the peak labeled as 1LO (D^0X) has a linewidth of about 6 meV, which prevents a definitive resolution. The LO-phonon replicas of the peak at 3.3650 eV can be separated from the two other closely spaced peaks at 3.3618 and 3.3605 eV. The peak at 3.2898 eV is the first LO-phonon replica of both the 3.3618- and 3.3605-eV lines, whereas the first LO-phonon replica of the 3.3650-eV line is seen as a shoulder on the high-energy side of this intense peak. Resolving the second- and higher-order LO replicas is even harder because the energy position (3.218–3.223 eV) falls in the spectral region where the DAP transition and its LO-phonon replicas are expected to appear in the PL spectra. In fact, Teke *et al.*[299] observed a radiative recombination peak at 3.217 eV that is attributed to the donor-acceptor-pair (labeled as DAP in Fig. 54) transition, along with its first, second, and third LO-phonon replicas at 3.145, 3.073, and 3.001 eV, respectively. Regarding the origin of the emission line at 3.2898 eV, Reynolds *et al.*[302] suggested that this line is associated with an acceptor-related transition based on their internal strain study by changing the postannealing temperatures, which disagrees with the interpretation by Teke *et al.*[299] Although the latter investigation differs somewhat, it reports at least two closely spaced peaks at 3.2898 and 3.2920 eV, which are about 72 meV apart from the main neutral-DBE lines at 3.3605 and 3.3650 eV. The temperature-dependent measurements also show that relative intensities of these LO-phonon replicas follow those of the main bound excitons. Additionally, LO-phonons replicas are expected to be roughly two orders of magnitude less intense than the neutral-donor-bound-exciton lines.[293] This is also similar to the case of GaN and other II-VI semiconductors, where donor-related bound-exciton lines couple only weakly with the optical phonons.

The relatively broad peak around 3.280 eV in Fig. 54 is the first LO-phonon replica associated with the most intense acceptor-bound-exciton line (3.3564 eV). This is indicated as 1LO (A^0X) in the spectrum. Finally, the first-, second-, and third-order LO-phonon replicas of the TES lines are also clearly observed in the PL spectra. These peaks are labeled as 1LO, 2LO, and 3LO (TES) and they are positioned at 3.252, 3.182, and 3.112 eV, respectively.

5. Temperature-dependent PL measurements

In order to provide additional support for some of the peak assignments in the low-temperature PL spectrum of the high-quality ZnO substrate investigated, Teke *et al.*[299] studied the temperature evolution of these peaks. The temperature-dependent measurements were performed between 10 and 300 K. Figure 55 shows only the PL spectra for temperatures up to 160 K because most of the important changes occur in this range. The spectrum for each temperature is displaced vertically for clarification.

The variation of both *A*- and *B*-exciton peak positions with temperature is shown in the inset of Fig. 55. The *A*- and *B*-exciton peaks can be tracked up to ~160 K, above which line broadening prevents a satisfactory distinction between the two. This is clearly seen for the room-temperature PL spectrum, where the peak position is at ~3.28 eV instead of the expected position of 3.31 eV [if the mostly accepted band gap of 3.37 eV (Ref. 158) and the measured binding energy of 60 meV were used]. As the temperature is in-

[This article is copyrighted as indicated in the article. Reuse of AIP content is subject to the terms at: http://scitation.aip.org/termsconditions. Downloaded to] IP: 128.172.48.58 On: Mon, 19 Oct 2015 20:45:44

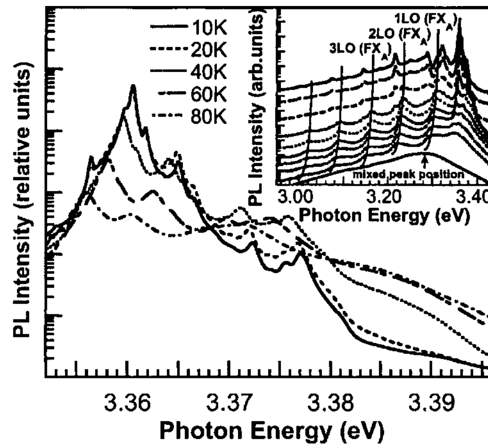

FIG. 55. Temperature-dependent PL spectrum for a forming-gas-annealed ZnO substrate. The inset shows the PL in the DAP and LO-phonon replica regions up to 160 K. The spectrum for each temperature is displaced vertically for clarity. The room-temperature PL data are also included at the bottom. The lines drawn on some peaks are for guidance. [Reprinted with permission from A. Teke, Ü. Özgür, S. Doğan, X. Gu, H. Morkoç, B. Nemeth, J. Nause, and H. O. Everitt, Phys. Rev. B **70**, 195207 (2004). Copyright 2004 by the American Physical Society.]

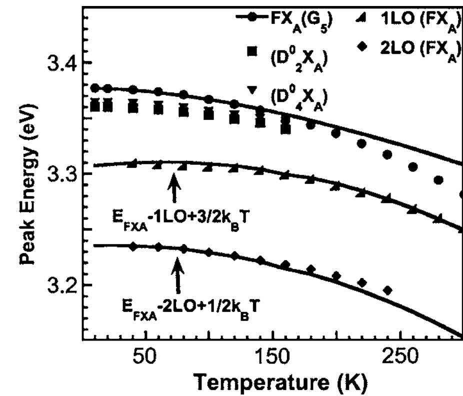

FIG. 56. Temperature-dependent peak positions of the A-free exciton, $FX_A^{n=1}(\Gamma_5)$ and its 1LO- and 2LO-phonon replicas. Also shown are the temperature evolutions of the peak positions of the two major neutral-donor bound exciton transitions at 3.3606 and 3.3650 eV. The $FX_A^{n=1}(\Gamma_5)$ data were fitted using the Varshni equation and the LO-phonon replicas were fitted with the equation shown on the figure. [Reprinted with permission from A. Teke, Ü. Özgür, S. Doğan, X. Gu, H. Morkoç, B. Nemeth, J. Nause, and H. O. Everitt, Phys. Rev. B **70**, 195207 (2004). Copyright 2004 by the American Physical Society.]

creased, the convergence of the A and B excitons, and the coupling of the 1LO-phonon replica with the line broadening of each of these peaks hamper an accurate determination of the peak positions above 160 K. Therefore, the room-temperature peak should be considered a combination of these multiple peaks.

The intensity of A and B free excitons increases with temperature up to 40 and 80 K, respectively, and then decreases as the temperature is increased further. From this observation, Teke *et al.*[299] attribute the 3.3771- and 3.3898-eV emission lines at 10 K to the free excitons corresponding to the A and B bands, respectively. The most intense acceptor-bound-exciton peak at 3.3564 eV $(A_1^0X_A)$, as well as the other two weak acceptor-related peaks labeled as $(A_2^0X_A)$ and $(A_3^0X_A)$, quenches gradually with increasing temperature and disappears above 40 K. The temperature evolution of the main neutral-donor-bound excitons was also traced within the temperature range of 10–160 K (see also the Fig. 55 inset). With increasing temperature, the main peaks related to $(D_2^0X_A)$ at 3.3605 eV and its TES along with their LO-phonon replicas quench. On the other hand, relative intensities of the bound-exciton emissions lying between this main DBE peak and the A-free-exciton peak increase initially, where the strength depends on the particular bound exciton, and then decrease at higher temperatures. The intensity of the bound-exciton peak at 3.3724 eV, which was attributed to the B exciton bound to the main donor rather than to a rotator state, follows the temperature behavior of the B exciton up to 40 K, supporting the assignment of Teke *et al.*[299] Although the B-free-exciton emission continues to increase up to 80 K, further increase of the donor-bound B-exciton intensity is prevented due to its partial dissociation above 40 K. The observed temperature characteristics of the free exciton and dominant bound exciton, where the relative intensity I_{FX}/I_{BX} is seen to increase with increasing temperature, can be interpreted using the approach of Viswanath *et al.*[319] for the study of GaN. Those authors also observed an increase consistent with the aforementioned ratio and inferred that with increasing temperature the dominant donor-bound exciton dissociates into a free exciton and a neutral donor. Based on this argument and the works of Reynolds *et al.*[306] and Hamby *et al.*,[308] Teke *et al.*[299] concluded that thermal dissociation of the 3.3605-eV bound exciton results in increase of the free excitons and the other shallower donor-bound excitons.

There is some controversy in the assignment of the 3.223-eV peak, which is close to the main DAP transition at low temperatures. Analyzing its temperature dependence, Thonke *et al.*[293] attributed this peak to the free-electron-acceptor (e,A^0) transition due to thermal ionization of the donor with increasing temperature. With the help of Hall measurements, they determined the acceptor ionization energy to be ~195 meV for the unintentional acceptor present in ZnO, the chemical origin of which was assumed to be the substitutional nitrogen on O sites. On the other hand, Hamby *et al.*[308] attributed this peak to the second LO-phonon replica of the A free exciton. Hamby *et al.* observed a very good agreement in terms of the temperature-dependent energy positions of this peak with that of the predicted values by taking into account the temperature broadening effect. Teke *et al.*[299] also assigned this peak to the 2LO-phonon replica of the A free exciton depending on its temperature evolution. As seen in Fig. 55, the main DAP line and its LO-phonon replicas quench with increasing temperature, while the adjacent line at 3.223 eV on the high-energy side increases and becomes more apparent at higher temperatures. The temperature dependence of this peak is similar to the A free exciton; it increases with increasing temperature up to 60 K and then decreases at higher temperatures. Also, by following the approach of Hamby *et al.*,[308] the variation of A free exciton and its 1LO and 2LO peak energies with temperature are plotted in Fig. 56. As seen in this figure, the expected and measured energy peak positions of the 1LO and 2LO replicas of the A free exciton agree well, supporting the assignments on these

[This article is copyrighted as indicated in the article. Reuse of AIP content is subject to the terms at: http://scitation.aip.org/termsconditions. Downloaded to] IP: 128.172.48.58 On: Mon, 19 Oct 2015 20:45:44

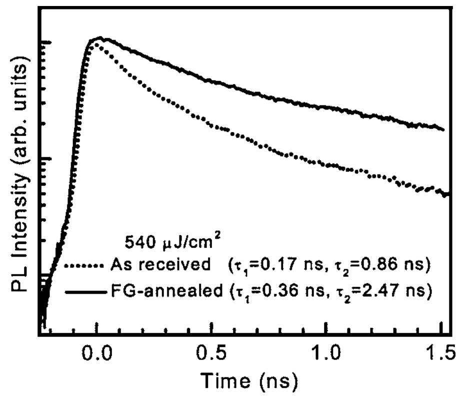

FIG. 57. Room-temperature time-resolved PL data for the as-received and the forming-gas-treated samples. [Reprinted with permission from A. Teke, Ü. Özgür, S. Doğan, X. Gu, H. Morkoç, B. Nemeth, J. Nause, and H. O. Everitt, Phys. Rev. B **70**, 195207 (2004). Copyright 2004 by the American Physical Society.]

peaks. It is also noted that the temperature variation of the *A*-free-exciton peak energy follows the Varshni formula[318] $E_g(T)=E_g(0)-\alpha T^2/(T+\beta)$, where $E_g(0)$ is the transition energy at 0 K, T is the temperature, and α and β are the temperature coefficients. In Fig. 56, a higher-order LO-phonon replica of the *A* free exciton also develops persistently with increasing temperature.

C. Time-resolved PL on ZnO

Time-resolved PL (TRPL) is a nondestructive and powerful technique commonly used for the optical characterization of semiconductors. The free-carrier or exciton lifetime, an important parameter related to material quality and device performance, can be measured by TRPL spectroscopy. The exciton lifetimes will vary with crystal quality, becoming longer as the quality improves. The efficiency of the radiative recombination is strongly related to the decay time of the particular transition.

Reynolds *et al.*[320] measured the recombination lifetime of the allowed (Γ_5) and forbidden (Γ_6, allowed by induced strain) free excitons at 2 K in a strained single-crystal ZnO grown by the hydrothermal method as 259 and 245 ps, respectively. The lifetime for the Γ_5 exciton was slightly higher, 322 ps, for an unstrained sample. They noted that free-exciton lifetimes are determined not only by the radiative decay but also by the nonradiative decay and by capture processes leading to bound excitons.[321] Evidently, the measured single exponential decays reflect the effects from all three.

Teke *et al.*[299] measured the room-temperature TRPL from bulk ZnO samples, one as received from Cermet, Inc., and the other annealed in forming gas (FG). Figure 57 shows the TRPL data for both samples at an excitation energy density of 540 μJ/cm^2. The time-resolved signals were integrated over a 10-nm-wide spectral region around the peak PL energy (3.266 eV). The instrument-limited rise implies that the relaxation processes to cool the carriers from 3.81-eV excitation-energy-defined states to the zero-momentum excitonic band-edge states are very fast. For both samples, the decaying part of the TRPL data was well described by a biexponential decay function: $A_1\exp(-t/\tau_1)+A_2\exp(-t/\tau_2)$. Table XII summarizes the decay constants and the amplitude ratios obtained from the fits.

The fast decay constant τ_1 is smaller for the as-received sample (170.4 ps), and most probably represents the effective nonradiative recombination at room temperature. The slow decaying component is attributed to the radiative lifetime of the free exciton. The 0.86-ns value measured for the as-received sample is reasonably consistent with the 0.97-ns value measured by Koida *et al.*[322] for single-crystal ZnO. The relative magnitude of the slow decaying component to the fast decaying component ($A_2/A_1=0.094$ for 540 μJ/cm^2) for the as-received sample suggests that the nonradiative processes are dominant. It has been proposed that the nonradiative recombination processes are governed by the defects introduced by the Zn vacancy complexes.[322] After forming-gas annealing the decay constants increased remarkably ($\tau_1=0.86$ ns and $\tau_2=2.47$ ns), and the slow decaying component became dominant ($A_2/A_1=2.54$ for 540 μJ/cm^2), suggesting an increase in radiative recombination. This is also supported by the fact that the PL intensity increased by almost a factor of 4 in the forming-gas-annealed ZnO sample compared to the as-received one. The increase in the decay times is clearly observed in Fig. 57.

When the excitation density was decreased from 540 to 54 μJ/cm^2, Teke *et al.*[299] observed a blueshift in the PL peak by 15 meV, most probably due to reducing strength of the band-gap renormalization. For the as-received sample the decay constants increase slightly with increasing excitation density, whereas the forming-gas-treated sample follows an opposite trend. In addition, compared to the forming-gas-treated sample, the as-received sample shows a more evident increase in the relative strength of the slow decaying component as the excitation density is increased, as the nonradiative centers begin to saturate.

TABLE XII. TRPL decay time constants and amplitude ratios for the ZnO samples at two different excitation energy densities. FX and DBE denote the free and donor-bound excitons, respectively [Teke *et al.* (Ref. 299)].

		540 μJ/cm^2			54 μJ/cm^2		
	Samples	τ_1 (ps)	τ_2 (ps)	A_2/A_1	τ_1 (ps)	τ_2 (ps)	A_2/A_1
300 K	As-received	170.4±1.8	863.9±14.8	0.094	116.5±1.5	585.0±6.4	0.060
(FX)	FG-annealed	358.7±8.8	2469±256	2.536	428.3±32.1	2969±115	2.476
85 K	As-received	310.2±2.5	1130±6.6	0.653	286.8±2.9	1000±5.9	0.820
(DBE)	FG-annealed	474.0±5.5	1285±14.6	0.614	366.4±4.1	1021±7.3	0.869

[This article is copyrighted as indicated in the article. Reuse of AIP content is subject to the terms at: http://scitation.aip.org/termsconditions. Downloaded to] IP: 128.172.48.58 On: Mon, 19 Oct 2015 20:45:44

The decay time constants of both as-received and forming-gas-annealed samples were also measured at 85 K.[299] At this temperature, the main donor-bound exciton still dominates the overall cw-PL spectrum even though A and B free excitons are clearly observed. However, a distinction between the bound and the free excitons could not be made in the TRPL measurements due to the resolution limitation of the experimental setup. Therefore, the TRPL data reflect mainly the decay due to the main donor-bound exciton. In order to measure purely the free-excitonic-emission decay time, the measurements had to be performed at temperatures above 160 K where the bound-exciton emission diminishes. The time constants measured at 85 K are also included in Table XII for two different excitation densities. The main DBE-emission lines in both samples are similar in terms of their intensities as observed from the time-integrated and the cw PL. Compared to the as-received sample, the forming-gas-annealed sample showed slightly larger decay constants. Additionally, the decay times decreased with decreasing excitation energy density. In contrast to the significant improvement in free-exciton lifetimes measured at room temperature, the postgrowth treatment is not observed to have a strong effect on the DBE decay times.

Epitaxial ZnO layers exhibit shorter carrier lifetimes, since they suffer from higher defect densities compared to the bulk samples. Koida *et al.*[322] studied the correlation between the excitonic PL lifetime at room temperature and point defect density in bulk and epitaxial ZnO layers. The defect density, Zn vacancy being the most probable defect, was analyzed by positron annihilation. The single-crystal sample showed biexponential behavior with decay constants of 0.97 and 14 ns, which were suggested to represent the free-exciton lifetime and the free-carrier lifetime including trapping and emission processes, respectively. For ZnO epitaxial layers grown by laser MBE on $ScAlMgO_4$ (SCAM) substrates, the single exponential TRPL decay time, which is mainly governed by nonradiative processes, increased from 46 to 110 ps with increasing growth temperature from 570 to 800 °C. However, since a homoepitaxial film exhibited the shortest decay time (36 ps) in spite of the smallest number of point defects among the epilayers, i.e., no clear correlation was found between the PL decay time and the point defect density, the nonradiative process was considered to be governed by certain defect species introduced by the presence of Zn vacancies such as vacancy complexes.

Jung *et al.*[323] reported a biexponential decay for high-quality ZnO epitaxial layers grown on sapphire by low-pressure metal-organic vapor-phase epitaxy. Room-temperature TRPL measurements produced decay times of 180 ps and 1 ns, most probably representing the nonradiative and the radiative excitonic recombination times, respectively, consistent with the measurements of Teke *et al.*[299] and Koida *et al.*[322] on bulk ZnO samples.

D. Refractive index of ZnO

Knowledge of the dispersion of the refractive indices of semiconductor materials is necessary for accurate modeling and design of devices. The wurtzite ZnO lacks cubic symmetry and therefore has anisotropic optical properties. The anisotropy results in uniaxial birefringence, two different refractive indices for polarization parallel (n_o, ordinary) and perpendicular (n_e, extraordinary) to the c axis. In this section a summary of reported results on ZnO dielectric constants and refractive index dispersion will be given.

In the early 1950s and 1960s, several workers reported the results of optical reflection measurements with light polarized parallel and perpendicular to the c axis, and used the Kramers-Kronig analysis to determine the dielectric functions. Mollwo[16] and Bond[17] have reported on refractive index dispersion of single-crystal ZnO using the method of minimum deviation at room temperature for the visible and near-infrared spectrum. Prisms fabricated from vapor-transport-grown ZnO were used. For light below the direct band edge, traditional angle-of-minimum deviation methods produced very accurate values of the refractive index for both $E \perp c$ and $E \parallel c$. Park and Schneider[24] then extended the measurements to the spectral region near the onset of the exciton absorption at temperatures down to liquid-helium temperature using transmission interferometry. A ZnO platelet sample (with the c axis lying in the plane of the platelet) grown by vapor-phase transport was used for the measurements. By lowering the temperature, the dispersion curves were observed to get sharper and blueshift. The refractive indices obtained at 4.2 K near the absorption edge are listed in Table XIII. Freeouf[20] obtained the dielectric functions above and below the band gap by measuring the reflectivity from 0.6 to 30 eV before applying the Kramers-Kronig analysis to determine the dielectric functions. Matz and Lütz[324] determined the optical functions of ZnO using nulling ellipsometry at several wavelengths defined by interference filters.

Hu *et al.*[325] used optical transmission to measure the optical functions of thin-film ZnO prepared by pulsed-laser deposition on α-SiO_2 substrates. The ordinary refractive indices deduced from transmittance oscillations were 0.02–0.03 lower than the bulk ZnO crystal data by Bond.[17] The existence of grain boundaries in the films was assumed to be the source for this difference. Additionally, the measurement technique introduced a considerably large error resulting in large variations in the data. The best fits for the ordinary index using the three-term Cauchy equation

$$n(\lambda) = A + \frac{B}{\lambda^2} + \frac{C}{\lambda^4}, \qquad (19)$$

produced parameters of $A = 1.9281$, $B = -1.1157 \times 10^{-5}\ \mu m^2$, and $C = 5.9696 \times 10^{-3}\ \mu m^4$, whereas the bulk ZnO crystal[17] was best characterized by $A = 1.9436$, $B = -1.9714 \times 10^{-5}\ \mu m^2$, and $C = 7.0918 \times 10^{-3}\ \mu m^4$.

The Kramers-Kronig technique is far less accurate than the ellipsometric technique, since it relies on less-accurate data (reflectance) and requires extrapolations to perform the Kramers-Kronig integrals. More recent measurements of complex dielectric functions were reported by Yoshikawa and Adachi[326] using spectroscopic ellipsometry in the photon energy range of 1.5–5.0 eV at room temperature. Samples

[This article is copyrighted as indicated in the article. Reuse of AIP content is subject to the terms at: http://scitation.aip.org/termsconditions. Downloaded to] IP: 128.172.48.58 On: Mon, 19 Oct 2015 20:45:44

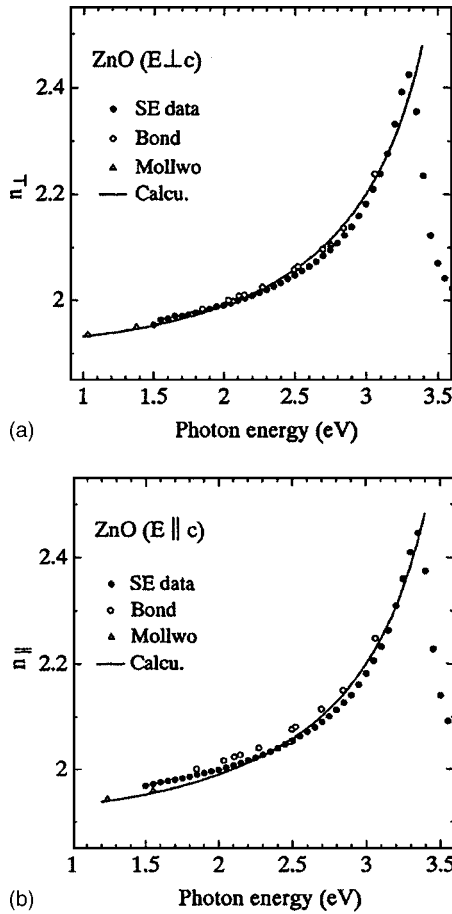

FIG. 58. Refractive index dispersion of ZnO for (a) $E \perp c$ and (b) $E \| c$ below the fundamental absorption edge. The solid circles represent the spectroscopic ellipsometry data of Yoshikawa and Adachi (Ref. 326). The open circles and open triangles represent the data obtained by Bond (Ref. 17) and Mollwo (Ref. 16), respectively. [Reprinted with permission from H. Yoshikawa and S. Adachi, Jpn. J. Appl. Phys. **36**, 6237 (1997). Copyright 1997, Institute of Pure and Applied Physics.]

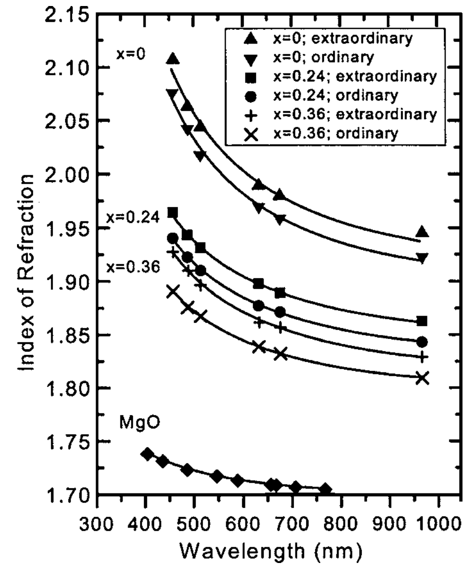

FIG. 59. The ordinary and extraordinary refractive indices of the $Mg_xZ_{1-x}nO$ films (x=0, 0.24, and 0.36). The solid curves are the least-squares fits to the first-order Sellmeier dispersion. The index of refraction of cubic MgO crystal measured by Stephens and Malitson (Ref. 23) is also plotted for comparison. [Reprinted with permission from C. W. Teng, J. F. Muth, Ü. Özgür, M. J. Bergmann, H. O. Everitt, A. K. Sharma, C. Jin, and J. Narayan, Appl. Phys. Lett. **76**, 979 (2000). Copyright 2000 American Institute of Physics.]

grown by vapor-phase methods with surfaces oriented parallel to the c axis were used and the data in the transparent region of ZnO have been analyzed. The data for polarization parallel ($E \| c$) and perpendicular ($E \perp c$) to the optical axis are shown in Fig. 58 along with the data from Mollwo[16] and Bond.[17] Also shown in the figures are fits to a first-order Sellmeier equation:

TABLE XIII. Some values of the refractive indices of ZnO at 4.2 K near the absorption edge [Park and Schneider (Ref. 24)].

$E \perp c$		$E \| c$	
λ (nm)	n	λ (nm)	n
366.43	9.843	363.71	3.525
366.72	6.734	365.67	2.917
367.01	9.414	367.54	2.722
369.04	3.089	369.79	2.598
371.19	2.747	371.52	2.539
373.51	2.595	373.85	2.478
375.65	2.513	375.68	2.441
377.84	2.454	377.90	2.407
379.69	2.417	380.49	2.374
381.87	2.382	381.90	2.358
385.86	2.332	383.44	2.343
387.43	2.316	385.08	2.328
390.92	2.286	388.70	2.300
392.85	2.272	392.83	2.273
394.89	2.258	395.02	2.260
397.04	2.245	399.92	2.237
399.39	2.232	405.31	2.215
401.89	2.220	408.19	2.204
		411.27	2.194

[This article is copyrighted as indicated in the article. Reuse of AIP content is subject to the terms at: http://scitation.aip.org/termsconditions. Downloaded to] IP: 128.172.48.58 On: Mon, 19 Oct 2015 20:45:44

TABLE XIV. Sellmeier coefficients for $Mg_xZn_{1-x}O$ films [After Teng *et al.* (Ref. 328)].

	Parameter	$x=0$	$x=0.24$	$x=0.36$
Ordinary index	B	2.60±0.02	2.37±0.003	2.27±0.004
$E\perp c$	C (μm)	0.2114±0.0037	0.1793±0.0012	0.1686±0.0008
Extraordinary index	B	2.66±0.02	2.43±0.01	2.32±0.01
$E\parallel c$	C (μm)	0.2143±0.0051	0.1815±0.0016	0.1801±0.0016

$$n(\lambda)^2 = A + \frac{B\lambda^2}{\lambda^2 - C^2}, \tag{20}$$

where A, B, and C are the fitting parameters, and λ is the wavelength. Best fits were obtained for $A=2.84$, $B=0.84$, and $C=0.319$ μm for $E\perp c$, and $A=2.85$, $B=0.87$, and $C=0.310$ μm for $E\parallel c$.

Jellison and Boatner[327] employed a two-modulator generalized ellipsometry (2-MGE) technique to determine the anisotropic optical functions of ZnO, using samples grown by chemical-vapor transport and hydrothermal methods. Near and above the band edge, the resulting dielectric functions from both samples were identical within the experimental error, whereas the refractive indices of he hydrothermal-grown sample were ~0.012±0.007 smaller than the refractive index of the vapor-transport-grown sample from 850 to 450 nm. 2-MGE is claimed to produce the most accurate results above the band edge, particularly more accurate than the results by Freeouf[20] in the measured spectral region of 3.3–5.0 eV, while the refractive indices determined below the direct band edge agree with the minimum-deviation methods[17] within an accuracy of ±0.003.

Using the prism-coupled waveguide technique, Teng *et al.*[328] measured the indices of refraction for $Mg_xZn_{1-x}O$ epitaxial films grown on c-plane sapphire substrates by pulsed-laser deposition. Measurements were performed for samples with x up to 0.36 in the wavelength range of 457–968 nm. The results are shown in Fig. 59 for the ordinary and the extraordinary refractive indices. The data were fit by the least-squares method to the first-order Sellmeier dispersion relationship with $A=1$ in Eq. (20). The data for the ZnO sample were best characterized with fitting parameters $B=2.60\pm0.02$ and $C=0.2114\pm0.0037$ μm for the ordinary index and $B=2.66\pm0.02$ and $C=0.2143\pm0.0051$ μm for the extraordinary index. The Sellmeier parameters for $Mg_xZn_{1-x}O$ films are summarized in Table XIV.

One of the most recent reports of dielectric functions of ZnO is by Ashkenov *et al.*[118] who characterized thin films grown by pulsed-laser deposition on c-plane sapphire and a single-crystalline sample grown by seeded chemical-vapor transport method. The static dielectric constant was obtained from infrared spectroscopic ellipsometry measurements. The high-frequency dielectric constant was calculated through the Lyddane-Sachs-Teller (LST) relation using the static constant and the TO- and LO-phonon mode frequencies. The results are compared with the data from some of the previous reports in Table XV.

Schmidt *et al.*[329] also reported room-temperature spectroscopic ellipsometry results on pulsed-laser-deposition-grown wurtzite $Mg_xZn_{1-x}O$ ($0<x<0.29$) thin films. The refractive index data were fit to a three-term Cauchy-approximation-type formula [Eq. (19)] and the anisotropic Cauchy model parameters A, B, and C for ZnO were obtained as 1.916, 1.76, and 3.9 for $E\perp c$, and 1.844, 1.81, and 3.6 for $E\parallel c$, respectively. For the $Mg_xZn_{1-x}O$ alloy system, linear dependence of the Cauchy parameters on x was assumed:

$$n(\lambda) = A + ax + \frac{B+bx}{\lambda^2} + \frac{C+cx}{\lambda^4}. \tag{21}$$

The coefficients b and c were found isotropic, and the parameters obtained from fits to Eq. (21) are listed in Table XVI. Surprisingly, for all the $Mg_xZn_{1-x}O$ thin films investigated the birefringence was found negative, unlike ZnO, which showed positive birefringence (0.05) in the transparency region. This change of the sign of the birefringence going from ZnO to the $Mg_xZn_{1-x}O$ alloy system is in contrast to the results reported by Teng *et al.*,[328] where a positive birefringence of approximately 0.025 for ZnO and $Mg_xZn_{1-x}O$ for all Mg contents was found. When compared to the ZnO data by Teng *et al.*[328] Jellison and Boatner,[327] Yoshikawa and Adachi,[326] and Hu *et al.*,[325] the ZnO ordinary and extraordinary refractive index values of Schmidt *et al.*[329] are about 0.02 lower and 0.03 higher, respectively, up to 700 nm, and the birefringence is larger.

TABLE XV. Static and high-frequency dielectric constants of ZnO.

Sample		Ashkenov *et al.* (Ref. 118)		Teng *et al.* (Ref. 328)	Yoshikawa and Adachi (Ref. 326)	Bond (Ref. 17)
		Thin film	Bulk	Thin film	Bulk	Bulk
ε_0[a]	$E\perp c$	7.46	7.77	7.44	7.61	7.65
	$E\parallel c$	8.59	8.91	8.36	8.50	8.57
ε_∞	$E\perp c$	3.61	3.70	3.60	3.68	3.70
	$E\parallel c$	3.76	3.78	3.66	3.72	3.75

[a]Calculated via the LST relation with the phonon mode parameters obtained by Ashkenov *et al.* (Ref. 118).

[This article is copyrighted as indicated in the article. Reuse of AIP content is subject to the terms at: http://scitation.aip.org/termsconditions. Downloaded to] IP: 128.172.48.58 On: Mon, 19 Oct 2015 20:45:44

TABLE XVI. Cauchy model parameters for the $Mg_xZn_{1-x}O$ alloy system [Schmidt *et al.* (Ref. 329)].

	A	B (10^{-2} μm^2)	C (10^{-3} μm^4)	a	b (10^{-2} μm^2)	c (10^{-3} μm^4)
$E \perp c$	1.916	1.76	3.9	−0.574	−4.51	−4.90
$E \parallel c$	1.844	1.81	3.6	−0.782		

E. Stimulated emission in ZnO

Even though *n*- and *p*-type dopings have been reported in ZnO thin-films,[330] there is no demonstration of electrically pumped lasing in ZnO-based structures. However, optically pumped stimulated emission (SE) has been observed by many researchers from ZnO epitaxial layers grown by a variety of methods.

Fabrication of low-dimensional structures such as quantum wells and dots has been the focus of semiconductor laser research to decrease the threshold for lasing. Efficient stimulated emission may be obtained from these quantum structures since the transfer integral at the band edge is larger than that of the bulk semiconductor. Excitonic emission may also be used to obtain efficient lasing, which may be realized for ZnO due to its larger exciton binding energy (~60 meV)[38,331] compared to other wide-band-gap semiconductors. Exciton-exciton scattering-induced stimulated emission is very important for the realization of low-threshold lasers since it occurs at a threshold lower than that for the electron-hole plasma (EHP) recombination. The demonstration of SE with excitonic origin paves the way for the realization of blue-violet laser diodes based on ZnO.

In the intermediate excitation density regime emissions due to biexcitonic, exciton-exciton and exciton-carrier interactions may be observed. The inelastic collision between the excitons results in an exciton excited into a higher state and a photon with energy[332]

$$E_n = E_{\mathrm{ex}} - E_b^{\mathrm{ex}}\left(1 - \frac{1}{n^2}\right) - \frac{3}{2}k_B T \quad (n = 2,3,4,\ldots,\infty), \tag{22}$$

where E_{ex} is the free-exciton energy, E_b^{ex} is the binding energy of the exciton, n is the quantum number of the envelope function, and $k_B T$ is the thermal energy. Equation (22) gives 99 meV, which is in good agreement with the experimental results which will be discussed below. At very high excitation intensities, an EHP forms beyond the "Mott density," which is calculated as

$$n_M = \frac{k_B T}{2a_B^3 E_B^{\mathrm{ex}}} \sim 3.7 \times 10^{19}\ \mathrm{cm}^{-3}, \tag{23}$$

where $a_B = 18$ Å is the exciton Bohr radius and $E_B^{\mathrm{ex}} = 60$ meV is the exciton binding energy of ZnO.

In the following sections experimental observations of SE and lasing in ZnO-based wurtzite thin films, polycrystalline thin films, and multiple-quantum wells will be discussed.

1. Thin films

Özgür *et al.*[333] have shown that ZnO layers deposited directly on *c*-plane sapphire substrates by rf magnetron sputtering could have optical quality sufficient for excitonic laser action. Pulsed excitation, time-integrated PL (TI-PL) was performed using ~100-fs pulses at room temperature with average excitation energy densities varying between 5 and 700 $\mu J/cm^2$. To obtain the SE thresholds (I_{th}), the spectrally integrated PL intensities were plotted as a function of the pump energy density. SE features were observed for the samples annealed above 800 °C; however, the as-grown samples did not show any sign of SE for the maximum energy density used. The spectrally resolved TI-PL for the sample annealed at 1000 °C is shown in the Fig. 60 inset. For excitation densities above ~50 $\mu J/cm^2$ SE emerges at 3.167 eV as a sharp feature on the lower-energy side of the spontaneous emission (SPE) peak and grows superlinearly. This SE peak has been attributed to exciton-exciton scattering and lies below the free-exciton energy by an exciton binding energy plus the mean kinetic energy $3/2k_BT$,[334,335] where k_BT is the thermal energy. This peak then slightly redshifts to 3.160 eV since the inelastic exciton-exciton scattering leaves one exciton in an excited state which in turn reduces the emission energy of the recombining exciton.[334] As the excitation density is increased above 250 $\mu J/cm^2$, a second peak emerges at 3.133 eV due to SE from the EHP. At these higher excitation densities, exciton wave functions start to overlap due to the increase in their density. Phase-space filling and Coulomb interactions cause excitons to lose their individual character by ionization and eventually an EHP is formed. This EHP-induced SE peak shifts and broadens with increasing excitation as a result of band-gap renormalization. The coexistence of the exciton-exciton scattering and the EHP originates from the spatial nonuniformity of the sample as well as the laser beam profile, i.e., the EHP and the

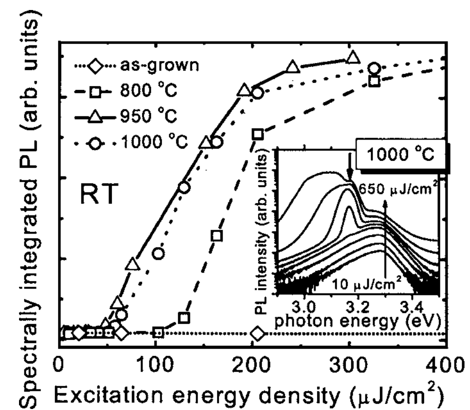

FIG. 60. Room-temperature (RT) spectrally integrated PL for the ZnO samples normalized to the spontaneous emission. The inset shows the spectrally resolved PL for the 1000 °C sample for different excitation densities. The downward-pointing arrow in the inset indicates the exciton-exciton scattering-induced SE peak. [Reprinted with permission from Ü. Özgür, A. Teke, C. Liu, S.-J. Cho, H. Morkoç, and H. O. Everitt, Appl. Phys. Lett. **84**, 3223 (2004). Copyright 2004, American Institute of Physics.]

[This article is copyrighted as indicated in the article. Reuse of AIP content is subject to the terms at: http://scitation.aip.org/termsconditions. Downloaded to] IP: 128.172.48.58 On: Mon, 19 Oct 2015 20:45:44

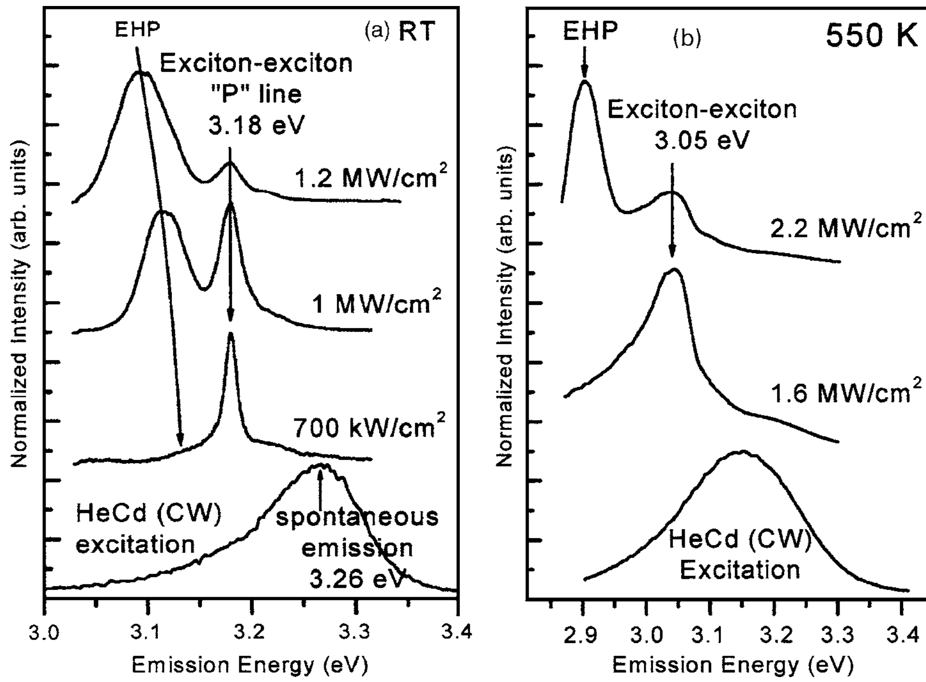

FIG. 61. Normalized PL spectra for various excitation intensities at (a) room temperature and at (b) 550 K [Reprinted with permission from D. M. Bagnall, Y. F. Chen, Z. Zhu, T. Yao, M. Y. Shen, and T. Goto, Appl. Phys. Lett. **73**, 1038 (1998). Copyright 1998, American Institute of Physics.]

exciton-exciton-scattering-induced SE may come from different regions of the sample excited by the laser.

Özgür *et al.*[333] observed the SE peak attributed to exciton-exciton scattering also for another rf-sputtered sample annealed at 950 °C, but not for the sample annealed at 800 °C. Due to the existence of exciton-exciton scattering, I_{th} for the 950 and 1000 °C samples (49 and 58 μJ/cm^2, respectively) were significantly lower than that for the 800 °C sample (130 μJ/cm^2). Figure 60 shows the PL data spectrally integrated between 3.1 and 3.4 eV for all the samples.

Stimulated emission and lasing, which could survive even at temperatures as high as 550 K, have been observed by Bagnall *et al.*[335,336] in ZnO thin films grown by plasma-enhanced MBE on *c*-plane sapphire. At room temperature, for excitation intensities exceeding 400 kW/cm^2 the exciton-exciton-scattering-related SE peak appeared at 3.18 eV and grew superlinearly. At higher excitation intensities (800 kW/cm^2) the electron-hole plasma peak appeared at 3.14 eV and broadened and redshifted due to band-gap renormalization with further increase in the excitation intensity. The thresholds for the SE lines were 1.2 and 1.9 MW/cm^2 for the exciton-exciton scattering and EHP mechanisms, respectively. Figure 61 shows the SE observed at room temperature and at 550 K.

Bagnall *et al.*[163] reported optically pumped room-temperature lasing from cleaved ZnO cavities even through they were unable to observe the longitudinal cavity modes directly. In a later study,[336] they could clearly see a very strong and stable mode structure on the room-temperature EHP emission peak of one of the ZnO epitaxial layers (see Fig. 62). Although its origin was not explicitly identified, the lasing was claimed to be produced by a naturally formed or "accidental" ~70-μm cavity as calculated from the 0.5-nm mode spacing. In the same samples, pump-probe measurements revealed that the optical gain forms when photoexcited hot carriers cool down to an EHP state.[337] Yu *et al.*[338] also observed optically pumped lasing in 60-nm-thick microcrystalline ZnO films grown on *c*-plane sapphire by laser MBE. However, the lasing mechanism was attributed to inelastic exciton-exciton scattering and a peak gain of 300 cm^{-1} was observed at a fluence of 3.8 μJ/cm^2. Although different optical pumping conditions could be a reason for the observed discrepancy, the different crystal properties of the investigated epitaxial layers should also play a critical role in lasing mechanisms.

By using the variable stripe length method, Chen *et al.*[334] measured the optical gain spectrum of ZnO epilayers which were grown on *c*-plane sapphire by plasma-assisted MBE (P-MBE) employing a thin MgO buffer layer. Figure 63 shows the stimulated-emission spectra with excitation density near I_{th} for various excitation stripe lengths. The sharp increase of the emission intensity with excitation

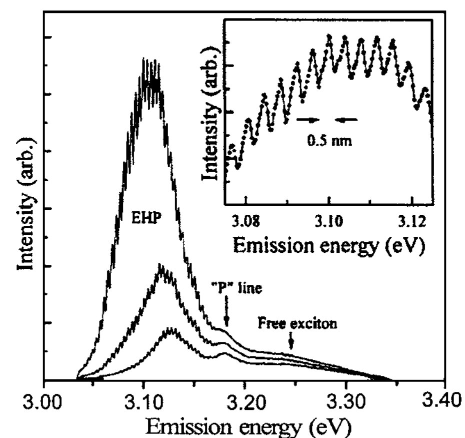

FIG. 62. Room-temperature laser emission spectra. The inset shows clearly the resolved mode.s [Reprinted from D. M. Bagnall, Y. F. Chen, M. Y. Shen, Z. Zhu, T. Goto, and T. Yao, J. Cryst. Growth **184–185**, 605 (1998), Copyright 1998, with permission from Elsevier.]

[This article is copyrighted as indicated in the article. Reuse of AIP content is subject to the terms at: http://scitation.aip.org/termsconditions. Downloaded to] IP: 128.172.48.58 On: Mon, 19 Oct 2015 20:45:44

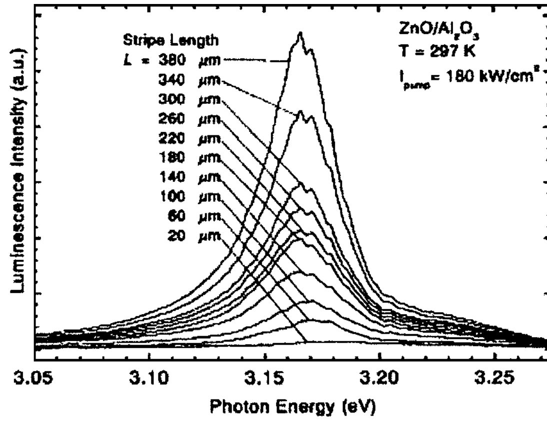

FIG. 63. Stimulated emission spectra for various excitation stripe lengths at room temperature. [Reprinted with permission from Y. Chen, N. T. Tuan, Y. Segawa, H.-J. Ko, S.-K. Hong, and T. Yao, Appl. Phys. Lett. **78**, 1469 (2001). Copyright 2001, American Institute of Physics.]

length indicates the presence of optical gain. Based on the one-dimensional optical amplifier mode for excited media, the spectra were analyzed by fitting to the equation

$$I(E) = \frac{I_0}{g}(e^{gL} - 1), \quad (24)$$

where g stands for the optical gain coefficient and L for the length of the excitation stripe. The evaluated optical gain as a function of photon energy is plotted in Fig. 64. At an excitation density of 180 kW/cm^2, close to I_{th}, the peak gain is about 40 cm^{-1} and it increases to 177 cm^{-1} with a redshift of about 6 meV as the excitation density increases to 220 kW/cm^2. The EHP peak appears at 3.135 eV with further increase of the excitation density to 300 kW/cm^2. Therefore, Chen *et al.*[334] argued that the observed optical

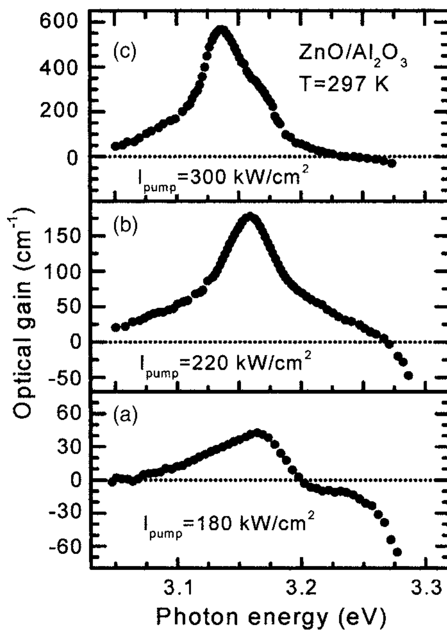

FIG. 64. Optical gain spectrum of a ZnO epilayer at excitation densities of (a) 180 kW/cm^2, (b) 220 kW/cm^2, and (c) 300 kW/cm^2 at RT. [Reprinted with permission from Y. Chen, N. T. Tuan, Y. Segawa, H.-J. Ko, S.-K. Hong, and T. Yao, Appl. Phys. Lett. **78**, 1469 (2001). Copyright 2001, American Institute of Physics.]

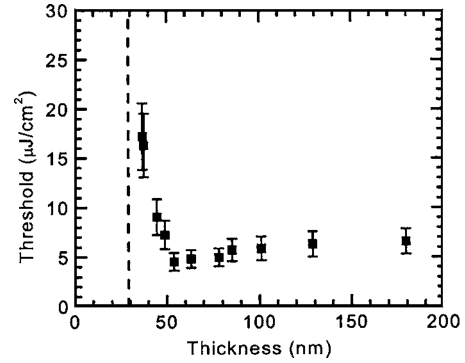

FIG. 65. Lasing threshold as a function of film thickness. A 500×30-μm^2 excitation stripe was used. The thickness values were determined from the RHEED pattern intensity oscillations. [Reprinted from P. Yu, Z. K. Tang, G. K. L. Wong, M. Kawasaki, A. Ohtomo, H. Koinuma, and Y. Segawa, J. Cryst. Growth **184–185**, 601 (1998), Copyright 1998, with permission from Elsevier.

gain resulted from the exciton-exciton scattering. For similar excitation densities, the peak gain seems smaller than that reported by Yu *et al.*,[338] which may be due to different pumping conditions as well as the lack of light confinement in some of the samples.

Yu *et al.*[338] have also investigated the effect of film thickness on the optical gain. The film also forms the propagation medium in the waveguide structure, and its thickness determines the mode of propagation. They attributed the large gain to the modification of the spontaneous emission rate by the dielectric planar waveguide structure of thin-film waveguides consisting of a thin ZnO layer (n_2=2.45) surrounded by air (n_1=1) on one side and sapphire (n_3=1.8) on the other. The film thickness values d, below which a guided mode of order m ceases to exist, can be calculated using the expression

$$\left(\frac{d}{\lambda}\right)_{\rm TE} = \frac{1}{2\pi\sqrt{n_2^2 - n_3^2}}\left[m\pi + \tan^{-1}\left(\frac{n_3^2 - n_1^2}{n_2^2 - n_3^2}\right)^{1/2}\right], \quad (25)$$

where λ is the wavelength in ZnO. For a thickness of 60 nm, only the TE$_0$ mode is supported; therefore, lasing emission should be TE polarized. For sufficiently thin films where the lowest-order TE guided mode exists, the spontaneous emission mostly goes into the TE$_0$ mode. This results in an increase in the SE and a reduction in the lasing threshold. There is an optimum thickness where the emission rate is maximum, and for thinner films this rate decreases rapidly and reaches zero at a cutoff value. Since all guided modes cease to exist below a finite layer thickness, no lasing occurs in very thin samples. According to Eq. (25), the cutoff and the lowest threshold occur at thickness values of 29 and 55 nm, respectively, consistent with the observations of Yu *et al.*[338] Figure 65 shows the lasing threshold as a function of the film thickness. As observed in this figure, the discrepancy in the threshold values from different measurements may also be due to varying thickness.

Kawasaki *et al.*[339] and Zu *et al.*[340] investigated the effects of nanocrystal size on stimulated emission in ZnO thin films fabricated on *c*-plane sapphire substrates by laser MBE. The films having small nanocrystal size of about 50 nm

[This article is copyrighted as indicated in the article. Reuse of AIP content is subject to the terms at: http://scitation.aip.org/termsconditions. Downloaded to] IP: 128.172.48.58 On: Mon, 19 Oct 2015 20:45:44

showed excitonic SE as well as the SE from the EHP. The spontaneous emission generated by exciton-exciton collisions, which showed a quadratic intensity dependence, was followed by SE from the same process at higher excitation intensities exhibiting an eighth-power dependence. With further increase of the excitation intensity the Coulomb interaction leads to ionization of excitons and the formation of a dense EHP. Therefore, the intensity of the excitonic SE peak is observed to reduce. This was not observed in previously mentioned reports due to the sample inhomogeneity. Another major observation was that, unlike the EHP-induced SE, the exciton-exciton-scattering-induced SE was not present in the films having larger nanocrystal size. Kawasaki *et al.*[339] concluded that there is an optimum hexagonally shaped microcrystallite size of $(50\ \mathrm{nm})^3$ for observing excitonic SE. Analyzing similar results, Ohtomo *et al.*[341] speculated that the excitonic stimulated emission is due to the giant oscillator strength that can occur in high-quality nanocrystals with a dimension larger than the exciton Bohr radius (~ 2 nm), but smaller than the optical wavelength (390 nm). For large-grain samples, the exciton superradiance effect becomes weak such that the exciton-exciton collision process should not occur. Thus, the grain boundaries between nanocrystals are considered to serve as barriers resulting in the confinement of excitons in nanocrystals.

2. Polycrystalline ZnO films and "random lasers"

As previously observed in Ti:sapphire and TiO_2 disordered systems,[342,343] there have been reports of "random lasing" in polycrystalline ZnO films as a result of strong scattering in disordered dielectric media.[344–346] It was shown that in the case of such strong scattering and gain, recurring scattering events could provide coherent feedback and result in lasing.[347] When the scattering mean free path becomes equal to or less than the wavelength, photon may return to a scatterer from which it was scattered before, and thereby closed-loop paths may be formed. If the amplification along such a loop path exceeds the loss, lasing could occur in the loop that serves as a resonator. Such a laser is called a "random laser," where the phase shift along the loop must be equal to a multiple of 2π. Unlike the traditional semiconductor lasers which have well-defined cavities, the random-laser cavities are "self-formed" due to strong optical scattering in the polycrystalline films. The main requirement to observe this kind of laser emission is that the particle size should be less than the emission wavelength. The photon localization in this case is similar to Anderson localization of electrons in disordered systems.[348]

Cao *et al.*[344,345] observed random-laser emission in polycrystalline ZnO. Figure 66 shows the evolution of the emission spectra as the pump intensity was increased.[345] At low excitation intensities, the spectrum consisted of a single broad spontaneous-emission peak. As the pump power increased, the emission peak became narrower due to the preferential amplification at frequencies close to the maximum of the gain spectrum. When the excitation intensity exceeded a threshold, very narrow peaks emerged in the emission spectra. The linewidth of these peaks was less than 0.3 nm, which was more than 30 times smaller than the linewidth of the amplified spontaneous-emission peak below the threshold. When the pump intensity increased further, more sharp peaks appeared. The frequencies of the sharp peaks depended on the sample position, that is, when the excitation spot was moved across the film, the frequencies of the sharp peaks changed. Above the threshold, the integrated emission intensity increased much more rapidly with the pump power, and the emission was measured to be strongly polarized, indicating that laser action has occurred in the ZnO films.

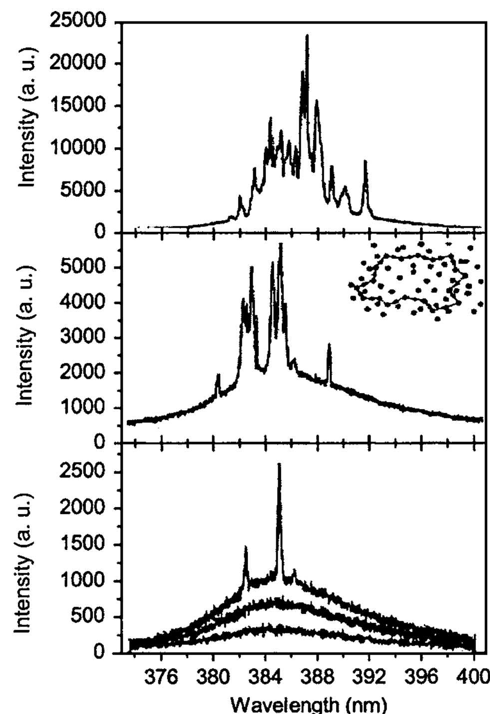

FIG. 66. Spectra of emission from the ZnO powder when the excitation intensities are (from bottom to top) 400, 562, 763, 875, and 1387 $\mathrm{kW/cm^2}$. The thickness of the film of the ZnO powder is 6 μm. The excitation area is about 1600 $\mu\mathrm{m}^2$. The inset is a schematic diagram showing the formation of a closed-loop path for light through recurring scattering in the powder. [Reprinted with permission from H. Cao, Y. G. Zhao, S. T. Ho, E. W. Seelig, Q. H. Wang, and R. P. H. Chang, Phys. Rev. Lett. **82**, 2278 (1999). Copyright 1999 by the American Physical Society.]

The characteristics of lasing in semiconductor polycrystalline films exhibit remarkable differences from that of a conventional laser. First of all, the laser emission from the ZnO polycrystalline films can be observed in all directions, and the laser emission spectrum varies with the observation angle. Second, the pump intensity required to reach the lasing threshold depends on the excitation area. As the excitation area decreases, the lasing threshold density increases, and when the excitation area is reduced to below a critical size, lasing stops because the closed-loop paths are too short, and the amplification along the loops is not high enough to achieve lasing. When the excitation area is increased, more lasing peaks emerge in the emission spectra that is explained by forming more closed-loop paths for light, and thus, increasing the number of lasing modes. The shape and size of the laser cavities change as the excitation spot is moved across the film. The size and shape of the laser resonators are determined by the optical gain coefficient, the grain size and

[This article is copyrighted as indicated in the article. Reuse of AIP content is subject to the terms at: http://scitation.aip.org/termsconditions. Downloaded to] IP: 128.172.48.58 On: Mon, 19 Oct 2015 20:45:44

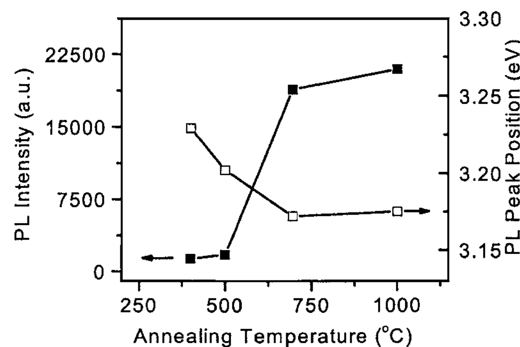

FIG. 67. PL intensity and PL peak position vs annealing temperature. [Reprinted with permission from S. Cho, J. Ma, Y. Kim, Y. Sun, G. K. L. Wong, and J. B. Ketterson, Appl. Phys. Lett. **75**, 2761 (1991). Copyright 1999, American Institute of Physics.]

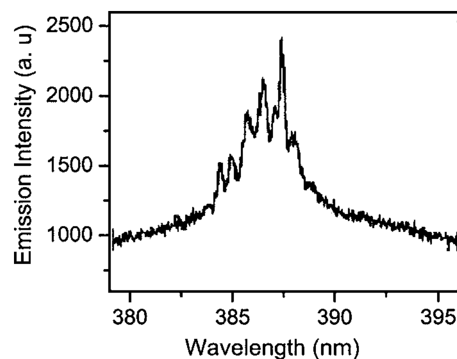

FIG. 68. Lasing spectra of the polycrystalline ZnO thin film obtained by oxidation of metallic Zn films. The threshold intensity (I_{th}) for the lasing was ~9 MW/cm^2. [Reprinted with permission from S. Cho, J. Ma, Y. Kim, Y. Sun, G. K. L. Wong, and J. B. Ketterson, Appl. Phys. Lett. **75**, 2761 (1999). Copyright 1999, American Institute of Physics.]

distribution, the scattering cross section, and the boundary conditions, so the lasing frequencies vary across the film.

The microlasers have potential applications in integrated photonic circuits. The demonstration of random lasers opens up the possibility of using disordered semiconductor microstructures as alternative sources of coherent light emission. The fabrication of the conventional microlasers requires expensive state-of-the-art crystal growth and microfabrication facilities. The realization of lasing in semiconductor polycrystalline films, which are nonepitaxially grown on amorphous fused silica substrates, provides a possibility to fabricate semiconductor lasers on many different types of substrates. As a result, fabrication of such a polycrystalline film-based microlaser is much easier and less expensive than that of most microlasers. In this context development of methods for growing high-quality polycrystalline ZnO films is important, since polycrystalline ZnO films also have many other applications as phosphors, coatings, etc., in various devices.[349]

Several authors suggested very simple methods for growing polycrystalline ZnO films by oxidation of metallic Zn films deposited on different substrates.[350–354] Dimova-Alyakova *et al.*[350] obtained polycrystalline ZnO films by oxidation of metal Zn films deposited on sapphire substrates by thermal evaporation. However, the quality of the films was quite poor as judged by the weak near-band-edge emission even at high excitation levels. Cho *et al.*[351] succeeded in preparing high-quality polycrystalline ZnO thin films having strong band-edge emission by oxidation of Zn films deposited on silica substrates by magnetron sputtering. Increasing the oxidation temperature from 300 to 1000 °C led to an increase in the average grain size from 18 to 61 nm. Also as a result, the PL peak intensity increased, FWHM decreased, and the peak position redshifted (due to quantum confinement effects in grains) as shown in Fig. 67. The PL FWHMs were 107 and 23 meV for the samples annealed at 700 and 1000 °C, respectively. Optically pumped lasing action in these ZnO polycrystalline films was observed with a threshold intensity of 9 MW/cm^2 (see Fig. 68). These results indicate that polycrystalline ZnO thin films prepared by thermal oxidation from metallic Zn films are suitable for fabrication of random lasers. The results reported by Chen *et al.*[352] were almost similar to those reported in this work.[351] However, Wang *et al.*[353] reported the optimum oxidizing temperature to be 410 °C at which the best crystallinity and the most intense PL emission were observed. The authors attributed this phenomenon to the low rate of formation of intrinsic defects at such a low temperature.

Alivov *et al.*[354] studied the properties (crystal, optical, and electrical) of polycrystalline ZnO films obtained by oxidizing metallic Zn layers which were electron-beam evaporated on various substrates. No predominating orientation was observed for the Zn and ZnO films deposited on glass, sapphire, and silica. Besides, the mean grain size in Zn films (120 nm) as well as in the subsequent ZnO films (size depending on the oxidation temperature) was also independent of the substrate nature. A dramatic improvement of the PL with increasing oxidation temperature was observed as in Ref. 351. The effect of oxygen partial pressure was studied recording the RT cathodoluminescence (CL) spectra of selected ZnO films oxidized at $T=800$ °C and at different oxygen partial pressures. As seen from Fig. 69 the UV CL intensity increased by almost a factor of 10 when the oxygen partial pressure was decreased from 760 to 5×10^{-5} Torr. FWHM of the UV CL band decreased from 125 to 81 meV in the same pressure range. When the annealing temperature was increased from 400 to 900 °C the mean grain size of the films increased from 138 to 245 nm, the resistivity ρ increased from 3.81×10^2 to 6.02×10^4 Ω cm, electron concentration decreased from 4.56×10^{15} to 7.32×10^{12} cm^{-3}, and mobility increased from 3.6 to 14.2 cm^2/V s. The varia-

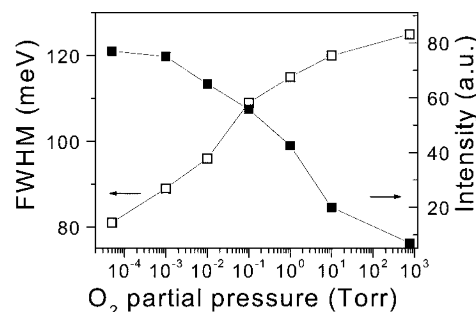

FIG. 69. The dependences of the UV CL peak intensity and FWHM as a function of oxygen partial pressure ($T=300$ K, electron-beam current of 1 μA was used for excitation) [after Alivov *et al.* (Ref. 354)].

[This article is copyrighted as indicated in the article. Reuse of AIP content is subject to the terms at: http://scitation.aip.org/termsconditions. Downloaded to] IP: 128.172.48.58 On: Mon, 19 Oct 2015 20:45:44

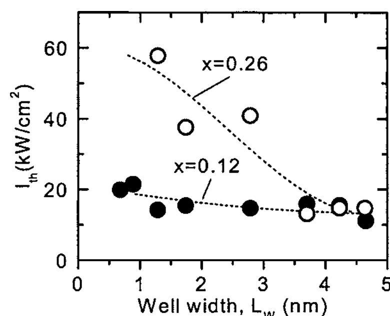

FIG. 70. Well width (L_w) dependence of the stimulated emission threshold (I_{th}) in the superlattices with $x=0.12$ (closed circles) and 0.26 (open circles). Stimulated emission did not take place for the $x=0.26$ films with L_w below 1 nm since the excitation energy is lower than the absorption energy. [Reprinted with permission from A. Ohtomo *et al.*, Appl. Phys. Lett. **77**, 2204 (2000). Copyright 2000, American Institute of Physics.]

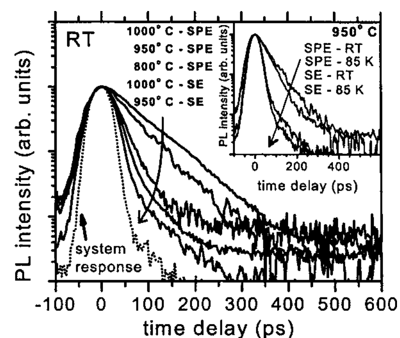

FIG. 71. Room-temperature (RT) TRPL for the spontaneous emission (SPE) and the stimulated emission (SE) from the annealed ZnO samples. The inset shows the 85-K and RT TRPL data for the sample annealed at 950 °C. [Reprinted with permission from Ü. Özgür, A. Teke, C. Liu, S.-J. Cho, H. Morkoç, and H. O. Everitt, Appl. Phys. Lett. **84**, 3223 (2004). Copyright 2004, American Institute of Physics.]

tion of the electrical properties with the oxygen partial pressure was very small compared to the oxidation temperature. The resistivity and mobility increased only by a factor of 2-4 when oxygen partial pressure was varied from 1.01×10^{-5} to 1.33×10^{-3} Pa.

3. Multiple-quantum wells

Stimulated emission has been observed also in quantum-well structures utilizing the alloys of ZnO. It is expected that the observation of the excitonic SE phenomenon should be favored in quantum wells owing to the enhanced binding energy of excitons and hence by the larger stability of the exciton states. However, in other II-VI materials SE has been mostly demonstrated only at low temperatures and rarely at room temperature. Ohtomo *et al.*[355] reported the observation of SE in ZnO/ZnMgO multiple-quantum wells (MQWs) up to 373 K, but did not elucidate the mechanism of SE. They investigated ten-period MQWs grown on SCAM substrates by laser MBE. The barriers were 5 nm thick, and the widths of the wells varied from 0.7 to 4.7 nm. The stimulated-emission threshold was observed to increase with decreasing well width and also with increasing Mg composition in the barriers. Figure 70 shows the variation of the SE threshold with well width for two sets of samples having 12% and 26% Mg in the barriers.

Sun *et al.*[356] later investigated the mechanism of SE in the same MQW samples. They observed SE induced by both exciton-exciton scattering and EHP recombination. The exciton-origined recombination mechanism of SE was studied further by measuring the temperature dependence of the SE peak position. It was observed that the exciton-exciton band has the same temperature-dependence characteristics as that of a ZnO single layer, supporting the notion that this emission in ZnO/MgZnO MQWs is indeed due to exciton-exciton scattering. Additionally, the measurements at 5 K revealed that the exciton binding energy increases with decreasing QW width. These binding energies were deduced from the energy difference between the exciton-exciton-scattering-related and the free-exciton emission lines.

4. Stimulated-emission dynamics

In order to investigate the effects of annealing and SE on carrier dynamics, TRPL spectroscopy was employed at room temperature and at 85 K by Özgür *et al.*[333] The TRPL measurements used the same optical pulse excitation source as the TI-PL measurements mentioned before in Sec. IV E 1, and the PL was detected by an ~45-ps resolution Hamamatsu streak camera. Figure 71 shows the TRPL data for three annealed samples at room temperature. The excitation densities were kept slightly below I_{th}(~30 μJ/cm^2) to measure the SPE decay times, while high excitation densities (~200 μJ/cm^2) were used to observe the recombination dynamics under the influence of SE. Single exponential decay fits revealed the spontaneous recombination times as 74, 59, and 30 ps for the samples annealed at 1000, 950, and 800 °C, respectively. The decay time for the as-deposited sample (not shown) was below the system resolution. Here, it should be noted that no deconvolution of the system response was performed for the TRPL data. The increase of the decay times with annealing temperature suggests a reduction in the density of nonradiative recombination centers. As expected, the SE-induced recombination occurs very fast (<30 ps). The TRPL data for above I_{th} excitations also show a much weaker and slower decaying component visible after the SE is over (~55 ps) with the characteristic decay time of the spontaneous recombination.

The spontaneous recombination times observed by Özgür *et al.*[333] for the rf-sputtered ZnO thin films are comparable with other values reported in the literature. Guo *et al.*[357] reported 30-ps room-temperature excitonic recombination times for ZnO thin films grown on Si by MOCVD. Koida *et al.*[358] measured recombination times of up to 110 ps for good-quality ZnO thin films grown on $ScAlMgO_4$ substrates by MBE. These decay times, including the ones measured by Özgür *et al.*,[333] are much shorter than those reported for bulk ZnO (Refs. 299 and 358) most probably due to effective nonradiative recombination in thin films at room temperature. Surprisingly, TRPL measurements performed on rf-sputtered ZnO thin films at 85 K did not show any significant change in decay times. The inset in Fig. 71 compares the room-temperature and the 85-K TRPL data for the

[This article is copyrighted as indicated in the article. Reuse of AIP content is subject to the terms at: http://scitation.aip.org/termsconditions. Downloaded to] IP: 128.172.48.58 On: Mon, 19 Oct 2015 20:45:44

950 °C annealed sample for both below and above I_{th} (950 °C). At 85 K the SPE decay time is 49 ps, indicating that an effective nonradiative recombination mechanism is still present. However, the characteristic single exponential decay along with the strong photon emission suggests that the radiative decay component is also fast. The slight decrease in the decay time at 85 K may be explained by increased absorption at low temperatures and the weak carrier density dependence of the recombination times.

V. DEFECTS IN ZnO

A. Predictions from first principles

As in any semiconductor, point defects affect the electrical and optical properties of ZnO as well. Kohan *et al.*[359] and Van de Walle[360] recently calculated formation energies and electronic structure of native point defects and hydrogen in ZnO by using the first-principles, plane-wave pseudopotential technique together with the supercell approach. In this theory, the concentration of a defect in a crystal depends upon its formation energy E^f in the following form:

$$c = N_{\rm sites} \exp\left(-\frac{E^f}{k_B T}\right), \tag{26}$$

where $N_{\rm sites}$ is the concentration of sites in the crystal where the defect can occur. A low formation energy implies a high equilibrium concentration of the defect; a high formation energy means that defects are unlikely to form.

The formation energy of a point defect in a charge state q is given by

$$E^f(q) = E^{\rm tot}(q) - n_{\rm Zn}\mu_{\rm Zn} - n_{\rm O}\mu_{\rm O} - qE_F, \tag{27}$$

where $E^{\rm tot}(q)$ is the total energy of a system containing $n_{\rm Zn}$ and $n_{\rm O}$ zinc and oxygen atoms, $\mu_{\rm Zn}$ and $\mu_{\rm O}$ are the chemical potentials for zinc and oxygen, respectively, and E_F is the Fermi energy. The total energy can be obtained from the state-of-art first-principles calculations that do not require any adjustable parameter or any input from experiments. The chemical potentials depend on the growth conditions. For the zinc-rich case $\mu_{\rm Zn}=\mu_{\rm Zn(bulk)}$ and for the oxygen-rich case $\mu_{\rm O}=\mu_{\rm O2}$. For intermediate II-VI ratios $\mu_{\rm O}<\mu_{\rm O2}$ and $\mu_{\rm Zn}<\mu_{\rm Zn(bulk)}$. However, the chemical potentials for Zn and O are not independent, since both species are in equilibrium with ZnO: $\mu_{\rm Zn}+\mu_{\rm O}<\mu_{\rm ZnO}$.

The results of calculations for oxygen and zinc vacancies, interstitials, and antisities in ZnO are shown in Fig. 72 for the two limiting zinc chemical-potential values. Note that there are two possible interstitial sites in the wurtzite ZnO: one is tetrahedrally coordinated (teth) and another is octahedrally coordinated (octh). It can be concluded that, depending on the partial pressure of Zn, the two most common defects in ZnO are likely to be oxygen and zinc vacancies. In particular, oxygen vacancies ($V_{\rm O}$) have lower formation energy than the zinc interstitials (Zn_i) and hence should be more abundant in Zn-rich conditions. In O-rich conditions, zinc vacancies ($V_{\rm Zn}$) should dominate. As for the electronic structure of the main point defects in ZnO, the oxygen vacancy has been identified as a negative-U defect, since with increasing Fermi level a transition occurs from the +2 to the neutral state. Zinc vacancy is expected to have charge −2 in *n*-type ZnO where its formation is more favorable. The transition level between the −1 and −2 charge states of $V_{\rm Zn}$ occurs at ~0.8 eV above the valence band. Thus, we may expect transitions from the conduction band or a shallow donor to the $V_{\rm Zn}$ acceptor at around 2.6 eV in *n*-type ZnO. Thus, the broad green luminescence commonly observed in *n*-type ZnO can be attributed to $V_{\rm Zn}$.[359] This proposal is similar to the earlier prediction that negatively charged gallium vacancies are responsible for the yellow luminescence in GaN.[361] The 2+/0 level of the oxygen vacancy is predicted at about 2.7 eV above the valence band.[360] Since the positive charge state of $V_{\rm O}$ is unstable in ZnO, an electron-paramagnetic-resonance (EPR) signal associated with this defect is not expected to be observable, at least in thermodynamically stable conditions.[360]

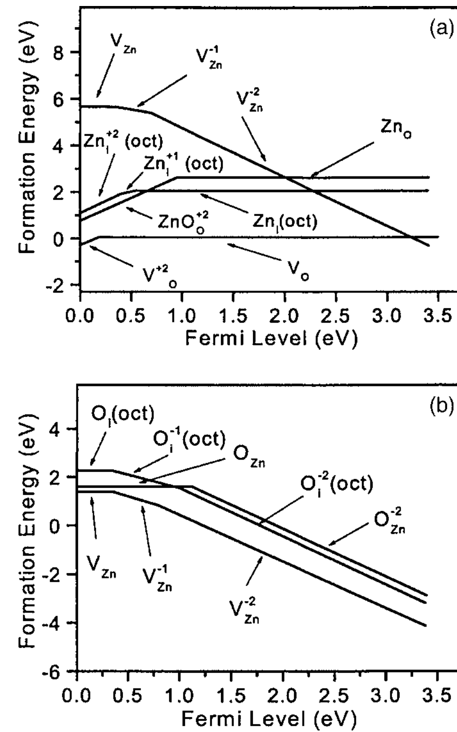

FIG. 72. Calculated defect formation energy for the main native point defects in ZnO as a function of the Fermi level. Only the lowest formation-energy values are shown. The zero of the Fermi level is set to the top of the valence band. (a) Zinc-rich conditions and (b) oxygen-rich conditions. [Reprinted with permission from A. F. Kohan, G. Ceder, D. Morgan, and C. G. Van de Walle, Phys. Rev. B **61**, 15019 (2000). Copyright 2000 by the American Physical Society.]

Hydrogen in ZnO has been also investigated by the above-mentioned first-principles calculations. Unlike other semiconductors (where hydrogen is amphoteric, i.e., occurs as H^+ in *p*-type material and H^- in *n*-type material), hydrogen in ZnO is always positive, i.e., always acts as a donor.[360] Hydrogen is tightly bound to an oxygen atom in ZnO, forming an OH bond with a length of about 1.0 Å. In *n*-type ZnO, the formation energy for hydrogen is only 1.56 eV. In *p*-type ZnO, incorporation of hydrogen is even more favorable. In fact, this may be beneficial for obtaining *p*-type ZnO. Indeed, incorporation of hydrogen during growth may increase acceptor solubility and suppress formation of compensating de-

[This article is copyrighted as indicated in the article. Reuse of AIP content is subject to the terms at: http://scitation.aip.org/termsconditions. Downloaded to] IP: 128.172.48.58 On: Mon, 19 Oct 2015 20:45:44

fects, similar to behavior of hydrogen during doping of GaN with Mg acceptor. Then, the problem may reduce to removal of hydrogen during a postgrowth annealing.

Among all the candidates for *p*-type doping, nitrogen was predicted to be the shallowest acceptor in ZnO.[362] Yan *et al.*[363] demonstrated that while N_O is a shallow acceptor, $(N_2)_O$ is a double-shallow donor, and competition between N and N_2 during doping of ZnO with N controls the doping type. These authors suggest that the use of N_2 or N_2O gas is not effective in *p*-type doping since energy must be supplied to break the strong N–N bond. It contrast, NO or NO_2 molecules can readily form N_O acceptors, taking advantage of the fact that O atoms are host atoms. Below we give a succinct account of native defects in ZnO.

B. Experimental studies of native and unintentionally introduced defects

There are only a few studies of point defects in ZnO up to date. Most of the experimental results have been obtained from the analysis of mainly the low-temperature photoluminescence (PL) data. In undoped ZnO, the well-known[25] green luminescence (GL) band peaking at about 2.5 eV usually dominates the defect-related part of the PL spectrum. Some information is available about the shallow donor-acceptor-pair (DAP) band having its main peak at about 3.22 eV. There are a few reports about other PL bands, in particular, the yellow luminescence in Li-doped ZnO.

1. Shallow acceptor in ZnO

Besides strong and rich exciton-related emissions in the photon energy range of 3.25–3.4 eV, PL spectrum of undoped high-quality ZnO usually contains a sharp peak at about 3.22 eV followed by at least two LO-phonon replicas. This emission has been attributed to the DAP transitions involving a shallow donor and a shallow acceptor.[364] This conclusion is based mostly on a characteristic transformation of the DAP emission lines to similar, but shifted, emission lines arising from transitions from the conduction band to the same shallow acceptor (*e-A* transitions) with increasing temperature (Fig. 73). The DAP line at 3.220 eV quenches and gives way to the *e-A* line at 3.236 eV at temperatures above 30 K due to thermal ionization of the shallow donors.[364] From the position of the *e-A* and DAP lines, the ionization energy of the unintentional shallow acceptor in ZnO has been estimated to be 195 ± 10 meV. The shallow acceptor is assumed to be N_O, which was dominant in the samples analyzed.[364]

In ZnO intentionally doped with N (with concentration up to 10^{19} cm^{-3}), a relatively broad line at 3.315 eV dominates the PL spectrum.[365] Look *et al.*[365] attributed this line to an acceptor-bound exciton (A^0X), associated with the N_O acceptor. A weaker and broader line (or shoulder) appearing at 3.238 eV has been attributed to the DAP emission, involving the N_O acceptor, superimposed with the LO-phonon replica of the dominant (A^0X) emission. The activation energy of the N_O acceptor has been estimated at 0.17–0.20 eV from the above PL experiments. In another study,[366] the PL spectrum of the *p*-type ZnO samples, doped with N by using NO gas,

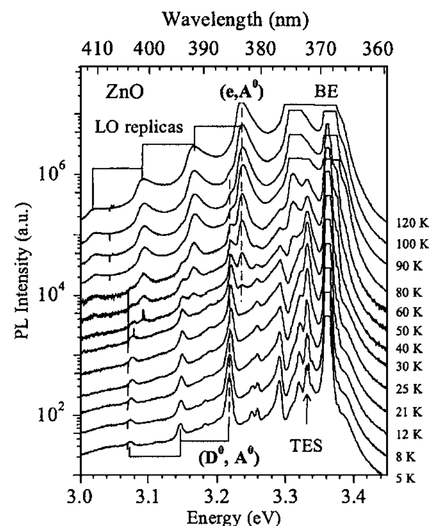

FIG. 73. PL spectra of undoped ZnO at different temperatures. The plots are vertically shifted for clarity. Between 30 and 100 K the DAP transition at 3.220 eV decreases, and the adjacent *e-A* transition at 3.236 eV increases. [Reprinted from K. Thonke, T. Gruber, N. Teofilov, R. Schönfelder, A. Waag, and R. Sauer, Physica B **308–310**, 945 (2001), Copyright 2001, with permission from Elsevier.]

also contained a strong line at 3.309 eV followed by two LO-phonon replicas, that could be attributed to the shallow N_O acceptor. A broad peak at 3.245 eV followed by LO-phonon replicas has been observed also by Matsui *et al.*[367] in N-doped ZnO grown by pulsed-laser deposition on ZnO and glass substrates. This line has been attributed to DAP transition involving the N_O acceptor. The characteristic DAP emission with the zero-phonon line at 3.235 eV was observed in the PL spectrum of N-doped ZnO (Fig. 74) and studied in more detail by Zeuner *et al.*[368] Transient PL studies on this band confirmed its DAP nature. Nonexponential decay of PL intensity after pulse excitation was attributed to transitions between distant pairs. The acceptor binding energy has been estimated at 165 ± 10 meV from these experiments.

In ZnO doped with As, a line at about 3.23–3.24 eV, followed by two LO-phonon replicas has been observed in the PL spectrum with an intensity exceeding the exciton emission intensity.[369] This emission has been attributed to the

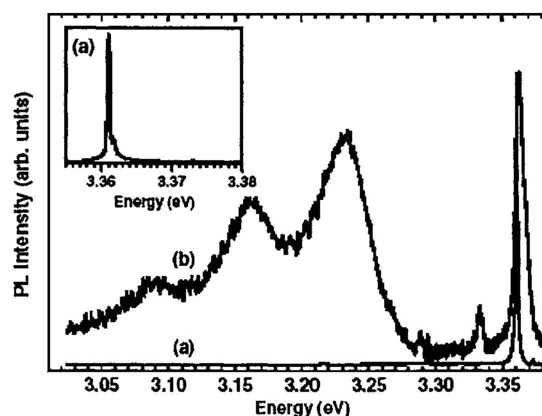

FIG. 74. Low-temperature PL spectra of the (a) undoped and (b) nitrogen-doped ZnO films. [Reprinted with permission from A. Zeuner, H. Alves, D. M. Hofmann, B. K. Meyer, A. Hoffmann, U. Haboeck, M. Strassburg, and M. Dworzak, Phys. Status Solidi B **234**, R7 (2002). Copyright 2002, Wiley.]

[This article is copyrighted as indicated in the article. Reuse of AIP content is subject to the terms at: http://scitation.aip.org/termsconditions. Downloaded to] IP: 128.172.48.58 On: Mon, 19 Oct 2015 20:45:44

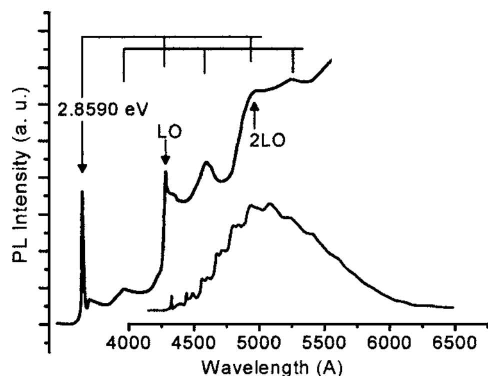

FIG. 75. GL band in ZnO at 1.6 K. The enlarged portion shows the fine structure at the high-energy side with the zero-phonon line at 2.859 eV. [Reprinted with permission from R. Dingle, Phys. Rev. Lett. **23**, 579 (1969). Copyright 1969 by the American Physical Society.]

shallow As acceptor, the activation energy of which was estimated at 180 ± 10 meV from the temperature dependence of the PL spectrum. Note that simultaneous with the DAP emission line, a sharp line at 3.325 eV appeared in these samples, tentatively attributed to the As acceptor-bound exciton.[369] In yet another study,[370] the 3.322- and 3.273-eV lines greatly increased with As doping, and the 3.219- and 3.172-eV lines dominated the PL spectrum at the highest chemical concentrations of the As dopant in the low 10^{20}-cm^{-3} range. Ryu *et al.*[370] attributed the 3.359-eV line to the (A^0X) exciton, the 3.322- and 3.273-eV lines to the As-related *e-A* transitions, and the 3.219- and 3.172-eV lines to the DAP transitions. The activation energies of the two As-related acceptors were estimated at 115 and 164 meV.

2. Green luminescence band

The nature of the GL, appearing at about 2.5 eV in undoped ZnO, remained controversial for decades. Although in the early studies it was unambiguously attributed to copper impurities, strong evidence was later presented in favor of the oxygen vacancy (V_O) as the defect responsible for the GL band. The architects of both mechanisms make compelling arguments. The controversy could perhaps be resolved if one assumes that while similar in position and width, these PL bands may actually be of different origins. As it will be shown below, the GL band with a characteristic fine structure is most likely related to the copper impurities, whereas the structureless GL band with nearly the same position and width may be related to a native point defect such as V_O or V_{Zn}.

a. Copper in ZnO. Dingle[371] studied wurtzite *n*-type ZnO crystals containing trace amounts of copper (4 ± 2 ppm), aluminum (<2 ppm), iron, magnesium, silicon, boron, and indium. The PL spectrum obtained in that sample was dominated by a broad GL band peaking at ~2.45 eV and revealing the characteristic fine structure (Fig. 75). The GL band decayed exponentially after a pulse excitation, with the characteristic time of 440 ± 10 ns. The zero-phonon line was composed of two sharp lines (*A* and *B* components) separated by ~0.1 meV (Fig. 76). The ratio of the intensities of the two lines remained constant over the temperature range of 1.6–20.4 K and was independent of the crystal origin.

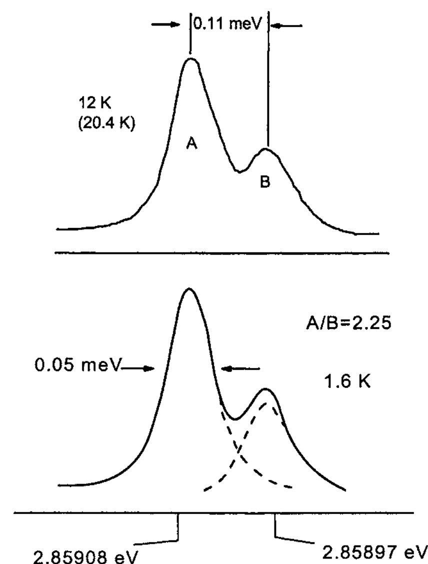

FIG. 76. High-resolution spectra in the region of the zero-phonon line near 2.859 eV. The intensity ratio $A/B=2.25\pm0.05$ is invariant in the temperature range of 1.6–20.4 K. [Reprinted with permission from R. Dingle, Phys. Rev. Lett. **23**, 579 (1969). Copyright 1969 by the American Physical Society.]

Dingle[371] also studied the behavior of these lines and the band as a function of temperature, under uniaxial pressure, magnetic field, and polarized excitation source. The defining information for the identification of the defect responsible for the GL band has been obtained from the splitting of the *A* and *B* lines in applied magnetic field. Each component of the zero-phonon line split into four symmetrically disposed components when the magnetic field was applied parallel or perpendicular to the crystal *c* axis. The Zeeman patterns generated by the *A* and *B* lines were identical, and the following *g* factors have been obtained for both components from analysis of the angle dependence of their splitting in magnetic field: $g_{\parallel}=0.73\pm0.05$ and $g_{\perp}=1.48\pm0.05$. These *g* factors are nearly identical to those obtained from EPR studies of a divalent copper ion Cu^{2+} in a zinc lattice site of ZnO ($g_{\parallel}=0.7383\pm0.0003$ and $g_{\perp}=1.5237\pm0.003$).[372] Moreover, the A/B ratio is in excellent agreement with the ratio of the two naturally abundant Cu isotopes, $Cu^{63}/Cu^{65}=2.24$. All these observations, including the absence of thermalization between the *A* and *B* lines in zero magnetic field, invariance of the A/B ratio in different samples, and identical Zeeman patterns for the *A* and *B* lines, provided the basis for the unequivocal identification of the GL band with its characteristic fine structure as being due to the Cu_{Zn} defect.[371] Dingle has suggested a model whereby in the ground state (in dark) Cu_{Zn} is a neutral acceptor with a hole in the $3d$ shell (electronic configuration $3d^9$). In the excited state (after excitation with light above 2.9 eV), the hole transfers from the *d* shell (which becomes $3d^{10}$) to sp^3 orbitals, where it becomes relatively loosely bound. Dingle assumed that the Cu acceptor ground state must lie above the shallow donor level in *n*-type ZnO, i.e., close to the conduction band. Mollwo *et al.*[373] estimated the energy separation between this level and the bottom of the conduction band as 190 meV, based on their results of electrical conductivity and Hall effect in Cu-doped

[This article is copyrighted as indicated in the article. Reuse of AIP content is subject to the terms at: http://scitation.aip.org/termsconditions. Downloaded to] IP: 128.172.48.58 On: Mon, 19 Oct 2015 20:45:44

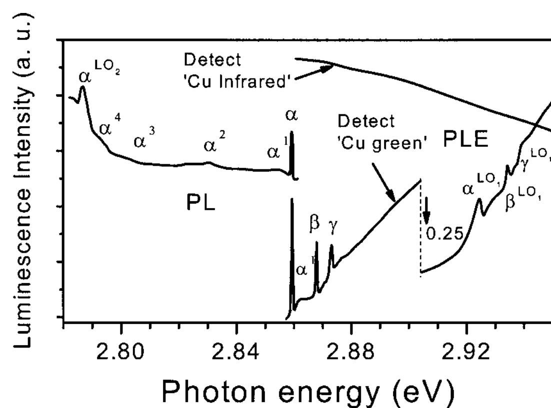

FIG. 77. PL and PLE spectra near the zero-phonon transition of the GL associated with Cu in ZnO. [Reprinted with permission from P. J. Dean, D. J. Robbins, S. G. Bishop, J. A. Savage, and P. Porteous, J. Phys. C: Solid state Phys. **14**, 2847 (1981). Copyright 1981, Institute of Physics.]

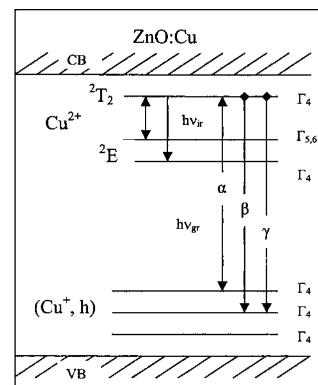

FIG. 78. A schematic diagram of the transitions in ZnO:Cu [after Dahan *et al.* (Ref. 376)].

ZnO. Accounting for the energy of the zero-phonon transition (2.86 eV), the excited state should then have a level at ~0.4 eV above the valence band, and the Bohr radius of the hole in the excited state in the effective-mass approximation should be about 2.4 Å. The luminescence process involves transfer of the Zn–O orbitals to a highly shielded, localized level in the 3*d* shell of the Cu atom.

The details of the ground state of the Cu_{Zn} acceptor in ZnO were established from the EPR and infrared-absorption studies.[372] The low-temperature absorption spectrum of the Cu-doped ZnO contained two sharp lines at 717 and 722 meV. The details of the absorption spectra, the Zeeman splitting in magnetic field, and the EPR data allowed Dietz *et al.*[372] to construct the following model of Cu_{Zn} in ZnO. The free-ion term ^2D of the Cu^{2+} ion is split by the tetrahedral crystal field into the $^2E(D)$ and $^2T_2(D)$ states that in turn are split by a combination of weaker spin-orbit coupling and the trigonal crystal field. At low temperatures, intracenter transitions from the lowest sublevel of the $^2T_2$ state to two sublevels of the ^2E state are responsible for the absorption lines at 717 and 722 meV. Assignment of two components of the line at 717 meV (split by ~0.1 meV) as being due to two isotopes of Cu was confirmed by their transformation into a single line in the crystals doped with only ^{63}Cu isotope. Dietz *et al.*[372] concluded that the Cu^{2+} t_2 wave function is radially expanded (more than *e* wave function) relative to the *d* wave function of the free Cu ion, and the t_2 hole spends about 60% of its time on the Cu^{2+} ion, while it spends the rest of the time in the oxygen sp^3 orbitals. The inverse $^2E(D) \rightarrow {}^2T_2(D)$ transition of the Cu^{2+} ions in ZnO (a zero-phonon line at 717 meV) has been observed under electron-beam excitation at low temperatures.[374]

The excited states of the Cu_{Zn} acceptor in ZnO have been revealed in the absorption and PL excitation (PLE) spectra, namely, a characteristic triplet, α, β, and γ, at 2.8594, 2.8680, and 2.8733 eV, respectively (Fig. 77).[375–378] The α line coincides with the zero-phonon line of the GL.[371] Remarkably, the isotope shift was also observed in the absorption and PLE spectra, at least for the α and β lines.[377] These lines have been attributed to transitions $Cu^{2+}(d^9)+h\nu \rightarrow [Cu^{+}(d^{10}),h]$ in which the excited state is split into three levels, corresponding to three valence bands *a*, *b*, and *c*. A schematic diagram of various transitions in Cu-doped ZnO is shown in Fig. 78. Dahan *et al.*[376] have introduced the concept of intermediately bound excitons to explain the experimental data associated with Cu in ZnO. They suggested that the tenth electron, bound to the Cu *d* shell, has a larger orbit (or swollen wave function) than the other *d*-shell electrons due to hybridization with the Bloch states of the host atoms (the covalent swelling). This tenth electron creates the potential capturing a hole, so that the tenth *d*-shell electron and a loosely bound hole can be considered as an exciton bound to Cu. Intermediately bound excitons are typically formed in crystals with hexagonal wurtzite-type lattice[379] such as ZnO. There are three close levels in the forbidden energy gap for such an exciton in ZnO:Cu according to three split levels of the top of the valence band. During the excitation process, all three excited states of the exciton can be observed, whereas only the lowest one is observed in emission at low temperature (Fig. 78). The theory of the intermediately bound excitons accounts very well the isotope shift and *g* factors of the α, β, and γ lines in ZnO:Cu.[376,377]

Kuhnert and Helbig[380] studied the broad phonon sideband of the GL in ZnO (having maximum at 2.4 eV and FWHM of 0.42 eV). The energy separation between the subsequent peaks is 72 meV, close to a LO-phonon mode of the ZnO crystal. The spectral distribution of the GL band can be described in terms of the one-dimensional configuration coordinate model. The Huang-Rhys factor $S=6.5$ was obtained from the fitting. Later, Reynolds *et al.*[381] also analyzed the phonon-related fine structure of the GL in ZnO, but identified the peak at ~2.26 eV as the zero-phonon line, while attributing the high-energy peaks to hot luminescence. In another work, Reynolds *et al.*[382] suggested that transitions from the two shallow donor states to the same deep level are partially responsible for the fine structure of the GL band. However, this picture is in conflict with the fact that different authors observed the same shape of the GL fine structure in different ZnO samples.[371,375,378,380]

Garces *et al.*,[383] studying PL of a bulk ZnO sample before and after annealing in air at 900 °C for 1 h, observed a remarkable transformation of a broad structureless green band peaking at 500 nm into a structured emission peaking near 510 nm with a structure identical to the Cu-related GL.

[This article is copyrighted as indicated in the article. Reuse of AIP content is subject to the terms at: http://scitation.aip.org/termsconditions. Downloaded to] IP: 128.172.48.58 On: Mon, 19 Oct 2015 20:45:44

These authors suggested that there are two distinct mechanisms giving rise to GL, and both involve Cu impurities but with different stable charge states (Cu^+ and Cu^{2+}) prior to optical excitation. Based on their EPR study of the samples they concluded that the structureless GL of the as-grown ZnO sample is due to DAP recombination between an electron bound to a shallow donor and a hole loosely bound to the Cu^+ ion before annealing, while the structured green emission after the 900 °C annealing was assigned to localized excitation of the isolated Cu^{2+} ion as originally suggested by Dingle.[371]

Alivov *et al.*[384] studied high-quality ZnO single-crystal films doped with copper by thermal diffusion using cathodoluminescence spectroscopy. Doping with copper increased the intensity of the green-emission band of the cathodoluminescence spectrum, whose peak, width, and shape at 78 and 300 K remained unchanged. At 4.2 K, a pronounced phonon structure with a phonon energy of 72 meV was detected in the cathodoluminescence green-emission band of the doped samples. In this case, the phonon peaks feature a triplet fine structure instead of the doublet one generally observed. This feature is attributed to radiative recombination of acceptor excitons that are localized at copper atoms and interact with each one of the subbands of the ZnO valence band. Analysis of the experimental data on the film cathodoluminescence and comparative studies of luminescence and electron-spin resonance in single crystals allowed the authors to conclude that the uncontrollable copper impurity typically existing in ZnO is responsible for green-emission luminescence in this material. Similar transformation of structureless GL band into a structured green emission after Cu doping was observed also by Leiter *et al.*[385] in bulk ZnO crystals.

b. Alternative models of the GL band in ZnO. Structureless GL band in ZnO was attributed also to V_{Zn} acceptor,[359,386–388] a complex defect involving Zn_i,[389] O_{Zn},[390] and V_O.[391–394] Different authors suggested also different types of electron transitions to explain the GL, such as from the V_O donor level located near the conduction band to the valence band (*D-h*-type recombination),[391] from V_O or another donor level to deep V_{Zn} acceptor level (DAP type),[387,388] from conduction band to the V_{Zn} acceptor (*e-A* type),[359] and between two states of V_O (intracenter transition).[393] The earlier notion of V_O in ZnO as being a donor with its 2+/+ and +/0 levels located near the conduction band has been recently reviewed by Van de Walle.[360] This author predicted that V_O in ZnO has only the level (2+/0) at about 2.7 eV above the valence band. Note also that the *D-h*-type recombination is very improbable in *n*-type semiconductor.[395] Moreover, the DAP-type recombination observed in Ref. 388 may not be the same PL band as the others detected since its maximum is at 2.3 eV (shifting to ~2.04 eV after time delay), i.e., in the yellow range.

Remarkable correlations attained between the intensity of the GL band, the concentration of free electrons, and the concentration of the defect identified as V_O at different annealing conditions or oxidation seemingly provided strong arguments in support of the model considering V_O as the defect responsible for the GL band.[391] However, this assignment and interpretation of the experimental results should be

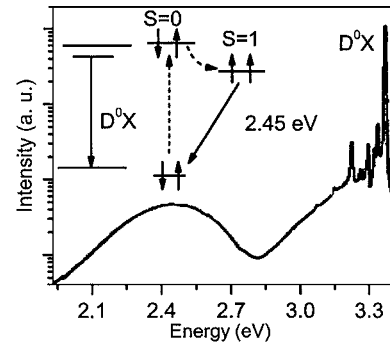

FIG. 79. PL spectrum of undoped ZnO excited with the 325-nm line of a HeCd laser (5 K). The inset shows a recombination model for the GL band peaked at 2.45 eV. [Reprinted with permission from F. H. Leiter, H. R. Alves, A. Hofstaetter, D. M. Hoffmann, and B. K. Meyer, Phys. Status Solidi B **226**, R4 (2001). Copyright 2001, Wiley.]

regarded with caution because Vanheusden *et al.*[391] have also assigned the EPR signal with $g=1.956$ to V_O, and the concentration of V_O was determined from the intensity of this signal. Later it was shown that isotropic EPR signal with $g=1.956$ is related to a shallow donor, whereas EPR signal from V_O is characterized with $g_\parallel=1.984$ and $g_\perp=2.025$.[393] Optically detected magnetic-resonance (ODMR) studies[393] have revealed that the structureless GL band peaking at about 2.45 eV anticorrelates with the isotropic signal at $g=1.956$ and correlates with two resonances (with $g_\parallel=1.984$ and $g_\perp=2.025$) arising from a spin-triplet system ($S=1$). Note that the g values obtained on the structureless GL band[393] and on the GL with a distinct phonon structure[371,383] are incompatible, and thus, these two PL bands are related to different defects. The triplet resonances were detected only in the energy range of the structureless GL band, while the shallow donor signal (with $g=1.956$) quenched the GL band and enhanced emission in the excitonic range. These findings strongly indicate that the shallow donor signal is transferred to the GL band by a shunt process or a spin-dependent energy-transfer mechanism.[393] Leiter *et al.*[393,394] have identified V_O as the defect responsible for the structureless GL band in ZnO, and demonstrated striking similarities of this defect to the anion vacancy in other ionic host crystals: BaO, SrO, CaO, and MgO (F centers). In the model of Leiter *et al.*,[393,394] the two-electron ground state of the neutral V_O is a diamagnetic singlet state. Absorption of a photon transfers the system into a singlet excited state. It relaxes nonradiatively into the emissive, paramagnetic state which can be detected by ODMR (Fig. 79).

3. Yellow luminescence band

Doping ZnO with Li acceptor results in the yellow luminescence (YL) band with a peak at about 2.2 eV and a FWHM of ~0.5 eV.[21] In contrast to the GL band, the YL band decays very slowly after switching off the excitation source, and can be observed also in the thermoluminescence spectrum.[21] Li-doped ZnO is highly resistive due to the deep location of the Li acceptor level (about 0.8 eV above the valence band).[21] The YL is polarized at low temperatures, which was explained by two metastable orientations of the Li_{Zn} center in the ZnO lattice.[21] ODMR studies of the YL

[This article is copyrighted as indicated in the article. Reuse of AIP content is subject to the terms at: http://scitation.aip.org/termsconditions. Downloaded to] IP: 128.172.48.58 On: Mon, 19 Oct 2015 20:45:44

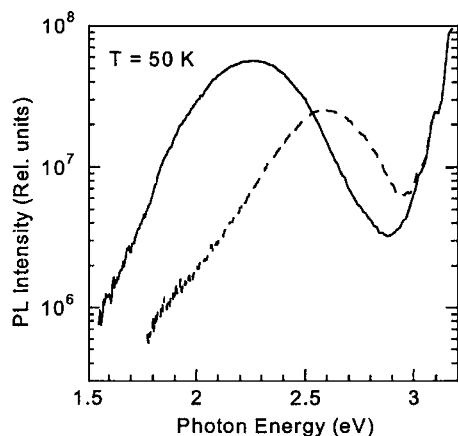

FIG. 80. PL spectrum of undoped bulk ZnO annealed at 150 °C in air for 1 h. The solid (dashed) curve—after (before) HeCd irradiation for 2 h with an excitation density of 0.3 W/cm^2. The excitation density during the measurements was 10^{-3} W/cm^2.

band in ZnO:Li suggest that the DAP-type transitions including a shallow donor and the Li acceptor dominate at low temperatures.[396]

We observed the YL with metastable behavior also in undoped bulk ZnO. Under irradiation with a He–Cd laser, the GL band gradually bleached, while the YL band emerged and eventually replaced the GL band (Fig. 80). The YL band saturated with excitation intensity above 10^{-3} W/cm^2, indicating low concentration of the related defects. The YL was observed also in time-resolved PL experiments. The decay of the YL is nonexponential at low temperature, allowing the possibility of the DAP transitions for this band. The YL band quenched at temperatures above 200 K with the activation energy of about 0.5 eV.

4. Red luminescence band

A red luminescence (RL) band emerged at about 1.75 eV in the PL spectrum of undoped bulk ZnO after it was annealed in air at 700 °C (Fig. 81). The RL band is broad with a FWHM of about 0.5 eV, and its shape is Gaussian. With increasing temperature, the RL band quenches with activation energy of about 15 meV in the range from 15 to 100 K. The quenching of the RL band apparently causes the emergence of the GL band (Fig. 81) This may be a result of competition for holes between the acceptors responsible for the GL and RL bands. At $T > 200$ K, the GL band quenches rapidly, so that the RL band is observed alone at room temperature (Fig. 81). Preliminary results of transient PL demonstrate that the low-temperature PL decay of the RL band is nearly exponential with a characteristic time of about 1 μs.

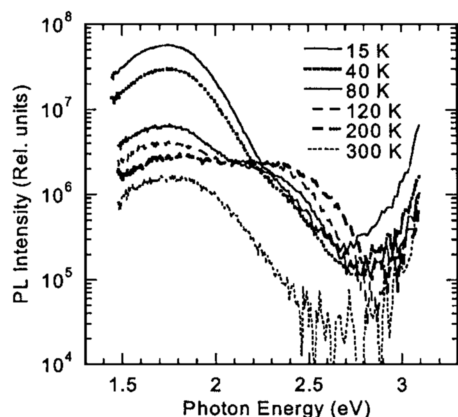

FIG. 81. PL spectrum of undoped bulk ZnO at different temperatures. The sample was annealed at 700 °C in air for 1 h. The excitation density is 10^{-3} W/cm^2.

VI. DOPING OF ZnO

ZnO has a strong potential for various short-wavelength optoelectronic device applications. In order to attain the potential offered by ZnO, both high-quality *n*- and *p*-type ZnO are indispensable. However, difficulty in bipolar carrier doping (both *n* and *p* types) is a major obstacle as seen in other wide-band-gap semiconductors such as GaN and II-VI compound semiconductors including ZnS, ZnSe, and ZnTe.[397–402] Unipolar doping has not been a surprising issue in wide-band-gap semiconductors: ZnO, GaN, ZnS, and ZnSe are easily doped to *n*-type, while *p*-type doping is difficult. The situation is opposite for ZnTe where *p*-type doping is easily obtained, while *n*-type doping is difficult.

A. *n*-type doping

ZnO with a wurtzite structure is naturally an *n*-type semiconductor because of a deviation from stoichiometry due to the presence of intrinsic defects such as O vacancies (V_O) and Zn interstitials (Zn_i). Undoped ZnO shows intrinsic *n*-type conductivity with very high electron densities of about 10^{21} cm^{-3}.[400] Although it is experimentally known that unintentionally doped ZnO is *n* type, whether the donors are Zn_i and V_O is still controversial. The first-principles study suggested that none of the native defects show high-concentration shallow donor characteristics.[359] However, Look *et al.*[146] suggested that Zn_i rather than V_O is the dominant native shallow donor in ZnO with an ionization energy of about 30–50 meV. It has also been suggested that the *n*-type conductivity of unintentionally doped ZnO films is only due to hydrogen (H), which, as was treated above (Sec. V), acts as a shallow donor with an ionization energy about 30 meV.[359,360,403,404] This assumption is valid since hydrogen is always present in all growth methods and can easily diffuse into ZnO in large amounts due to its large mobility. First-principles calculations also suggested that unintentionally incorporated hydrogen acts as a source of conductivity and behaves as a shallow donor in ZnO.[124]

n-type doping of ZnO is relatively easy compared to *p*-type doping. Group-III elements Al, Ga, and In as substitutional elements for Zn and group-VII elements Cl and I as substitutional elements for O can be used as *n*-type dopants.[405] Doping with Al, Ga, and In has been attempted by many groups, resulting in high-quality, highly conductive *n*-type ZnO films.[406–412] Myong *et al.*[406] grew Al-doped ZnO films by photoassisted MOCVD method and obtained highly conductive films with a minimum resistivity of 6.2×10^{-4} Ω cm. Ataev *et al.*[407] reported resistivities as low as 1.2×10^{-4} Ω cm for Ga-doped ZnO films grown by chemical-vapor deposition. Ko *et al.*[411] also succeeded in Ga doping of ZnO films grown on GaN templates by plasma-

[This article is copyrighted as indicated in the article. Reuse of AIP content is subject to the terms at: http://scitation.aip.org/termsconditions. Downloaded to] IP: 128.172.48.58 On: Mon, 19 Oct 2015 20:45:44

TABLE XVII. Calculated nearest-neighbor bond lengths, the defect energy levels (E_i) for negatively charged substitutional impurities, and the energy (ΔE) required to form the positively charged *AX* center from the substitutional acceptors [Park *et al.* (Ref. 419)].

	Element	Bond length (Å)	E_i (eV)	ΔE
	Li	2.03	0.09	0.21
Group I	Na	2.10	0.17	1.04
	K	2.42	0.32	1.38
	N	1.88	0.40	0.13
Group V	P	2.18	0.93	–0.46
	As	2.23	1.15	–0.18

assisted MBE. Thus, *n*-type doping of ZnO is developed very well. Such films are successfully used in various applications as *n*-type layers in light-emitting diodes as well as transparent Ohmic contacts as will be discussed below.

B. *p*-type doping

As mentioned repeatedly it is very difficult to obtain *p*-type doping in wide-band-gap semiconductors, such as GaN and ZnSe. The difficulties can arise from a variety of causes. Dopants may be compensated by low-energy native defects, such as Zn_i or V_O,[413] or background impurities (H). Low solubility of the dopant in the host material is also another possibility.[414] Deep impurity level can also be a source of doping problem, causing significant resistance to the formation of shallow acceptor level.

Known acceptors in ZnO include group-I elements such as lithium (Li),[21,415,416] Na, and K, copper (Cu),[417] silver (Ag),[418] Zn vacancies, and group-V elements such as N, P, and As. However, many of these form deep acceptors and do not contribute significantly to *p*-type conduction. It has been believed that the most promising dopants for *p*-type ZnO are the group-V elements, although theory suggests some difficulty in achieving shallow acceptor level.[419]

A number of theoretical studies have addressed the fundamental microscopic aspects of doping in wide-band-gap semiconductors. The majority of these studies have dealt with the manner in which dopant solubility[397,420] or native defects[421,422] such as vacancies, interstitials, and antisites interfere with doping. Recently, various substitutional impurities for ZnO were examined as *p*-type dopants by using the first-principles pseudopotential method.[419,423,424]

p-type doping in ZnO may be possible by substituting either group-I elements (Li, Na, and K) for Zn sites or group-V elements (N, P, and As) for O sites. It was shown that group-I elements could be better *p*-type dopants than group-V elements in terms of shallowness of acceptor levels as shown in Table XVII.[419] However, group-I elements tend to occupy the interstitial sites, in part mitigated by their small atomic radii, rather than substitutional sites, and therefore, act mainly as donors instead.[425] Moreover, significantly larger bond length for Na and K (see Table XVII) than ideal Zn–O bond length (1.93 Å) induces lattice strain, increasingly forming native defects such as vacancies which compensate the very dopants. These are among the many causes leading to difficulties in attaining *p*-type doping in ZnO. A similar behavior is observed for group-V elements except for N. Both P and As also have significantly larger bond lengths and, therefore, are more likely to form antisites to avoid the lattice strain. The antisites, A_{Zn}, are donorlike and provide yet another unwelcome possible mechanism for compensating acceptors. It then appears that perhaps the best candidate for *p*-type doping in ZnO is N because among the group-V impurities, N has the smallest ionization energy, it does not form the N_{Zn} antisite, and the *AX* center of N is only metastable.[419]

Kobayashi *et al.*[426] also predicted that N is a good candidate for a shallow *p*-type dopant in ZnO although N is not very soluble in ZnO, suggesting that N doping can be achievable by ion implantation. Somewhat related to the current topic, Wu *et al.*[427] have demonstrated shallow N acceptors in N^+-implanted ZnSe using PL measurements. It is now well known that reactive N produced *p*-type ZnSe which led to demonstration of laser diodes before supplanted by GaN-based diode lasers.[428] However, *p*-type doping of ZnO has not been successful using pure nitrogen source,[429] while acceptor concentrations as high as 10^{18} cm^{-3} have been obtained for ZnSe using an N_2 plasma source.[430] This implies that N acceptors are more readily compensated in ZnO as compared to ZnSe.

1. Nitrogen doping

Helped by success with ZnSe nitrogen has been explored for *p*-type doping of II-VI semiconductors.[430–432] A number of groups have expended a good deal of effort in an attempt to realize *p*-type ZnO using nitrogen (N) as a possible shallow acceptor dopant. Various types of nitrogen sources including N_2, NO, N_2O, NH_3, and Zn_3N_2 have been used depending on the growth technique, as elaborated on below.

Iwata *et al.*[433] have attempted *p*-type doping of ZnO using MBE by simultaneously introducing O_2 and N_2 through a rf plasma source. Although a nitrogen concentration as high as 10^{19} cm^{-3} was obtained, conduction-type conversion from *n*-type to *p*-type did not occur. However, some promising results were reported recently. Look *et al.*[365] reported *p*-type ZnO by MBE with N doping (performed by Eagle Picher) using Li-diffused semi-insulating ZnO substrates and an N_2 rf plasma source. Nitrogen-surface concentration (10^{19} cm^{-3}) in the N-doped ZnO film measured by secondary-ion-mass spectroscopy (SIMS) was two orders of magnitude higher than that in undoped ZnO, implying the presence of high doping. The N-doped ZnO showed *p*-type behavior with a hole concentration of 9×10^{16} cm^{-3} and a hole mobility of 2 cm^2/V s. The PL spectrum of Fig. 82 shows a strong peak near 3.32 eV probably due to neutral-acceptor-bound excitons. The estimated acceptor level was between 170 and 200 meV based on the low-temperature PL measurements.

Ashrafi *et al.*[434] also used nitrogen as a *p*-type dopant in conjunction with H_2O vapor as an oxygen source in metal-organic MBE. Thermal annealing increased the net acceptor concentration (N_A-N_D) by approximately two orders of magnitude ($\sim5\times10^{16}$ cm^{-3}). Ashrafi *et al.* observed *p*-type conductivity in spite of higher H concentration than that of N, suggesting that H may be more closely correlated to

[This article is copyrighted as indicated in the article. Reuse of AIP content is subject to the terms at: http://scitation.aip.org/termsconditions. Downloaded to] IP: 128.172.48.58 On: Mon, 19 Oct 2015 20:45:44

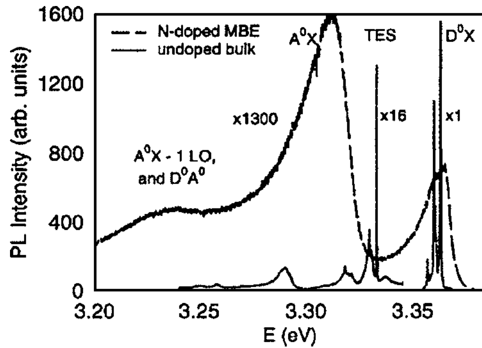

FIG. 82. PL spectra, at 2 K, for two ZnO samples, an undoped bulk sample and a N-doped, MBE-grown epitaxial layer. [Reprinted with permission from D. C. Look, D. C. Reynolds, C. W. Litton, R. L. Jones, D. B. Eason, and G. Cantwell, Appl. Phys. Lett. **81**, 1830 (2002). Copyright 2002, American Institute of Physics.]

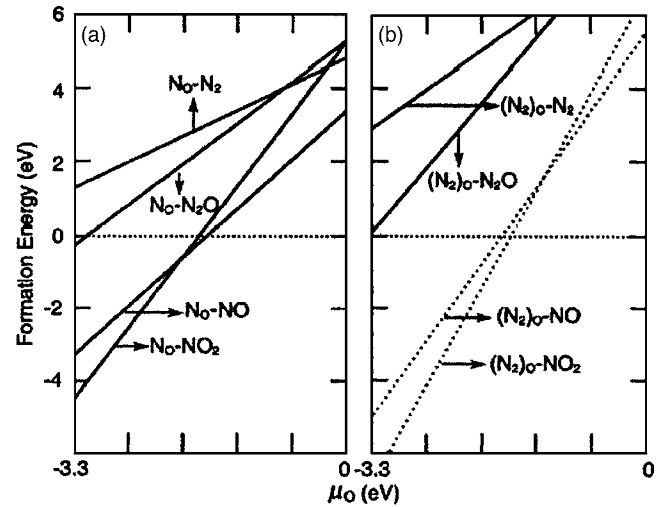

FIG. 83. (a) Calculated formation energies of N_O as functions of the O chemical potential formed by atomic N (stripped off a N_2 or a N_2O molecule), NO, or NO_2 molecule. $\mu_O=-3.3$ is the Zn-rich limit condition and $\mu_O=0$ is the O-rich limit condition. (b) Calculated formation energies of a $(N_2)_O$ as functions of the O chemical potential for the defects formed by N_2, N_2O, NO, and NO_2 molecules. [Reprinted with permission from Y. Yan, S. B. Zhang, and S. T. Pantelides, Phys. Rev. Lett. **86**, 5723 (2001). Copyright 2001 by the American Physical Society.]

p-type conductivity rather than being simply a shallow donor or causing passivation, as the theory suggests.

Several groups obtained *p*-type ZnO films by adding NH_3 in O_2 or H_2 gas as a nitrogen source. Minegishi *et al.*[435] reported the growth of *p*-type ZnO using chemical-vapor deposition (CVD). The NH_3 gas was simultaneously added in the hydrogen carrier gas with excess Zn. The resistivity of the resulting films was high (100 Ω cm), suggesting that the acceptor level is relatively deep with a subsequent low free-hole concentration. Ye *et al.*[436] also used NH_3 as the nitrogen source for dc reactive magnetron sputtering of *p*-type ZnO. Results show a hole concentration of 3.2×10^{17} cm^{-3} and a resistivity of 35 Ω cm. Ye *et al.* proposed that the excess zinc and interstitial hydrogen play an important role in *p*-type doping as suggested by Ashrafi *et al.*[434] However, the role of hydrogen in N-doped ZnO was explained somewhat differently by Wang *et al.*[437] They argued that when NH_3 increases in the MOCVD chamber, more hydrogen atoms are absorbed onto the substrate surface and introduced in the film due to the O–H bond which is stronger than the Zn–N bond, resulting in a decrease in the nitrogen concentration.

Lu *et al.*[438] investigated *p*-type ZnO growth as a function of ammonia concentration in NH_3–O_2 ambient using dc reactive magnetron sputtering. While N-doped *p*-type ZnO films were achieved at ammonia concentration of 25%–75%, intrinsic ZnO film and zinc polycrystal film were obtained at 0% and 100% ammonia concentrations, respectively. It cannot be understated that despite reports of *p*-type conductivity, the issue is still controversial. Much of the problem arises from very low mobilities in Hall experiments and a good deal of carrier localization in these ZnO films doped with impurities thought to lead to *p*-type doping. The reference to *p*-type conductivity here merely reflects what has been reported, and nothing more. At 50% ammonia concentration, better electrical properties were obtained: hole concentration of 7.3×10^{17} cm^{-3}, hole mobility of 1.3 cm^2/V s, and resistivity of 31 Ω cm. The results showed that the nitrogen incorporation in ZnO is increased in the presence of NH_3, enhancing the hole concentration. However, when ammonia concentration is high (100%), the densities of V_O and Zn_i are increased due to absence of O_2 in ambient, resulting in zinc polycrystalline film.

One chain of thought is that to attain *p*-type ZnO through N doping it may be necessary to provide oxygen also to suppress oxygen vacancy V_O. One approach could be to use an O_2/N_2 mixture. However, at least in one instance, such an effort did not turn out successful and *p*-type conductivity was not obtained, even though various ratios of O_2/N_2 were employed.[439]

As a nitrogen source some researchers used N_2O gas, which is a mild oxidizing gas (stronger than O_2 and weaker than NO_2 as an oxidizing agent). Very pertinent to the topic of discussion is that the dissociation energy (N–N: 5.16 eV and N–O: 6.37 eV) and ionization potential (N_2O: 12.9 eV) of N_2O are lower than those of N_2 (N–N: 9.76 eV and N_2: 15.65 eV).[440] In this vein, Guo *et al.*[440] used N_2O plasma for nitrogen doping of ZnO film by PLD. They found that nitrogen doping was enhanced using the active N formed by N_2O gas flowing through an electron-cyclotron-resonance (ECR) source. The samples showed *p*-type conductivity with a hole concentration in the range of 3×10^{18}–6×10^{18} cm^{-3}, resistivity in the range of 2–5 Ω cm, and hole mobility in the range of 0.1–0.4 cm^2/V s.

Based on first principles Yan *et al.*[441] proposed that the nitric oxide (NO) gas without an ECR plasma source is more efficient as a N source than N_2O or N_2. The model indicated that the defect formation energy of N on oxygen site, N_O, from NO should be lower than that from N_2O. As shown in Fig. 83 the formation energy of N_O is negative under Zn-rich conditions, implying that no additional energy is required for N_O formation, while the formation energy of N_O from N_2 is positive, suggesting that additional energy is needed (e.g., plasma or high temperature). Even though the formation energy of N_O from N_2O is negative, the energy is much larger than that from NO. Therefore, it was suggested that NO molecules can be incorporated spontaneously to form N_O defects in ZnO.

[This article is copyrighted as indicated in the article. Reuse of AIP content is subject to the terms at: http://scitation.aip.org/termsconditions. Downloaded to] IP: 128.172.48.58 On: Mon, 19 Oct 2015 20:45:44

Wang *et al.*[442] attempted nitrogen doping in ZnO films by plasma-assisted MOCVD using diethyl zinc (DEZn) and N_2 gas, but *p*-type behavior was not obtained. However, Li *et al.*[443,444] claimed to have succeeded in *p*-type doping of ZnO films, by reacting DEZn with NO gas. In this case, NO gas was used to supply both O and N for *p*-type doping. Results indicated that N can be incorporated into ZnO films without plasma or high-temperature process and a high N concentration was obtained only under Zn-rich conditions as predicted by Yan *et al.*[441] It should be stated that N does indeed incorporate as an acceptor. However, a sufficient amount of acceptors should be generated to overcome the *n*-type background or any other donorlike defects introduced through parasitic processes.

As discussed earlier, the solubility of nitrogen in ZnO is low and N from NO is more efficiently incorporated into ZnO than that from N_2. However, a different approach for growing N-doped *p*-type ZnO films was reported in Ref. 445. *p*-type ZnO was obtained after thermal annealing of zinc oxynitride (ZnON) alloy films deposited by rf reactive magnetron sputtering. The samples were grown at a relatively low substrate temperature of 200 °C compared to others[436,438] and were subjected to postgrowth thermal annealing, resulting in the transformation from ZnON alloy to ZnO. In this case, annealing at a temperature of 600 °C led to *p*-type behavior of the films. Further increase of the annealing temperature to 1000 °C in oxygen ambient eliminated all the N dopants and replaced them by O even though the crystalline quality was improved. Results indicated that there is a tradeoff between N-doping efficiency and crystalline quality.

Lin *et al.*[446] obtained what has been referred to as *p*-type ZnO by nitrogen-ion implantation of ZnO films grown on Si substrates with SiN buffer layers using rf magnetron sputtering. The *p*-type ZnO films implanted with $5\times10^{12}-1\times10^{14}$ cm^{-2} N^+ dose showed good electrical properties (hole concentration of $5.0\times10^{16}-7.3\times10^{17}$ cm^{-3}, hole mobility of 2.51–6.02 cm^2/V s, and resistivity of 10.1–15.3 Ω cm).

While most studies on N-doped *p*-type ZnO have been based on deposition methods, other approaches such as oxidation have been attempted as well. N-doped ZnO was obtained by oxidizing Zn_3N_2 films, which were deposited by dc magnetron sputtering.[447] A sample oxidized at 500 °C showed *p*-type characteristics with a hole concentration of 5.8×10^{18} cm^{-3}. However, oxidization at a higher temperature of 550 °C resulted in *n*-type conductivity which was stated to be due to insufficient N atoms to form N acceptors.

Enhancement of N doping in ZnO by thermal treatment has been undertaken. Garces *et al.*[448,449] observed the formation of nitrogen acceptors in N-doped ZnO crystals using photoinduced electron-paramagnetic-resonance (EPR) method after annealing in air or nitrogen atmosphere at a temperature range of 600–900 °C. The pathway for this was reported to be due to nitrogen substitution for the shallow impurity donors during the thermal treatment.

Solid-source chemical-vapor deposition[450] (SS-CVD) was also used for nitrogen doping of ZnO. Zinc acetate dihydrate [$Zn(CH_3COO)_2\cdot2H_2O$, solid] and ammonium acetate (CH_3COONH_4, solid) were used as the precursor and the nitrogen source, respectively. The samples showed *p*-type conductivity with a hole concentration of 9.8×10^{17} cm^{-3}, resistivity of 20 Ω cm, and hole mobility of 0.97 cm^2/V s.

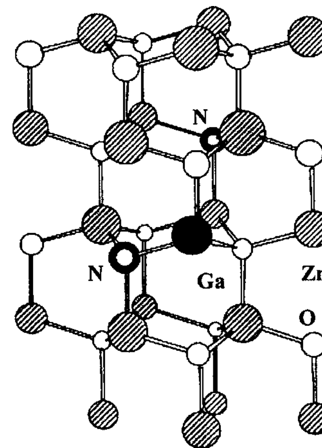

FIG. 84. Crystal structure of a supercell for ZnO:(Ga, 2N). [Reprinted from T. Yamamoto, Thin Solid Films **420–421**, 100 (2002), Copyright 2002, with permission from Elsevier.]

Despite the above-mentioned reports on successful growth of *p*-type ZnO films by N doping, there were also a number of reports in which the authors were not able to reproduce these results even when the same growth methods, growth conditions, and N precursors were used.[440,451–453] Therefore, even if one assumes that the reported results represent truly *p*-type ZnO, the reproducibility still remains to be a major problem, and this must be solved before ZnO can be used in optoelectronics applications such as homojunction LEDs and laser diodes (LDs). Finally, until ZnO *p-n* junctions with at least good injection efficiencies are attained, questions will be raised.

2. Codoping method: Nitrogen+group III

Although nitrogen has been considered as the best candidate for *p*-type doping for ZnO, it is well known that the solubility of N in ZnO is low. Therefore, it is necessary to find methods which can enhance the solubility limit of N in ZnO. For this purpose, a donor-acceptor codoping method has been proposed in order to realize highly conducting *p*-type ZnO,[454,455] and the experimental studies based on this approach have been performed.[456–462]

Recently, Yamamoto and Katayama-Yoshida[454] proposed the codoping method to solve the unipolarity in ZnO based on *ab initio* electronic band-structure calculations. The enhancement in solubility to a level well above the solubility limit was explained in terms of the formation of ion pairs between donor and acceptor ions and a consequent reduction in the Madelung energy. While the Madelung energy decreases with group-III elements (Al, Ga, and In) for *n*-type doping, it increases with group-V element N for *p*-type doping, indicating localization of the N states.

Figure 84 shows the crystal structure of supercells for ZnO:(Ga, 2N) and the formation of complexes, III-N pairs, which occupy the nearest-neighbor sites and the next-nearest-neighbor sites based on *ab initio* total-energy calculations. It is also indicated that there were no stable configu-

[This article is copyrighted as indicated in the article. Reuse of AIP content is subject to the terms at: http://scitation.aip.org/termsconditions. Downloaded to] IP: 128.172.48.58 On: Mon, 19 Oct 2015 20:45:44

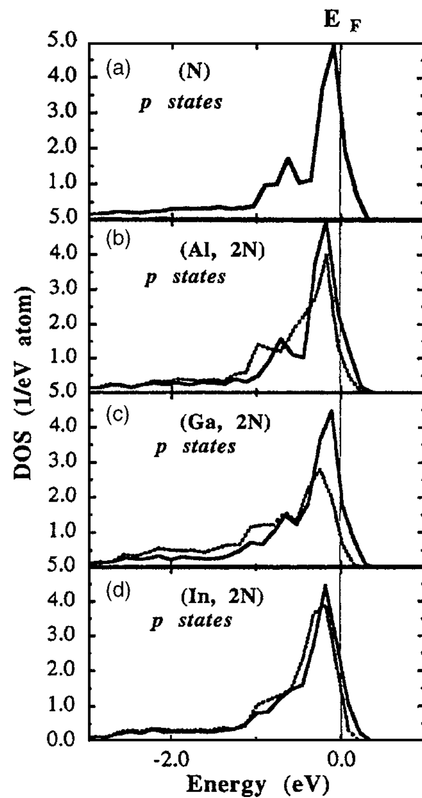

FIG. 85. Site-decomposed DOS of p states at the N sites for (a) ZnO:N, (b) ZnO:(Al, 2N), (c) ZnO:(Ga, 2N), and (d) ZnO:(In, 2N). The dotted curve indicates the DOS at the N atom sites close to the reactive donor codopant; the solid curve indicates the DOS at the sites of next-nearest-neighbor N atoms. [Reprinted from T. Yamamoto and H. Katayama-Yoshida, J. Cryst. Growth **214/215**, 552 (2000), Copyright 2000, with permission from Elsevier.]

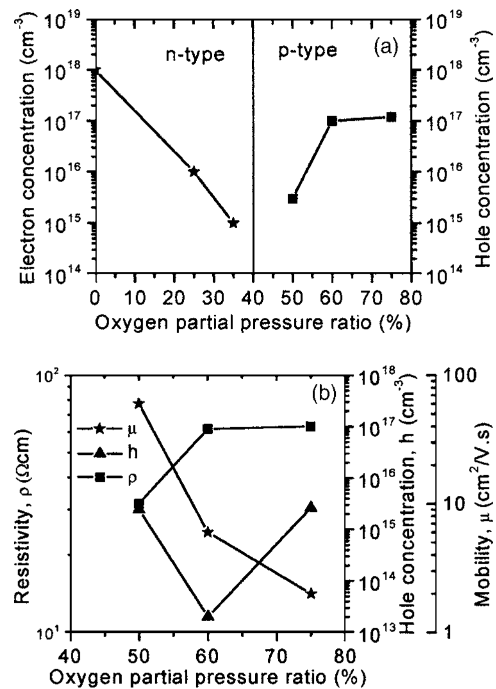

FIG. 86. (a) Effect of oxygen partial pressure ratio on conduction type of codoped ZnO films. (b) Hole concentration, resistivity, and Hall mobility as a function of oxygen partial pressure. [Reprinted with permission from A. V. Singh, R. M. Mehra, A. Wakahara, and A. Yoshida, J. Appl. Phys. **93**, 396 (2003). Copyright 2003, American Institute of Physics.]

rations for ZnO:2N with the same N concentration, holding out the possibility that N incorporation can be enhanced with the group-III elements.

It is reported that codoping of N with the reactant dopants lowers the acceptor level in the band gap due to strong interaction between N acceptors and reactive donor codopants. As shown in Figs. 85(b)–85(d) the shift of the DOS peak toward the top of the valence band implies that the acceptor levels are lowered. Yamamoto and Katayama-Yoshida[454] also proposed the codoping with Li as an acceptor with F as reactive donor codopants for the growth of low-resistivity p-type ZnO.

A SIMS study on the solubility limits of Ga and N in ZnO showed the enhancement of N solubility limit in coimplanted ZnO by a factor of 400 as compared to that in N-implanted ZnO. Using the codoping method, Joseph *et al.*[463] successfully grew what was termed as p-type ZnO films by a PLD system combined with a plasma gas source. For Ga and N codoping, N_2O gas was used as the nitrogen source instead of N_2 gas, since N_2O gas is effective in suppressing oxygen vacancies, and introduce N as an acceptor simultaneously. p-type conductivity was confirmed using Hall and Seebeck coefficient measurements with a resistivity of 0.5 Ω cm, a carrier concentration of 5×10^{19} cm^{-3}, and a very low mobility of 0.07 cm^2/V s. The very low mobility brings the p-type conductivity in question. It was also indicated that low-temperature formation is essential for nonequilibrium growth in the codoping technique. Although p-type conductivity was observed in codoped ZnO films, the origin of p-type characteristics is not clear due to the lack of characterization, such as the donor and acceptor levels in the band gap for the Ga and N dopants.

Ohshima *et al.*[459] have attempted to synthesize p-type ZnO by PLD using various codoping methods including the ablation of ZnO:Ga target in NO gas, and Al and N codoping using an ion gun and a microwave ECR source. Although they could identify the presence of Ga–N bond in ZnO, p-type ZnO film could not be obtained.

It was reported that the types of conductivity and carrier concentration in Ga and N codoped ZnO are dependent on the O_2 partial pressure in the sputtering gas mixture. Singh *et al.*[464] observed n-type conduction for deposited films for oxygen partial pressures between 0% and 40%. The conduction type of films deposited in the 40%–50% oxygen partial pressure range was not clearly identifiable due to large resistivity. But the films deposited with partial pressures higher than 50% showed p-type conduction. Assuming that the p-type conductivity is real, this dependence of the conduction type on oxygen partial pressure showed the important role of oxygen vacancies in the type of conductivity achieved. Thus, as the O_2 partial pressure increases, V_O and Zn_i are suppressed or the background donor concentration is insufficient to compensate the acceptors from N substitution in ZnO, paving the way for p-type conduction [see Fig. 86(a)]. When the O_2 partial pressure ratio was increased from 50% to 60%, the mobility and resistivity decreased while the hole concentration increased, as shown in Fig.

[This article is copyrighted as indicated in the article. Reuse of AIP content is subject to the terms at: http://scitation.aip.org/termsconditions. Downloaded to] IP: 128.172.48.58 On: Mon, 19 Oct 2015 20:45:44

86(b). However, further increase in the O_2 partial pressure ratio caused a decrease in the mobility and an increase in the resistivity, probably because of the degradation of crystal quality due to oxygen-induced defects.

There were also reports on codoping experiments in which indium[465] (In) and aluminum[466] (Al) were used as group-III codoping metals. In codoping studies with In ultrasonic ultraspray pyrolysis method was used for growth. The aqueous solutions $Zn(CH_3OO)_2 \cdot H_2O$ (AR, 0.5 mol/l), $(CH_3OONH_4)_2$ (AR, 2.5 mol/l), and $In(NO)_3$ (AR, 0.5 mol/l) were used as the sources of the Zn, N, and In, respectively. The grown *p*-type ZnO films had low film resistivity ($1.7 \times 10^{-2}\ \Omega$ cm), high hole concentration (2.44×10^{18} cm^{-3}), and incredibly high hole mobility (155 cm^2/V s) which brings the validly of these results into question. Al+N codoping was performed during growth of ZnO films in a N_2O+O_2 atmosphere on glass substrates by dc reactive magnetron sputtering. At a substrate temperature of 500 °C, *p*-ZnO was realized with hole densities as large as 1.1×10^{17} cm^{-3}.

In other codoping experiments, however,[457,458,461] no *p*-type conductivity was observed even though a N concentration as high as 2×10^{20} cm^{-3} was obtained in ZnO. However, such codoped ZnO layers in these experiments exhibited a dramatic increase (by eight to nine orders of magnitude) in resistivity. The formation of N–Ga–N acceptor centers in the samples was suggested to be the reason.

3. Other dopants in group V

While most efforts on *p*-type doping of ZnO have focused on nitrogen doping with/without codopants because of its relatively shallow level, considerably fewer studies have considered other group-V elements for substitutional doping on the O sites[370,467–472] Only in some of these studies inversion of the film's conductivity type was observed.

Aoki *et al.*[467] used the PLD technique to produce phosphorus-doped *p*-type ZnO films using a zinc-phosphide (Zn_3P_2) compound as the phosphorus source. In this process, a Zn_3P_2 film deposited on a ZnO substrate was exposed to excimer laser radiation in high-pressure nitrogen or oxygen ambient and was consequently decomposed into Zn and P atoms which diffuse into ZnO, resulting in the formation of P-doped ZnO through the replacement of O atoms by P atoms. In this case, a *p-n*-junction-like behavior was observed between an *n*-type ZnO substrate and a surface P-doped layer although Hall measurements did not confirm *p*-type conductivity. Similar results were obtained by Lee *et al.*[473] who also transformed a Zn_3P_2 layer on ZnO/sapphire to *p*-type ZnO by laser annealing.

Recently, Kim *et al.*[468] reported that a phosphorus-doped *n*-type ZnO film grown by rf sputtering using P_2O_5 as the phosphorus source led to *p*-type ZnO by thermal annealing at a temperature above 800 °C in N_2 ambient (Fig. 87). During the thermal activation of dopants, P_2O_5 dissociates and consequently the phosphorus atoms act as acceptors and oxygen atoms may compensate oxygen vacancies which otherwise would act as compensating donors. The ZnO films showed *p*-type behavior with a hole concentration of 1.0×10^{17}–1.7×10^{19} cm^{-3}, a mobility of 0.53–3.51 cm^2/V s, and a low resistivity of 0.59–4.4 Ω cm. The PL spectrum showed a strong peak at 3.35 eV, which is probably due to neutral-acceptor-bound excitons as observed by Look *et al.*[425] Afterwards such *p*-type ZnO films were grown on *n*-type GaN to fabricate *p*-ZnO-/*n*-GaN-type heterostructures.[474] Quite good *p-n* heterojunctions and electroluminescense properties were observed.

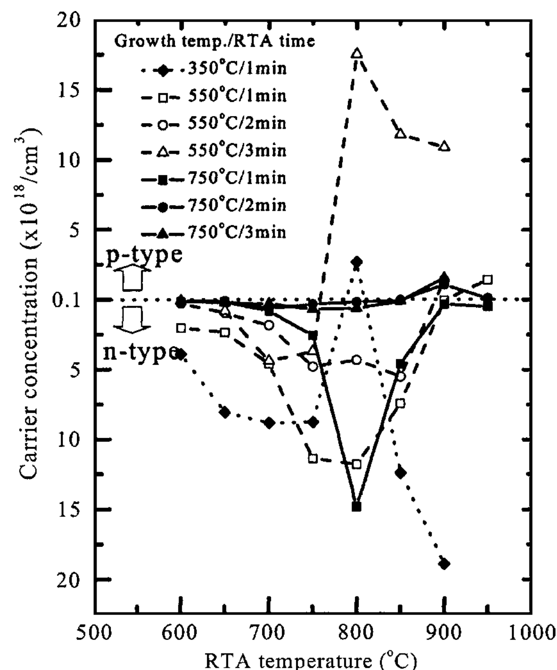

FIG. 87. Carrier concentration of phosphorus-doped ZnO thin films treated by RTA [Reprinted with permission from K.-K. Kim, H.-S. Kim, D.-K. Hwang, J.-H. Lim, and S.-J. Park, Appl. Phys. Lett. **83**, 63 (2003). Copyright 2003, American Institute of Physics.]

Another group was unsuccessful in achieving *p*-type ZnO using phosphorus;[472] however, they recently demonstrated *p*-type behavior in P-doped ZnMgO layers grown by pulsed-laser deposition.[475] The different behavior of phosphorus in ZnO and ZnMgO layers is still not clear. Phosphorus-doped $Zn_{0.9}Mg_{0.1}O$ targets were fabricated using high-purity ZnO (99.9995%) and MgO (99.998%), with P_2O_5 (99.998%) serving as the doping agent. The majority-carrier-type was determined from capacitance-voltage characteristics of metal-insulator-semiconductor devices fabricated, and the hole concentration and mobility were estimated to be 2×10^{18}/cm^3 and 0.01–0.001 cm^2/V s, respectively. Minority-carrier transport properties of *p*-$Zn_{0.9}Mg_{0.1}O$ were studied by employing electron-beam-induced current and cathodoluminescence methods,[476] and the electron diffusion length and lifetime were found to be ~2.12 μm and ~34 ns, respectively. Both of these values increased after electron-beam irradiation. Using these *p*-type layers $Zn_{0.9}Mg_{0.1}O$/ZnO *p-n* junctions were fabricated with good rectifying diodelike current-voltage characteristics.[475,477]

Ryu *et al.*[469] employed GaAs substrates as an arsenic source for *p*-type doping of ZnO by PLD. In this case, a *p*-type ZnO layer was produced at the ZnO/GaAs interface after thermal annealing. Recently, *p*-type ZnO films were grown on different substrates, ZnO, SiC, and sapphire, rather

[This article is copyrighted as indicated in the article. Reuse of AIP content is subject to the terms at: http://scitation.aip.org/termsconditions. Downloaded to] IP: 128.172.48.58 On: Mon, 19 Oct 2015 20:45:44

than GaAs, and As was supplied from an effusion cell in the PLD system. Thus, the postannealing process was not necessary in order to diffuse As into the ZnO film.[470,471]

As a conclusion to this section we can state that despite of a large number of recent reports on *p*-type ZnO growth by various methods,[50] no reproducible high-quality *p*-type layers are available yet. Further efforts to solve this problem are needed. In particular, careful analysis of the experimental data (particularly the interpretation of the Hall data in cases of very low Hall mobilities), better understanding of the physical properties of point defects in ZnO, and development of some unconventional methods would be useful.

VII. ZnO-BASED DILUTE MAGNETIC SEMICONDUCTORS

The III-V and II-VI diluted magnetic semiconductors (DMSs) have attracted considerable attention because the spin-dependent magnetic phenomena can be manipulated in these low-dimensional tailored magnetic thin films for various spin-based devices to unprecedented capabilities.[478] Generally, $3d$ transition-metal ions (some species of magnetic ions, i.e., ions bearing a net magnetic moment) are substituted for the cations of the host semiconductors. As a consequence, the electronic structure of the substituted $3d$ transition-metal impurities in semiconductors is influenced by two competing factors: strong $3d$-host hybridization and strong Coulomb interactions between $3d$-$3d$ electrons. The latter is responsible for the multiplet structures observed in d-d optical-absorption spectra. On the other hand, as specifically shown for the Mn-doped systems the hybridization between the transition-metal $3d$ and the host valence band gives rise to the magnetic interaction between the localized $3d$ spins and the carriers in the host valence band.[479]

With the significant advance of the materials engineering of thin-film and nanoscale heterostructures, the quantized energy levels in semiconductor nanostructures can be coupled either with local magnetic fields created by integrated submicron ferromagnetic structures or with the exchange fields of magnetic ions into the semiconductor lattice itself, hence providing a foundation for quantum spin devices[480] including single-electron spin transistors that rely on spin-dependent tunneling into a magnetic quantum dot (QD) and magnetic field-effect transistor (M-FET) that employ injection of spin-polarized carriers into transport channels.[481]

The observation of ferromagnetic transitions in III-V and II-VI semiconductors at high temperature (Curie temperature >100 K)[482–490] has attracted a great deal of attention recently. Demonstration of long spin-coherence time in semiconductors[491] and rapid development of the information storage technology using ferromagnetic metals have heightened the research activities in this field. As semiconductors have many potential advantages over metals because they can be easily manipulated to form an appropriate heterostructure with impurities, the actual fabrication of ferromagnetic semiconductors that work at room temperature remains very attractive for device applications. The recent discussion of ferromagnetism, albeit controversial, at temperatures much higher than the room temperature in (Ga,Mn)N,[492] (Zn,Mn)O,[488] (Zn,Co)O,[485,487,489,490] and (Zn,V)O (Ref. 486) has fueled hopes that these materials will indeed have profound technological impact.

If accomplished, above room-temperature ferromagnetism could form the basis for charge, spin-based, or mixed spin- and charge-based devices. The devices utilizing spin in one form or another fall into a newly coined nomenclature, spintronics. Spintronics is a paradigm in which the spin degree of freedom of the electron is harnessed either by exploiting the spin property in conventional charge-based devices or utilizing the spin alone. For successful incorporation of spin into existing semiconductor technology several technical issues such as efficient injection, transport, manipulation, and detection of spin polarization as well as spin-polarized currents must be resolved. Faster and less-power consuming transistors could be achieved since flipping the spin takes 10–50 times less power and is ten times faster than transporting an electron through the channel in traditional FETs. Potential applications for ferromagnetic semiconductors and oxides include electrically controlled magnetic sensors and actuators, high-density ultralow-power memory and logic, spin-polarized light emitters for optical encoding, advanced optical switches and modulators, and devices with integrated magnetic, electronic, and optical functionality. Challenges are formidable in that in addition to coherent spin injection, the device dimensions must be comparable if not less than the spin-coherence lengths.

Assuming that ZnO can be made ferromagnetic by doping with transition metals such as Mn, Fe, Cr, Co, etc., or when spin injecting contacts to ZnO can be found, the material would be suitable for spin FETs. In ZnO, the equilibrium solubility limit of $3d$ transition metals such as Mn is larger than 10 mol %, and the electron effective mass is as large as $\sim 0.3 m_e$, where m_e is free-electron mass. Therefore the amount of injected spins and carriers in the film can be large, thus making Mn-doped ZnO ideal for the fabrication of spintronic devices. If made ferromagnetic, it can be used for drain and source in FET. Several groups have fabricated (Zn,TM)O [TM=Sc,[493,494] Ti,[493,494] V,[486,493,494] Cr,[485,493,494] Mn,[485,488,493–499] Fe,[494] Co,[485,487,489,490,493,494,500] Ni,[485,493,494,501] Cu (Refs. 493 and 494)] films by different techniques. Although there is a great deal of controversy and discrepancy about the actual ferromagnetic Curie temperature and source of ferromagnetism in transition-metal-doped ZnO films found in various reports, T_C values above the room temperature are reported.[49]

In this section, an overview of the physics and some generic features of ZnO-based DMS heterostructures are provided. Since several interesting quantum structures derived from the ZnO-based DMS (particularly, substituting Zn site by Mn) provide a valuable framework for understanding of spin transport and dynamics in magnetically active quantum semiconductor structures, theoretical studies of magnetism in ZnO DMS are described first. Then, a brief summary of the main experimental results on ZnO-based DMS have been put forth for the explanation of the ferromagnetism in these compound semiconductors.

[This article is copyrighted as indicated in the article. Reuse of AIP content is subject to the terms at: http://scitation.aip.org/termsconditions. Downloaded to] IP: 128.172.48.58 On: Mon, 19 Oct 2015 20:45:44

A. Theory of ZnO-based magnetic semiconductors

There are two basic approaches in understanding the magnetic properties of dilute magnetic semiconductors. The first group of approaches, which are based on the general mean-field theory, implicitly assumes that the dilute magnetic semiconductor is a more-or-less random alloy, e.g., (Zn, TM)O, in which transition-metal (TM) substitutes for one of the lattice constituents. The ferromagnetism occurs through interactions between the local moments of the TM atoms, which are mediated by free carriers in the material. The spin-spin coupling is also assumed to be a long-range interaction, allowing use of a mean-field approximation. Virtual crystal approximation is used to calculate the effective spin density due to the TM-ion distribution. The direct TM-TM interactions are antiferromagnetic so that the Curie temperature T_C for a given material with a specific TM concentration and hole density is determined by a competition between the ferromagnetic and antiferromagnetic interactions. The second group of approaches suggests that the magnetic atoms form clusters that produce the observed ferromagnetism. It is experimentally difficult to verify the mechanism responsible for the observed magnetic properties, because depending on the growth conditions employed for growing the DMS material, it is likely that one could readily produce samples consisting of single-phase random alloys, nanoclusters of the magnetic atoms, precipitates and second-phase formation, or a combination of these. To decide which mechanism is applicable, one should carefully correlate the measured magnetic and magnetoelectric properties with material analysis methods that are capable of detecting other phases or precipitates. If, for example, the magnetic behavior of the DMS is a characteristic of a known ferromagnetic second phase, then clearly the mean-field models are not applicable.

Principally, the majority of DMS studied in an extensive way until now involved Mn^{2+} ion as a legitimate member of the transition-metal family to be embedded in various II-VI and III-V hosts. The easy substitution of Mn for the group-II elements in both zinc-blende and wurtzite structures occurs mainly due to the fact that the $3d$ orbitals of Mn^{2+} are exactly half-filled. As a consequence, all five spins are parallel in this orbital by Hund's rule and that will cost a considerable energy to add an electron with opposite spin to the atom, resulting in a *complete* $3d^5$ orbit. Therefore, Mn^{2+} has a relatively large magnetic moment (spin $S=5/2$ and angular momentum $L=0$) with characteristic of a half-filled d shell and can be incorporated in sizable amounts (up to 35% of Mn) into ZnO host without affecting much the crystallographic quality of the DMS, whereas about 5% is tolerable for III-V-based hosts. Additionally, Mn^{2+} is electrically neutral in II-VI hosts acting as neither acceptor nor donor, while it acts as an acceptor in the III-V-based DMS. In view of this, Mn atom resembles a group-II element, hence has attracted many researchers to produce these materials using both thin-film and bulk growth techniques. With the advancement of enhanced MBE growth techniques, heterostructures containing a variety of band alignments, strain configurations, and DMS alloys can and have been fabricated. One may employ the band-gap engineering techniques to create new DMS materials by manipulating the various physical parameters involved. Apart from this, the presence of local moments allows the spin engineering of phenomena through the exploitation of two classes of exchange interactions. The first one is the d-d superexchange between d electrons of the magnetic ions, and the second one is the sp-d exchange between the d electrons and the band electrons or holes. This interaction is ferromagnetic for conduction-band states and mainly antiferromagnetic for valence bands. This interaction determines the spin splitting of the band states in an external magnetic field, giving rise to interesting magneto-optical and magnetotransport responses in the DMS samples.

To obtain the Curie temperature from the magnetic measurements, the Curie-Weiss law is used:

$$\frac{M}{H} = \frac{C_0 x}{T - \Theta_0 x}, \tag{28}$$

where M is the magnetization, H is the magnetic field, T is the temperature, x is the transition-metal composition, and Θ_0 and C_0 are the Curie-Weiss temperature and the Curie constant for $x=1$, respectively. The Curie constant may be expressed as[496]

$$C_0 = \frac{(g\mu_B)^2 S(S+1)n}{3k_B} = C_M \frac{\rho}{\mu}, \tag{29}$$

where g is the intrinsic Lande g factor, n is the number of cation sites per unit volume, C_M is the Curie constant for $x=1$, ρ is the mass density, μ is the molar mass, S is the effective spin per transition-metal ion ($S=3/2$ for Mn^{2+}), μ_B is the Bohr magneton, and k_B is the Boltzman constant. Using Eqs. (28) and (29) one can estimate Θ_0 and C_M. The effective exchange integral between the nearest-neighbor transition ions can be estimated from

$$\frac{J_1}{k_B} = \frac{3\Theta_0}{3zS(S+1)}, \tag{30}$$

where z is the number of nearest-neighbor cations ($z=12$ for the wurtzite structure). A negative value of J_1 indicates that the interactions between the magnetic ions are antiferromagnetic, suggesting that superexchange is likely the dominant mechanism.

For an external magnetic field B applied along the z direction, the magnetization M_Z of a DMS alloy containing Mn^{2+} ions is empirically written as

$$M_Z = N_0\langle S_Z\rangle + N_0 S_{\rm sat} B_{5/2}(5\mu_B B/k_B T_{\rm eff}), \tag{31}$$

where N_0 is the density of Mn^{2+} ions and $B_{5/2}(x)$ is the Brillouin function for $S=5/2$, $S_{\rm sat}$ is the saturation value for the spin of an individual Mn^{2+} ions (i.e., smaller than 5/2), and the rescaled temperature $T_{\rm eff}=T+T_0$. Along with the distribution of magnetic ions on a DMS lattice, isolated spins, pairs of spins, and triplets are also distributed. Hence the magnetization is dominated by the paramagnetic response of isolated single spins, which are antiferromagnetically coupled. However, if we consider a DMS heterostructure, the ferromagnetic s-d exchange interaction between conduction electrons and local moments results in an enhanced electronic spin splitting as described below:

[This article is copyrighted as indicated in the article. Reuse of AIP content is subject to the terms at: http://scitation.aip.org/termsconditions. Downloaded to] IP: 128.172.48.58 On: Mon, 19 Oct 2015 20:45:44

$$\Delta E = g\mu_B B + f(\Psi)(N_0\alpha)\langle S_Z\rangle, \qquad (32)$$

where $f(\Psi)$ is the wave-function overlap between the confined state and local moments and α is the s-d exchange integral. The spin splitting is dominated by the second term in Eq. (32), because the intrinsic g factor for electrons in ZnO is small.[493] The exchange integral for the heavy-hole states is typically $\sim$5 times larger than that for the conduction-band and light-hole states. Because of this reason, in most optical experiments, which probe heavy-hole excitations, the spin splitting is dominated by that of the valence-band states. The effect of magnetic field on the confined electronic states in DMS heterostructures is generally probed using magneto-optical spectroscopy, such as magnetophotoluminescence, magnetoabsorption, and Faraday/Kerr effect.

Progress towards understanding the (Zn,Mn)O-based materials and, in particular, the mechanism limiting the Curie temperature T_C requires careful investigation of the transport behavior, namely, precise knowledge of the hole density p. The Hall resistivity in magnetic materials is given by

$$\rho_{xy} = \rho_{xy}^0 + \rho_{xy}^a = R_0 B + R_a(\rho_{xx})M, \qquad (33)$$

where the normal contribution ρ_{xy}^0 is proportional to the external magnetic field B, $R_0 = 1/pe$, and the anomalous contribution ρ_{xy}^a is proportional to the macroscopic magnetization M. The term R_a arises from the spin-orbit interaction, which induces anisotropy between scattering of spin-up and spin-down electrons. The Hall measurements should be carried out in the applied magnetic-field limit where the magnetization is saturated (i.e., at low temperature and very high magnetic field).

Furthermore, ferromagnetism in DMS has been accounted for by the formation of bound magnetic polarons.[502–509] The bound magnetic polarons are formed by the alignment of the spins of many transition-metal ions with that of much lower number of weakly bound carriers such as excitons within a polariton radius. The localized holes of the polarons interact with the transition-metal impurities surrounding them, thus producing an effective magnetic field and aligning all spins. The interaction distance (boundary) grows as the temperature decreases. Neighboring magnetic polarons overlap and interact via magnetic impurities forming correlated clusters of polarons. One observes a ferromagnetic transition when the size of such clusters is equal to the size of the sample. This model is inherently attractive for low carrier density systems such as many of the electronic oxides. The polaron model is applicable to both p- and n-type host materials.[505] Even though the direct exchange interaction of the localized holes is antiferromagnetic, the interaction between bound magnetic polarons may be ferromagnetic for sufficiently large concentrations of magnetic impurities. This enables ferromagnetic ordering of the Mn ions in an otherwise insulating or semi-insulating material.

A key development that focused attention on wide-band-gap semiconductors as being the most promising for achieving high Curie temperatures was the work of Dietl *et al.*[47] By employing the mean-field theory based on the Zener ferromagnetism model[510] Dietl *et al.*[47] and Dietl[511] evaluated the

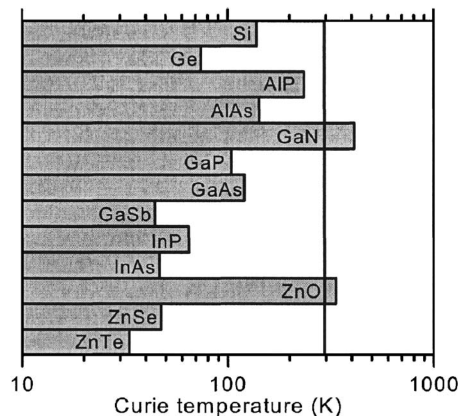

FIG. 88. Computed values of the Curie temperature T_C for various p-type semiconductors containing 5% of Mn and 3.5×10^{20} holes/cm^3. [Reprinted with permission from T. Dietl, H. Ohno, F. Matsukura, J. Cibert, and D. Ferrand, Science **287**, 1019 (2000). Copyright 2000 AAAS.]

Curie temperatures (T_C) for various semiconductors. According to the Zener model, the short bond lengths in wide-band-gap materials, such as ZnO, lead to a strong coupling between the holes (which reside on the anions) and the spins (localized on the magnetic cations) when doped with transition metals. It is suggested that the holes in the extended or weakly localized states mediate the long-range interactions between the localized spins on both sides of the metal-insulator transition in the III-V and II-VI magnetic semiconductors. This allows the use of the mean-field approximation. According to their model, the Curie temperature is determined by a competition between the ferromagnetic and antiferromagnetic interactions. The model takes into account the anisotropy of the carrier-mediated exchange interaction related to the spin-orbit coupling in the host material. The T_C is proportional to the density of Mn ions and the hole density. By extending the model to wurtzite semiconductors, Dietl *et al.* evaluated T_C for ZnO and for wurtzite GaN. The values of T_C computed for various semiconductors containing 5% of Mn and 3.5×10^{20} holes/cm^3 are presented in Fig. 88. This prediction has stimulated considerable research in semiconductors, resulting in the observation of a spontaneous magnetic moment at room temperature in transition-metal-doped nitrides and oxides.

The theory by Dietl *et al.*[47] assumes that the ferromagnetic correlations among the Mn ions, which provide the spin after substituting the group II or III site, are mediated by the holes from the shallow acceptors. The model suggests that the carrier-mediated ferromagnetism in n-type material may be observed only at low temperatures with shallow donors, while higher temperatures for p-type materials ($>$300 K for p-type GaN and ZnO) are predicted.

In addition to the prediction of Dietl *et al.*, ferromagnetism in magnetic-ion-doped ZnO has been theoretically investigated by *ab initio* calculations based on the local-density approximation by Sato and Katayama-Yoshida.[512–514] Again, the results suggest that ferromagnetic ordering of Mn is favored when mediated by holes. The transition from the antiferromagnetic state to the ferromagnetic state took place as the holes were introduced, but no transition was found by n-type doping. However, for V, Cr, Fe, Co, and Ni dopants,

[This article is copyrighted as indicated in the article. Reuse of AIP content is subject to the terms at: http://scitation.aip.org/termsconditions. Downloaded to] IP: 128.172.48.58 On: Mon, 19 Oct 2015 20:45:44

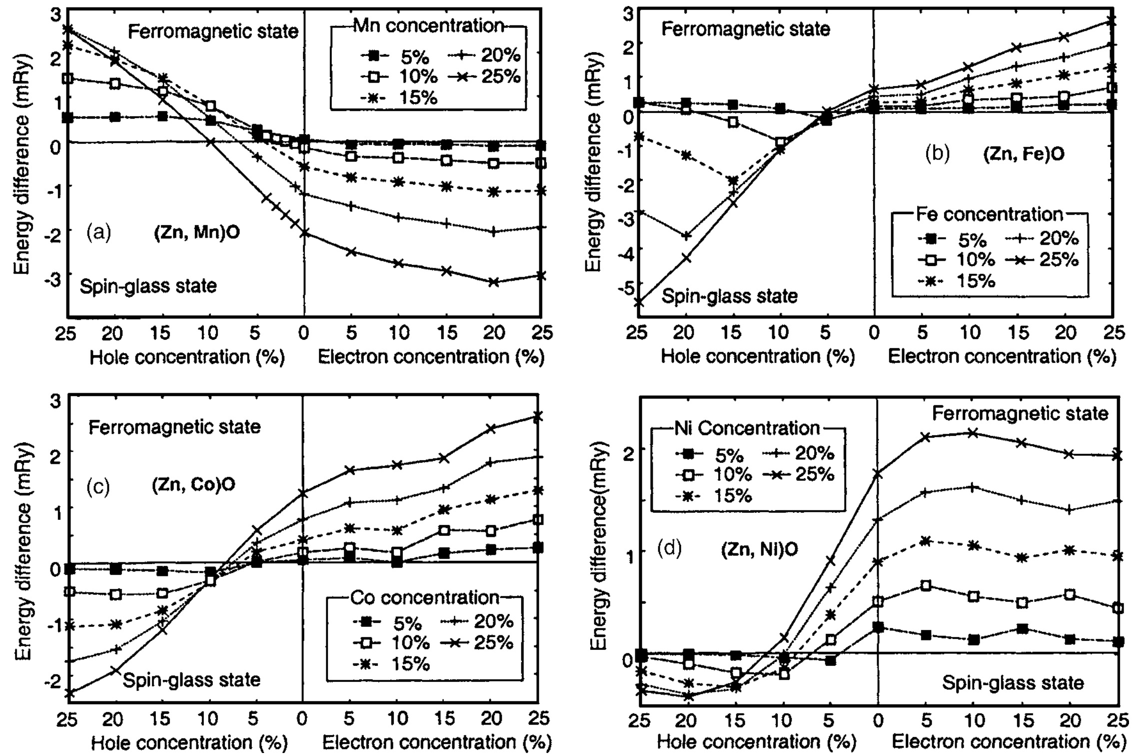

FIG. 89. Stability of the ferromagnetic state in (a) Mn-, (b) Fe-, (c) Co-, and (d) Ni-doped ZnO as a function of the carrier concentration. The vertical axis is the energy difference between the ferromagnetic and the spin-glass state. A positive-energy difference indicates a more stable ferromagnetic state. [Reprinted with permission from K. Sato and H. Katayama-Yoshida, Semicond. Sci. Technol. **17**, 367 (2002). Copyright 2002, Institute of Physics.]

ferromagnetic ordering in ZnO is predicted to occur without the need of additional charge carriers. Analyzing the density of states, it was suggested that the ferromagnetism originated from a competition between the ferromagnetic double-exchange interaction and the antiferromagnetic superexchange interaction. Figure 89 shows the transition in ZnTMO (TM=Mn, Fe, Co, Ni) with acceptor doping for different TM concentrations. Notice that the ferromagnetism becomes weaker for Fe-, Co-, and Ni- doped ZnO with increasing hole concentration. The stability of the ferromagnetic state for $3d$ transition-metal-doped ZnO for no additional carrier doping is shown in Fig. 90. It was also found that the ferromagnetic state was the ground state for V, Cr, Fe, Co, and Ni in ZnO. As a conclusion, acceptor-doped (Zn,Mn)O and ZnO doped with other $3d$ transition metals were proposed as candidates of a ferromagnet.

Monte Carlo simulations of carrier-mediated ferromagnetism in Mn-doped III-V semiconductors which deviate from the mean-field approach have appeared.[515,516] The mean-field theory usually overestimates the stability of ordered phases, which may lead to overly optimistic predictions for critical temperatures.[516] The kinetic-exchange model finds that collective spin-wave excitations are important and allows self-consistent accounting of spatial inhomogeneities, free-carrier exchange and free-carrier spin polarization.[516–518]

In a more recent theoretical study, Wang and Jenna[519] investigated the electronic structure and magnetism of a model Mn-doped ZnO thin film using first-principles calculations. Magnetic coupling between Mn ions was found to be antiferromagnetic in agreement with the calculations of Sato and Katayama-Yoshida.[512] Since Mn and Zn have the same valence, no free holes are present to mediate ferromagnetism when Mn atoms substitute Zn atoms. It was concluded that to obtain ferromagnetism in the ZnMnO system, treatments, such as codoping and/or defects, are needed. At high Mn concentrations, Mn atoms were found to cluster around O in the ZnMnO thin film. These results agree with the experimental results of Ueda *et al.*,[485] Fukumura *et al.*,[496] and Yoon *et al.*[520] who did not observe any ferromagnetic interaction in the Mn-doped ZnO system.

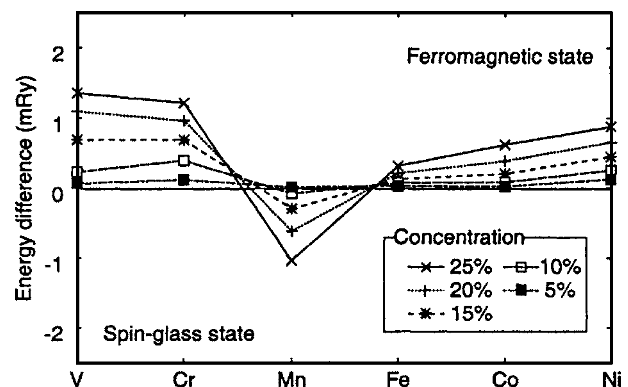

FIG. 90. Stability of the ferromagnetic state in V-, Cr-, Mn-, Fe-, Co-, and Ni-doped ZnO without any additional carrier doping for different dopant concentrations. The vertical axis is the energy difference between the ferromagnetic and the spin-glass state. A positive energy difference indicates a more stable ferromagnetic state. [Reprinted with permission from K. Sato and H. Katayama-Yoshida, Semicond. Sci. Technol. **17**, 367 (2002). Copyright 2002, Institute of Physics.]

[This article is copyrighted as indicated in the article. Reuse of AIP content is subject to the terms at: http://scitation.aip.org/termsconditions. Downloaded to] IP: 128.172.48.58 On: Mon, 19 Oct 2015 20:45:44

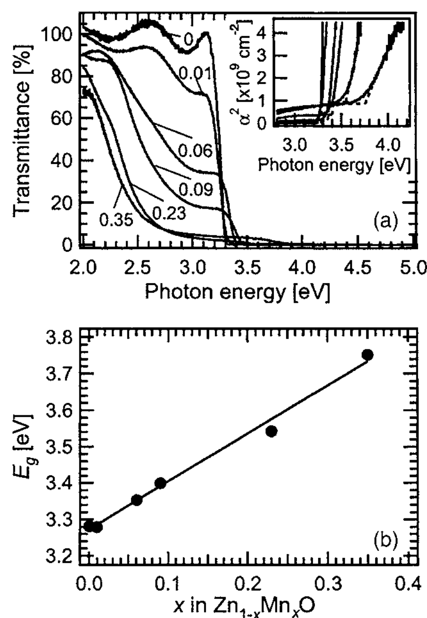

FIG. 91. (a) Transmission spectra of the $Zn_{1-x}Mn_xO$ films measured at room temperature for various x values. The numbers in the figures denote x. The inset shows the photon energy dependence of squared absorption constant (α^2) around the band gap (E_g). (b) Variation of E_g with Mn content. The solid line is a fitted line expressed as $E_g=3.273+1.32x$ eV. [Reprinted with permsission from T. Fukumura, Z. Jin, A. Ohtomo, H. Koinuma, and M. Kawasaki, Appl. Phys. Lett. **75**, 3366 (1999). Copyright 1999, American Institute of Physics.]

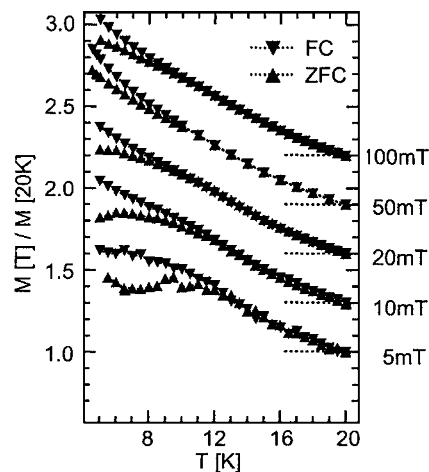

FIG. 92. Magnetization normalized at 20 K for a $Zn_{0.64}Mn_{0.36}O$ film measured during ZFC and FC runs in various magnetic fields. The curves are vertically shifted as represented by the dotted lines. [Reprinted with permission from T. Fukumura, Z. Jin, M. Kawasaki, T. Shono, T. Hasegawa, S. Koshihara, and H. Koinuma, Appl. Phys. Lett. **78**, 958 (2001). Copyright 2001, American Institute of Physics.]

B. Experimental results on ZnO-based magnetic semiconductors

It is certainly fair to state that the origin of ferromagnetism in wide-band-gap semiconductors is still not totally understood. Setting the controversy aside for the time being, what has been reported experimentally will be discussed in this section.

The incorporation of Mn into ZnO was investigated by Fukumura *et al.*[495] The solubility of Mn into ZnO exceeded the equilibrium limit (~13%) as a result of nonequilibrium PLD film growth process, and Mn content of more than 35% was obtained. With increasing Mn content both of the lattice constants a and c of wurtzite $Zn_{1-x}Mn_xO$ increased and the band gap expanded with considerable midgap absorption. Figure 91 shows the optical transmittance at room temperature for the $Zn_{1-x}Mn_xO$ films with different Mn contents. As the Mn content is increased, the midgap absorption around 3 eV develops and the absorption edge blueshifts.

Report of ferromagnetism alone is not sufficient. A more instructive measurement is that of the temperature dependence of the field-cooled (FC) and zero-field-cooled (ZFC) magnetizations performed in a superconducting quantum interference device (SQUID) magnetometer, which is typically employed by experienced practitioners. Ferromagnetism is shown by the separation in the FC and ZFC curves. In material known to have second phases, the magnetization versus temperature behavior shows either a spin-glass-type transition or cusps corresponding to the presence of multiple phases.

Using a SQUID magnetometer, Fukumura *et al.*[496] measured the magnetization for a $Zn_{0.64}Mn_{0.36}O$ thin film grown by pulsed-laser deposition. The temperature dependence of the magnetization (M vs T) was measured during cooling in a magnetic field (FC) and during warming in a magnetic field after cooling without the magnetic field (ZFC). As shown in Fig. 92, the magnetization for the ZFC measurement deviates from that in the FC measurement at ~10 K, an indication of spin-glass behavior. As H goes to 0, the spin-freezing temperature is obtained as ~13 K. The temperature dependence of the magnetization showing a spin-glass behavior with the large magnitude of the negative Curie-Weiss temperature corresponds to a stronger antiferromagnetic exchange coupling than other II-VI DMSs. The effective Mn content that is linked to the net magnetization compared to the fully saturated magnetization of the Mn^{2+} spin is very small (0.021), also implying a strong antiferromagnetic exchange coupling. This result is consistent with the *ab initio* calculations by Sato and Katayama-Yoshida[512] who predicted a transition from the antiferromagnetic state to the ferromagnetic state only with the introduction of holes.

To investigate the magneto-optical properties, Ando *et al.*[493] measured the magnetic circular dichroism (MCD) spectra of ZnO films alloyed with Sc, Ti, V, Cr, Mn, Co, Ni, and Cu using pulsed-laser deposition. MCD detects the relative difference of the circular polarization-dependent optical absorption under an applied magnetic field. The films alloyed with Sc, Ti, V, and Cr did not show any noticeable magneto-optical effect while the films with Mn, Co, Ni, and Cu had pronounced negative MCD peaks near the band edge of the host ZnO. The MCD amplitudes for these films decreased with increasing temperature while that of undoped ZnO was almost temperature independent. The $Zn_{0.84}Co_{0.16}O$ sample showed a negative MCD signal up to 200 K. The MCD signal near the semiconductor band gap comes from the Zeeman splitting (ΔE) of the conduction and valence bands, which may be estimated along with the effective g factor using the equation

[This article is copyrighted as indicated in the article. Reuse of AIP content is subject to the terms at: http://scitation.aip.org/termsconditions. Downloaded to] IP: 128.172.48.58 On: Mon, 19 Oct 2015 20:45:44

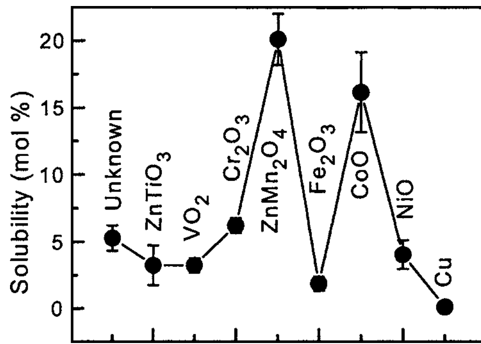

FIG. 93. Solubility limit of TM ions in ZnO. The upper and lower limits of the error bars correspond, respectively, to the lowest x of the pixels precipitated and the highest x of the pixels without precipitation. The precipitated phases were also shown. [Reprinted with permission from Z. Jin *et al.*, Appl. Phys. Lett. **78**, 3824 (2001). Copyright 2001, American Institute of Physics.]

$$\mathrm{MCD} = -\frac{45}{\pi}\Delta E\frac{d\alpha}{dE} = -\frac{45}{\pi}g\mu_B H\frac{d\alpha}{dE}, \tag{34}$$

where α is the optical-absorption coefficient, E is the photon energy, μ_B is the Bohr magnetron, and H is the magnetic field. For $Zn_{1-x}Co_xO$, the effective g values are estimated to be $\sim$4 for $x=0.012$ and $\sim$9 for $x=0.016$ which are much smaller than the typical values for other II-VI host magnetic semiconductors. The results showing strong MCD signals indicate that ZnO alloyed with Mn, Co, Ni, and Cu is diluted magnetic semiconductor with strong exchange interaction between *sp*-band carriers and localized d electrons.

Jin *et al.*[494] determined the solubility limits of transition-metal dopants in ZnO thin films grown by laser MBE. Figure 93 shows these limits determined by the presence of impurity peaks in x-ray-diffraction patterns. The transition-metal compositions were measured by electron probe microanalysis. Magneto-optical responses (measured by MCD) coincident with absorption spectra were observed for Mn- and Co-doped samples.

Cathodoluminescence (CL) measurements on the same samples showed two peaks at 2.97 and 3.71 eV for Cr-doped samples at the expense of the exciton emission peak of pure ZnO. The authors argue that these peaks are due to oxygen-rich local structures created by Cr doping, since similar but broader peaks were also observed in undoped ZnO thin films treated under oxygen-rich conditions.[521] CL measurements also revealed that Mn is a quencher for luminescence. Despite of all these results, no indication of ferromagnetism was observed for $Zn_{1-x}TM_xO$ (TM=Sc, Ti, V, Cr, Mn, Fe, Co, Ni, Cu) films down to 3 K.

Ueda *et al.*[485] also investigated $Zn_{1-x}TM_xO$ films [n-type ($x=0.05-0.25$): TM=Co, Mn, Cr, Ni] grown on sapphire substrates by PLD. The Co-doped ZnO films showed the maximum solubility limit. In $Zn_{1-x}Co_xO$, only a few films showed ferromagnetic features, while the others showed spin-glass-like behaviors. Some of them exhibited ferromagnetic behaviors with a Curie temperature higher than room temperature. The reproducibility of the method was poor (less than 10%). The crystal structures of the $Zn_{1-x}TM_xO$ films were characterized using 2θ-θ XRD measurements. The typical XRD pattern of a $Zn_{1-x}Co_xO$ film formed on a sapphire substrate is shown in Fig. 94. All of the films were single phase and had c-axis preferred orientation. The Co content dependence of the c-axis lattice constant, $d(002)$, is shown in Fig. 94. The $d(002)$ values increased linearly as the Co concentration increased, which indicates that the Co ions systematically substituted for the Zn ions in the film without changing the wurtzite structure. The investigated $Zn_{0.75}Co_{0.25}O$ film showed absorption peaks around 570, 620, and 660 nm. These are typical d-d adsorption levels of Co^{2+} ions in a tetragonal crystal field. These XRD and absorption results suggest that the Co ions substituted for the Zn as 2^+ ions without changing the wurtzite structure. CoO, which is well known to a have a very weak ferromagnetism, could not be detected in the XRD. Furthermore, the magnitude of the observed magnetism is too large to be attributed to the weak magnetization of CoO. Also, no Co phase was observed in the XRD. Therefore, the authors argue that the observed ferromagnetism is most probably due to the double-exchange mechanism even though there is no direct proof. In contrast to above room temperature T_C values reported by Ueda *et al.*, Kim *et al.*[522] reported spin-glass behavior for homogeneous $Zn_{1-x}Co_xO$ films and room-temperature ferromagnetism was found only in inhomogeneous films supporting the attribution of the observations to the presence of Co clusters.

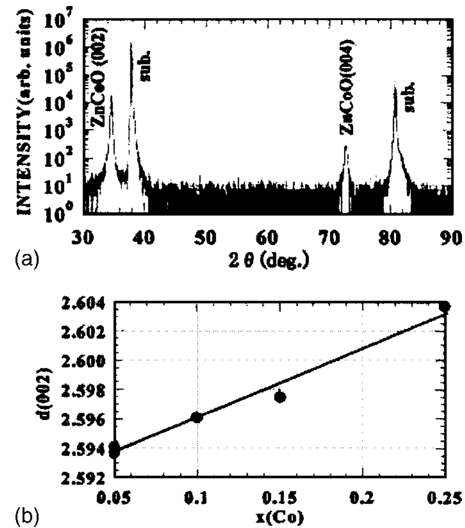

FIG. 94. (a) 2θ-θ XRD pattern of the $Zn_{0.95}Co_{0.05}O$ film, and (b) Co content (x) dependency of the c-axis lattice constant [$d(002)$] in $Zn_{1-x}Co_xO$ films. [Reprinted with permission from K. Ueda, H. Tabata, and T. Kawai, Appl. Phys. Lett. **79**, 988 (2001). Copyright 2001, American Institute of Physics.]

Saeki *et al.*[486] reported Curie temperatures higher than 350 K for V-doped ZnO films [n-type $Zn_{1-x}V_xO$ ($x=0.05-0.15$)] grown by PLD. They found out that only the samples with carrier concentrations as high as 10^{18} cm^{-3} showed ferromagnetism, while the insulating samples were not ferromagnetic. The transmittance spectrum for the $Zn_{0.95}V_{0.05}O$ film was also measured and showed absorption peaks around 480, 560, and 850 nm, which correspond to typical d-d transitions of V^{2+} ions in a tetrahedral crystal field (Fig. 95).

By increasing the Mn content (x) in $Zn_{1-x}Mn_xO$ thin films, Jung *et al.*[497] also observed an increase in the c-axis

[This article is copyrighted as indicated in the article. Reuse of AIP content is subject to the terms at: http://scitation.aip.org/termsconditions. Downloaded to] IP: 128.172.48.58 On: Mon, 19 Oct 2015 20:45:44

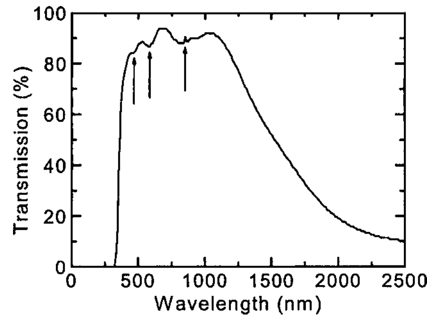

FIG. 95. Optical transmission spectra for the $Zn_{0.95}V_{0.05}O$ film. Typical absorption peaks of V^{2+} ions are indicated with arrows. [Reprinted from H. Saeki, H. Tabata, and T. Kawai, Solid State Commun. **120**, 439 (2001), Copyright 2001, with permission from Elsevier.]

lattice constant and fundamental band-gap energy. The band-gap energy of the films increased from 3.27 eV for $x=0.0$ to 3.36 eV and 4.2 for $x=0.1$ and 0.3, respectively, indicating that ZnMnO alloys are formed by the Mn incorporation. Figure 96 shows the absorption spectra for the $Zn_{1-x}Mn_xO$ alloys with $x=0.0$, 0.1, and 0.3. The films are observed to exhibit ferromagnetic ordering below $T_C=30$ and 45 K for the films containing 10% and 30% Mn, respectively.

The magnetic properties of Ni-doped ZnO thin films were reported by Wakano *et al.*[501] Ni was found to dissolve in ZnO up to 25% without precipitation. For films doped with 3%–25% Ni, ferromagnetism was observed at 2 K.

A review by Pearton *et al.*[523] focuses on the magnetic properties of promising materials such as GaN, GaP, and ZnO. The introduction of Mn into these and other materials under the right conditions is found to produce ferromagnetism near or above room temperature. The mechanism for the observed magnetic behavior is complex and appears to depend on a number of factors, including Mn–Mn spacing, and carrier density and type. For example, in a simple carrier-mediated exchange mechanism, the free-carrier/Mn ion interaction can be either ferromagnetic or antiferromagnetic depending on the separation of the Mn ions.

In all of the studies mentioned above, the ZnO material was *n* type. The theory of Dietl *et al.*[47] predicting high-temperature ferromagnetism for Mn-doped ZnO is specifi-

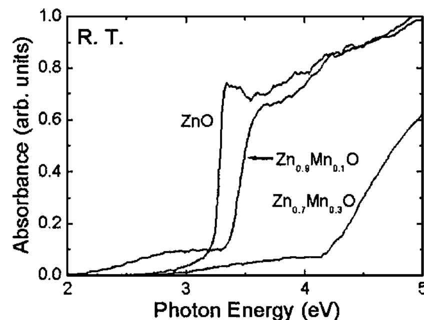

FIG. 96. Room-temperature UV absorbance spectra of $Zn_{1-x}Mn_xO$ ($x=0.0$, 0.1, and 0.3) films. The absorbance spectra show a strong UV absorbance at 3.22–4.2 eV. Note that the absorbance edge of the $Zn_{1-x}Mn_xO$ films blueshifts with increasing Mn content. [Reprinted with permission from S. W. Jung, S.-J. An, G.-C. Yi, C. U. Jung, S.-I. Lee, and S. Cho, Appl. Phys. Lett. **80**, 4561 (2002). Copyright 2002, American Institute of Physics.]

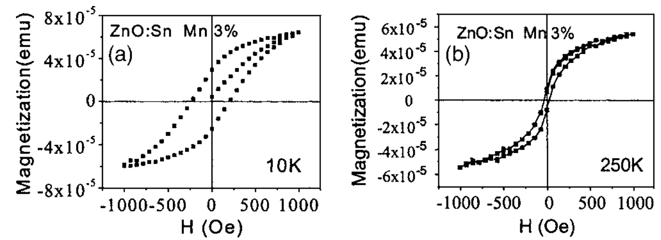

FIG. 97. *M* vs *H* curve for the 3% Mn-implanted ZnO:Sn single-crystal sample at (a) 10 K and (b) 250 K. [Reprinted with permission from D. P. Norton, S. J. Pearton, A. F. Hebard, N. Theodoropoulou, L. A. Boatner, and R. G. Wilson, Appl. Phys. Lett. **82**, 239 (2003). Copyright 2003, American Institute of Physics.]

cally for *p*-type materials. The experimental results reported in the literature for Mn-doped ZnO that is *n* type due to group-III donor impurities are consistent with this prediction and show no ferromagnetism. However, Pearton *et al.*[523] appear to have obtained preliminary evidence of ferromagnetism in *n*-type ZnO, in which Mn and Sn serve as the transition metal and donor impurities, respectively.

Along the above lines, Norton *et al.*[500] reported an evidence for ferromagnetism with a Curie temperature of ~250 K in ZnO codoped with Mn and Sn. Here, Sn behaves as a doubly ionized donor introducing deep states in the energy gap. Figure 97 shows the *M* vs *H* curve for this particular ZnO:Sn single-crystal sample. By taking the difference between the field-cooled and zero-field-cooled magnetization measurements between 4.2 and 300 K, the para- and diamagnetic contributions to the magnetization are subtracted and only the measure of the hysteretic ferromagnetic regime was obtained. As shown in Fig. 98, the ferromagnetism persists up to ~250 K for both the 3% and 5% Mn-doped samples, while the difference is more pronounced for the former. From the XRD measurements, no evidence was observed for Mn–O phases, although the diffraction is inadequate to detect secondary phases at the level necessary. However, they argue that the only ferromagnetic phase, Mn_3O_4, cannot account for the ferromagnetic transition temperature of ~250 K, since it has a Curie temperature of 42 K.

The ferromagnetic properties of Mn-doped ZnO observed by Kim *et al.*[499] agree well with the previously reported experimental results by Jung *et al.*[497] but contrast with the observation of spin-glass behavior in the Mn-doped ZnO films by Fukumura *et al.*[495] The same controversy has been also reported for the Co-doped ZnO film.[485] These controversial results may perhaps originate from the poor reproducibility of the sample or employment of measurement techniques that are incapable of distinguishing carrier-mediated ferromagnetism from others. Different growth conditions and the problems with reproducibility may also be responsible for discrepancy in the reported Curie temperatures.

Kim *et al.*[499] argued that the physical origin of the ferromagnetic properties of the ZnMnO films prepared by the sol-gel method on Si substrates comes from precipitates of Mn_3O_4 at the interface of the films. Even though manganese oxides, such as MnO, MnO_2, and Mn_3O_4, were not identified in the XRD spectrum, TEM images showed that the film/substrate interface was not atomically sharp. The energy dis-

[This article is copyrighted as indicated in the article. Reuse of AIP content is subject to the terms at: http://scitation.aip.org/termsconditions. Downloaded to] IP: 128.172.48.58 On: Mon, 19 Oct 2015 20:45:44

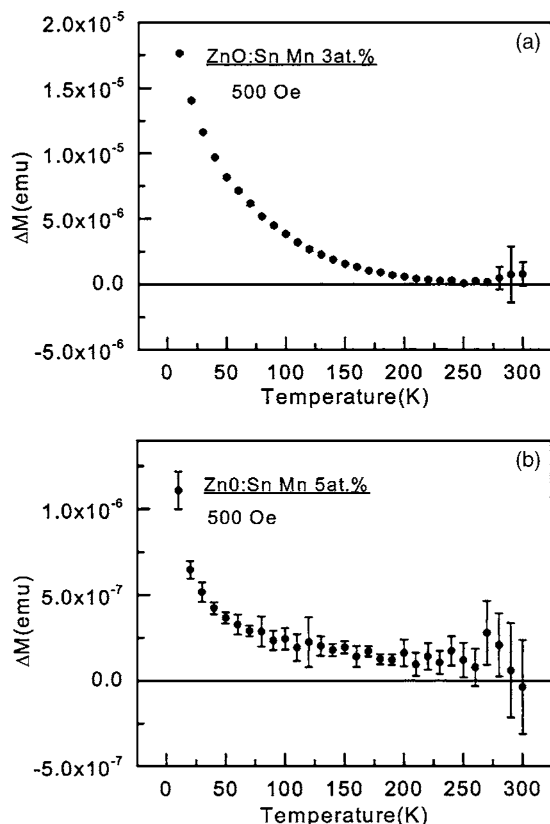

FIG. 98. Temperature dependence of the difference between field-cooled and zero-field-cooled magnetizations for (a) 3% and (b) 5% implanted Mn concentrations in *n*-type ZnO:Sn single crystal. [Reprinted with permission from D. P. Norton, S. J. Pearton, A. F. Hebard, N. Theodoropoulou, L. A. Boatner, and R. G. Wilson, Appl. Phys. Lett. **82**, 239 (2003). Copyright 2003, American Institute of Physics.]

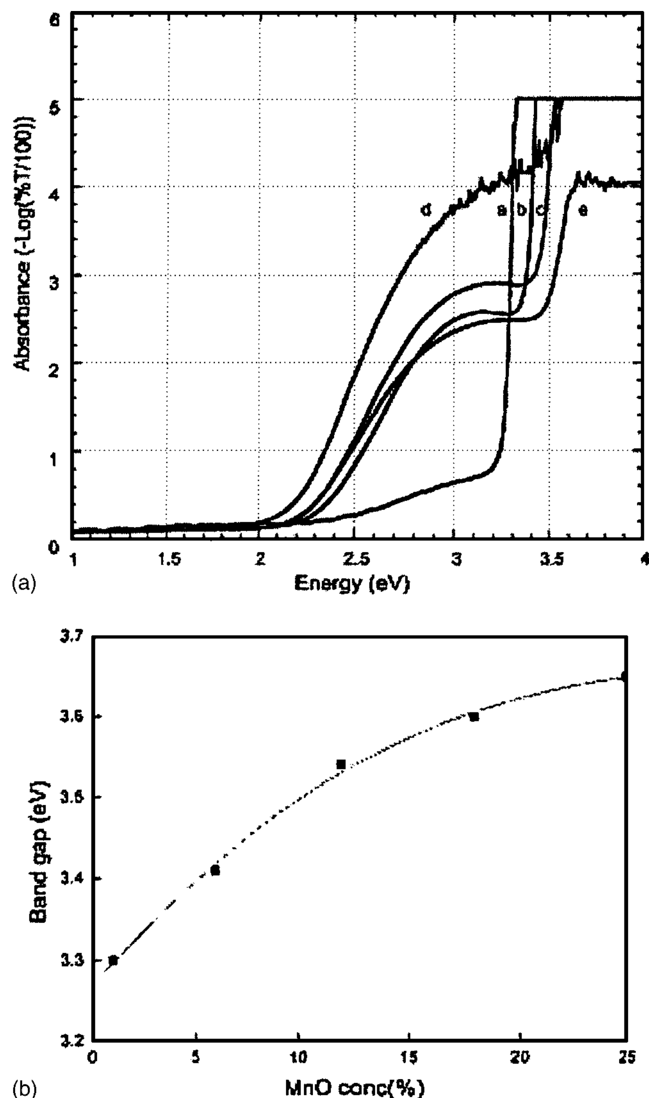

FIG. 99. (a) Optical absorbance spectra of $Zn_{1-x}Mn_xO$ films. a, b, c, d, and e correspond to $x=0.01$, 0.05, 0.12, 0.18, and 0.25, respectively. (b) Variation of the band gap of $Zn_{1-x}Mn_xO$ films with x. The data fit well in a second-order polynomial equation $E_g=3.270+2.762x-4.988x^2$ (solid line). [Reprinted with permission from A. Tiwari, C. Jin, A. Kvit, D. Kumar, J. F. Muth, and J. Narayan, Solid State Commun. **121**, 371 (2002). Copyright 2002, American Institute of Physics.]

persive spectroscopy (EDS) measurements performed on the interfacial region showed significant amounts of Mn compared to the region away from the interface. MnO and MnO_2 cannot be regarded as possible candidates for the ferromagnetic precipitates at the interface since they are both antiferromagnetic below 116 and 84 K, respectively.[497] However, ferromagnetic long-range order has been observed for Mn_3O_4.[524] The Mn:O ratio measured at the interface (close to 3:4) also indicates that Mn_3O_4 is the most probable cause for the observed ferromagnetism in the ZnMnO films.

Rode *et al.*[487] investigated the microstructure and the magnetic properties of cobalt-substituted ZnO thin films deposited on sapphire (0001) substrates by pulsed-laser deposition. Films with 25% of Co were ferromagnetic at room temperature with clear out-of-plane anisotropy. It was found out that lower growth pressures result in more oxygen vacancies, inducing free electrons which mediate the ferromagnetic exchange interactions as suggested by Sato and Katayama-Yoshida.[512] Besides the ferromagnetic behavior, evidence of an out-of-plane easy magnetization axis was clearly observed. The authors claim that this observed crystal anisotrophy supports the assumption that the ferromagnetism arises from the (Zn,Co)O phase.

The dependence of ZnMnO band gap on Mn content has been studied also by Tiwari *et al.*[525] Due to the nonequilibrium nature of the laser-material interaction, high Mn contents ($x=0.36$) could be introduced using PLD. Optical transmittance showed an increase in the insulating band gap (E_g) with increase in Mn atomic fraction x following the relation $E_g=3.270+2.760x-4.988x^2$ eV. dc magnetization measurements on these samples showed the paramagnetic nature of the ZnMnO system. Figure 99(a) shows the optical absorbance spectra of the ZnMnO films. As seen from this figure, the absorption edge moves towards the higher-energy side as the Mn content increases. This indicates the increase in the band gap of the system. Significant amount of midgap absorption is also observed in these samples. This phenomenon was also reported in earlier studies and was attributed to the charge-transfer transition between donor and acceptor ionization levels of Mn ions and the band continuum.[495,497]

Cheng and Chien[526] also found no ferromagnetic ordering in Mn-doped ZnO thin films. The magnetic properties of a $Zn_{0.93}Mn_{0.07}O$ film were measured by a SQUID magneto-

[This article is copyrighted as indicated in the article. Reuse of AIP content is subject to the terms at: http://scitation.aip.org/termsconditions. Downloaded to] IP: 128.172.48.58 On: Mon, 19 Oct 2015 20:45:44

meter at various temperatures with fields up to 5 T. The Auger electron spectroscopy showed homogeneous distribution of Mn in the film and the magnetic properties verified that the film was paramagnetic. The magnetic properties of Mn-doped ZnO are expected to be strongly influenced by the carrier type (p or n) and carrier density.[47,512] However, these characteristics of Mn-doped ZnO films are not well known experimentally at present.

In contrast to earlier work (Fukumura *et al.*[496] found a spin-glass behavior, Jung *et al.*[497] observed ferromagnetic ordering with a $T_C \sim 45$ K, Tiwari *et al.*[525] ruled out the room-temperature ferromagnetism, and Cheng and Chien[526] discovered paramagnetic behavior) Sharma *et al.*[488] claimed to have confirmed the ferromagnetism in Mn-doped ZnO. In this particular report room-temperature ferromagnetism was observed in bulk pellets, thin films, and powder form of Mn-doped ZnO. The authors attributed their achievement to the unique feature of their sample preparation having to do with low-temperature processing. When standard high-temperature ($T=700$ °C) methods were used, the samples were found to exhibit clustering and were not ferromagnetic at room temperature. No trace of any secondary phase or other impurities was found in ferromagnetic resonance (FMR), EDS, and also x-ray-diffraction measurements. However, the average local Mn concentration in bulk pellets ($\sim$0.3%) determined by the EDS technique was found to be much lower than the nominal composition (2%). The FMR data suggest T_C well above 425 K. Sintering the pellets above 700 °C completely suppressed ferromagnetism to below room temperature. Mn-doped ZnO became inhomogeneous with the increase in sintering temperature, probably because of Mn clustering or formation of other phases such as $Zn_2Mn_3O_8$, $ZnMn_3O_7$, and Mn_2O_3. The increased number of free electrons and the onset of clustering of Mn, in the high-temperature processed samples, deviate the system far from the ideal Mn-doped ZnO. Again, the field is riddled with controversy which may dissipate in time.

Ramachandran *et al.*[489] observed room-temperature ferromagnetism in $Zn_{0.9}Co_{0.1}O$ epitaxial films grown by pulsed-laser deposition. Electron-energy-loss spectroscopy (EELS) was used to determine the oxidation state at various points in the films. The oxidation state of cobalt was found not to change across the film, and a +2 oxidation state was induced which suggests a uniform substitution of Zn by Co. Atomic-scale structural characterization including high-resolution TEM, scanning transmission electron microscopy-atomic number (STEM-Z) contrast, and EELS was done to provide evidence for the absence of any nanosized clusters or second phase. XRD, TEM, and STEM-Z contrast measurements also supported the premise that Co nanoclusters and second phases could not be the cause for the observed room-temperature ferromagnetism.

In addition, optical measurements on a $Zn_{0.9}Co_{0.1}O$ sample grown at 500 °C revealed three absorption edges at 658, 616, and 568 nm, which were correlated with the *d*-*d* transitions of the tetrahedrally coordinated Co^{2+} ions (Fig. 100). Using the results from both optical and structural measurements Ramachandran *et al.*[489] concluded that the room-temperature ferromagnetism is an inherent property of the material caused by the presence of cobalt in high-spin configuration in a tetrahedral crystal field.

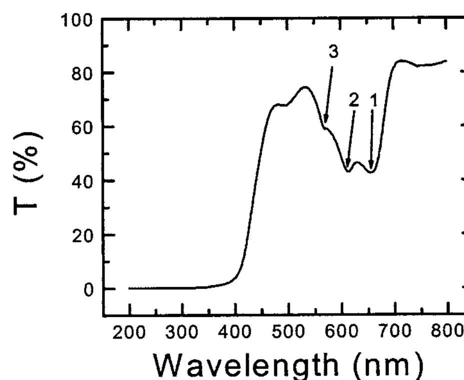

FIG. 100. Optical transmission spectrum of the $Zn_{0.9}Co_{0.1}O$ film grown at 500 °C. The absorption edges at 658, 616, and 568 nm are indicated as 1, 2, and 3, respectively. [Reprinted with permission from S. Ramachandran, A. Tiwari, and J. Narayan, Appl. Phys. Lett. **84**, 5255 (2004). Copyright 2004, American Institute of Physics.]

Lin *et al.*[490] reported that additional Cu doping into bulk $Zn_{0.98}Co_{0.02}O$ is essential to achieve room-temperature ferromagnetism. From the results of x-ray and EDX mapping, the $Zn_{0.97}Cu_{0.01}Co_{0.02}O$ film grown by standard solid-state reaction method was observed to have a homogeneous distribution with no secondary phases.

However, because of the lack of detailed microstructural characterization in the reports mentioned above, there is still a good deal of controversy over the fate of these magnetic impurities (nanosize clusters/precipitates and/or individual atoms in substitutional sites) and whether the magnetic behavior is an intrinsic property of the films or due to the presence of nanoclusters of a magnetic phase or a combination of both. Most experimental reports concerning room-temperature ferromagnetism in DMS employ x-ray diffraction, selected-area diffraction patterns, transmission electron microscopy, photoemission, or x-ray absorption to determine whether the magnetic atoms are substituting for one of the lattice constituents to form an alloy. Given the level of dilution of the magnetic atoms, it is often very difficult to categorically determine the origin of the ferromagnetism. For example, a recent study[500] reported the presence of Co nanoclusters in Co^+-implanted ZnO (exhibiting RT ferromagnetism), but did not preclude the possibility of the component of the magnetic property due to Co substitution of the Zn in ZnO lattice. In addition, there are still extreme variations in the reported magnetic behavior with some films exhibiting only paramagnetism and even those with ferromagnetism showing a wide range of apparent Curie temperatures. In short, the origin of this ferromagnetism is not yet clear.

VIII. BAND-GAP ENGINEERING

A crucial step in designing modern optoelectronic devices is the realization of band-gap engineering to create barrier layers and quantum wells in device heterostructures. In order to realize such optoelectronic devices, two important

[This article is copyrighted as indicated in the article. Reuse of AIP content is subject to the terms at: http://scitation.aip.org/termsconditions. Downloaded to] IP: 128.172.48.58 On: Mon, 19 Oct 2015 20:45:44

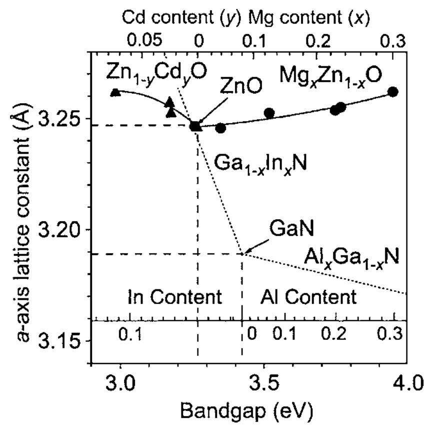

FIG. 101. Optical and structural properties of $Cd_yZn_{1-y}O$ and $Mg_xZn_{1-x}O$ alloy films mapped out in a plane of a-axis length and room-temperature band-gap energy. The same curves for (In, Ga)N and (Al, Ga)N alloys are also shown. The alloy compositions are shown on the top axis. [Reprinted with permission from T. Makino, Y. Segawa, M. Kawasaki, A. Ohtomo, R. Shiroki, K. Tamura, T. Yasuda, and H. Koinuma, Appl. Phys. Lett. **78**, 1237 (2001). Copyright 2001, American Institute of Physics.]

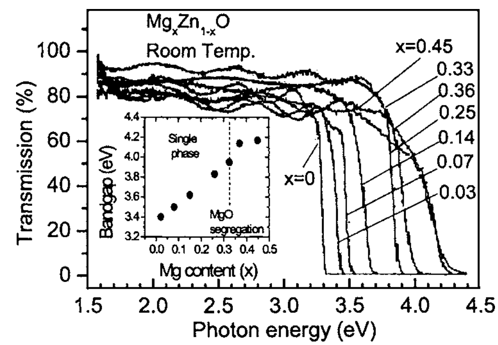

FIG. 102. Transmittance spectra of $Mg_xZn_{1-x}O$ films measured at room temperature. The inset shows the band gap (E_g) determined from the spectra assuming an $\alpha^2 \propto (h\nu - E_g)$ dependence, where α and $h\nu$ are the absorption coefficient and the photon energy, respectively. [Reprinted with permission from A. Ohtomo, M. Kawasaki, T. Koida, K. Masubuchi, and H. Koinuma, Appl. Phys. Lett. **72**, 2466 (1998). Copyright 1998, American Institute of Physics.]

requirements should be satisfied; one is p-type doping of ZnO as discussed previously, and the other is modulation of the band gap. While p-type doping of ZnO is under intensive study, the latter has been demonstrated by the development of $Mg_xZn_{1-x}O$ (Refs. 527–540 and $Cd_yZn_{1-y}O$ alloys,[537,541–547] allowing modulation of band gap in a wide range. The energy gap $E_g(x)$ of the ternary semiconductor $A_xZn_{1-x}O$ (where A=Mg or Cd) is determined by the following equation:[548]

$$E_g(x) = (1-x)E_{ZnO} + xE_{AO} - bx(1-x), \tag{35}$$

where b is the bowing parameter and E_{AO} and E_{ZnO} are the band-gap energies of compounds AO and ZnO, respectively. The bowing parameter b depends on the difference in electronegativities of the end binaries ZnO and AO. The band gap can be increased (decreased) by incorporating Mg (Refs. 528–530) [Cd (Refs. 541, 542, and 545)] into ZnO.

Figure 101 shows the a lattice parameter as a function of room-temperature E_g values in $Cd_yZn_{1-y}O$ and $Mg_xZn_{1-x}O$ alloys. A (Cd,Zn)O/(Mg,Zn)O superlattice (SL), having a perfect lattice match between layers and a maximum barrier height of 0.09 eV, can be obtained by choosing an appropriate combination of Cd and Mg concentrations, because both a parameters are monotonically increasing functions of alloy composition. This is a major advantage when compared to (In,Ga)N/(Al,Ga)N SLs since in the case of wurtzite structure, if the lattice constant of the well layer differs from that of the barrier layer, strain field exists inside the well layers which causes polarization charge. The same parametric plots for (In,Ga)N and (Al,Ga)N are shown by the dashed curves in Fig. 101.

A. $Mg_xZn_{1-x}O$ alloy

$Mg_xZn_{1-x}O$ alloy has been considered as a suitable material for the barrier layers in ZnO/(Mg,Zn)O superlattice structures[537] because alloying ZnO with MgO ($E_g \sim 7.7$ eV) enables widening of band gap of ZnO. According to the phase diagram of the ZnO–MgO binary system, the thermodynamic solid solubility of MgO in ZnO is less than 4 mol %.[549] In addition, ZnO has a wurtzite structureal (a =3.24 Å and c=5.20 Å), while MgO has a cubic structure (a=4.24 Å).

One of the reports on the synthesis of $Mg_xZn_{1-x}O$ with a Mg content of up to 33% was by Ohtomo *et al.*[527] by PLD. It was found that MgO segregates in the wurtzite MgZnO lattice above 33% of Mg content, limiting the maximum band gap to 3.9 eV. XRD studies show that the a-axis length gradually increases and the c-axis length decreases with increasing Mg content, and therefore the cell volume is hardly changed. Figure 102 shows the transmittance spectra measured at room temperature. The band gap E_g linearly increases with x up to 4.15 eV for $0 \leq x \leq 0.36$ and saturates at higher Mg concentrations due to MgO segregation (Fig. 102, inset). This indicates that $Mg_xZn_{1-x}O$ is a suitable material for barrier layers in ZnO/(Mg,Zn)O heterostructures with a band-gap offset up to 0.85 eV. Linear dependence of E_g on x up to x=0.36 shows that the bowing parameter b is 0 eV, although a final declaration must wait for additional and more refined experiments. Increasing the Mg composition further resulted in $Mg_xZn_{1-x}O$ films in metastable cubic phase with band gaps above 5.0 eV.[529] The Mg content strongly depended on the growth temperature, consequently showing strong dependence of band-gap energy on the growth temperature ranging from room temperature to 750 °C.

Gruber *et al.*[530] grew MgZnO epilayers and ZnO–MgZnO quantum well structures by MOVPE and studied their properties. All the samples were grown on GaN/sapphire templates in a horizontal flow reactor at a growth temperature of 600 °C. A 1-μm ZnO buffer was also included to improve structural quality. Diethylzinc (DEZn), bis(methylcyclopentadienyl)magnesium ($MeCp_2Mg$), and nitrous oxide were used as the zinc, magnesium, and oxygen precursors, respectively. The Mg incorporation into the ZnO host material and its effect on the band gap was determined by PL measurements. An increase of 200 meV in the band gap at a Mg concentration of 10% has been achieved, and using MgZnO as the barrier material, ZnO–MgZnO quantum wells with different well widths were grown. The quantum

[This article is copyrighted as indicated in the article. Reuse of AIP content is subject to the terms at: http://scitation.aip.org/termsconditions. Downloaded to] IP: 128.172.48.58 On: Mon, 19 Oct 2015 20:45:44

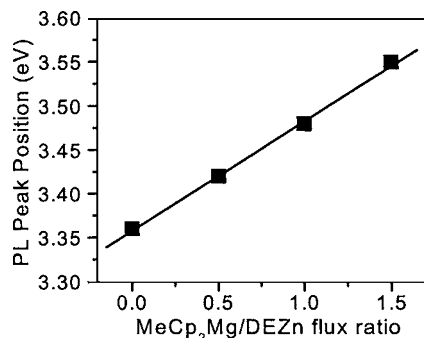

FIG. 103. The PL energy position of the band edge and Mg concentration x of the $Mg_xZn_{1-x}O$ epilayers as a function of the $MeCp_2Mg$ to DEZn flux ratio. [Reprinted with permission from T. Gruber, C. Kirchner, R. Kling, F. Reuss, and A. Waag, Appl. Phys. Lett. **84**, 5359 (2004). Copyright 2004, American Institute of Physics.].

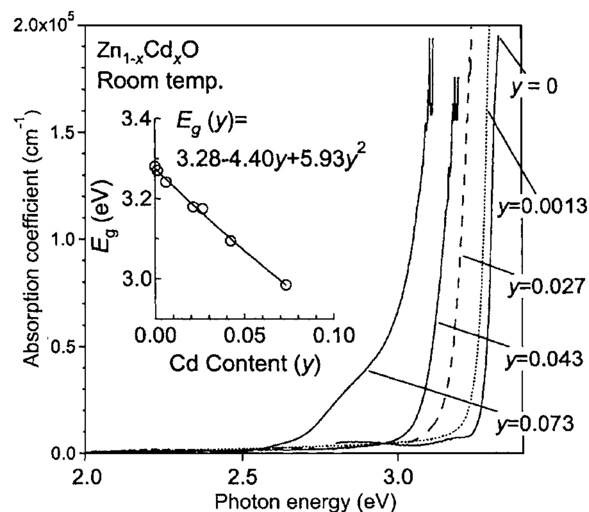

FIG. 104. Concentration (y) dependence of absorption spectra of $Cd_yZn_{1-y}O$ epilayers obtained at room temperature. The curves, from right to left correspond to those of the samples with y=0, 0.0013, 0.027, 0.043, and 0.073. [Reprinted with permission from T. Makino, Y. Segawa, M. Kawasaki, A. Ohtomo, R. Shiroki, K. Tamura, T. Yasuda, and H. Koinuma, Appl. Phys. Lett. **78**, 1237 (2001). Copyright 2001, American Institute of Physics.]

well luminescence showed the quantization behavior and an enhancement in the exciton binding energy ($E_b > 96$ meV). The exciton binding energy is much higher than that in ZnO and needs corroboration. Figure 103 shows the blueshift of the PL emission for the deposited $Zn_{1-x}Mg_xO$ epilayers as a function of the Mg supply (composition) during growth (i.e., the relative $MeCp_2Mg$/DEZn flux ratio). This dependence is almost linear, suggesting zero band-gap bowing.

Ohmoto *et al.*[528] studied the thermal stability of wurtzite-phase $Mg_xZn_{1-x}O$ alloy and $ZnO/Mg_xZn_{1-x}O$ bilayers grown by laser molecular-beam epitaxy. The bowing parameter of the as-grown films calculated using the band-gap values obtained from the absorption spectra is very high (b =3.11). When a $Mg_{0.23}Zn_{0.78}O$ film was annealed, the segregation of MgO started at 850 °C and the band gap was reduced to the value of that for an x=0.15 film after annealing at 1000 °C. The $Mg_{0.15}Zn_{0.85}O$ films showed no change in the band gap even after annealing at 1000 °C. From these results the authors concluded that the thermodynamic solubility limit of MgO in the $Mg_xZn_{1-x}O$ epitaxial film is about 15%. In addition, the thermal diffusion of Mg across the $Mg_xZn_{1-x}O$/ZnO interface was observed only after annealing above 700 °C.

B. $Cd_yZn_{1-y}O$ alloy

As discussed earlier, $Mg_xZn_{1-x}O$ alloy films have been considered as a suitable material for barrier layers due to its wider band gap than that of ZnO. For narrower band gaps, which are desirable for wavelength tenability and attaining band gaps corresponding to the visible spectrum, the $Cd_yZn_{1-y}O$ alloy would be a good candidate because of the small direct band gap of CdO (2.3 eV).[550] A decrease in the band gap down to 2.99 eV could be achieved by incorporating Cd^{2+} with y=0.07.

Recently, Makino *et al.*[540] have demonstrated the single-phase $Cd_yZn_{1-y}O$ alloy films grown by PLD on sapphire (0001) and $ScAlMgO_4$ (0001) substrates with Cd content of up to 7%. It is indicated that both a- and c-lattice constants increase as the Cd content increases and the ratio of c/a also monotonically increases in contrast to that for the $Mg_xZn_{1-x}O$ alloy as mentioned earlier. As shown in Fig. 104, the band-gap energy E_g decreases as the Cd content increases and can be estimated as $E_g(y)=3.29-4.40y+5.93y^2$. The band gap was observed to decrease from 3.28 down to 3.0 eV by introducing 7% of Cd. Figure 104 shows concentration (y) dependence of the room-temperature absorption spectra in the as-grown films. The spectrum of $Cd_{0.07}Zn_{0.93}O$ encompassed a broad shoulder on the lower-energy side, indicating the formation of a cadmium-rich phase, the density of which is relatively low. The band-gap energies (E_g) are plotted in the inset of Fig. 104.

The MOVPE method was also utilized for the growth of 150-nm-thick $Cd_yZn_{1-y}O$ layers on c-plane sapphire substrates using DEZn, dimethylcadmium (DMCd), and tertiary butanol as zinc, cadmium, and oxygen precursors, respectively.[544] A decrease in the PL peak energy up to 300 meV was observed with increasing Cd composition, while introducing a lattice mismatch of only 0.5% with respect to binary ZnO. The redshift of the PL peaks of the samples correlated very well with the Cd concentrations in the $Cd_yZn_{1-y}O$ layers determined by high-resolution XRD and the resulting dependence strongly deviated from a linear behavior and was described by $E_{PL}=(3.35-9.19y+8.14y^2)$ eV. However, the samples in this work were shown to consist of laterally distinguishable regions with different Cd incorporation. Therefore, the corresponding very large bowing parameter (b=8.14 eV) is not very reliable and is inconsistent with the results of Makino *et al.*[540]

Vigil *et al.*[546] used the spray pyrolysis method to grow $Cd_yZn_{1-y}O$ alloys. The band gap decreased from 3.28 to 2.51 eV when the composition y was changed from 0 to 1. The variation in the band gap as a function of Zn concentration was measured by optical transmission and a nonlinear dependence with a bowing parameter of approximately 0.54 was observed, which is in discord with the other results discussed above.

Ma *et al.*[542] succeeded in depositing good-quality $Cd_xZn_{1-x}O$ thin films on glass and sapphire substrates using

[This article is copyrighted as indicated in the article. Reuse of AIP content is subject to the terms at: http://scitation.aip.org/termsconditions. Downloaded to] IP: 128.172.48.58 On: Mon, 19 Oct 2015 20:45:44

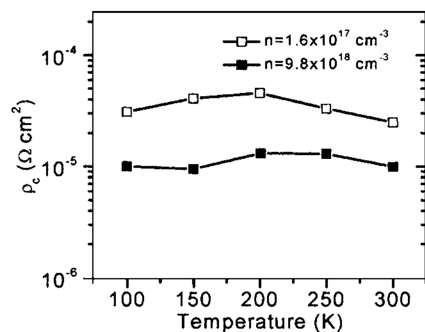

FIG. 105. The experimental specific contact resistances as a function of temperature for unintentionally doped (open circles) and heavily Ga-doped (solid circles) ZnO [after Sheng *et al.* (Ref. 555)].

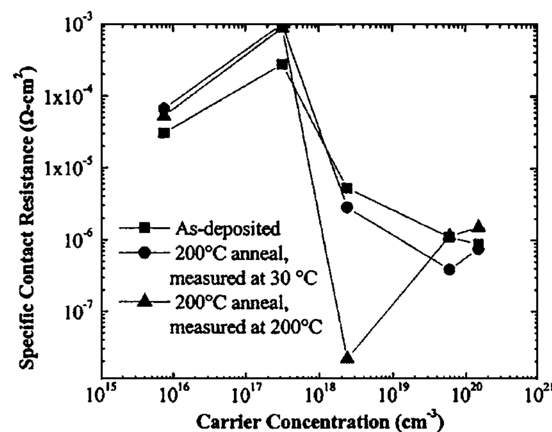

FIG. 106. Specific contact resistance vs carrier concentration of the as-deposited Ohmic contact measured at 30 °C, and at 30 and 200 °C, after annealing at 200 °C for 1 min. [Reprinted with permission from K. Ip, Y. Heo, K. Balik, D. P. Norton, S. J. Pearton, and F. Ren, Appl. Phys. Lett. **84**, 544 (2004). Copyright 2004, American Institute of Physics.]

the dc reactive magnetron sputtering method. The samples exhibited good transmittance (over 85%) in the visible spectral range and a redshift was observed in the PL with increasing Cd composition. The films with $x \leqslant 0.53$ have structures of pure $Cd_xZn_{1-x}O$ with the c axis perpendicular to the substrate surface, while the films with $x=0.77$ were mixtures of a hexagonal ZnO phase and a cubic CdO phase. The band gaps of the $Zn_{1-x}Cd_xO$ alloy films $(0 \leqslant x \leqslant 0.53)$ could be nonlinearly tuned from 3.28 to 2.65 eV with the Cd contents from $x=0$ to $x=0.53$.

IX. PROCESSING, DEVICES, AND HETEROSTRUCTURES

A. Ohmic contacts to ZnO

An Ohmic contact can be defined as having a linear and symmetric current-voltage relationship for both positive and negative voltages and is so important for carrying electrical current into and out of the semiconductor, ideally with no parasitic resistance. It is well known that parasitic resistance, in the form of contact resistance, is one of the major obstacles in realizing long-lifetime operation of optical and electrical devices. The major loss of device performance is often caused by high-resistance metal-semiconductor Ohmic contacts through thermal stress and or contact failure.[551] Thus, in order to attain high-performance ZnO-based optical and electrical devices, it is essential to achieve Ohmic contacts that have both low resistance and are thermally stable and reliable. This can be achieved either by performing surface preparation to reduce the metal-semiconductor barrier height which would allow to increase carrier tunneling probability or by increasing the effective carrier concentration of the surface perhaps taking advantage of oxygen loss.[552–555]

Ohmic-contact metallization should be one of the main goals in improving device performance which plays an important role in device technology.[553] Although a low-resistance Ohmic contact on wide-band-gap semiconductors can be obtained by thermal annealing, surface roughness and structural degradation of the interface can be induced during the thermal annealing process,[556,557] resulting in poor device performance and reliability.[558] Therefore, it may in some instances be preferable to develop low-resistance Ohmic contacts without the use of a thermal annealing process. For that reason, in the case of Ohmic-contact technology, nonalloyed Ohmic contacts with low specific contact resistance are preferred,[555,559–561] particularly for shallow junction and low-voltage devices since they provide smooth metal-semiconductor interfaces resulting from the limited interface reaction. However, Ohmic-contact metallization technology in ZnO has not been explored extensively until now, a picture which still holds in these early stages of development.

Lee *et al.*[561] have achieved low-resistance and nonalloyed Ohmic contacts to epitaxially grown n-ZnO formed by exposing n-ZnO to an inductively coupled hydrogen and argon plasmas. It has been shown that the specific contact resistivity[562] of the resulting Ohmic contacts drastically decreased from 7.3×10^{-3} to $4.3\times10^{-5}\ \Omega\,\mathrm{cm}^2$ by hydrogen-plasma treatment using Ti/Au metallization schemes. The specific contact resistivity of the Ar-plasma-treated sample has also decreased to $5.0\times10^{-4}\ \Omega\,\mathrm{cm}^2$ which is lower by an order of the magnitude compared to that of the as-grown sample, and this decrease has been attributed to the formation of shallow donor by ion bombardment leading to oxygen vacancies on the ZnO surface. This result is comparable to the result reported by Kim *et al.*,[556] using the same metallization schemes after annealing at 300 °C. The specific contact resistance was measured to be $2\times10^{-2}\ \Omega\,\mathrm{cm}^2$ for the as-deposited contact, and 2×10^{-4} and $1\times10^{-3}\ \Omega\,\mathrm{cm}^2$ for the contacts annealed at 300 and 500 °C, respectively.[556] Annealing at 300 °C for 1 min resulted in high-quality Ohmic contacts, leading to a reduction by two orders of magnitude in specific contact resistance compared to the as-deposited contacts. This enhancement has been attributed to the combined effects of the increases in the carrier concentration near the ZnO layer surface and the contact area.

Kim *et al.*[559] have investigated nonalloyed Al and Al/Pt Ohmic contacts on n-type ZnO and found that the I-V characteristics of the as-deposited Al and Al/Pt contacts on n-type ZnO reveal linear behavior with specific contact resistivities of 8.0×10^{-4} and $1.2\times10^{-5}\ \Omega\,\mathrm{cm}^2$, respectively. Pt overlayer on Al contact, compared to the case without the overlayer, has resulted in a large reduction in the specific contact resistivity on n-type ZnO. This reduction has been

[This article is copyrighted as indicated in the article. Reuse of AIP content is subject to the terms at: http://scitation.aip.org/termsconditions. Downloaded to] IP: 128.172.48.58 On: Mon, 19 Oct 2015 20:45:44

attributed to the prevention of surface oxide layer (Al–O) by the Pt metal. A nonalloyed In-based Ohmic contact which has been formed on a hydrothermally grown *n*-type ZnO substrate by KrF excimer laser irradiation with 0.3 J/cm^2 and metal deposition without any impurity doping has been investigated by Akane *et al.*[560] The In-deposited laser-irradiated sample exhibited Ohmic behavior with a resistivity of $7\times10^{-1}\ \Omega\ cm^2$. The same, however, was not the case for unirradiated samples with and without the contact metal which indicates that the laser irradiation enables current conduction into the *n*-type ZnO substrate. A decrease in the current density was also observed after 5-min postannealing at 300 °C, which resulted in degradation of the electrical properties. In addition, Ti/Au contacts showed thermal degradation after annealing at temperatures in excess of 300 °C (Ref. 556) and the same behavior was observed by Akane *et al.*[560] for In Ohmic contacts annealed at 300 °C for 5 min. Kim *et al.*[563] have investigated Ru Ohmic contacts to *n*-type ZnO. In spite of the fact that the as-deposited Ru contact yielded a specific contact resistivity of $2.1\times10^{-3}\ \Omega\ cm^2$, the contact annealed at 700 °C for 1 min yielded a specific contact resistance of $3.2\times10^{-5}\ \Omega\ cm^2$, about two orders of magnitude smaller compared to the as-deposited one without showing any electrical and thermal degradation observed in the case of Ti/Au and In contacts. It was also shown that prolonged annealing (10 min) at the same temperature caused no significant electrical and surface morphology degradation, indicating that Ru is suitable for high-temperature ZnO devices.[563] The surface modification (by means of applying a high-energy beam of Ga ions before the metal deposition) and Pt direct-write metal deposition approach have been applied to unintentionally doped *n*-type ZnO films and linear Ohmic-contact characteristics have been achieved.[553,564] The specific contact resistivity values for surface-modification doses $D_{s1}=1\times10^{17}\ cm^{-2}$, $D_{s2}=3\times10^{17}\ cm^{-2}$, and $D_{s3}=3\times10^{16}\ cm^{-2}$ have been obtained as 3.1, 3.3, and $3.7\times10^{-4}\ \Omega\ cm^2$, respectively. These values are one order of magnitude lower than the lowest specific contact resistance ($4.1\times10^{-3}\ \Omega\ cm^2$) for Pt direct write without surface-modified contacts.[553,564]

Sheng *et al.*[555] have fabricated Al/Au nonalloyed Ohmic contacts on epitaxial $Mg_xZ_{1-x}O$ ($0\leqslant x\leqslant0.34$) making use of the low barrier height of Al on ZnO.[565] The specific contact resistance has been investigated as a function of Mg composition in ZnO films and it has been shown that with increasing Mg composition (increasing band gap) the specific contact resistance increased from 2.5×10^{-5} to $9.1\times10^{-3}\ \Omega\ cm^2$. This represents an increase of more than two orders of magnitude as compared to a ZnO sample with an electron concentration of $1.6\times10^{17}\ cm^{-3}$. The experimental specific contact resistances as a function of temperature for unintentionally and heavily Ga-doped ZnO have been given in Fig. 105. It has been shown that if the electron concentrations increased (by Ga doping during the growth), the specific contact resistivity would decrease because of the increased tunneling. Another observation was that, even if the specific contact resistivity did not change as a function of temperature, the heavily doped ZnO showed lower specific contact resistivity than that for the unintentionally doped ZnO.[555]

Ip *et al.*[566] could obtain a minimum specific contact resistance of $6\times10^{-4}\ \Omega\ cm^2$ for Ti/Al/Pt/Au contacts on undoped ($n=10^{17}\ cm^{-3}$) bulk ZnO. The contacts did not show Ohmic behavior in the as-deposited state and reached their minimum resistance after 250 °C annealing. This value was essentially independent of the surface cleaning procedure employed, including sequential solvent cleaning or H_2 plasma exposure. Higher annealing temperatures degraded the specific contact resistance, and Auger electron spectroscopy depth profiling revealed increasing intermixing of the metal layers and reaction of Ti with ZnO. The Al was observed to outdiffuse to the surface at temperatures as low as 350 °C, and the contact metallization was almost completely intermixed by 600 °C.

The carrier-concentration dependence of the Ti/Al/Pt/Au Ohmic-contact resistance on P-doped *n*-type ZnO thin films ($7.5\times10^{15}-1.5\times10^{20}\ cm^{-3}$) has also been reported.[567,568] Even in the as-deposited state, low specific contact resistances in the range from 3×10^{-4} to $8\times10^{-7}\ \Omega\ cm^2$ were observed. The lowest specific contact resistance of $8\times10^{-7}\ \Omega\ cm^2$ for nonalloyed Ohmic contacts was achieved in the sample with a carrier concentration of $1.5\times10^{20}\ cm^{-3}$ when measured at 30 °C. In the annealed samples, minimum specific contact resistances of 3.9×10^{-7} and $2.2\times10^{-8}\ \Omega\ cm^2$ were obtained in the samples with carrier concentrations of $6.0\times10^{19}\ cm^{-3}$ measured at 30 °C and $2.4\times10^{18}\ cm^{-3}$ measured at 200 °C, respectively. Figure 106 shows the dependence of specific contact resistance on carrier concentration for the as-deposited and annealed contacts. Temperature-dependent measurements showed that the dominant transport mechanisms were tunneling in the contacts for the most highly doped films and thermionic emission for the more lightly doped films. As in the bulk ZnO case, Auger electron spectroscopy detected Ti–O interfacial reaction and intermixing between Al and Pt at 200 °C. The significant changes in morphology even for low-temperature (200 °C) anneals suggest that more thermally stable contact schemes should be investigated.

Some of the various Ohmic-contact metallization schemes to *n*-type ZnO are summarized in Table XVIII together with carrier concentration, specific contact resistance, and method used to measure the specific contact resistivity. Recently, Al,[569–571] Al/Au,[572] Ti,[573] In,[574] InGa (Ref. 575) metallizations were also used to obtain Ohmic contacts. Despite some progress in ZnO-based devices, there is still difficulty in the reproducible growth of *p*-type ZnO and very limited information about Ohmic contacts to *p*-type ZnO material.[475,576,577] For that reason, the Ohmic contact to the *p*-type ZnO material will not be discussed here.

B. Schottky contacts to ZnO

In spite of the fact that high-quality Schottky contacts are critical for ZnO device applications, there is little information about the Schottky contacts on ZnO to date. The chemical reactions between the metal and the semiconductor,

[This article is copyrighted as indicated in the article. Reuse of AIP content is subject to the terms at: http://scitation.aip.org/termsconditions. Downloaded to] IP: 128.172.48.58 On: Mon, 19 Oct 2015 20:45:44

TABLE XVIII. Ohmic contacts to *n*-type ZnO for various metallization schemes. *c*-TLM stands for circular transmission line method.

Metallization	Type	Annealing conditions	Carrier concentration (cm^{-3})	ρ_c at RT ($\Omega\ cm^2$)	Method of ρ_c measurement	Ref.
Al/Au	*n*	⋯	1.6×10^{17}	2.5×10^{-5} for ZnO 9.1×10^{-5} for $Mg_{0.34}Zn_{0.66}O$	TLM	555
Ti/Au	*n* (Al-doped)	As grown 300 °C for 1 min 500 °C for 1 min	2×10^{17}	2.0×10^{-2} as deposited 2.0×10^{-4} annealed at 300 °C 1.0×10^{-3} annealed at 500 °C	*c*-TLM	556
Al	*n* (Al-doped)	Nonannealed	2×10^{18}	8.0×10^{-4}	*c*-TLM	559
Al/Pt	*n* (Al-doped)	Nonannealed	2×10^{18}	1.2×10^{-5}	*c*-TLM	559
In	*n*	Nonannealed 300 °C for 5 min	Unintentionally doped	7.0×10^{-1} as deposited (KrF preirradiation) 7.3×10^{-1} annealed at 300 °C	TLM	560
Ti/Au	*n* (Al-doped)	⋯	7×10^{17}	7.3×10^{-3} as deposited 4.3×10^{-5} H_2 plasma, 5.0×10^{-4} Ar plasma	TLM	561
Ru	*n*	As grown 700 °C for 1 min	3×10^{18}	2.1×10^{-3} as deposited 3.2×10^{-5} annealed at 700 °C	*c*-TLM	563
Pt-Ga	*n*	⋯	Unintentionally doped	4.1×10^{-3} without surface modification 3.1×10^{-4} for dose of $D_{s1}=1\times10^{17}$ cm^{-2}, 3.3×10^{-4} for dose of $D_{s2}=3\times10^{17}$ cm^{-2} 3.7×10^{-4} for dose of $D_{s3}=3\times10^{16}$ cm^{-2}	TLM	553 and 564
Ti/Al/Pt/Au	*n*	250 °C	Unintentionally doped (10^{17})	6×10^{-4}	*c*-TLM	566
Ti/Al/Pt/Au	*n* (*P*-doped)	As grown 200 °C	1.5×10^{20} 6.0×10^{19}	8.0×10^{-7} 3.9×10^{-7}	TLM	567 and 568

the surface states, the contaminants, the defects in the surface layer, and the diffusion of the metal into the semiconductor are well-known problems in the formation of Schottky contacts. For instance, in the case of ZnO Al is expected to produce the most dissociated cations (Zn) in ZnO because of its strong reaction with anions (O) in ZnO. This results in low barrier height and leakage current.

To create Schottky barrier with undoped ZnO, a high work function can be applied to the surface of a ZnO crystal. Although many publications[575,578] show that Au has some serious problems at high temperatures (>340 K), it has widely been applied to ZnO to form Schottky barriers.[573–575,578–580] Other metals used for the same purpose are Ag,[569–571,574,578,579] Pd,[580,581] and Pt.[582–585] It has been found that all these reactive metals form relatively high Schottky barriers of 0.6–0.84 eV to the *n*-type ZnO.

Although Schottky barrier heights were reported by Mead[579] for various metal contacts on vacuum-cleaved *n*-type ZnO surfaces in 1965, the thermal stability of the Schottky diodes fabricated on ZnO has not been extensively studied. It was observed that Au Schottky contacts resulted in poor current-voltage characteristics and degraded easily with thermal cycling of the samples.[571] This study showed that the thermal stability of Ag Schottky contacts was better than that of Au Schottky contacts. Mead[579] measured barrier heights for Ag and Au Schottky contacts as 0.68 and 0.65 eV, respectively. Neville and Mead[580] investigated surface-barrier systems consisting of Au and Pd on bulk ZnO, which were chemically prepared by concentrated phosphoric acid, concentrated HCl, and organic solvents and showed an ideality factor very close to unity (1.05). Koppa *et al.*[573] have investigated Au Schottky contacts on *n*-type ZnO wafers which were clean, stoichiometric, highly ordered, and smooth after exposure to an O_2/He plasma. Significant improvement in the *I-V* characteristics of as-deposited Au Schottky contacts was observed relative to those characteristics measured for similar contacts deposited on the same surfaces of the as-received wafers. Compared to the contacts on the as-received material which showed microampere leakage currents and ideality factors of $n>2$, contacts on plasma-cleaned wafers cooled in vacuum showed leakage current of about 36 nA at −4 V, a barrier height of 0.67 eV, and an ideality factor of 1.86. Furthermore, contacts on plasma-cleaned wafers cooled in the unignited plasma gas followed by 30-s exposure to the plasma at room temperature showed a leakage current of about 20 pA at −7 V, a barrier height of 0.60 eV, and an ideality factor of 1.03.[573]

Au and Ag Schottky contacts on epiready (0001) Zn surface of undoped *n*-ZnO samples have been investigated by Polyakov *et al.*,[578] comparing their barrier heights and thermal stabilities. Schottky barrier heights of 0.65–0.69 eV and diode ideality factors of 1.6–1.8 have been obtained by capacitance-voltage and current-voltage measurements, respectively. The ideality factor had a value close to 2 for almost all the samples studied due to an increase of the tunneling current through the junction.[586] Both the Au and the Ag Schottky diodes have shown degradation, but with different degradation characteristics, after heating in vacuum up to temperatures even as low as 365 K. Sheng *et al.*[570] have fabricated Ag Schottky contacts on the $(11\bar{2}0)$ *a* surface of an epitaxial ZnO film grown by MOCVD. The Schottky barrier height at room temperature was determined to be 0.69 eV by thermionic emission using *I-V-T* measurements. The ideality factor decreased from 1.37 to 1.29 as the temperature was increased from 265 to 340 K. The reason for

[This article is copyrighted as indicated in the article. Reuse of AIP content is subject to the terms at: http://scitation.aip.org/termsconditions. Downloaded to] IP: 128.172.48.58 On: Mon, 19 Oct 2015 20:45:44

TABLE XIX. Schottky contacts to n-type ZnO.

Metal	Deposition method	ϕ_B (eV)	Method of ϕ_B measurement	Ideality factor (n)	Method of n measurement	Ref.
Ag	Electron beam	0.84		1.5	*I-V*	569
Ag	Electron beam	0.69	*C-V*, *I-V*	1.37 at 265 K 1.33 at RT 1.29 at 340 K	*I-V*	570
Au	Electron beam	⋯ 0.67 0.60		>2 as received 1.86 (plasma cleaned) 1.03 (unignited plasma, 30-s plasma)	*I-V*	573
Au	Vacuum	0.50	*I-V*	1.3–1.6	*I-V*	574
Au	⋯	⋯	⋯	1.19	*I-V*	575
Au	Vacuum	0.65	*C-V*	1.6–1.8	*I-V*	578
Ag	Vacuum	0.69	*C-V*	1.6–1.8	*I-V*	578
Au	Thermal	0.71	Photoresponse	⋯		579
Ag	Thermal	0.68	Photoresponse	⋯		579
Au	Thermal	0.66	*C-V*, *I-V*, Photoresponse	1.05	*I-V*	580
Pt	Electron beam	0.89 0.93	*I-V* *C-V*	1.15 (hydrogen peroxide cleaned)	*I-V*	582
Pt	Electron beam	0.7	*I-V*	1.5 (ozone cleaned)	*I-V*	583 and 584
W	Sputtering	0.49		2 (ozone cleaned)		
Pt	Electron beam	As deposited 0.61 (303 K) 0.46 (473 K) Annealed 0.42 (303 K) 0.40 (473 K)	*I-V*	As deposited 1.70 (303 K) 3.43 (473 K) Annealed (1 min at 300 °C) 4.29 (303 K) 4.78 (473 K)	*I-V*	585

the high ideality factor of 1.33 obtained by fitting the thermionic emission theory to the experimental forward *I-V* curve at room temperature could most probably be due to the existence of an interfacial layer and surface states.[570] For nonideal Schottky diodes, the flatband barrier height, which is obtained by modifying the measured one, is more meaningful. By doing so, the flatband barrier heights were determined from *I-V* and *C-V* measurements to be 0.89 and 0.92 eV, respectively.[570]

The Au and Ag Schottky contacts have been prepared by vacuum evaporation onto the $(000\bar{1})$ O-terminated surface of the ZnO crystal and characterized by measuring the *I-V* and *C-V* relationships in a temperature range of 90–300 K by Ohashi *et al.*[574] A barrier height of 0.5 eV was obtained for the Au Schottky contact which is lower than that reported for the same contact by others.[578–580] In this case of Ohashi *et al.*, the low value of the barrier height was attributed to the high donor density. The greater than unity ideality factors (1.3–1.6) obtained for the Schottky contacts are most probably due to relatively high carrier concentration leading to the increase of tunneling current through the junction.

Ip *et al.*[585] obtained the annealing and temperature dependences of the Schottky barrier height of Pt contacts on P-doped n-type ($n=10^{16}$ cm^{-3}) thin-film ZnO deposited by PLD. The carrier concentration in the films was 7.5×10^{15} cm^{-3} with a corresponding mobility of 6 cm^2/V s. For the unannealed samples, the barrier height ranged from 0.61 ± 0.04 eV at 30 °C to 0.46 ± 0.06 eV at 200 °C with saturation current densities from 1.5×10^{-4} (30 °C) to 6.0×10^{-2} A cm^{-2} (100 °C), respectively. The ideality factors increased from 1.70 at 30 °C to 3.43 at 200 °C. The measured barrier height for Pt on ZnO is similar to the value reported for both Au and Ag rectifying contacts on this material mentioned above. The barrier height reduced significantly to 0.42 eV after annealing at 300 °C (1 min) and the reverse current was larger than that predicted by thermionic emission alone in both as-deposited and annealed contacts.

Table XIX summarizes the common Schottky metals for n-type ZnO. As can be seen in this table, the ideality factor for the ZnO Schottky contacts is higher than unity in the majority of the studies. This has been explained by different mechanisms such as the prevalence of tunneling,[586] the presence of an interface layer, surface states,[570] increased surface conductivity,[573] and or the influence of deep recombination centers.[578]

C. Heterostructure devices

To reiterate, ZnO is considered as a prospective material for fabricating LED structures emitting in the UV region, because of its large excition binding energy (60 meV). As discussed in Sec. VI B the growth of reproducible p-type ZnO films is not developed yet, and therefore fabrication of ZnO p-n homojunction-based LEDs has not been possible. For this reason n-type ZnO growth on other available and comparable p-type materials could provide an alternative way for at least demonstrating the advantages of ZnO. This subject has received a great deal of attention recently, and heterojunctions of good quality have been realized using various p-type materials such as Si,[587–589] GaN,[590,591]

[This article is copyrighted as indicated in the article. Reuse of AIP content is subject to the terms at: http://scitation.aip.org/termsconditions. Downloaded to] IP: 128.172.48.58 On: Mon, 19 Oct 2015 20:45:44

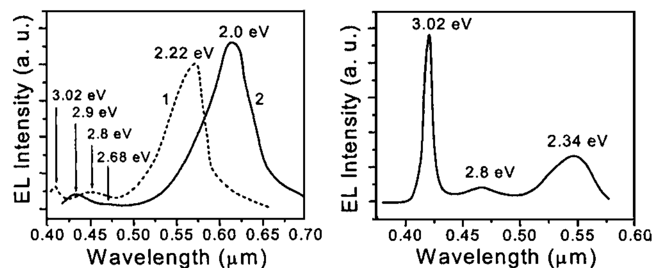

FIG. 107. Spectral characteristics of the type-I (left: curve 1 at 77 K, curve 2 at 300 K) and type-II (right: 77 K) p-ZnTe/n-ZnO heterostructures. [Reprinted with permission from A. E. Tsurkan, N. D. Fedotova, L. V. Kicherman, and P. G. Pas'ko, Semiconductors **6**, 1183 (1975). Copyright 1975, American Institute of Physics.]

AlGaN,[592] $SrCu_2O_2$,[593,594] NiO,[595] ZnTe,[596] Cu_2O,[597,598] CdTe,[599] SiC,[600,601] diamond,[602] $ZnRh_2O_4$,[603] and ZnO/GaAs.[604] Some details of these heterostructures concerning their growth and properties can be found in a recent review.[50] However, electroluminescence under forward bias was observed only in a few cases.[587,590–597] In other cases the p-n heterojunctions were considered for uses as ultraviolet photodetectors (PDs), and their photoresponse properties were studied. Among the transparent conductive oxide (TCO) materials available, ZnO is promising for PDs due to its good electrical and optical properties in addition to its low costs, nontoxicity, and relatively low deposition temperature. Besides, ZnO-based PDs are expected to have superior resistance to ionizing radiation and high-energy particles. Such a PD has a significant advantage over the indium-tin oxide (ITO) because it is simpler to fabricate. There have been a number of reports on photoresponse properties of ZnO-based PDs.[588,589,595,600,603,604] In this section, LEDs followed by PDs are discussed.

1. Light-emitting devices

In 1967, Drapak[597] fabricated ZnO-based heterostructure LED. He used Cu_2O as a p-type layer that was obtained by thermal oxidation of a Cu metal layer deposited on vapor-phase-grown ZnO substrates. The fabricated LED structures revealed EL in both forward and reverse biases, and broad spectra with maxima at 540 nm were observed.

Tsurkan *et al.*[596] grew p-ZnTe on n-ZnO substrates. They fabricated two sets of heterostructures with different carrier concentrations in both p-ZnTe and n-ZnO. In the first type (set I) heterostructure hole and electron concentrations were 9×10^{17} and 2×10^{17} cm^{-3}, and in the second type (set II) 5×10^{14} and 8×10^{18} cm^{-3}, respectively. For both types intense electro luminescence (EL) was observed under forward bias; however, spectra obtained from sets I and II heterostructures were different, as shown in Fig. 107. In set I heterostructures the EL spectrum was dominated by a broad yellow band with maxima at 2.0 and 2.22 eV at 300 and 77 K, respectively. On the other hand, the spectra in set II heterostructures consisted of an intense narrow band in the violet region with a maximum at 3.02 eV and a set of much weaker bands peaking at 2.8 and 2.34 eV, as seen in Fig. 107. A yellow band in set I p-ZnTe/n-ZnO heterostructures was explained by the authors as a result of electron injection from low-resistive n-ZnO into high-resistive p-ZnTe. In set II heterostructures violet emission at 3.02 eV was attributed to hole injection from low-resistive p-ZnTe into higher-resistive n-ZnO and was supposed to result from donor-acceptor recombination.

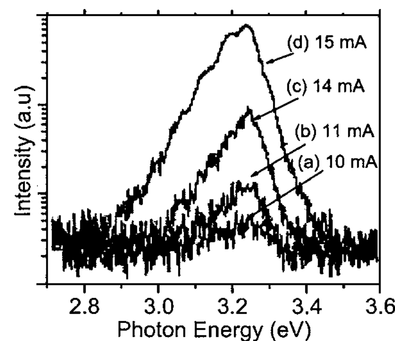

FIG. 108. Emission spectra of the p-$SrCu_2O_2$/n-ZnO p-n junction LED for several currents. The electric currents were (a) 10 mA, (b) 11 mA, (c) 14 mA, and (d) 15 mA, respectively. [Reprinted with permission from H. Ohta, K. Kawamura, M. Orita, M. Hirano, N. Sarukura, and H. Hosono, Appl. Phys. Lett. **77**, 475 (2000). Copyright 2000, American Institute of Physics.]

Ohta *et al.*[593] fabricated p-$SrCu_2O_2$/n-ZnO-type heterostructures. A Y_2O_3-stabilized ZrO_2 (YSZ) single-crystal (111) with an extremely flat surface was used as a substrate. An ITO epilayer, used as a transparent n electrode, was grown on the substrate by PLD. Then, n-ZnO and p-$SrCu_2O_2$ layers were successively deposited in the same PLD chamber. By controlling the deposition atmosphere, n-type ZnO conductivity was achieved. The p-type conductivity was controlled by substituting K^+ ions for Sr^{2+} sites in $SrCu_2O_2$. The I-V characteristics had a diodelike behavior with a turn-on voltage of ~3 V. At room temperature and under forward biased conditions the band-edge UV emission had a maximum at 382 nm. The EL spectra at various injection currents are shown in Fig. 108. An abrupt increase in the EL intensity with increasing injection current was observed without a significant change in the spectral shape or the peak energy. However, the external quantum efficiency of the diode was very low (<0.001%) because of what was termed to be the interface nonuniformity. The 3-V turn-on voltage is in good agreement with the band-gap energy of ZnO. The authors attributed the observed UV emission to a transition associated with the electron-hole plasma in ZnO.

The most important factor in realizing high-quality heterostructure devices is the structural relationship between the semiconductors forming the heterojunctions, because the lattice mismatch causes extended defects with detrimental effects at the interface which act mainly as nonradiative centers. For this reason using materials with close lattice parameters is essential for fabricating high-quality heterostructure devices. As discussed in Sec. II (Table VIII), among all the non-ZnO-related semiconductors, semiconductor GaN is the one which has a very close lattice parameters to ZnO, with a lattice mismatch of 1.8%. Therefore, in the absence of p-type ZnO, fabricating heterostructures using p-type GaN and n-type ZnO is promising. Recently there have been several reports on such heterostructures.[590–592]

[This article is copyrighted as indicated in the article. Reuse of AIP content is subject to the terms at: http://scitation.aip.org/termsconditions. Downloaded to] IP: 128.172.48.58 On: Mon, 19 Oct 2015 20:45:44

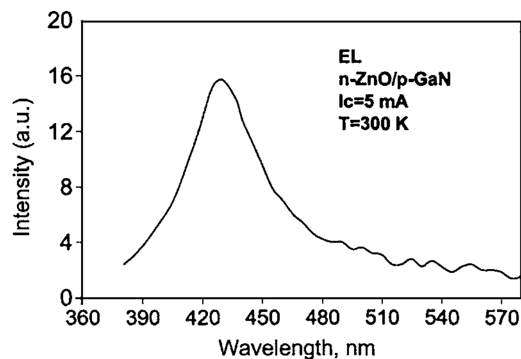

FIG. 109. Electroluminescence spectrum of an n-ZnO/p-GaN heterostructure. [Reprinted with permission from Ya. I. Alivov, J. E. Van Nostrand, D. C. Look, M. V. Chukichev, and B. M. Ataev, Appl. Phys. Lett. **83**, 2943 (2003). Copyright 2003, American Institute of Physics.]

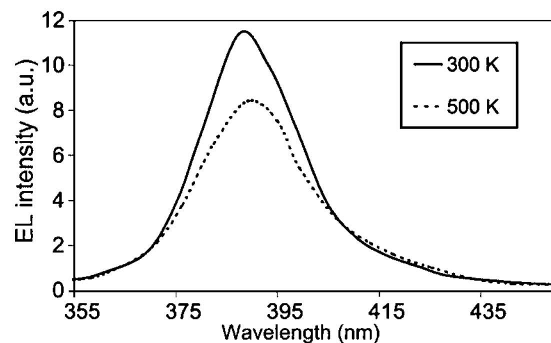

FIG. 111. Electroluminescence spectra of an n-ZnO/p-$Al_{0.12}Ga_{0.88}N$ heterostructure light-emitting diode at 300 and 500 K. [Reprinted with permission from Ya. I. Alivov, E. V. Kalinina. A. E. Cherenkov,D. C. Look, B. M. Ataev, A. K. Omaev, M. V. Chukichev, and D. M. Bagnall, Appl. Phys. Lett. **83**, 4719 (2003). Copyright 2003, American Institute of Physics.]

Alivov *et al.*[590] have reported growth, processing, and fabrication of n-ZnO/p-GaN heterojunction LED devices, where the 1-μm-thick CVD-grown n-ZnO (Ga-doped) and the MBE-grown p-GaN (Mg-doped) layers had carrier concentrations of 4.5×10^{18} and 3×10^{17} cm^{-3}, respectively. Cathodoluminescence measurements have shown two sets of peaks appearing at 390 and 510 nm, and 383 and 430 nm for ZnO and GaN, respectively. EL was observed under forward bias and the spectrum consisted of a band with a maximum at 430 nm as depicted in Fig. 109, and it has been pointed out that EL emerges from p-GaN, where the radiative recombination occurs, since the probable band alignment favors electron injection from the n-ZnO to the p-GaN.

To favor hole injection into ZnO thereby promote emission in that material, Alivov *et al.*[592] fabricated n-ZnO/p-$Al_{0.12}Ga_{0.88}N$ heterojunction LEDs on 6H-SiC substrates, a schematic depiction of which is shown in Fig. 110. Diode-like, rectifying *I-V* characteristics, with a turn-on voltage of $\sim$3.2 V and a low reverse leakage current of $\sim10^{-7}$ A were observed at room temperature. As shown in Fig. 111, an intense 389-nm UV emission, which was stable at temperatures up to 500 K, is observed when the diode is forward biased. It was also shown that this emission originated from the excitonic recombination within the ZnO layer. The energy diagram for this heterostructure obtained from the Anderson model[605] shows a higher barrier for electrons than that for holes (valence- and conduction-band offsets of 0.11 and 0.45 eV, respectively). Therefore, hole injection from wider-band-gap $Al_{0.12}Ga_{0.88}N$ side ($E_g\sim3.64$ eV) into ZnO side ($E_g\sim3.3$ eV) of the heterojunction is much more likely and is responsible for recombination emission in ZnO as opposed to the p-GaN/n-ZnO case where the electron injection from ZnO to GaN with a concomitant emission in GaN dominated the spectrum. It should be pointed out, of course, that the Anderson model describes the band diagram for the ideal case where there is no lattice mismatch between contacting materials and there are no imperfections at the interface; however, it allows us to sketch the most probable heterojunction band alignment.

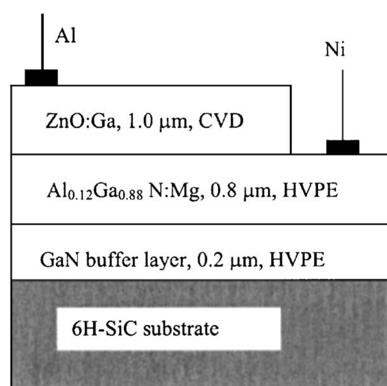

FIG. 110. Schematic diagram of the n-ZnO/p-$Al_{0.12}Ga_{0.88}N$ heterojunction LED structure [after Alivov *et al.* (Ref. 592)].

Similar results were obtained recently from n-$Mg_{0.1}Zn_{0.9}O$/n-ZnO/p-$Al_{0.16}Ga_{0.84}N$/p-GaN triple heterostructure LEDs fabricated by Osinsky *et al.*[606] The strong electroluminescence at 390 nm, observed under forward bias, was also attributed to excitonic recombination in the ZnO layer. These results show that p-AlGaN is a good candidate for fabricating efficient heterostructure LEDs with ZnO active layers.

For potential ZnO-based laser diodes, lasing would occur due to excitonic UV transitions and would therefore lead to much lower threshold currents compared to other materials. It is well known that employing a p-n-n (or n-p-p) -type double heterostructure (DH) (a quantum well straddled by larger band-gap barrier layers) is a very effective means to achieving low threshold laser diodes owing to better carrier and optical confinement that provides higher internal quantum efficiencies, lower diffraction losses, superinjection, and weaker temperature dependence. The carrier confinement, resulting from the potential barriers at both sides of the heterojunctions, increases the carrier density in the recombination region and practically eliminates the spread of the injected carriers beyond the active region. Consequently, growth of ZnO-based DH placing ZnO between wider-band-gap p- and n-type materials (for example, GaN, ZnMgO, and AlGaN) could pave the way for fabrication of laser diodes with ZnO as the active layer. Recently Alivov *et al.*[607] demonstrated high-quality p-GaN/n-ZnO/n-GaN DH with good *I-V* and EL characteristics. A 0.7-μm-thick Mg-doped p-type GaN layer was deposited first on a c-plane sapphire substrate by OMVPE. On this composite an unintentionally doped 0.4 -μm-thick n-type ZnO layer was grown by plasma-assisted

[This article is copyrighted as indicated in the article. Reuse of AIP content is subject to the terms at: http://scitation.aip.org/termsconditions. Downloaded to] IP: 128.172.48.58 On: Mon, 19 Oct 2015 20:45:44

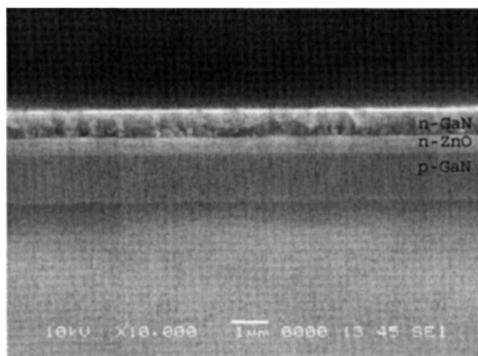

FIG. 112. Scanning electron microscope image of the grown n-GaN/n-ZnO/p-GaN double heterostructure [after Alivov *et al.* (Ref. 607)].

MBE at a substrate temperature of 600 °C. Finally, a 0.4-μm-thick n-GaN layer was grown at 550 °C on the n-ZnO layer by plasma-assisted MBE. In Fig. 112 scanning electron microscopy of this n-GaN/n-ZnO/p-GaN double heterostructure is presented, indicating sharp interfaces to the extent discernable by scanning electron microscopy (SEM). Fabricated diode structure exhibited rectifying diodelike behavior with low leakage current of 4.4×10^{-7} A and a breakdown voltage of 12 V. At room temperature EL was observed under forward bias, which blueshifted with increasing bias, as shown in Fig. 113. From a comparison of EL with the PL spectra of n-ZnO and p-GaN it was concluded that the emission is primarily from the ZnO region of the DH. Since DH lasers are greatly dependent on the physical properties of the well layer and its thickness which in this case is ZnO, by modifying these parameters the quality of such DH could be significantly improved.

2. Photodiodes

There have been many reports regarding the photoresponse properties of the ZnO-based heterojunctions.[588,589,595,600,603,604] For example, Jeong *et al.*[588] reported on the photoelectric properties of n-ZnO/p-Si photodiode (PD) which detect UV photons in the depleted n-ZnO and simultaneously detect visible photons in the depleted p-Si by employing two related photoelectric mechanisms. The *I-V* measurements obtained while the photodiodes are exposed to radiation in a wavelength range of

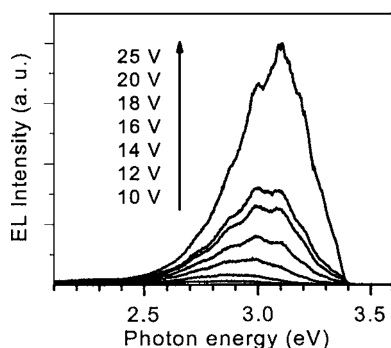

FIG. 113. Electroluminescence spectra of the n-GaN/n-ZnO/p-GaN double heterostructure diode at various forward biases [after Alivov *et al.* (Ref. 607)].

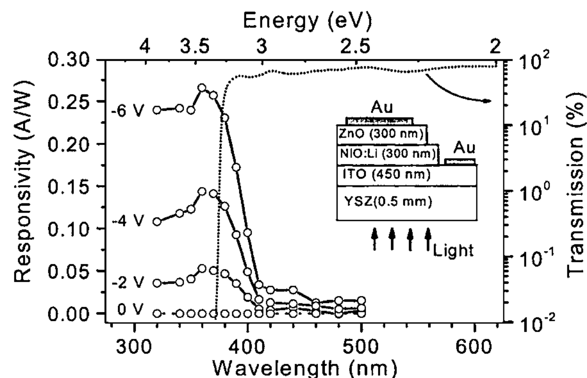

FIG. 114. Spectral response of the p-$ZnRh_2O_4$/n-ZnO diode at several reverse-bias voltages. The device structure is also shown in the inset. [Reprinted with permission from H. Ohta, M. Hirano, K. Nakahara, H. Maruta, T. Tanabe, M. Kamiya, T. Kamiya, and H. Hosono, Appl. Phys. Lett. **83**, 1029 (2003). Copyright 2003, American Institute of Physics.]

310–650 nm showed a linear increase in photocurrent with reverse bias. In the visible range, the photocurrent rose rapidly with bias but saturated beyond a critical voltage. The diodes exhibited high responsivities of 0.5 and 0.3 A/W for UV (310-nm) and red (650-nm) photons, respectively, under a 30-V bias with a minimum near 380 nm which corresponds to the band gap of ZnO.

Transparent window p-NiO/n-ZnO PDs were heteroepitaxially grown by Ohta *et al.*[595] on a YSZ (111) substrate by PLD combined with a solid-phase-epitaxy technique. The fabricated diodes exhibited clear rectifying *I-V* characteristics with an ideality factor of ~2 and a forward turn-on voltage of ~1 V. Spectral responsivity measurements were performed via photoexcitation from the substrate side using a monochromated Xe lamp light under several reverse-bias conditions. A photoresponsivity as high as ~0.3 A W^{-1} was achieved at 26-V reverse bias under irradiation by 360-nm light that corresponds to the ZnO energy gap.

Ohta *et al.*[603] also reported on transparent *p-n* heterojunctions composed of p-$ZnRh_2O_4$ and n-ZnO thin layers grown by reactive solid-phase epitaxy technique (Fig. 114). Polycrystalline $ZnRh_2O_4$ was deposited on a ZnO epitaxial layer at room temperature. Thermal annealing of the bilayer sample at 950 °C in air converted the polycrystalline $ZnRh_2O_4$ layer to what was reported to be an epitaxial single-crystalline layer. The resultant *p-n* heterojunctions had an abrupt interface and exhibited distinct rectifying *I-V* characteristics with a threshold voltage of ~2 V that is in agreement with the band-gap energy of $ZnRh_2O_4$. The photovoltage originating mainly from the n-ZnO layer was also observed.

As discussed above, the critical factor influencing the properties of heterostructures is the similarity of the lattice parameters. In this respect 6H-SiC seems to be a good candidate since it has a relatively small lattice mismatch with ZnO (~4%, Table VIII), and p-6H-SiC substrates are commercially available. Alivov *et al.*[600,601] fabricated n-ZnO/p-6H-SiC-type PDs growing 0.5-μm-thick n-ZnO layer on p-type 6H-SiC substrates at 600 °C by plasma-assisted MBE and demonstrated high-quality *p-n* heterojunctions. Ohmic contacts to the 250-μm-diameter mesastructures were made

[This article is copyrighted as indicated in the article. Reuse of AIP content is subject to the terms at: http://scitation.aip.org/termsconditions. Downloaded to] IP: 128.172.48.58 On: Mon, 19 Oct 2015 20:45:44

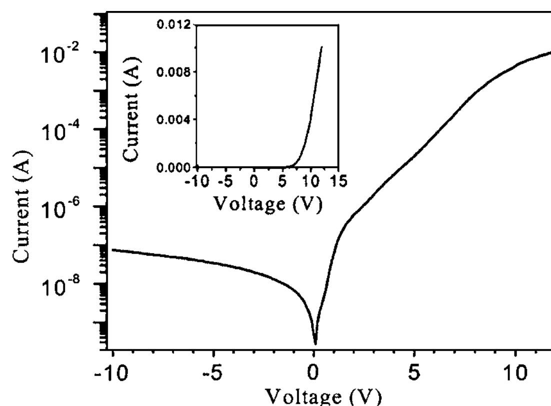

FIG. 115. Room-temperature *I-V* characteristics of *n*-ZnO/*p*-SiC heterojunctions [Reprinted with permission from Ya. I. Alivov, Ü. Özgür, S. Doğan, D. Johnstone, V. Avrutin, N. Onojima, C. Liu, J. Xie, Q. Fan, and H. Morkoç, Appl. Phys. Lett. **86**, 241108 (2005). Copyright 2005, American Institute of Physics.]

by vacuum evaporation of 300/1000-Å-thick Au/Al and Au/Ni metal layers to *n*-ZnO and *p*-SiC layers, respectively. The *I-V* characteristics of the *n*-ZnO/*p*-SiC heterostructures shown in Fig. 115 revealed a diodelike behavior with turn-on and soft breakdown voltages of ~5 and −23 V, respectively, and low leakage current of $\sim 10^{-7}$ A under −10-V reverse bias. When illuminated from the ZnO side of the heterostructure, the *n*-ZnO/*p*-6H-SiC structures exhibited quite good photosensitivity to UV radiation with a maximum at ~3.283 eV, as illustrated in Fig. 116. Photoresponse as high as 0.045 A/W at −7.5-V reverse bias was observed.

D. Metal-insulator-semiconductor diodes

In the absence of *p-n* junctions, electroluminescence properties of ZnO could be exploited by fabricating metal-insulator-semiconductor (MIS) structures which do not require *p*-type ZnO. In spite of this, there have been only a few reports on such MIS structures.[461,608,609] Shimizu *et al.*[608] fabricated a MIS diode with an insulating ZnO layer obtained by keeping the ZnO crystal in a 30% solution of H_2O_2. At room temperature (RT) this diode emitted in the defect-related green region of the spectrum, with a peak at 2.5 eV. Minami *et al.*[609] used an insulating SiO layer deposited by thermal evaporation, and under forward bias the device emitted in the UV region (3.13 eV) at 300 K. The current-voltage characteristics of the diodes showed a typical nonlinear behavior.

In a more recent work by Alivov *et al.*[461] ion implantation was employed to produce an insulating ZnO layer. In this work, 2-μm-thick ZnO:Ga films were implanted with 180-keV N^+ ions to a dose of 1.2×10^{14} cm^{-2} at a sample temperature of 773 K. The penetration depth at the ion energy of 180 keV, calculated by a transport of ions in matter (TRIM) program, was about 0.25 μm which sets the thickness of the insulating layer to 0.25 μm. MIS diodes were fabricated by first masking the surface and then using a 10% HNO_3 aqueous solution to remove part of the upper (insulating) ZnO layer to provide access to the conducting ZnO layer below for Ohmic-contact formation. The top Au metal layer, deposited thermally onto the insulating layer (*i*-layer), was 1.8 mm in diameter. The Ohmic contact to the lower conducting layer was made by indium evaporation. The *I-V* characteristics of a typical diode are shown in Fig. 117. This figure shows a quite good, rectifying behavior of the MIS diode, with a threshold voltage near 3 V and a reverse current of about 10^{-6} A (or current density of 3.93×10^{-5} A/cm^2). Under forward bias (metal positive), UV light emission was observed at RT with a maximum at ~388 nm (3.197 eV) and a FWHM of 128 meV. A typical EL spectrum at 30-mA forward current is shown in Fig. 118 (curve *a*). As can be seen, the EL spectrum of the LED is very similar to the CL spectrum of the ZnO layer, from

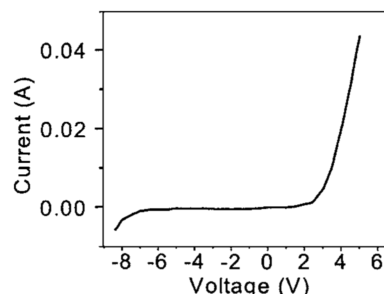

FIG. 117. Current-voltage characteristics of the ZnO MIS diode. [Reprinted from Ya. I. Alivov, D. C. Look, B. M. Ataev, M. V. Chukichev, V. V. Mamedov, V. I. Zinenko, Yu. A. Agafonov, and A. N. Pustovit, Solid-State Electron. **48**, 2343 (2004), Copyright 2004, with permission from Elsevier.]

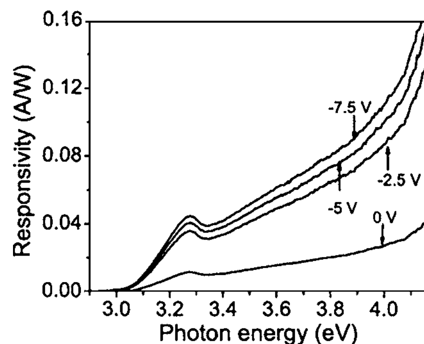

FIG. 116. Spectral photoresponse of the *n*-ZnO/*p*-SiC photodiode structure at various reverse biases. [Reprinted with permission from Ya. I. Alivov, Ü. Özgür, S. Doğan, D. Johnstone, V. Avrutin, N. Onojima, C. Liu, J. Xie, Q. Fan, and H. Morkoç, Appl. Phys. Lett. **86**, 241108 (2005). Copyright 2005, American Institute of Physics.]

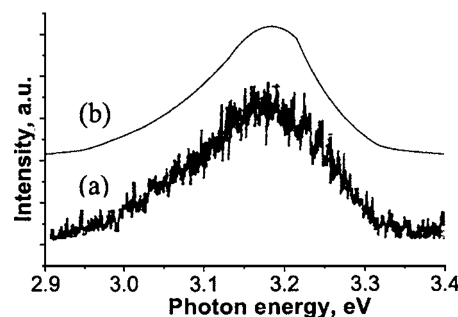

FIG. 118. Room-temperature (a) EL and (b) CL spectra of the MIS diode and ZnO layer, respectively. [Reprinted from Ya. I. Alivov, D. C. Look, B. M. Ataev, M. V. Chukichev, V. V. Mamedov, V. I. Zinenko, Yu. A. Agafonov, and A. N. Pustovit, Solid-State Electron. **48**, 2343 (2004), Copyright 2004, with permission from Elsevier.]

[This article is copyrighted as indicated in the article. Reuse of AIP content is subject to the terms at: http://scitation.aip.org/termsconditions. Downloaded to] IP: 128.172.48.58 On: Mon, 19 Oct 2015 20:45:44

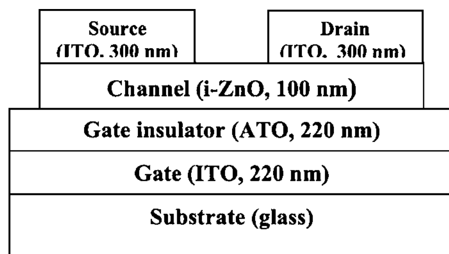

FIG. 119. The schematics of a typical TTFT structure. [Reprinted with permission from R. L. Hoffman, B. J. Norris, and J. F. Wager, Appl. Phys. Lett. **82**, 733 (2003). Copyright 2003, American Institute of Physics.]

which it can be concluded that the radiation mechanisms in both cases are similar, that is very probably excitonic in nature. No EL emission was observed under reverse-bias conditions for both MIS structure and that without an insulating layer. It is known that the properties of the MIS diodes depend strongly on the properties of the isolation layer—on its thickness and electrical properties. Creating a MIS diode in this manner, therefore, is of special interest since ion implantation is a very controllable technology and suitable for fabrication of various microelectronics structures. Moreover, diodes of this type are of interest not only in the design of light emitters, but also in the development of transparent transistors.

E. Transparent thin-film transistors

There has been a great interest in transparent electronics lately,[610] especially in conjunction with transparent thin-film transistors (TTFTs), because it is expected that the characteristics of TTFT will not degrade on exposure to visible light due to the wide band gap of its active channel layer, whereas the characteristics of amorphous or poly-Si TFT do degrade. Therefore, measures would not be required in this case to shield the active channel layer from visible light. ZnO for this purpose is considered as one of the best candidates because of properties such as high voltage, temperature, and radiation tolerance. Besides, high-quality crystalline ZnO films can be grown at relatively low deposition temperatures on various substrates including amorphous glasses. In this vein, a number of reports are already available on ZnO-based TTFT (Refs. 611–616) using various methods for ZnO growth.

The most important electrical parameters in quantifying TFT performance are the drain-current on-to-off ratio and active channel mobility. In terms of these parameters, the best TTFT performance has been reported by Hoffman *et al.*[613] Highly transparent ZnO-based TTFTs with optical transmittance (including substrate) of ~75% for visible light have been fabricated by rf sputtering method. A typical schematic of TTFT structure reported is shown in Fig. 119. A glass substrate was blanket coated with a 200-nm-thick layer of sputtered ITO and a 220-nm-thick layer of aluminum-titanium oxide (ATO) deposited by atomic layer deposition. ITO, a highly transparent and n-type conductor, served as the TTFT gate. The ATO layer acted as the gate insulator. The ZnO channel and ITO source/drain electrode films were deposited via ion-beam sputtering in 1024 Torr of Ar/O_2

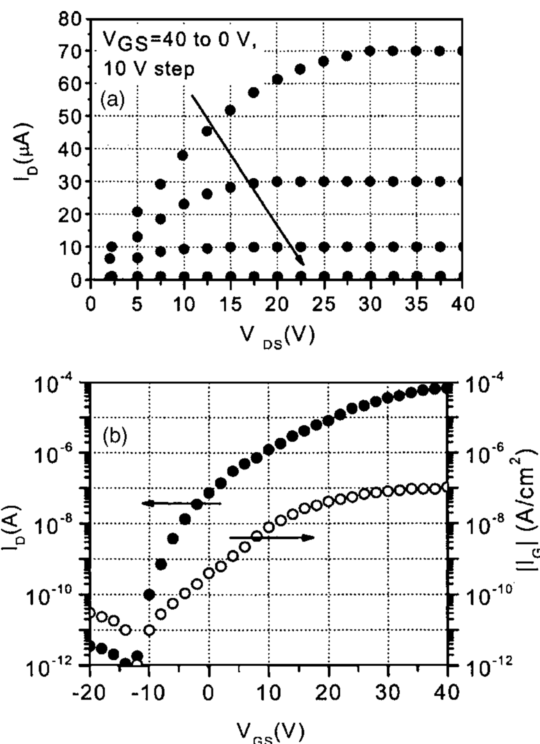

FIG. 120. Electrical characteristics of TTFT: (a) drain-current–drain-voltage (I_D-V_{DS}) characteristics; (b) transfer characteristics and gate leakage current for a TTFT with a width-to-length ratio of 10:1 for V_{DS}=10 V. [Reprinted with permission from R. L. Hoffman, B. J. Norris, and J. F. Wager, Appl. Phys. Lett. **82**, 733 (2003). Copyright 2003, American Institute of Physics.]

(80%/20%); the substrate was unheated during deposition. Shadow masks were used to pattern the ZnO channel and ITO source/drain electrodes. The channel width and length were 15 000 and 1500 μm, respectively, with a width-to-length ratio of 10:1, the source/drain contact dimensions were $15\,000 \times 1500\ \mu m^2$. After deposition of the ZnO layer, a rapid thermal anneal, typically at 600–800 °C in O_2, was employed to increase the ZnO channel resistivity in order to improve the electrical quality of the ATO/ZnO interface, and to enhance the crystallinity of the ZnO layer. Following the deposition of the ITO source/drain electrodes, a 300 °C rapid thermal annealing in O_2 was performed to improve the transparency of the ITO layer. Figure 120 displays dc drain-current–drain-voltage (I_D-V_{DS}) curves for a TTFT. Current-voltage measurements indicate n-channel, enhancement-mode TFT operation with excellent drain-current saturation and a drain-current on-to-off ratio of $\sim 10^7$. Typical TTFT dc transfer characteristics [$\log(I_D)$-V_{GS}] and gate leakage current [$\log(|I_G|)$-V_{GS}], involving the drain current I_D, gate current I_G, and the gate voltage V_{GS}, are presented in Fig. 120. These curves indicate a maximum drain-current on-to-off ratio of $\sim 10^7$. In Ref. 614 channel mobility as high as 25 cm^2/V was also reported.

In another report, Carcia *et al.*[616] fabricated ZnO thin-film transistors by rf magnetron sputtering on heavily doped n-type Si substrates held near room temperature. In this structure, the substrate side was coated with a thermal oxide layer of ~100 nm thick. Ti–Au source and drain electrodes 200 μm wide with a 20-μm gap (10-nm Ti followed by 100-nm Au) were deposited and patterned directly on the

[This article is copyrighted as indicated in the article. Reuse of AIP content is subject to the terms at: http://scitation.aip.org/termsconditions. Downloaded to] IP: 128.172.48.58 On: Mon, 19 Oct 2015 20:45:44

thermal silicon oxide layer by traditional photolithography. Ti–Au was also deposited on the back of Si to serve as a common gate electrode. A ZnO film of about 100 nm thick was then sputtered between the source and drain electrodes using a shadow mask. The best devices achieved in this work had field-effect mobility of more than 2 $cm^2/V\,s$ and an on/off ratio $>10^6$. These ZnO films had a resistivity $\sim 10^5\ \Omega\,cm$, with a high optical transparency >80% for wavelength >400 nm.

X. ZnO NANOSTRUCTURES

One-dimensional semiconductor nanowires and nanorods have attracted increasing attention due to their physical properties arising from quantum confinement (such as electronic quantum transport and enhanced radiative recombination of carriers). Nanowires have promising potentials in extensive applications and are the fundamental building blocks for fabricating short-wavelength nanolasers, field-effect transistors, ultrasensitive nanosized gas sensors, nanoresonators, transducers, actuators, nanocantilevers, and field emitters (FEs).[617–620] These nanostructures are the ideal systems for studying transport mechanisms in one-dimensional (1D) systems, which are of benefit not only for understanding the fundamental phenomena in low-dimensional systems but also for developing new generation nanodevices with high performance. Many nanowires made of materials such as Si, C, InP, GaAs, CdS, SnO_2, GaN, ZnO, and In_2O_3 have been fabricated for different applications using mostly a catalyst-assisted vapor-liquid-solid (VLS) growth method (solid-vapor process).[617,618,621,622] Among these materials ZnO is considered to be the most prospective one due to its large exciton binding energy (60 meV), high electromechanical coupling constant, and resistivity to harsh environment. Therefore, 1D ZnO structures stimulated so much attention, and a large number of publications have appeared lately reporting nanostructures of various shapes (nanowires, nanobelts, nanorings, nanotubes, nanodonuts, nanopropellers, etc.) grown by different methods.[617,618,621–640]

The growth of patterned and aligned one-dimensional nanostructures is important for device applications. Aligned growth of ZnO nanorods has been successfully achieved on a solid substrate via the VLS process with the use of catalysts, which initiate and guide the growth.[617] There were also other techniques employed for the growth of vertically aligned ZnO nanorods which did not use any catalyst.[631] The VLS processes are usually carried out in a horizontal tube furnace, as shown in Fig. 121.[619] In this schematic, the carrier gas is introduced from the left end of the alumina tube and is pumped out at the right end. The source material(s) is (are) loaded on an alumina boat and positioned at the center of the alumina tube, where the temperature is the highest. The substrate temperature usually drops with the distance of its location from the position of the source material(s). The local temperature determines the type of product that will be obtained.

In VLS nanowire growth, metals, such as Au, Fe, and Sn, act as catalysts and play a pivotal role in forming liquid alloy droplets with the nanowire component for deposition

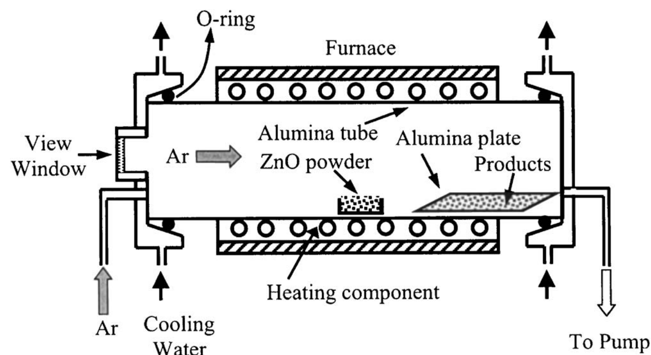

FIG. 121. A schematic diagram of the horizontal tube furnace for growth of ZnO nanostructures by the solid-vapor phase process [after Wang (Ref. 619)].

on a preferred site. For the 1D ZnO nanowires grown via the VLS process, the commonly used catalyst is Au. The spatial distribution of the catalyst particles determines the pattern of the nanowires. This step can be achieved using a variety of mask technologies for producing complex configurations. Nanowire growth begins after the liquid becomes supersaturated with reactant materials and continues as long as the catalyst alloy remains in the liquid state and the reactants are available. By choosing the optimum match between the substrate lattice and the nanowires, the epitaxial orientation relationship between the nanowire and the substrate results in the aligned growth of nanowires normal to the substrate. The size of the catalyst particles defines the diameter of the nanowires, and the epitaxial growth on the substrate results in the vertical alignment. The growth terminates when the temperature is below the eutectic temperature of the catalyst alloy or the reactant is no longer available. As a result, a nanowire obtained from the VLS process typically has a solid catalyst nanoparticle at its tip with a diameter comparable to that of the connected nanowires. Therefore, by just looking at the end of the nanowire to see whether it has a catalyst particle, one can determine if the nanowire growth was governed by a VLS process. Structurally, ZnO has three types of fast growth directions: $\langle 2\bar{1}\bar{1}0\rangle$, $\langle 01\bar{1}0\rangle$, and $\pm[0001]$. Together with the polar surfaces due to atomic terminations, ZnO exhibits a wide range of structures that can be grown by tuning the growth rates along these directions. The nanowires grow along [0001] and their side surfaces are enclosed by $\{2\bar{1}\bar{1}0\}$.

Self-organized (0001)-oriented ZnO nanowires have been synthesized on sapphire substrates with a catalyzed vapor-phase transport process using a Au thin film as the catalyst.[622] Selective nanowire growth can be readily achieved by patterning the Au thin film before growth. Typical SEM images of nanowire arrays grown on sapphire $(11\bar{2}0)$ substrates with patterned Au thin film are presented in Fig. 122. These results confirm that the ZnO nanowires grow only in the Au-coated areas, and the growth ends with Au–Zn alloy clusters on the tip of each nanowire. By adjusting the growth time, the nanowires could be grown up to 10 μm in length. The diameters of these wires range from 20 to 150 nm, whereas more than 95% of them have diameters of 70–100 nm. The diameter dispersity is due to the inhomogeneous sizes of the Au nanocluster catalysts when

[This article is copyrighted as indicated in the article. Reuse of AIP content is subject to the terms at: http://scitation.aip.org/termsconditions. Downloaded to] IP: 128.172.48.58 On: Mon, 19 Oct 2015 20:45:44

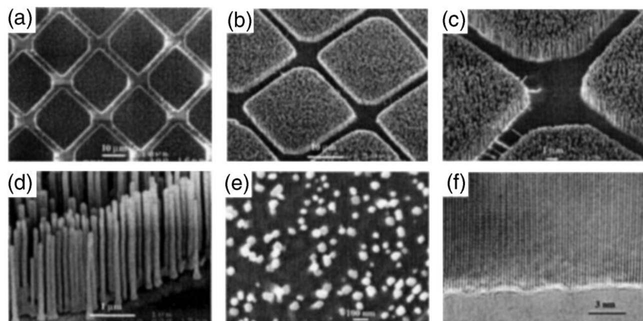

FIG. 122. Scanning electron microscope images of ZnO nanowire arrays grown on sapphire substrates [(a)–(e)]. A top view of the well-faceted hexagonal nanowire tips is shown in (e). (f) High-resolution TEM image of an individual ZnO nanowire showing its ⟨0001⟩ growth direction. [Reprinted with permission from M. H. Huang, S. Mao, H. Feick, H. Yan, Y. Wu, H. Kind, E. Weber, R. Russo, and P. Yang, Science **292**, 1897 (2001). Copyright 2001 AAAS.]

the substrate is annealed during the growth process. Haupt *et al.*[639] were able to reduce the average diameter of the nanowires below 30 nm using the same technique. The capability of patterned nanowire growth helps to fabricate nanoscale light emitters in a controllable fashion.

Room-temperature PL spectra of ZnO nanowires showed a strong band-edge emission at ~377 nm. In addition, a very weak blue band (440–480 nm) and an almost negligible green band (510–580 nm) were observed. These samples were explored for possible stimulated emission at room temperature by measuring the excitation density-dependent emission with excitation from the fourth harmonic of a Nd:yttrium-aluminum-garnet (Nd:YAG) laser (266 nm, 3-ns pulse width). Light emission was collected in the direction normal to the end surface plane (along the *c* axis) of the nanowires, and lasing was observed in the absence of any fabricated mirrors with increasing pump power, as shown in Fig. 123. At low excitation intensities, the spectrum consists of a single broad spontaneous emission peak (Fig. 123) with a full width at half maximum of 17 nm. When the excitation intensity exceeds a threshold of 40 kW/cm^2 sharp peaks emerged in the emission spectra. The linewidths of these peaks are 0.3 nm, which are 50 times smaller than the linewidth of the spontaneous emission peak. Above the threshold, the integrated emission intensity increases rapidly with the pump power indicating that stimulated emission takes place in these nanowires. The observed single or multiple sharp peaks between 370 and 400 nm represent different lasing modes. The lasing action in these nanowire arrays without any fabricated mirrors is possible if one considers these single-crystalline, well-faceted nanowires as natural resonance cavities. One end of the nanowire is the epitaxial interface between the sapphire and ZnO, whereas the other end is the sharp (0001) plane of the ZnO nanocrystals. Both ends served as good laser cavity mirrors, since the refractive index for ZnO is more than that for sapphire and air (2.45, 1.8, and 1, respectively). This natural cavity or waveguide formation in nanowires provides a simple approach to forming a nanowire laser cavity without cleavage and etching.

Park *et al.*[631] reported on the metal-organic vapor-phase epitaxial (MOVPE) growth of ZnO nanorods. The nanorods

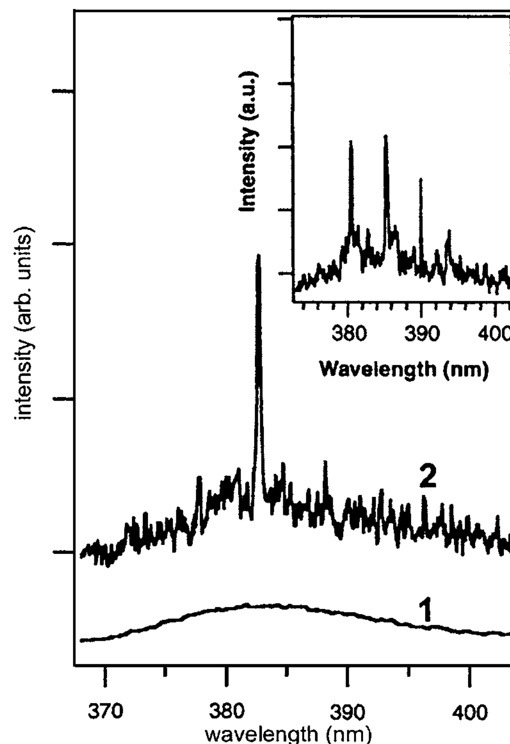

FIG. 123. Emission spectra from nanowire arrays below (line a) and above (line b and inset) the lasing threshold. The pump power levels for these spectra are 20, 100, and 150 kW/cm^2, respectively. The spectra are offset for easy comparison. [Reprinted with permission from M. H. Huang, S. Mao, H. Feick, H. Yan, Y. Wu, H. Kind, E. Weber, R. Russo, and P. Yang, Science **292**, 1897 (2001). Copyright 2001 AAAS.]

were grown on Al_2O_3 (0001) substrates at 400 °C without employing any metal catalysts usually needed in other methods (Fig. 124). The mean diameter of nanorods obtained by MOVPE was as small as 25 nm, smaller than the typical diameters of 50–100 nm for those prepared by other deposition methods.[622] Furthermore, the ZnO nanorods were well aligned vertically, showing uniformity in their diameters, lengths, and densities as revealed from electron microscopy. The results of θ-2θ scan, θ-rocking curve, and ϕ-scan measurements on the nanorods are presented in Fig. 125. Only the (002) and (004) diffraction peaks are visible in the XRD θ-2θ scans shown in Fig. 125(a), and a small full width at half maximum (FWHM) value of 0.6° was obtained from the XRD θ-rocking curve measurements [Fig. 125(b)]. Furthermore, Fig. 125(c) shows a sixfold rotational symmetry in the azimuthal scan. These results clearly indicate that the ZnO nanorods were epitaxially grown with homogeneous in-plane alignment as well as *c*-axis orientation. The PL spectra of the nanorods showed strong and narrow excitonic emission with a dominant peak at 3.29 eV and an extremely weak deep-level emission at 2.5 eV, indicating the high optical quality of the nanorods.

Li *et al.*[633] prepared ZnO nanoneedles on a silicon wafer through chemical-vapor deposition. The diameters of the needle tips were in the range of 20–50 nm. High-resolution transmission electron microscopy revealed that the nanoneedles were single crystals growing along the [0001] direction and exhibiting multiple tip surface perturbations, and were just 1–3 nm in dimension. Field-emission measure-

[This article is copyrighted as indicated in the article. Reuse of AIP content is subject to the terms at: http://scitation.aip.org/termsconditions. Downloaded to] IP: 128.172.48.58 On: Mon, 19 Oct 2015 20:45:44

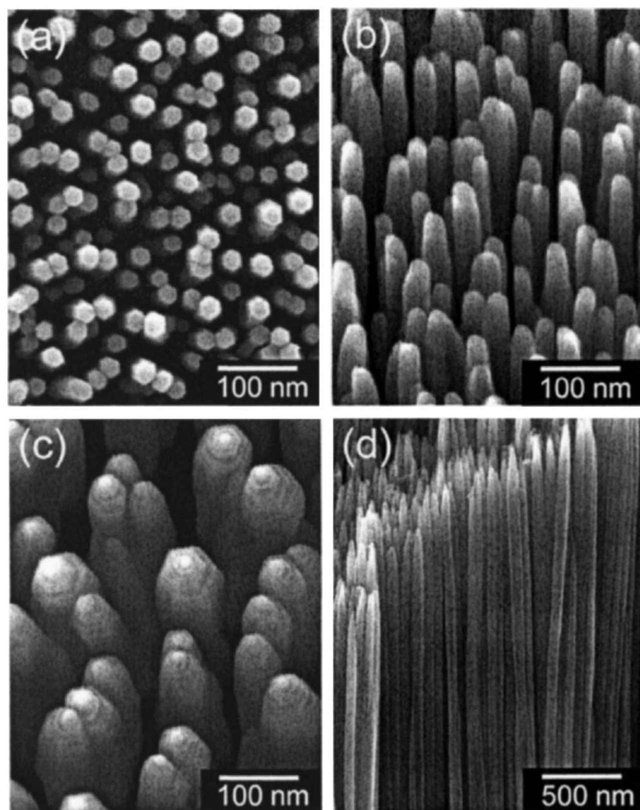

FIG. 124. FE-SEM (a) plan-view and (b) tilted images of ZnO nanorods with a mean diameter of 25 nm and (c) tilted and (d) cross-sectional images of ZnO nanorods with a mean diameter of 70 nm. In (c), hexagon-shaped pyramids with flat terraces and steps are seen at the ends of the nanorods. [Reprinted with permission from W. I. Park, D. H. Kim, S.-W. Jung, and G.-C. Yi, Appl. Phys. Lett. **80**, 4232 (2002). Copyright 2002, American Institute of Physics.]

ments on the prepared nanostructures showed fairly low turn-on and threshold fields of 2.5 and 4.0 V/mm, respectively. The nanosize perturbations on the nanoneedle tips are assumed to cause such excellent field-emission performance. The high emission current density, high stability, and low turn-on field make the ZnO nanoneedle arrays one of the promising candidates for high brightness field-emission electron sources and flat-panel displays.

Könenkamp *et al.*[641] fabricated vertical nanowire LEDs using ZnO nanowires grown by electrodeposition from aqueous solutions on fluorine-doped SnO_2-coated glass substrates. Since during electrodeposition, the growth of ZnO columns (100–200 nm in diameter and 2 μm in length) proceeded under electron injection from the underlying SnO_2 layer, a good electronic contact between SnO_2 and ZnO was assumed. The space between the nanowires was filled with polystyrene and a 0.5–1.5-μm coating of poly(3,4-ethylenedioxythiophene)(PEDOT)/poly(styrenesulfonate) was applied to establish a *p*-type contact to the nanowire tips. Finally, a 100-nm-thick Au layer was deposited by vacuum evaporation to provide a Schottky-barrier-type contact for hole injection. EL was observed from the device at a threshold of 10 V with a current density of ~100 mA/cm^2 at the nanowire tips. Similar to PL from uncoated nanowires, EL showed a broad defect-related emission centered at 620 nm. The more than an order of magnitude weaker UV band-edge

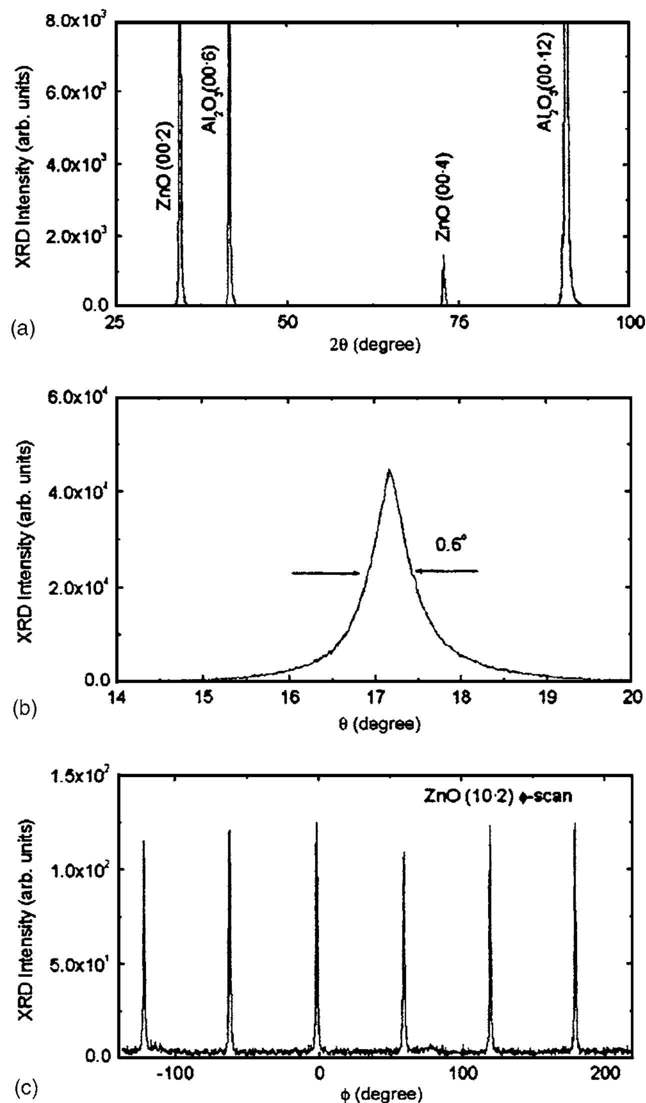

FIG. 125. XRD (a) θ-2θ scan, (b) rocking curve, and (c) azimuthal (ϕ) scan measurement results of ZnO nanorods. From the XRD θ-2θ scan data, only two peaks are shown at 34.32° and 72.59° which correspond to ZnO (002) and (004) peaks, respectively. The rocking curve also shows a FWHM value of 0.6°. A sixfold symmetry in the ϕ-scan data is also observed, indicating in-plane alignment of the nanorods. [Reprinted with permission from W. I. Park, D. H. Kim, S.-W. Jung, and G.-C. Yi, Appl. Phys. Lett. **80**, 4232 (2002). Copyright 2002, American Institute of Physics.]

emission was observed as a shoulder at 384 nm. Even though further improvements are needed on the device to enhance the UV emission, the ZnO nanowire LEDs showed a stable operation for ~1 h.

Nanobelts are nanowires that have a well-defined geometrical shape and side surfaces. Nanobelts of ZnO are usually grown by sublimation of ZnO powder without a catalyst.[642] Due to differences in surface energies among (0001), $\{01\bar{1}0\}$, and $\{2\bar{1}\bar{1}0\}$, freestanding nanobelts and nanowires of ZnO are usually dominated by the lower-energy, nonpolar surfaces such as $\{01\bar{1}0\}$ and $\{2\bar{1}\bar{1}0\}$. When there is no doping, the nanobelt grows along $[01\bar{1}0]$, with top and bottom flat surfaces $\pm(2\bar{1}\bar{1}0)$ and side surfaces $\pm(0001)$. Pan *et al.*[642] were able to grow nanobelts with each nanobelt having a uniform width along its entire length and the typical

[This article is copyrighted as indicated in the article. Reuse of AIP content is subject to the terms at: http://scitation.aip.org/termsconditions. Downloaded to] IP: 128.172.48.58 On: Mon, 19 Oct 2015 20:45:44

widths and thicknesses of the nanobelts were in the range of 50–300 nm and 10–30 nm, respectively. For investigation of quantum confinement effects, ultrasmall nanobelts having good size uniformity with an average diameter of 5.5 nm have been grown using a catalyst.[643] In comparison with the PL from nanobelts of an average width of 200 nm, the 5.5-nm nanobelts exhibited a 14-nm shift (387–373 nm) in the emission peak, indicating the quantum confinement.

ZnO nanobelts dominated by (0001) polar surfaces could also be grown by introducing In and/or Li doping.[644] In this case, the nanobelts grow along $[2\bar{1}\bar{1}0]$ (the *a*-axis), with their top/bottom large surface ±(0001) and the side surfaces $\pm(01\bar{1}0)$. These polar nanobelts tend to roll into an enclosed ring or a spiral shape to reduce the electrostatic energy. When the surface charges are not compensated during the growth, rolling of the nanobelt to form a circular ring would minimize or neutralize the overall dipole moment, reducing the spontaneous polarization-induced electrostatic energy. The minimization of the total energy, which has contributions from spontaneous polarization and elasticity produced by bending, determines the stable shape of the nanobelt.

Heo *et al.*[645] measured the temperature and the gas-ambient dependence of current-voltage characteristics of single ZnO nanorods grown by catalyst-driven MBE on Au-coated sapphire substrates. Individual nanorods were removed from the substrate and placed between Ohmic-contact pads 3.7 μm apart. The conductivity of the nanorods was increased by a postgrowth anneal in hydrogen gas at 400 °C. In the temperature range from 25 to 150 °C, the resistivity of nanorods treated in H_2 at 400 °C prior to measurement showed an activation energy of 0.089±0.02 eV and was insensitive to the ambient used (C_2H_4, N_2O, O_2 or 10% H_2 in N_2). By sharp contrast, the conductivity of nanorods not treated in H_2 was sensitive to trace concentrations of gases in the measurement ambient even at room temperature, with increased currents in the presence of hydrogen, demonstrating their potential as gas sensors. Similar devices containing multiple nanorods were also shown to have $I-V$ characteristics that are sensitive to the presence of ozone (O_3).[646]

Fabrication of single Pt/ZnO nanowire Schottky diodes was reported by Heo *et al.*[647] The ZnO nanowires were grown by site-selective MBE and then transferred to SiO_2-coated Si substrates. The diodes exhibited ideality factors of 1.1 at 25 °C and very low (1.5×10^{-10} A, equivalent to 2.35 A cm^{-2}, at −10 V) reverse currents. A strong photoresponse was also observed, with the current-voltage characteristics becoming Ohmic when the diodes were illuminated by 366-nm wavelength light. The on-off current ratio at 0.15/−5 V was ~6. Depending on these results, the thermionic emission was suggested to be the dominant current transport mechanism within the nanowire and densities of bulk and surface traps were assumed low.

ZnO nanorods and nanobelts have been successfully utilized for FETs.[648–652] Arnold *et al.*[648] fabricated FETs by depositing dispersed ZnO nanobelts on predefined gold electrode arrays. A SiO_2 gate dielectric with a thickness of 120 nm and a back gate electrode fabricated by evaporating gold on the *p*+ Si side of the substrate were used. By forming

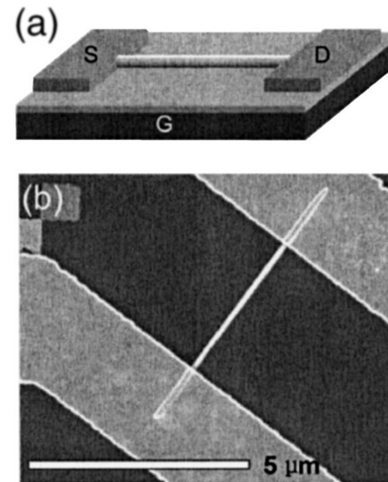

FIG. 126. (a) Schematic side view and (b) field-emission scanning electron microscopy image of a ZnO nanorod FET device. ZnO nanorod FETs with back gate geometry were fabricated on SiO_2/Si by deposition of Au/Ti metal electrodes for source-drain contacts on the nanorod ends. [Reprinted with permission from W. I. Park, J. S. Kim, G.-C. Yi, M. H. Bae, and H.-J. Lee, Appl. Phys. Lett. **85**, 5052 (2004). Copyright 2004, American Institute of Physics.]

metal electrode/nanostructure electrical contacts, where electrode gaps were as small as 100 nm and as large as 6 μm, and by capacitively coupling the nanostructure to a nearby gate electrode, a FET was produced using a nanobelt. A typical nanobelt FET showed a gate threshold voltage of −15 V, a switching ratio of nearly 100, and a peak conductivity of $1.25\times10^{-3}\ \Omega^{-1}\ \mathrm{cm}^{-1}$.[648]

High-performance *n*-channel FETs with back gate geometry were also fabricated using *e*-beam lithography along with high-quality ZnO nanorods prepared by catalyst-free MOVPE.[649] The nanorods were dispersed on SiO_2/Si substrates where the 250-nm-thick SiO_2 layer was used as an insulating gate oxide on heavily doped *n*-type Si. Au/Ti Ohmic contacts were placed only on the nanorod ends. As shown in Fig. 126 the source-drain electrodes were separated by 2–5 μm using *e*-beam lithography and lift-off method. At room temperature, typical ZnO nanorod FETs exhibited good electrical characteristics with a transconductance of 140 nS and a mobility of 75 cm^2 V^{-1} s^{-1} (at a gate voltage of 2.4 V). This electron mobility is higher than that of the ZnO thin-film transistors,[653] presumably due to high purity and low defect concentrations of single-crystal ZnO nanorods as a result of the employed catalyst-free growth method. The device characteristics significantly improved after coating the nanorod surface with a polyimide thin layer. As shown in Fig. 127 ZnO single nanorod FETs with polyimide coating had excellent conductance response to gate voltage (V_g) with a large turn-on/off ratio of 10^4-10^5, a high transconductance of 1.9 μS, and high electron mobility above 1000 cm^2 V^{-1} s^{-1}. To investigate the reproducibility of the polyimide passivation effect on the device performance, 13 different nanorod FETs were tested. The highest mobility value observed after polyimide coating was 3100 cm^2/V s, which is even higher than that of the state-of-the-art planar Si MOSFETs. As for the origin of enhanced ZnO nanorod FET characteristics, the authors claim that polyimide coating sup-

[This article is copyrighted as indicated in the article. Reuse of AIP content is subject to the terms at: http://scitation.aip.org/termsconditions. Downloaded to] IP: 128.172.48.58 On: Mon, 19 Oct 2015 20:45:44

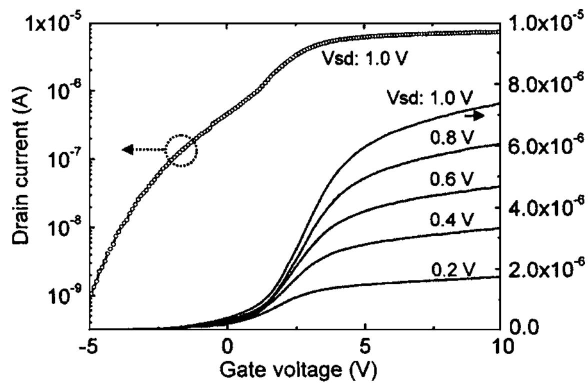

FIG. 127. Source-drain current (I_{sd}) vs gate voltage (V_g) curves (solid line) as a function of source-drain voltage (V_{sd}) and log scale plot (open circles) of I_{sd}-V_g (V_{sd}=1.0 V) for a ZnO single nanorod FET after polyimide coating on the device. [Reprinted with permission from W. I. Park, J. S. Kim, G.-C. Yi, M. H. Bae, and H.-J. Lee, Appl. Phys. Lett. **85**, 5052 (2004). Copyright 2004, American Institute of Physics.]

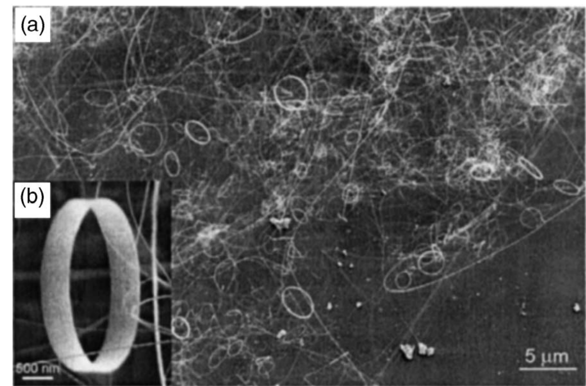

FIG. 128. (a) Low-magnification SEM image of the as-synthesized ZnO nanorings. (b) High-magnification SEM image of a freestanding single-crystal ZnO nanoring, showing uniform and perfect geometrical shape. The ring diameter is 1–4 μm, the thickness of the ring is 10–30 nm, and the width of the ring shell is 0.2–1 μm. [Reprinted with permission from X. Y. Kong, Y. Ding, R. Yang, and Z. L. Wang, Science **303**, 1348 (2004). Copyright 2004 AAAS.]

presses the chemisorption process[654,655] which decreases the transistor gain. Passivation of defects which deteriorate the FET characteristics by trapping and scattering carriers,[656,657] and formation of a gate structure surrounded with dielectrics were also listed as possible effects of polyimide coating improving the device characteristics of the ZnO nanorod FETs.

Heo *et al.*[652] fabricated single ZnO nanowire MOSFETs on SiO_2-coated Si substrates with top gate electrodes. The separation of the source/drain electrodes was 7 μm, and (Ce,Tb)$MgAl_{11}O_{19}$ with a thickness of 50 nm was used as the gate dielectric. The depletion-mode transistors exhibited good pinch-off and saturation characteristics, a threshold voltage of ~−3 V, and a maximum transconductance of 0.3 mS/mm. When illuminated with ultraviolet light (366 nm), the drain-source current increased by approximately a factor of 5 and the maximum transconductance was ~5 mS/mm. Part of the increase in the drain-source current was due to photoconductivity in the portion of the wire uncovered by the gate metal. The estimated channel mobility was ~3 $cm^2/V\,s$, and the on/off ratio at V_G of 0–3 V and V_{DS} of 10 V was ~25 in the dark and ~125 under UV illumination.

ZnO nanowire FETs were also utilized for O_2 detection.[650] Single-crystal ZnO nanowires synthesized using a vapor trapping CVD method were configured as FETs, and the adsorption of oxygen molecules was shown to cause the depletion of the FET channel. Oxygen is chemisorbed to ZnO surface at vacancy sites, forming O_2^- and resulting in a surface charge depletion layer thus leading to a reduction in the electrical conductivity. Moreover, detection sensitivity could be modulated by the gate voltage, and it was shown to increase with decreasing nanowire radius from 270 to 20 nm. The single nanowire photoconductivity spectrum was also measured for these FETs and the transconductance was observed to decrease with illumination. It was demonstrated that the nanowire FETs could be reversibly turned on and off by applying a switching illumination. These results indicate the high potential of ZnO for nanoscale electronics, optoelectronics, and chemical sensing devices.

ZnO nanobelts were also considered for applications as nanosensors and nanoactuators. The piezoelectric coefficient of a ZnO nanobelt was measured using an AFM with a conductive tip.[658] ZnO nanobelts were dispersed on a (100) Si wafer coated with Pd. The nanobelts were then coated with another 5-nm layer of Pd. It was ensured that the top and bottom surfaces of the nanobelts were not short circuited. The effective piezoelectric coefficient d_{33} for the (0001) surface of the nanobelts was measured by piezoresponse force microscopy. The d_{33} coefficient was found to vary from 26.7 to 14.3 pm V^{-1} with increasing frequency from 30 to 150 kHz. These values are considerably larger than that for bulk ZnO (9.9 pm V^{-1}).

In a study by Kong *et al.*[623] single-crystal nanorings of ZnO were grown by the solid-vapor process. The raw material was a mixture of ZnO (melting point of 1975 °C), indium oxide, and lithium carbonate powders at a weight ratio of 20:1:1, and it was placed at the highest-temperature (1400 °C) zone of a horizontal tube furnace. ZnO decomposes at such a high temperature into Zn^{2+} and O^{2-} at low pressure (~10^{-3} Torr), and this decomposition process is the key step for controlling the anisotropic growth of the nanobelts. After a few minutes of evaporation and decomposition, the Ar carrier gas was introduced at a flux of 50 sccm. The synthesis process was conducted at 1400 °C for 30 min. The condensation products were deposited onto a silicon substrate placed in a temperature zone of 200–400 °C under Ar pressure of 500 Torr. The as-synthesized sample was composed of many freestanding nanorings at a significant percentage (20%–40%) of the yield [Fig. 128(a)] with 70% reproducibility from run to run. The rings had typical diameters of ~1–4 μm and thin, wide shells that were ~10–30 nm thick. SEM images recorded at high magnification clearly show the perfect circular shape of the complete rings, with uniform shapes and flat surfaces, as recorded in Fig. 128(b). Two types of nanoring structures were found. The type-I structure is the single-crystal entity nanoring with nearly perfect circular shape, although there is electron-diffraction contrast caused by nonuniform deformation along

[This article is copyrighted as indicated in the article. Reuse of AIP content is subject to the terms at: http://scitation.aip.org/termsconditions. Downloaded to] IP: 128.172.48.58 On: Mon, 19 Oct 2015 20:45:44

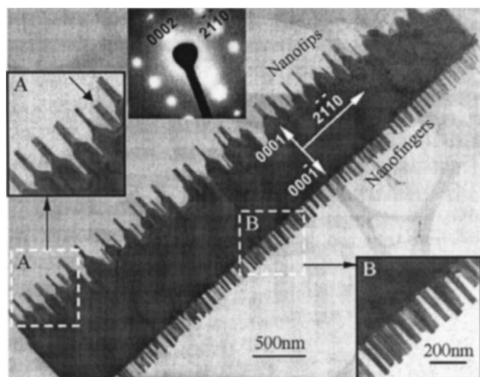

FIG. 129. Transmission electron microscopy image of a double-sided comb structure, showing the distinct arrays of nanotips and nanofingers on the two sides. The inset is the corresponding electron-diffraction pattern and the enlargements of the two selected areas, as indicated. [Reprinted with permission from Z. L. Wang, X. Y. Kong, and J. M. Zuo, Phys. Rev. Lett. **91**, 185502 (2003). Copyright 2003 by the American Physical Society.]

the circumference. The type-II structure nanoring is a single crystal, which again implies that the nanoring shell is a uniformly deformed, single-crystal ribbon around the circumference.

Wang *et al.*[637] reported that the Zn-terminated ZnO (0001) polar surface is chemically active and the oxygen terminated {0001} polar surface is inert during the growth of nanocantilever arrays. It should be pointed out that the (0001) surface is the Zn-polar surface which upon exposure to O could be O terminated. On the other hand, the $(000\bar{1})$ surface is the O-polar surface. Caution must be exercised to avoid any confusion. Those authors grew relatively long and wide "comblike" nanocantilever arrays from the (0001)-Zn surface (Fig. 129) by a self-catalyzed process due to the enrichment of Zn at the growth front. The chemically inactive {0001}-O surface did not initiate any growth. The (0001)-Zn surface tended to have tiny Zn clusters at the growth front, as evidenced by the high-resolution TEM image. The Zn clusters as well as the local enrichment in Zn at the growth front tend to initiate the growth of ZnO analogous to the vapor-liquid-solid growth process. Therefore, the self-catalyzed effect of the Zn clusters resulted in a fast growth of the nanotips. The {0001}-O terminated surface, however, is likely to be inert and may not exhibit an effective self-catalyzed effect; thus, the surface may not initiate the growth of nanocantilevers. By changing the growth kinetics so that there is no growth on the {0001}-O terminated surface, a comblike structure with long teeth only on one side has been grown, as depicted in Fig. 129, with the top/bottom surfaces being $\pm(01\bar{1}0)$ and the side surfaces $\pm(2\bar{1}\bar{1}0)$. It is possible that a change in the growth condition results in the disappearance of the {0111} type of facets; thus, the chemically inert {0001} surface does not initiate any teeth growth. The nanofingers shown in Fig. 129 could serve as nanocantilever arrays.

Combining microelectromechanical system (MEMS) technology with self-assembled nanobelts cost effective cantilevers with much heightened sensitivity may be produced for a range of devices and applications such as force, pressure, mass, thermal, biological, and chemical sensors. Semiconducting nanobelts are ideal candidates for cantilever applications, since they are structurally defect-free single crystals and provide a significant improvement in the cantilever sensitivity due to their reduced dimensions. Individual ZnO nanobelts could be aligned on Si chips to have a range of lengths and therefore different resonance frequencies.[619]

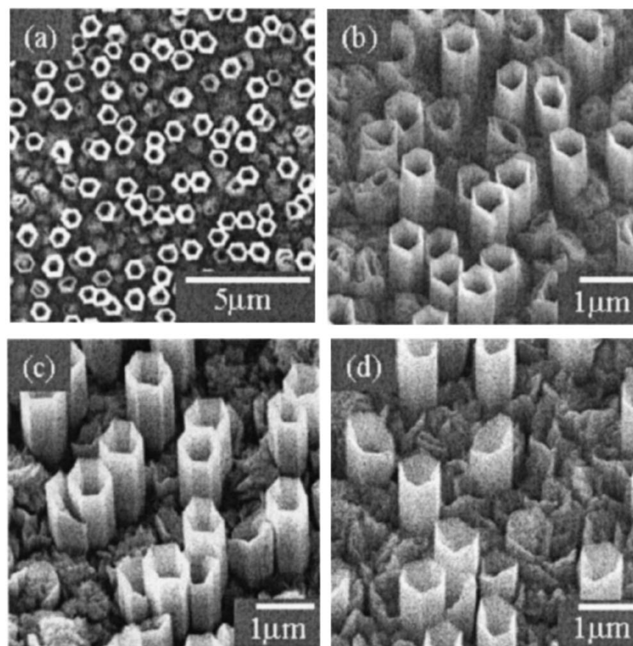

FIG. 130. SEM images of ZnO tubes formed at 400 °C under different reactor pressures. (a) Top image of the tubes obtained at 0.3 Torr. [(b)–(d)] SEM images taken with an inclination angle of the tubes obtained at 0.3, 0.6, and 1.0 Torr, respectively. [Reprinted with permission from B. P. Zhang, N. T. Binh, K. Wakatsuki, Y. Segawa, Y. Yamada, N. Usami, M. Kawasaki, and H. Koinuma, Appl. Phys. Lett. **84**, 4098 (2004). Copyright 2004, American Institute of Physics.]

Zhang *et al.*[659] reported on the formation of ZnO tubes by MOCVD at temperatures of 350–450 °C. The tubes obtained were grown epitaxially on sapphire (0001) substrates with both the ZnO *c* axis and the growth direction being parallel to the substrate normal. All of the tubes had hexagonal cross sections and the same in-plane orientation. The characteristics of the tubes were found to depend strongly on both the growth temperature and reactor pressure. Figure 130 shows SEM images of the tubes formed at 400 °C under different reactor pressures. Figure 130(a) indicates that all of the tubes have hexagonal shapes and all the hexagons have the same in-plane orientation. Figures 130(b)–130(d) show the SEM images taken with an inclination angle of the tubes obtained at 0.3, 0.6, and 1.0 Torr, respectively. The density of the hexagonal ZnO tubes decreased from 4 to 0.6 μm^{-2} with increasing pressure from 0.3 to 3 Torr. The well-defined hexagonal shape is an indication of epitaxial growth and consequently single-crystal nature of the tubes. The XRD studies (rocking curve, θ-2θ scan, and ϕ-scan measurements) of the samples showed that the tubes were well aligned both in the growth plane (in-plane) and along the growth direction (out-of-plane). The growth temperature also greatly influenced the tube formation. In the temperature range of 350–450 °C, the density of the tubes increased from 0.04 to 1 μm^{-2} and the outer sizes of the tubes decreased from 1.0 to 0.4 μm with increasing temperature.

[This article is copyrighted as indicated in the article. Reuse of AIP content is subject to the terms at: http://scitation.aip.org/termsconditions. Downloaded to] IP: 128.172.48.58 On: Mon, 19 Oct 2015 20:45:44

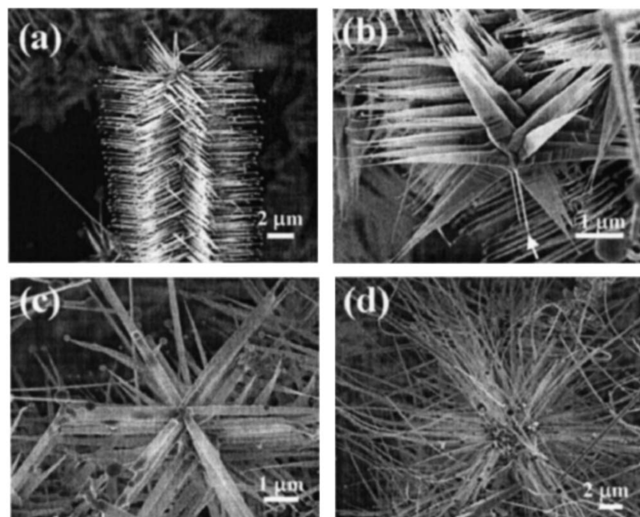

FIG. 131. SEM images of bunches of ZnO nanopropeller arrays rooted at Al_2O_3 substrate grown at various temperatures: (a) a single column of the as-synthesized ZnO nanopropeller arrays; (b) front view of a column of ZnO nanopropeller arrays with nanowires at the central axis, which was collected from a lower-temperature zone (∼620 °C); (c) a column of ZnO nanopropeller arrays with uniform nanoribbon shape and smoother surface, which was collected from a medium-temperature zone (∼650 °C); and (d) a column of ZnO nanopropeller arrays with long nanoribbons, which was collected from a higher-temperature zone (∼680 °C). [Reprinted with permission from P. X. Gao, and Z. L. Wang, Appl. Phys. Lett. **84**, 2883 (2004). Copyright 2004, American Institute of Physics.]

However, no tubes were obtained at 500 °C. Therefore, the tube density can be modified by changing either the growth temperature or the reactor pressure, and the tube size can be tuned with the growth temperature.

As another example of various types of nanostructures, polar-surface-dominated ZnO nanopropeller arrays were synthesized using a two-step high-temperature solid-vapor deposition process by Gao and Wang.[634] The first step involves the growth of the nanopropeller axis which is a straight nanowire along the *c* axis and enclosed by {2110} surfaces. In the second step, the sixfold symmetric nanoblades are formed along the crystallographic equivalent *a* axes (⟨2110⟩) perpendicular to the nanowire, and the array is formed by epitaxial growth of nanoblades on the nanowire. The growth of the nanopropeller arrays on polycrystalline Al_2O_3 substrates was conducted at 600–700 °C for 60 min (step I) and then at 800–900 °C for 30 min (step II) under pressure of 200 mbars. Figure 131(a) shows a top view of the well-aligned ZnO nanopropeller arrays on a polycrystalline Al_2O_3 substrate grown in a relatively high temperature zone (∼680 °C, step I). Each nanopropeller array column consists of six arrays of triangular-shaped blades of 4–5 μm in length and propeller arrays with a diameter of ∼10 μm. The columns of the nanopropellers maintain their sixfold arrays of parallel nanoribbon blades around the central nanowire, as seen in Fig. 131(b). The morphology and shape of the nanopropellers depended on the local temperature, surface diffusion rate, and availability of Zn–O vapor. In a lower-temperature region, due to a relatively slower surface diffusion and the decrease in supply of the vapor as more source material is being consumed, a triangular-shaped structure was formed. In the medium-temperature region, a faster diffusion of the Zn–O vapor and higher surface mobility lead to the formation of uniform and longer nanoblades.

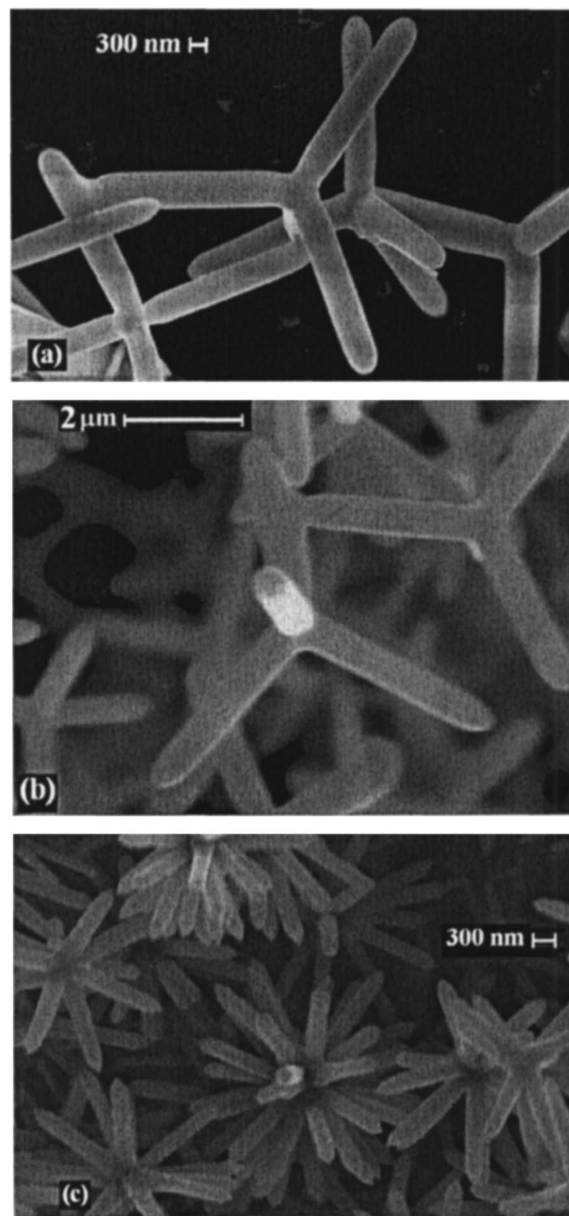

FIG. 132. Representative SEM images of ZnO nanostructures: (a) ZnO prepared from Zn, (b) ZnO prepared from ZnO:C, and (c) ZnO prepared from ZnO:C:GeO_2. [Reprinted with permission from A. B. Djurišić, Y. H. Leung, W. C. H. Choy, K. W. Cheah, and W. K. Chan, Appl. Phys. Lett. **84**, 2635 (2004). Copyright 2004, American Institute of Physics.]

There have also been reports on the growth of ZnO tetrapod structures.[635,636] In Ref. 636 such structures were prepared either from oxidation of Zn in air or by heating a mixture of ZnO and graphite (1:1) at 1100 °C in a tube furnace. Djurišić *et al.*[636] also fabricated ZnO samples by heating a mixture of ZnO, GeO_2, and graphite at 1100 °C and studied the morphology of the fabricated structures as a function of GeO_2 percentage up to 10%. Figure 132 shows the representative SEM images of the obtained ZnO structures. Similar tetrapod structures are obtained for both starting materials (Zn and ZnO:C). When GeO_2 is added to the starting material (ZnO:C), multipod structures started to form, as illustrated in Fig. 132(c). With increasing GeO_2 con-

[This article is copyrighted as indicated in the article. Reuse of AIP content is subject to the terms at: http://scitation.aip.org/termsconditions. Downloaded to] IP: 128.172.48.58 On: Mon, 19 Oct 2015 20:45:44

centration in the starting material, larger amount of multipod structures appeared (for small GeO_2 content, both tetrapods and multipods were formed). It was concluded that Ge enables nucleation of additional legs on the core which would normally develop into a tetrapod.

XI. SUMMARY

A comprehensive review of properties, preparation, processing, and device applications of ZnO is presented. Zinc oxide (ZnO) material has been a subject of varying degrees of research effort over the decades. This effort has recently been intensified for better understanding of its physical properties as well as for developing high-quality ZnO films and crystals for device applications. ZnO has some unique properties and some advantages over other wide-gap materials, such as GaN which is widely used today for production of short-wavelength light-emitting devices. These features include large exciton binding energy of 60 meV which should pave the way for excition-based lasing action with very low threshold currents, and on the practical side the availability of large-size bulk ZnO crystals. However, despite much effort *p*-type ZnO with the requisite reproducibility and quality is still lacking. This is in part due to strong self-compensation effects when *p*-type dopants are attempted. Clearly, this issue must be overcome before ZnO can be of practical use, as was the case for GaN. However, some alternative methods, such as fabrication of *p*-*n* heterojunction metal-insulator-semiconductor diodes, are also considered for exploiting the advantages of ZnO, at least in the interim time period. ZnO is also shown to be a promising material for spintronics and transparent thin-film transistors. Of particular interest to nanoscale structures and devices, ZnO is very favorable as compared to other wide-band-gap semiconductors in that this material lends itself nicely to the production of nanostructures from which functional devices have already been fabricated. In short, this review provides critical treaties of the science and technology of ZnO.

ACKNOWLEDGMENTS

The research effort at VCU is funded by grants from AFOSR (monitored by Dr. T. Steiner and Dr. G. L. Witt), ONR (monitored by Dr. C. E. C. Wood), BMDO (monitored by C. W. Litton), and NSF (monitored by Dr. V. Hess). The authors owe a great depth of gratitude to Dr. R. J. Collins, Dr. D. C. Reynolds, Dr. C. W. Litton, Dr. Y. S. Park, and Dr. D. Langer for their contributions to the field of ZnO and many discussions and exchange of ideas and support. The authors are also thankful to B. Nemeth and J. Nause of Cermet, Inc., for collaborations on many ZnO-related topics and supply of high-quality melt-grown ZnO substrates. Naturally this manuscript would not have been possible without the contributions of all the authors contained in these pages and elsewhere. Finally, the authors would like to thank Professor Hosun Lee and Professor Martin Muñoz for reviewing the manuscript and their colleagues in the group for their support, encouragement, and interest in this work.

[1]C. W. Bunn, Proc. Phys. Soc. London **47**, 835 (1935).
[2]H. Braekken and C. Jore, Det Norske Videnskabers Skrifter (The Norwegian Science Scripts) NR8, 1 (1935) (in Norwegian)
[3]R. B. Heller, J. McGannon, and A. H. Weber, J. Appl. Phys. **21**, 1283 (1950).
[4]T. B. Rymer and G. D. Archard, Research (London) 5, 292 (1952).
[5]A. Cimino, M. Marezio, and A. Santoro, Naturwiss. **12**, 348 (1957).
[6]T. J. Gray, J. Am. Ceram. Soc. **37**, 534 (1954).
[7]G. P. Mohatny and L. V. Azaroff, J. Chem. Phys. **35**, 1268 (1961).
[8]A. A. Khan, Acta Crystallogr., Sect. A: Cryst. Phys., Diffr., Theor. Gen. Crystallogr. **A24**, 403 (1968).
[9]R. R. Reeber, J. Appl. Phys. **41**, 5063 (1970).
[10]D. C. Reynolds and T. C. Collins, Phys. Rev. **185**, 1099 (1969).
[11]D. G. Thomas, J. Phys. Chem. Solids **15**, 86 (1960).
[12]Y. S. Park, C. W. Litton, T. C. Collins, and D. C. Reynolds, Phys. Rev. **143**, 512 (1965).
[13]R. J. Collins and D. A. Kleinman, J. Phys. Chem. Solids **11**, 190 (1959).
[14]R. L. Weiher, Phys. Rev. **152**, 736 (1966).
[15]W. S. Bear, Phys. Rev. **154**, 785 (1967).
[16]E. Mollwo, Z. Angew. Phys. **6**, 257 (1954).
[17]W. L. Bond, J. Appl. Phys. **36**, 1674 (1965).
[18]W. Y. Liang and A. D. Yoffe, Phys. Rev. Lett. **20**, 59 (1968).
[19]A. R. Hutson, J. Appl. Phys. **32**, 2287 (1961).
[20]J. L. Freeouf, Phys. Rev. B **7**, 3810 (1973).
[21]O. F. Schirmer and D. Zwingel, Solid State Commun. **8**, 1559 (1970).
[22]J. J. Hopfield and D. G. Thomas, Phys. Rev. Lett. **15**, 22 (1965).
[23]R. E. Stephens and I. H. Malitson, J. Res. Natl. Bur. Stand. **49**, 249 (1952).
[24]Y. S. Park and J. R. Schneider, J. Appl. Phys. **39**, 3049 (1968).
[25]G. Heiland, E. Mollwo, and F. Stöckmann, Solid State Phys. **8**, 191 (1959).
[26]T. C. Damen, S. P. S. Porto, and B. Tell, Phys. Rev. **142**, 570 (1966).
[27]C. A. Arguello, D. L. Rousseau, and S. P. S. Porto, Phys. Rev. **181**, 1351 (1969).
[28]R. H. Callender, S. S. Sussman, M. Selders, and R. K. Chang, Phys. Rev. B **7**, 3788 (1973).
[29]J. M. Calleja and M. Cardona, Phys. Rev. B **16**, 3753 (1977).
[30]M. Tsuboi and A. Wada, J. Chem. Phys. **48**, 2615 (1968).
[31]S. P. S. Porto and R. S. Krishnan, J. Chem. Phys. **47**, 1009 (1967).
[32]S. S. Mitra, O. Brafman, W. B. Daniels, and R. K. Crawford, Phys. Rev. **186**, 942 (1969).
[33]G. Galli and J. E. Coker, Appl. Phys. Lett. **16**, 439 (1970).
[34]M. Shiloh and J. Gutman, J. Cryst. Growth **11**, 105 (1971).
[35]D. F. Croxall, R. C. C. Ward, C. A. Wallace, and R. C. Kell, J. Cryst. Growth **22**, 117 (1974).
[36]D. C. Reynolds (private communication).
[37]W. Kern and R. C. Heim, J. Electrochem. Soc. **117**, 562 (1970).
[38]D. C. Look, Mater. Sci. Eng., B **80**, 381 (2001).
[39]E. Ohshima, H. Ogino, I. Niikura, K. Maeda, M. Sato, M. Ito, and T. Fukuda, J. Cryst. Growth **260**, 166 (2004).
[40]Please visit the web site http://www.cermetinc.com/products.htm
[41]J.-M. Ntep, S. S. Hassani, A. Lusson, A. Tromson-Carli, D. Ballutaud, G. Didier, and R. Triboulet, J. Cryst. Growth **207**, 30 (1999).
[42]D. C. Look, D. C. Reynolds, J. W. Hemski, R. L. Jones, and J. R. Sizelove, Appl. Phys. Lett. **75**, 811 (1999).
[43]A. Y. Polyakov *et al.*, J. Appl. Phys. **94**, 2895 (2003).
[44]S. O. Kucheyev, J. S. Williams, C. Jagadish, J. Zou, C. Evans, A. J. Nelson, and A. V. Hamza, Phys. Rev. B **67**, 094115 (2003).
[45]X. Gu, M. A. Reshchikov, A. Teke, D. Johnstone, H. Morkoc, B. Nemeth, and J. Nause, Appl. Phys. Lett. **84**, 2268 (2004); J. Mater. Sci. **15**, 373 (2004).
[46]F. Hamdani *et al.*, J. Appl. Phys. **83**, 983 (1998).
[47]T. Dietl, H. Ohno, F. Matsukura, J. Cibert, and D. Ferrand, Science **287**, 1019 (2000).
[48]S. J. Pearton *et al.*, J. Phys.: Condens. Matter **16**, R209 (2004).
[49]S. J. Pearton, W. H. Heo, M. Ivill, D. P. Norton, and T. Steiner, Semicond. Sci. Technol. **19**, R59 (2004).
[50]D. C. Look and B. Claflin, Phys. Status Solidi B **241**, 624 (2004).
[51]D. C. Look, B. Claflin, Ya. I. Alivov, and S. J. Park, Phys. Status Solidi A **201**, 2203 (2004).
[52]S. J. Pearton, D. P. Norton, K. Ip, Y. W. Heo, and T. Steiner, Superlattices Microstruct. **34**, 3 (2004).
[53]S. J. Pearton, D. P. Norton, K. Ip, Y. W. Heo, and T. Steiner, Prog. Mater. Sci. **50**, 293 (2005).
[54]D. P. Norton, Y. W. Heo, M. P. Ivill, K. Ip, S. J. Pearton, M. F. Chisholm,

[This article is copyrighted as indicated in the article. Reuse of AIP content is subject to the terms at: http://scitation.aip.org/termsconditions. Downloaded to] IP: 128.172.48.58 On: Mon, 19 Oct 2015 20:45:44

and T. Steiner, Mater. Today **7**, 34 (2004).

[55]V. A. Nikitenko, J. Appl. Spectrosc. **52**, 367 (1992).

[56]J. E. Jaffe and A. C. Hess, Phys. Rev. B **48**, 7903 (1993).

[57]J. E. Jaffe, J. A. Snyder, Z. Lin, and A. C. Hess, Phys. Rev. B **62**, 1660 (2000).

[58]*CRC Handbook of Chemistry and Physics*, 58th ed. (CRC, Boca Raton, 1977).

[59]E. Kisi and M. M. Elcombe, Acta Crystallogr., Sect. C: Cryst. Struct. Commun. **C45**, 1867 (1989).

[60]C. H. Bates, W. B. White, and R. Roy, Science **137**, 993 (1962).

[61]L. Gerward and J. S. Olsen, J. Synchrotron Radiat. **2**, 233 (1995).

[62]J. M. Recio, M. A. Blanco, V. Luaña, R. Pandey, L. Gerward, and J. Staun Olsen, Phys. Rev. B **58**, 8949 (1998).

[63]J. C. Jamieson, Phys. Earth Planet. Inter. **3**, 201 (1970).

[64]S. Desgreniers, Phys. Rev. B **58**, 14102 (1998).

[65]H. Karzel *et al.*, Phys. Rev. B **53**, 11425 (1996).

[66]R. Ahuja, L. Fast, O. Eriksson, J. M. Wills, and B. Johansson, J. Appl. Phys. **83**, 8065 (1998).

[67]J. M. Recio, R. Pandey, and V. Luana, Phys. Rev. B **47**, 3401 (1993).

[68]M. Wilson and P. A. Madden, Mol. Phys. **90**, 75 (1997).

[69]L.-G. Liu and W. A. Bassett, *Elements, Oxides, and Silicates: High-Pressure Phases with Implications for the Earth's Interior* (Oxford University, New York, 1986).

[70]A. Zaoui and W. Sekkal, Phys. Rev. B **66**, 174106-1 (2002).

[71]T. Kogure and Y. Bando, J. Electron Microsc. **47**, 7903 (1993).

[72]A. B. M. A. Ashrafi, A. Ueta, A. Avramescu, H. Kumano, I. Suemune, Y.-W. Ok, and T.-Y. Seong, Appl. Phys. Lett. **76**, 550 (2000).

[73]S.-K. Kim, S.-Y. Jeong, and C.-R. Cho, Appl. Phys. Lett. **82**, 562 (2003).

[74]W. L. Bond, Acta Crystallogr. **13**, 814 (1960).

[75]F. J. Himpsel, Adv. Phys. **32**, 1 (1983).

[76]U. Rössler, Phys. Rev. **184**, 733 (1969).

[77]D. W. Langer and C. J. Vesely, Phys. Rev. B2, 4885 (1970).

[78]R. A. Powell, W. E. Spicer, and J. C. McMenamin, Phys. Rev. Lett. **27**, 97 (1971).

[79]R. A. Powell, W. E. Spicer, and J. C. McMenamin, Phys. Rev. B **6**, 3056 (1972).

[80]L. Ley, R. A. Pollak, F. R. McFeely, S. P. Kowalezyk, and D. A. Shirley, Phys. Rev. B **9**, 600 (1974).

[81]C. J. Vesely, R. L. Hengehold, and D. W. Langer, Phys. Rev. B **5**, 2296 (1972).

[82]S. Bloom and I. Ortenburger, Phys. Status Solidi B **58**, 561 (1973).

[83]J. R. Chelikowsky, Solid State Commun. **22**, 351 (1977).

[84]I. Ivanov and J. Pollmann, Phys. Rev. B **24**, 7275 (1981).

[85]D. H. Lee and J. D. Joannopoulos, Phys. Rev. B **24**, 6899 (1981).

[86]P. Schröer, P. Krüger, and J. Pollmann, Phys. Rev. B **47**, 6971 (1993).

[87]S. Massidda, R. Resta, M. Posternak, and A. Baldereschi, Phys. Rev. B **52**, R16977 (1995).

[88]P. Schröer, P. Krüger, and J. Pollmann, Phys. Rev. B **49**, 17092 (1994).

[89]D. Vogel, P. Krüger, and J. Pollmann, Phys. Rev. B **52**, R14316 (1995).

[90]R. T. Girard, O. Tjernberg, G. Chiaia, S. Söderholm, U. O. Karlsson, C. Wigren, H. Nylèn, and I. Lindau, Surf. Sci. **373**, 409 (1997).

[91]C. B. Duke, A. R. Lubinsky, S. C. Chang, B. W. Lee, and P. Mark, Phys. Rev. B **15**, 4865 (1977).

[92]C. B. Duke, R. J. Meyer, A. Paton, and P. Mark, Phys. Rev. B **18**, 4225 (1978).

[93]Y. R. Wang and C. B. Duke, Surf. Sci. **192**, 309 (1987).

[94]W. Göpel, J. Pollmann, I. Ivanov, and B. Reihl, Phys. Rev. B **26**, 3144 (1982).

[95]G. Zwicker and K. Jacobi, Solid State Commun. **54**, 701 (1985).

[96]K. Ozawa, K. Sawada, Y. Shirotori, K. Edamoto, and M. Nakatake, Phys. Rev. B **68**, 125417 (2003).

[97]S. H. Wei and A. Zounger, Phys. Rev. B **37**, 8958 (1988).

[98]J. L. Martins, N. Troullier, and S. H. Wei, Phys. Rev. B **43**, 2213 (1991).

[99]Y.-N. Xu and W. Y. Ching, Phys. Rev. B **48**, 4335 (1993).

[100]O. Zakharov, A. Rubio, X. Blasé, M. L. Cohen, and S. G. Louie, Phys. Rev. B **50**, 10780 (1994).

[101]N. A. Hill and U. Waghmare, Phys. Rev. B **62**, 8802 (2000).

[102]J. E. Jaffe, R. Pandey, and A. B. Kunz, Phys. Rev. B **43**, 14030 (1991).

[103]E. Hückel, Z. Phys. **70**, 204 (1931).

[104]A. Polian, M. Grimsditch, and I. Grzegory, J. Appl. Phys. **79**, 3343 (1996).

[105]T. B. Bateman, J. Appl. Phys. **35**, 3309 (1962).

[106]F. D. Murnaghan, Proc. Natl. Acad. Sci. U.S.A. **30**, 244 (1944).

[107]A. Dal Corso, M. Posternak, R. Resta, and A. Baldereschi, Phys. Rev. B **50**, 10715 (1994).

[108]J. F. Nye, *Physical Properties of Crystals* (Clarendon, Oxford, 1975).

[109]F. Bernardini, V. Fiorentini, and D. Vanderbilt, Phys. Rev. B **56**, R10024 (1997).

[110]H. Morkoç, *Nitride Semiconductors and Devices* (Springer, Berlin, 1999).

[111]F. Decremps, J. Zhang, B. Li, and R. C. Liebermann, Phys. Rev. B **63**, 224105 (2001); F. Decremps, J. Pellicer-Porres, A. Marco Saitta, J.-C. Chervin, and A. Polian, Phys. Rev. B **65**, 092101 (2002).

[112]N. Soga and O. L. Anderson, J. Appl. Phys. **38**, 2985 (1967).

[113]S. O. Kucheyev, J. E. Bradby, J. S. Williams, C. Jagadish, and M. V. Swain, Appl. Phys. Lett. **80**, 956 (2002); S. O. Kucheyev, J. E. Bradby, J. S. Williams, C. Jagadish, M. Toth, M. R. Phillips, and M. V. Swain, Appl. Phys. Lett. **77**, 3373 (2000).

[114]J. C. Phillips, *Bonds and Bands in Semiconductors* (Academic, New York, 1973).

[115]M. A. Stroscio and M. Dutta, *Phonons in Nanostructures* (Cambridge University Press, Cambridge, 2001).

[116]B. H. Bairamov, A. Heinrich, G. Irmer, V. V. Toporov, and E. Ziegler, Phys. Status Solidi B **119**, 227 (1983).

[117]Y. F. Lu, H. Q. Ni, and Z. M. Ren, J. Appl. Phys. **88**, 498 (2000).

[118]N. Ashkenov *et al.*, J. Appl. Phys. **93**, 126 (2003).

[119]M. Rajalakshmi, A. K. Arora, B. S. Bendre, and S. Mahamuni, J. Appl. Phys. **87**, 2445 (2000).

[120]S. Minomura, *High Pressure in Science and Technology*, Proceedings of the Ninth AIRAPT International High Pressure Conference on High Pressure in Science and Technology, edited by C. Homan, R. K. MacCrane, and E. Whalley(North-Holland, New York, 1984), p. 277.

[121]S. Limpijumnong and W. R. L. Lambrecht, Phys. Rev. Lett. **86**, 91 (2001); J. Serrano, A. Rubio, E. Hernández, A. Muñoz, and A. Mujica, Phys. Rev. B **62**, 16612 (2000).

[122]A. Kaschner *et al.*, Appl. Phys. Lett. **80**, 1909 (2002).

[123]C. Bundesmann, N. Ashkenov, M. Schubert, D. Spemann, T. Butz, E. M. Kaidashev, M. Lorenz, and M. Grundmann, Appl. Phys. Lett. **83**, 1974 (2003).

[124]C. G. Van de Walle, Phys. Rev. Lett. **85**, 1012 (2000).

[125]M. D. McCluskey, S. J. Jokela, K. K. Zhuravlev, P. J. Simpson, and K. G. Lynn, Appl. Phys. Lett. **81**, 3807 (2002); E. V. Lavrov, J. Weber, F. Börrnert, C. G. Van de Walle, and R. Helbig, Phys. Rev. B **66**, 165205 (2002).

[126]E. V. Lavrov, Physica B **340–342**, 195 (2003).

[127]E. V. Lavrov, J. Weber, F. Börrnert, C. G. Van de Walle, and R. Helbig, Phys. Rev. B **66**, 165205 (2002).

[128]M. D. McCluskey, S. J. Jokela, K. K. Zhuravlev, P. J. Simpson, and K. G. Lynn, Appl. Phys. Lett. **81**, 3807 (2002).

[129]S. J. Jokela, M. D. McCluskey, and K. G. Lynn, Physica B **340–342**, 221 (2003).

[130]N. H. Nickel and K. Fleischer, Phys. Rev. Lett. **90**, 197402 (2003).

[131]J. A. Wolk, J. W. Ager III, K. J. Duxstad, E. E. Haller, N. R. Taskar, D. R. Dorman, and D. J. Olego, Appl. Phys. Lett. **63**, 2756 (1993).

[132]H. Ibach, Phys. Status Solidi **33**, 257 (1969).

[133]M.-Y. Han and J.-H. Jou, Thin Solid Films **260**, 58 (1995); F. Z. Aoumeur, Kh. Benkabou, and B. Belgoumène, Physica B **337**, 292 (2003).

[134]C. M. Bhandari and D. M. Rowe, *Thermal Conduction in Semiconductors* (Wiley, New York, 1988).

[135]C. Kittel, *Introduction to Solid State Physics*, 6th ed. (Wiley, New York, 1986), p. 150.

[136]D. I. Florescu, V. M. Asnin, F. H. Pollak, R. J. Molnar, and C. E. C. Wood, J. Appl. Phys. **88**, 3295 (2000).

[137]D. I. Florescu, L. G. Mourokh, F. H. Pollak, D. C. Look, G. Cantwell, and X. Li, J. Appl. Phys. **91**, 890 (2002).

[138]F. H. Pollak, Ü. Özgür, S. Doğan, X. Gu, S.-J. Cho, H. Morkoç, and J. Nause (unpublished).

[139]T. Olorunyolemi, A. Birnboim, Y. Carmel, O. C. Wilson, Jr., and I. K. Lloyd, J. Am. Ceram. Soc. **85**, 1249 (2002).

[140]T. Tsubota, M. Ohtaki, K. Eguchi, and H. Arai, J. Mater. Chem. **7**, 85 (1997).

[141]M. Ohtaki, T. Tsubota, K. Eguchi, and H. Arai, J. Appl. Phys. **79**, 1816 (1996).

[142]S. Katsuyama, Y. Takagi, M. Ito, K. Majima, H. Nagai, H. Sakai, K. Yoshimura, and K. Kosuge, J. Appl. Phys. **92**, 1391 (2002).

[143]T. Tsubota, M. Ohtaki, K. Eguchi, and H. Arai, J. Mater. Chem. **8**, 409 (1998).

[144]K. F. Cai, E. Müller, C. Drašar, and A. Mrotzek, Mater. Sci. Eng., B **104**,

[This article is copyrighted as indicated in the article. Reuse of AIP content is subject to the terms at: http://scitation.aip.org/termsconditions. Downloaded to] IP: 128.172.48.58 On: Mon, 19 Oct 2015 20:45:44

45 (2003).
[145] W. N. Lawless and T. K. Gupta, J. Appl. Phys. **60**, 607 (1986).
[146] J. D. Albrecht, P. P. Ruden, S. Limpijumnong, W. R. L. Lambrecht, and K. F. Brennan, J. Appl. Phys. **86**, 6864 (1991);D. C. Look, J. W. Hemsky, and J. R. Sizelove, Phys. Rev. Lett. **82**, 2552 (1999);D. C. Look, D. C. Reynolds, J. R. Sizelove, R. L. Jones, C. W. Litton, G. Cantwell, and W. C. Harsch, Solid State Commun. **105**, 399 (1998).
[147] D. S. Ginley and C. Bright, Mater. Res. Bull. **25**, 15 (2000); E. M. Kaidashev *et al.*, Appl. Phys. Lett. **82**, 3901 (2003).
[148] H. Kato, M. Sano, K. Miyamoto, and T. Yao, Jpn. J. Appl. Phys., Part 1 **42**, 2241 (2003);K. Iwata, P. Fons, S. Niki, A. Yamada, K. Matsubara, K. Nakahara, and H. Takasu, Phys. Status Solidi A **180**, 287 (2000);K. Miyamoto, M. Sano, H. Kato, and T. Yao, Jpn. J. Appl. Phys., Part 2 **41**, L1203 (2002);J. Cryst. Growth **265**, 34 (2004);T. Edahiro, N. Fujimura, and T. Ito, J. Appl. Phys. **93**, 7673 (2003).
[149] T. Yamamoto, T. Shiosaki, and A. Kawabata, J. Appl. Phys. **51**, 3113 (1980).
[150] T. Mitsuyu, S. Ono, and K. Wasa, J. Appl. Phys. **51**, 2464 (1980).
[151] A. Hachigo, H. Nakahata, K. Higaki, S. Fujii, and S. Shikata, Appl. Phys. Lett. **65**, 2556 (1994).
[152] J. G. E. Gardeniers, Z. M. Rittersma, and G. J. Burger, J. Appl. Phys. **83**, 7844 (1998).
[153] S. K. Tiku, C. K. Lau, and K. M. Lakin, Appl. Phys. Lett. **36**, 318 (1980).
[154] M. Kasuga and M. Mochizuki, J. Cryst. Growth **54**, 185 (1981).
[155] V. Srikant, V. Sergo, and D. R. Clarke, Appl. Phys. Lett. **16**, 439 (1995).
[156] K.-K. Kim, J.-H. Song, H.-J. Jung, W.-K. Choi, S.-J. Park, and J.-H. Song, J. Appl. Phys. **87**, 3573 (2000); K.-K. Kim, J.-H. Song, H.-J. Jung, W.-K. Choi, S.-J. Park, J.-H. Song, and J.-Y. Lee, J. Vac. Sci. Technol. A **18**, 2864 (2000).
[157] P. Fons, K. Iwata, S. Niki, A. Yamada, and K. Matsubara, J. Cryst. Growth **201–202**, 627 (1999).
[158] Y. Chen, D. M. Bagnall, H.-J. Koh, K.-T. Park, K. Hiraga, Z.-Q. Zhu, and T. Yao, J. Appl. Phys. **84**, 3912 (1998).
[159] R. D. Vispute *et al.*, Appl. Phys. Lett. **73**, 348 (1998).
[160] Y. Liu, C. R. Gorla, S. Liang, N. Emanetoglu, Y. Lu, H. Shen, and M. Wraback, J. Electron. Mater. **29**, 69 (2000).
[161] M. Kasuga and S. Ogawa, Jpn. J. Appl. Phys., Part 1 **22**, 794 (1983).
[162] N. Takahashi, K. Kaiya, T. Nakamura, Y. Momose, and H. Yamamoto, Jpn. J. Appl. Phys., Part 2 **38**, L454 (1999).
[163] D. M. Bagnall, Y. F. Chen, Z. Zhu, T. Yao, S. Koyama, M. Y. Shen, and T. Goto, Appl. Phys. Lett. **70**, 2230 (1997).
[164] Z. K. Tang, G. K. L. Wong, P. Yu, M. Kawasaki, A. Ohtomo, H. Koinuma, and Y. Segawa, Appl. Phys. Lett. **72**, 3270 (1998).
[165] J. Narayan, K. Dovidenko, A. K. Sharma, and S. Oktyabrsky, J. Appl. Phys. **84**, 2597 (1998).
[166] H. J. Ko, Y. F. Chen, Z. Zhu, T. Hanada, and T. Yao, J. Cryst. Growth **208**, 389 (2000).
[167] R. J. Lad, P. D. Funkenbusch, and C. R. Aita, J. Vac. Sci. Technol. **17**, 808 (1980).
[168] W. Shih and M. Wu, J. Cryst. Growth **137**, 319 (1994).
[169] D. Hwang, K. Bang, M. Jeong, and J. Myoung, J. Cryst. Growth **254**, 449 (2003).
[170] A. Ohtomo, K. Tamura, K. Saikusa, K. Takahashi, T. Makino, Y. Segawa, H. Koinuma, and M. Kawasaki, Appl. Phys. Lett. **75**, 2635 (1999).
[171] T. Sekiguchi, S. Miyashita, K. Obara, T. Shishido, and N. Sakagami, J. Cryst. Growth **214/215**, 72 (2000).
[172] T. Sakagami, M. Yamashita, T. Sekiguchi, S. Miyashita, K. Obara, and T. Shishido, J. Cryst. Growth **229**, 98 (2001).
[173] W.-J. Li, E.-W. Shi, W.-Z. Zhong, and Z.-W. Yin, J. Cryst. Growth **203**, 186 (1999).
[174] K. Matsumoto and K. Noda, J. Cryst. Growth **102**, 137 (1990).
[175] J. Nause, III-Vs Review **12**, 28 (1999).
[176] M. Suscavage *et al.*, MRS Internet J. Nitride Semicond. Res. **4S1**, G3.40 (1999).
[177] M. A. L. Johnson, S. Fujita, W. H. Rowland, Jr., W. C. Hughes, J. W. Cook, Jr., and J. F. Schetzina, J. Electron. Mater. **21**, 157 (1992).
[178] K. Kobayashi, T. Matsubara, S. Matsushima, S. Shirakata, S. Isomura, and G. Okada, Thin Solid Films **266**, 106 (1995).
[179] M. A. L. Johnson, S. Fujita, W. H. Rowland, Jr., W. C. Hughes, J. W. Cook Jr., and J. F. Schetzina, J. Electron. Mater. **25**, 855 (1996).
[180] Y. Chen *et al.*, J. Cryst. Growth **181**, 165 (1997).
[181] Y. Chen, H.-J. Ko, S.-K. Hong, and T. Yao, Appl. Phys. Lett. **76**, 559 (2000).
[182] P. Fons, K. Iwata, S. Niki, A. Yamata, K. Matsubara, and M. Watanabe, J. Cryst. Growth **200**, 532 (2000).
[183] K. Nakamura, T. Shoji, and H.-B. Kang, Jpn. J. Appl. Phys., Part 2 **39**, L534 (2000).
[184] H.-B. Kang, K. Yoshida, and K. Nakamura, Jpn. J. Appl. Phys., Part 1 **37**, 5220 (1998).
[185] K. Sakurai, M. Kanehiro, K. Nakahara, T. Tanabe, S. Fujita, and S. Fujita, J. Cryst. Growth **209**, 522 (2000).
[186] H. Kato, M. Sano, K. Miyamota, and T. Yao, Jpn. J. Appl. Phys., Part 2 **42**, L1002 (2003).
[187] D. Kohl, M. Henzler, and G. Heiland, Surf. Sci. **41**, 403 (1974).
[188] J. L. Vossen, Phys. Thin Films **9**, 1 (1977).
[189] Z. Y. Xue, D. H. Zhang, Q. P. Wang, and J. H. Wang, Appl. Surf. Sci. **195**, 126 (2002).
[190] Y. M. Lu, W. S. Hwang, W. Y. Liu, and J. S. Yang, Mater. Chem. Phys. **72**, 269 (2001).
[191] S. Jeong, B. Kim, and B. Lee, Appl. Phys. Lett. **82**, 2625 (2003).
[192] S. J. Chen, Y. C. Liu, J. G. Ma, Y. M. Lu, J. Y. Zhang, D. Z. Shen, and X. W. Fan, J. Cryst. Growth **254**, 86 (2003).
[193] W. Water and S.-Y. Chu, Mater. Lett. **55**, 67 (2002).
[194] X. H. Li, A. P. Huang, M. K. Zhu, Sh. L. Xu, J. Chen, H. Wang, B. Wang, and H. Yan, Mater. Lett. **57**, 4655 (2003).
[195] S. K. Park and J. H. Je, Physica C **254**, 167 (1995).
[196] K. Tominaga, S. Iwamura, Y. Shintani, and O. Tada, Jpn. J. Appl. Phys., Part 1 21, 519 (1981).
[197] S. J. Doh, S. I. Park, T. S. Cho, and J. H. Je, J. Vac. Sci. Technol. A **17**, 3003 (1999).
[198] S. Maniv, W. D. Westwood, and E. Colombini, J. Vac. Sci. Technol. **20**, 162 (1982).
[199] J.-H. Jou, M.-Y. Han, and D.-J. Cheng, J. Appl. Phys. **71**, 4333 (1992).
[200] J. Hinze and K. Ellmer, J. Appl. Phys. **88**, 2443 (2000).
[201] K. Ozaki and M. Gomi, Jpn. J. Appl. Phys., Part 1 **41**, 5614 (2002).
[202] M. K. Ryu, S. H. Lee, M. S. Jang, G. N. Panin, and T. W. Kang, J. Appl. Phys. **92**, 154 (2002).
[203] C. Liu, Ü. Özgür, A. Teke, and H. Morkoç (unpublished).
[204] Y. Chen, D. Bagnall, and T. Yao, Mater. Sci. Eng., B **75**, 190 (2000).
[205] K.-K. Kim, H.-S. Kim, D.-K. Hwang, J.-H. Lim, and S.-J. Park, Appl. Phys. Lett. **83**, 63 (2003).
[206] S. Tüzemen, G. Xiong, J. Wilkinson, B. Mischuck, K. B. Ucer, and R. T. Williams, Physica B **308–310**, 1197 (2001).
[207] M. Kadota and M. Minakata, Jpn. J. Appl. Phys., Part 1 **37**, 2923 (1998).
[208] M. Kadota, T. Miura, and M. Minakata, J. Cryst. Growth **237–239**, 523 (2002).
[209] H.-B. Kang, K. Nakamura, S.-H. Lim, and D. Shindo, Jpn. J. Appl. Phys., Part 1 **37**, 781 (1998); H.-B. Kang, K. Nakamura, K. Yoshida, and K. Ishikawa, Jpn. J. Appl. Phys., Part 2 **36**, L933 (1997).
[210] P. Fons, K. Iwata, S. Niki, A. Yamada, K. Matsubara, and M. Watanabe, J. Cryst. Growth **209**, 532 (2000).
[211] K. Sakurai, D. Iwata, S. Fujita, and S. Fujita, Jpn. J. Appl. Phys., Part 1 **38**, 2606 (1999).
[212] N. Izyumskaya, V. Avrutin, W. Schoch, W. A. El-Shaer, F. Reuss, T. Gruber, and A. Waag, J. Cryst. Growth **269**, 356 (2004).
[213] K. Nakahara *et al.*, Jpn. J. Appl. Phys., Part 1 **40**, 250 (2001).
[214] T. Ohgaki, N. Ohashi, H. Kakemoto, S. Wada, Y. Adachi, H. Haneda, and T. Tsurumi, J. Appl. Phys. **93**, 1961 (2003).
[215] P. Fons, K. Iwata, A. Yamada, K. Matsubara, S. Niki, K. Nakahara, T. Tanabe, and H. Takasu, Appl. Phys. Lett. **77**, 1801 (2000).
[216] P. Fons, K. Iwata, A. Yamada, K. Matsubara, S. Niki, K. Nakahara, T. Tanabe, and H. Takasu, J. Cryst. Growth **227–228**, 911 (2001).
[217] K. Sakurai, M. Kanehiro, K. Nakahara, T. Tanabe, S. Fujita, and S. Fujita, J. Cryst. Growth **214/215**, 92 (2000).
[218] M. Sano, K. Miyamoto, H. Kato, and T. Yao, Jpn. J. Appl. Phys., Part 2 **42**, L1050 (2003).
[219] X. Du, M. Murakami, H. Iwaki, Y. Ishitani, and A. Yoshikawa, Jpn. J. Appl. Phys., Part 2 **41**, L1043 (2002).
[220] X. Wang, H. Iwaki, M. Murakami, X. Du, Y. Ishitani, and A. Yoshikawa, Jpn. J. Appl. Phys., Part 2 **42**, L99 (2003).
[221] K. Nakahara, H. Takasu, P. Fons, K. Iwata, A. Yamada, K. Matsubara, R. Hunger, and S. Niki, J. Cryst. Growth **227–228**, 923 (2001).
[222] K. Ogata, K. Koike, T. Tanite, T. Komuro, F. Yan, S. Sasa, M. Inoue, and M. Yano, J. Cryst. Growth **251**, 623 (2003).
[223] Y. Chen, H. J. Ko, S. Hong, T. Yao, and Y. Segawa, J. Cryst. Growth **214/215**, 87 (2000); Y. F. Chen, H. J. Ko, S. K. Hong, K. Inaba, Y. Segawa, and T. Yao, *ibid.* **227–228**, 917 (2001).
[224] K. Miyamoto, M. Sano, H. Kato, and T. Yao, Jpn. J. Appl. Phys., Part 2

[This article is copyrighted as indicated in the article. Reuse of AIP content is subject to the terms at: http://scitation.aip.org/termsconditions. Downloaded to] IP: 128.172.48.58 On: Mon, 19 Oct 2015 20:45:44

41, L1203 (2002).
[225] A. Ohtomo *et al.*, Appl. Phys. Lett. **72**, 2466 (1998).
[226] H. Kato, M. Sano, K. Miyamoto, and T. Yao, Jpn. J. Appl. Phys., Part 1 **42**, 2241 (2003).
[227] T. Ohnishi, A. Ohtomo, M. Kawasaki, K. Takahashi, M. Yoshimoto, and H. Koinuma, Appl. Phys. Lett. **72**, 824 (1998).
[228] S. Hong, T. Hanada, Y. Chen, H. Ko, T. Yao, D. Imai, K. Araki, and M. Shinohara, Appl. Surf. Sci. **190**, 491 (2002).
[229] I. Ohkubo, A. Ohtomo, T. Ohnishi, Y. Mastumoto, H. Koinuma, and M. Kawasaki, Surf. Sci. **443**, L1043 (1999).
[230] S. K. Hong *et al.*, Phys. Rev. B **65**, 115331 (2002).
[231] H. J. Ko, Y. Chen, S. Hong, and T. Yao, J. Cryst. Growth **209**, 816 (2000); S. Hong, H. J. Ko, Y. Chen, T. Hanada, and T. Yao, *ibid.* **214/215**, 81 (2000).
[232] C. Liu, S.-J. Cho, and H. Morkoç (unpublished).
[233] H. J. Ko, S. Hong, Y. Chen, and T. Yao, Thin Solid Films **409**, 153 (2002); S. Hong, H. J. Ko, Y. Chen, T. Hanada, and T. Yao, Appl. Surf. Sci. **159–160**, 441 (2000).
[234] S. Hong, H. Ko, Y. Chen, and T. Yao, J. Cryst. Growth **209**, 537 (2000).
[235] M. Fujita, N. Kawamota, T. Tatsumi, K. Yamagishi, and Y. Horikoshi, Jpn. J. Appl. Phys., Part 1 **42**, 67 (2003).
[236] N. Kawamoto, M. Fujita, T. Tatsumi, and Y. Horikoshi, Jpn. J. Appl. Phys., Part 1 **42**, 7209 (2003).
[237] L. N. Dinh, M. A. Schildbach, M. Balooch, and W. McLean II, J. Appl. Phys. **86**, 1149 (1999).
[238] A. Tsukazaki *et al.*, Nat. Mater. **4**, 42 (2005).
[239] A. Fouchet, W. Prellier, B. Mercey, L. Méchin, V. N. Kulkarni, and T. Venkatesan, J. Appl. Phys. **96**, 3228 (2004).
[240] W. Prellier, A. Fouchet, B. Mercey, C. Simon, and B. Raveau, Appl. Phys. Lett. **82**, 3490 (2003).
[241] H. Sankur and J. T. Cheung, J. Vac. Sci. Technol. A **1**, 1806 (1983).
[242] T. Nakayama, Surf. Sci. **133**, 101 (1983).
[243] S. Choopun, R. D. Vispute, W. Noch, A. Balsamo, R. P. Sharma, T. Venkatesan, A. Iliadis, and D. C. Look, Appl. Phys. Lett. **75**, 3947 (1999).
[244] A. V. Singh, R. M. Mehra, N. Buthrath, A. Wakahara, and A. Yoshida, J. Appl. Phys. **90**, 5661 (2001).
[245] K. Matsubara, P. Fons, K. Iwata, A. Yamada, and S. Niki, Thin Solid Films **422**, 176 (2002).
[246] V. Craciun, J. Elders, J. G. E. Gardeniers, and I. W. Boyd, Appl. Phys. Lett. **65**, 2963 (1994).
[247] A. Kh. Abduev, B. M. Ataev, and A. M. Bagamadova, Izv. Akad. Nauk SSSR, Neorg. Mater. **11**, 1928 (1987).
[248] R. A. Rabadanov, S. A. Semiletov, and Z. A. Magomedov, Solid State Phys. **12**, 1431 (1979).
[249] B. M. Ataev, A. M. Bagamadova, V. V. Mamedov, A. K. Omaev, and R. A. Rabadanov, J. Cryst. Growth **198–199**, 1222 (1999).
[250] M. V. Chukichev, B. M. Ataev, V. V. Mamedov, Ya. Alivov, and I. I. Khodos, Semiconductors **36**, 1052 (2002).
[251] B. M. Ataev, I. K. Kamilov, A. M. Bagamadova, V. V. Mamedov, A. K. Omaev, and M. Kh. Rabadanov, J. Tech. Phys. **69**, 138 (1999).
[252] K. Kaiya, K. Omichi, N. Takahashi, T. Nakamura, S. Okamoto, and H. Yamamoto, Thin Solid Films **409**, 116 (2002).
[253] N. Takashi, M. Makino, T. Nakamura, and H. Yamamoto, Chem. Mater. **14**, 3622 (2002).
[254] C. K. Lau, S. K. Tiku, and K. M. Lakin, J. Electrochem. Soc. **127**, 1843 (1980).
[255] F. T. J. Smith, Appl. Phys. Lett. **43**, 1108 (1983).
[256] C. R. Gorla, N. W. Emanetoglu, S. Liang, W. E. Mayo, and Y. J. Lu, J. Appl. Phys. **85**, 2595 (1999).
[257] Y. Kashiwaba, K. Haga, H. Watanabe, B. P. Zhang, Y. Segawa, and K. Wakatsuki, Phys. Status Solidi B **229**, 921 (2002).
[258] T. Yasuda and Y. Segawa, Phys. Status Solidi B **241**, 676 (2004).
[259] T. Gruber, C. Kirchner, and A. Waag, Phys. Status Solidi B **229**, 841 (2002).
[260] T. Gruber, C. Kirchner, K. Thonke, R. Sauer, and A. Waag, Phys. Status Solidi A **192**, 166 (2002).
[261] N. Oleynik *et al.*, Phys. Status Solidi A **192**, 189 (2002).
[262] N. Oleynik *et al.*, J. Cryst. Growth **248**, 14 (2003).
[263] T. Kaufmann, G. Fuchs, and W. Webert, Cryst. Res. Technol. **23**, 635 (1988).
[264] B. Hahn, G. Heindel, E. Pschorr-Schoberer, and W. Gebhardt, Semicond. Sci. Technol. **13**, 788 (1998).
[265] V. Sallet, J. F. Rommeluere, A. Lusson, A. Riviere, S. Fusil, O. Gorochov, and R. Triboulet, Phys. Status Solidi B **229**, 903 (2002).
[266] C. Kirchner, T. Gruber, F. Reuss, K. Thonke, A. Waag, C. Giessen, and M. Heuken, J. Cryst. Growth **248**, 20 (2003).
[267] K. Ogata, K. Maejima, Sz. Fujita, and Sg. Fujita, J. Electron. Mater. **30**, 659 (2001).
[268] K. Ogata, T. Kawanishi, K. Maejima, K. Sakurai, Sz. Fujita, and Sg. Fujita, J. Cryst. Growth **237**, 553 (2002).
[269] K. Ogata, K. Maejima, Sz. Fujita, and Sg. Fujita, J. Cryst. Growth **248**, 25 (2003).
[270] A. Dadgar *et al.*, J. Cryst. Growth **267**, 140 (2004).
[271] K. Ogata, T. Kawanishi, K. Sakurai, S.-W. Kim, K. Maejima, Sz. Fujita, and Sg. Fujita, Phys. Status Solidi B **229**, 915 (2002).
[272] C. R. Gorla, N. W. Emanetoglu, S. Liang, W. E. Mayo, Y. Lu, M. Wraback, and H. Shen, J. Appl. Phys. **85**, 2595 (1999).
[273] W. I. Park, S.-J. An, G.-C. Yi, and H. M. Jang, J. Mater. Res. **16**, 1358 (2001); W. I. Park, G.-C. Yi, and H. M. Jang, Appl. Phys. Lett. **79**, 2022 (2001).
[274] B. Zhang, L. Manh, K. Wakatsuki, T. Ohnishi, M. Lippmaa, N. Usami, M. Kawasaki, and Y. Segawa, Jpn. J. Appl. Phys., Part 1 **42**, 2291 (2003).
[275] B. Zhang *et al.*, Jpn. J. Appl. Phys., Part 2 **42**, L264 (2003).
[276] Y. Ma *et al.*, J. Cryst. Growth **255**, 303 (2003); Y. Ma *et al.*, J. Appl. Phys. **95**, 6268 (2004).
[277] T. P. Smith, W. J. Mecouch, P. Q. Miraglia, A. M. Roskowski, P. J. Hartlieb, and R. F. Davis, J. Cryst. Growth **257**, 255 (2003).
[278] T. P. Smith, H. A. McLean, D. J. Smith, P. Q. Miraglia, A. M. Roskowski, and R. F. Davis, J. Electron. Mater. **33**, 826 (2004).
[279] T. P. Smith, H. McLean, D. J. Smith, and R. F. Davis, J. Cryst. Growth **265**, 390 (2004).
[280] K. Ogata, K. Maejima, Sz. Fujita, and Sg. Fujita, J. Cryst. Growth **248**, 25 (2003).
[281] S. Muthukumar, H. F. Sheng, J. Zhong, Z. Zhang, N. W. Emanetoglu, and Y. C. Lu, IEEE Trans. Nanotechnol. **2**, 50 (2003).
[282] J. Zhong, S. Muthukumar, G. Saraf, H. Chen, Y. Chen, and Y. Lu, J. Electron. Mater. **33**, 654 (2004).
[283] W. I. Park, D. H. Kim, S.-W. Jung, and G.-C. Yi, Appl. Phys. Lett. **80**, 4232 (2002).
[284] M.-C. Jeong, B.-Y. Oh, W. Lee, and J.-M. Myoung, J. Cryst. Growth **268**, 149 (2004).
[285] W. Lee, M.-C. Jeong, and J.-M. Myoung, Acta Mater. **52**, 3949 (2004).
[286] H. Yuan and Y. Zhang, J. Cryst. Growth **263**, 119 (2004).
[287] R. Kling, C. Kirchner, T. Gruber, F. Reuss, and A. Waag, Nanotechnology **15**, 1043 (2004).
[288] W. I. Park, S. J. An, J. L. Yang, G. C. Yi, S. Hong, T. Joo, and M. Kim, J. Phys. Chem. B **108**, 15457 (2004).
[289] W. I. Park, J. S. Kim, G. C. Yi, M. H. Bae, and H. J. Lee, Appl. Phys. Lett. **85**, 5052 (2004).
[290] A. Mang, K. Reimann, and St. Rübenacke, Solid State Commun. **94**, 251 (1995).
[291] D. C. Reynolds, D. C. Look, B. Jogai, C. W. Litton, G. Cantwell, and W. C. Harsch, Phys. Rev. B **60**, 2340 (1999).
[292] W. R. L. Lambrecht, A. V. Rodina, S. Limpijumnong, B. Segall, and B. K. Meyer, Phys. Rev. B **65**, 075207 (2002).
[293] K. Thonke, T. Gruber, N. Teofilov, R. Schönfelder, A. Waag, and R. Sauer, Physica B **308–310**, 945 (2001).
[294] C. Boemare, T. Monteiro, M. J. Soares, J. G. Guilherme, and E. Alves, Physica B **308–310**, 985 (2001).
[295] W. R. L. Lambrecht, A. V. Rodina, S. Limpijumnong, B. Segall, and B. K. Meyer, Phys. Rev. B **65**, 075207 (2002).
[296] J. L. Birman, Phys. Rev. Lett. **2**, 157 (1959).
[297] D. C. Reynolds, D. C. Look, B. Jogai, and T. C. Collins, Appl. Phys. Lett. **79**, 3794 (2001).
[298] J. F. Muth, R. M. Kolbas, A. K. Sharma, S. Oktyabrsky, and J. Narayan, J. Appl. Phys. **85**, 1884 (1999).
[299] A. Teke, Ü. Özgür, S. Doğan, X. Gu, H. Morkoç, B. Nemeth, J. Nause, and H. O. Everitt, Phys. Rev. B **70**, 195207 (2004).
[300] S. F. Chichibu, T. Sota, G. Cantwell, D. B. Eason, and C. W. Litton, J. Appl. Phys. **93**, 756 (2003).
[301] S. F. Chichibu, A. Tsukazaki, M. Kawasaki, K. Tamura, Y. Segawa, T. Sota, and H. Koinuma, Appl. Phys. Lett. **80**, 2860 (2002).
[302] D. C. Reynolds, D. C. Look, B. Jogai, R. L. Jones, C. W. Litton, H. Harsch, and G. Cantwell, J. Lumin. **82**, 173 (1999).
[303] K. Hümmer and P. Gebhardt, Phys. Status Solidi B **85**, 271 (1978).
[304] J. F. Muth, R. M. Kolbas, A. K. Sharma, S. Oktyabrsky, and J. Narayan, J. Appl. Phys. **85**, 7884 (1999).

[This article is copyrighted as indicated in the article. Reuse of AIP content is subject to the terms at: http://scitation.aip.org/termsconditions. Downloaded to] IP: 128.172.48.58 On: Mon, 19 Oct 2015 20:45:44

[305] T. Makino *et al.*, Appl. Phys. Lett. **77**, 975 (2000).
[306] D. C. Reynolds, D. C. Look, B. Jogai, C. W. Litton, T. C. Collins, W. Harsch, and G. Cantwell, Phys. Rev. B **57**, 12151 (1998).
[307] X. T. Zhang *et al.*, J. Lumin. **99**, 149 (2002).
[308] D. W. Hamby, D. A. Lucca, M. J. Klopfstein, and G. Cantwell, J. Appl. Phys. **93**, 3214 (2003).
[309] H. Alves, D. Pfisterer, A. Zeuner, T. Riemann, J. Christen, D. M. Hofmann, and B. K. Meyer, Opt. Mater. (Amsterdam, Neth.) **23**, 33 (2003).
[310] D. C. Reynolds, D. C. Look, B. Jogai, C. W. Litton, T. C. Collins, H. Harsch, and G. Cantwell, Appl. Phys. Lett. **79**, 3794 (2001).
[311] J. J. Hopfield and D. G. Thomas, J. Phys. Chem. Solids **12**, 276 (1960).
[312] S. K. Suga, P. Cho, P. Heisinger, and T. Koda, J. Lumin. **12**, 109 (1967).
[313] C. Weisbuch and R. Ulbrich, Phys. Rev. Lett. **39**, 654 (1977).
[314] *Numerical Data and Functional Relationship in Science and Technology*, Landolt/Bornstein New Series III Vol. 41B, edited by U. Rosler (Springer, Berlin, 1999).
[315] J. Rorison, D. C. Herbert, D. J. Dean, and M. S. Skolnick, J. Phys. C **17**, 6435 (1984).
[316] A. Kobayashi, O. F. Sankey, and J. D. Dow, Phys. Rev. B **28**, 946 (1983).
[317] J. R. Haynes, Phys. Rev. Lett. **4**, 361 (1960).
[318] Y. P. Varshni, Physica (Amsterdam) **34**, 149 (1967); L. Wang and N. C. Giles, J. Appl. Phys. **94**, 973 (2003).
[319] A. K. Viswanath, J. I. Lee, S. Yu, D. Kim, Y. Choi, and C. H. Hong, J. Appl. Phys. **84**, 3848 (1998).
[320] D. C. Reynolds, D. C. Look, B. Jogai, J. E. Hoelscher, R. E. Sherriff, M. T. Harris, and M. J. Callahan, J. Appl. Phys. **88**, 2152 (2000).
[321] A. Kobayashi, O. F. Sankey, and J. D. Dow, Phys. Rev. B **28**, 946 (1983).
[322] T. Koida, S. F. Chichibu, A. Uedono, A. Tsukazaki, M. Kawasaki, T. Sota, Y. Segawa, and H. Koinuma, Appl. Phys. Lett. **82**, 532 (2003).
[323] S. W. Jung, W. I. Park, H. D. Cheong, G.-C. Yi, H. M. Jang, S. Hong, and T. Joo, Appl. Phys. Lett. **80**, 1924 (2002).
[324] R. Matz and H. Lütz, Appl. Phys. **18**, 123 (1979).
[325] W. S. Hu, Z. G. Liu, J. Sun, S. N. Zhu, Q. Q. Xu, D. Feng, and Z. M. Ji, J. Phys. Chem. Solids **58**, 853 (1997).
[326] H. Yoshikawa and S. Adachi, Jpn. J. Appl. Phys., Part 1 **36**, 6237 (1997).
[327] G. E. Jellison, Jr. and L. A. Boatner, Phys. Rev. B **58**, 3586 (1998).
[328] C. W. Teng, J. F. Muth, Ü. Özgür, M. J. Bergmann, H. O. Everitt, A. K. Sharma, C. Jin, and J. Narayan, Appl. Phys. Lett. **76**, 979 (2000).
[329] R. Schmidt *et al.*, Appl. Phys. Lett. **82**, 2260 (2003).
[330] K.-K. Kim, H.-S. Kim, D.-K. Hwang, J.-H. Lim, and S.-J. Park, Appl. Phys. Lett. **83**, 63 (2003).
[331] D. C. Reynolds, D. C. Look, B. Jogai, C. W. Litton, G. Cantwell, and W. C. Harsch, Phys. Rev. B **60**, 2340 (1999).
[332] C. Klingshirn, Phys. Status Solidi B **71**, 547 (1975).
[333] Ü. Özgür, A. Teke, C. Liu, S.-J. Cho, H. Morkoç, and H. O. Everitt, Appl. Phys. Lett. **84**, 3223 (2004).
[334] Y. Chen, N. T. Tuan, Y. Segawa, H.-J. Ko, S.-K. Hong, and T. Yao, Appl. Phys. Lett. **78**, 1469 (2001).
[335] D. M. Bagnall, Y. F. Chen, Z. Zhu, T. Yao, M. Y. Shen, and T. Goto, Appl. Phys. Lett. **73**, 1038 (1998).
[336] D. M. Bagnall, Y. F. Chen, M. Y. Shen, Z. Zhu, T. Goto, and T. Yao, J. Cryst. Growth **184–185**, 605 (1998).
[337] A. Yamamoto, T. Kido, T. Goto, Y. Chen, T. Yao, and A. Kasuya, Appl. Phys. Lett. **75**, 469 (1999).
[338] P. Yu, Z. K. Tang, G. K. L. Wong, M. Kawasaki, A. Ohtomo, H. Koinuma, and Y. Segawa, J. Cryst. Growth **184–185**, 601 (1998).
[339] M. Kawasaki *et al.*, Mater. Sci. Eng., B **56**, 239 (1998).
[340] P. Zu, Z. K. Tang, G. K. L. Wong, M. Kawasaki, A. Ohtomo, H. Koinuma, and Y. Segawa, Solid State Commun. **103**, 459 (1997).
[341] A. Ohtomo *et al.*, Mater. Sci. Eng., B **54**, 24 (1998).
[342] N. M. Lawandy, R. M. Balachandran, A. S. L. Gomes, and E. Sauvain, Nature (London) **368**, 436 (1994).
[343] D. S. Wiersma, M. P. van Albada, and A. Lagendijk, Phys. Rev. Lett. **75**, 1739 (1995).
[344] H. Cao, Y. G. Zhao, H. C. Ong, S. T. Ho, J. Y. Dai, J. Y. Wu, and R. P. H. Chang, Appl. Phys. Lett. **73**, 3656 (1998).
[345] H. Cao, Y. G. Zhao, S. T. Ho, E. W. Seelig, Q. H. Wang, and R. P. H. Chang, Phys. Rev. Lett. **82**, 2278 (1999).
[346] A. Mitra and R. K. Thareja, J. Appl. Phys. **89**, 2025 (2001).
[347] D. S. Wiersma and A. Lagendijk, Phys. Rev. E **54**, 4256 (1996).
[348] P. W. Anderson, Phys. Rev. **109**, 1492 (1958).
[349] I. P. Kuz'mina and V. A. Nikitenko, *Zinc Oxides: Production and Optical Properties* (Nauka, Moscow, 1984).
[350] D. I. Dimova-Alyakova, M. M. Malov, V. V. Dmitriev, V. D. Chernyi, and M. N. Mendakov, Moscow Energetical Institute Transactions (Trudy MEI) **192**, 78 (1974) (in Russian).
[351] S. Cho, J. Ma, Y. Kim, Y. Sun, G. K. L. Wong, and J. B. Ketterson, Appl. Phys. Lett. **75**, 2761 (1999).
[352] S. J. Chen *et al.*, J. Cryst. Growth **240**, 467 (2002).
[353] Y. G. Wang, S. P. Lau, H. W. Lee, S. F. Yu, B. K. Tay, X. H. Zhang, and H. H. Hng, J. Appl. Phys. **94**, 354 (2003).
[354] Ya. I. Alivov, A. V. Chernykh, M. V. Chukichev, and R. Y. Korotkov, Thin Solid Films **473**, 241 (2005).
[355] A. Ohtomo *et al.*, Appl. Phys. Lett. **77**, 2204 (2000).
[356] H. D. Sun *et al.*, Appl. Phys. Lett. **77**, 4250 (2000).
[357] B. Guo, Z. R. Qiu, and K. S. Wong, Appl. Phys. Lett. **82**, 2290 (2003).
[358] T. Koida, S. F. Chichibu, A. Uedono, A. Tsukazaki, M. Kawasaki, T. Sota, Y. Segawa, and H. Koinuma, Appl. Phys. Lett. **82**, 532 (2003).
[359] A. F. Kohan, G. Ceder, D. Morgan, and C. G. Van de Walle, Phys. Rev. B **61**, 15019 (2000).
[360] C. G. Van de Walle, Physica B **308–310**, 899 (2001).
[361] J. Neugebauer and C. G. Van de Walle, Appl. Phys. Lett. **69**, 503 (1996).
[362] A. Kobayashi, O. F. Sankey, and J. D. Dow, Phys. Rev. B **28**, 946 (1983).
[363] Y. Yan, S. B. Zhang, and S. T. Pantelides, Phys. Rev. Lett. **86**, 5723 (2001).
[364] K. Thonke, T. Gruber, N. Trofilov, R. Schönfelder, A. Waag, and R. Sauer, Physica B **308–310**, 945 (2001).
[365] D. C. Look, D. C. Reynolds, C. W. Litton, R. L. Jones, D. B. Eason, and G. Cantwell, Appl. Phys. Lett. **81**, 1830 (2002).
[366] J. F. Rommeluère, L. Svob, F. Jomard, J. Mimila-Arroyo, A. Lusson, V. Sallet, and Y. Marfaing, Appl. Phys. Lett. **83**, 287 (2003).
[367] H. Matsui, H. Saeki, H. Tabata, and T. Kawai, J. Electrochem. Soc. **150**, G508 (2003).
[368] A. Zeuner, H. Alves, D. M. Hofmann, B. K. Meyer, A. Hoffmann, U. Haboeck, M. Strassburg, and M. Dworzak, Phys. Status Solidi B **234**, R7 (2002).
[369] C. Morhain *et al.*, Phys. Status Solidi B **229**, 881 (2002).
[370] Y. R. Ryu, T. S. Lee, and H. W. White, Appl. Phys. Lett. **83**, 87 (2003).
[371] R. Dingle, Phys. Rev. Lett. **23**, 579 (1969).
[372] R. E. Dietz, H. Kamimura, M. D. Sturge, and A. Yariv, Phys. Rev. **132**, 1559 (1963).
[373] E. Mollwo, G. Müller, and P. Wagner, Solid State Commun. **13**, 1283 (1973).
[374] B. M. Kimpel and H. J. Schulz, Phys. Rev. B **43**, 9938 (1991).
[375] I. J. Broser, R. K. F. Germer, H.-J. E. Schulz, and K. P. Wisznewski, Solid-State Electron. **21**, 1597 (1978).
[376] P. Dahan, V. Fleurov, P. Thurian, R. Heitz, A. Hoffmann, and I. Broser, J. Phys.: Condens. Matter **10**, 2007 (1998).
[377] P. Dahan, V. Fleurov, P. Thurian, R. Heitz, A. Hoffmann, and I. Broser, Phys. Rev. B **57**, 9690 (1998).
[378] P. J. Dean, D. J. Robbins, S. G. Bishop, J. A. Savage, and P. Porteous, J. Phys. C **14**, 2847 (1981).
[379] P. Dahan, V. Fleurov, and K. Kikoin, J. Phys.: Condens. Matter **9**, 5355 (1997).
[380] R. Kuhnert and R. Helbig, J. Lumin. **26**, 203 (1981).
[381] D. C. Reynolds, D. C. Look, B. Jogai, J. E. Van Nostrand, R. Jones, and J. Jenny, Solid State Commun. **106**, 701 (1998).
[382] D. C. Reynolds, D. C. Look, and B. Jogai, J. Appl. Phys. **89**, 6189 (2001).
[383] N. Y. Garces, L. Wang, L. Bai, N. C. Giles, L. E. Halliburton, and G. Cantwell, Appl. Phys. Lett. **81**, 622 (2002).
[384] Ya. I. Alivov, M. V. Chukichev, and V. A. Nikitenko, Semiconductors **38**, 34 (2004).
[385] F. H. Leiter, H. R. Alves, N. G. Romanov, D. M. Hoffmann, and B. K. Meyer, Physica B **308–310**, 908 (2001).
[386] X. Yang *et al.*, J. Cryst. Growth **252**, 275 (2003).
[387] B. Guo, Z. R. Qiu, and K. S. Wong, Appl. Phys. Lett. **82**, 2290 (2003).
[388] H.-J. Egelhaaf and D. Oelkrug, J. Cryst. Growth **161**, 190 (1996).
[389] N. O. Korsunska, L. V. Borkovska, B. M. Bulakh, L. Yu. Khomenkova, V. I. Kushnirenko, and I. V. Markevich, J. Lumin. **102–103**, 733 (2003).
[390] B. Lin, Z. Fu, and Y. Jia, Appl. Phys. Lett. **79**, 943 (2001).
[391] K. Vanheusden, C. H. Seager, W. L. Warren, D. R. Tallant, and J. A. Voigt, Appl. Phys. Lett. **68**, 403 (1996); K. Vanheusden, W. L. Warren, C. H. Seager, D. R. Tallant, J. A. Voigt, and B. E. Gnade, J. Appl. Phys. **79**, 7983 (1996); K. Vanheusden, C. H. Seager, W. L. Warren, D. R.

[This article is copyrighted as indicated in the article. Reuse of AIP content is subject to the terms at: http://scitation.aip.org/termsconditions. Downloaded to] IP: 128.172.48.58 On: Mon, 19 Oct 2015 20:45:44

Tallant, J. Caruso, M. J. Hampden-Smith, and T. T. Kodas, J. Lumin. **75**, 11 (1997).
[392] S. A. Studenikin, N. Golego, and M. Cocivera, J. Appl. Phys. **84**, 2287 (1998).
[393] F. H. Leiter, H. R. Alves, A. Hofstaetter, D. M. Hoffmann, and B. K. Meyer, Phys. Status Solidi B **226**, R4 (2001).
[394] F. H. Leiter, H. R. Alves, N. G. Romanov, D. M. Hoffmann, and B. K. Meyer, Physica B **340–342**, 201 (2003).
[395] M. A. Reshchikov and R. Y. Korotkov, Phys. Rev. B **64**, 115205 (2001).
[396] R. T. Cox, D. Block, A. Hervé, R. Picard, C. Santier, and R. Helbig, Solid State Commun. **25**, 77 (1978).
[397] G. F. Neumark, Phys. Rev. Lett. **62**, 1800 (1989).
[398] D. J. Chadi, Phys. Rev. Lett. **72**, 534 (1994).
[399] S. B. Zhang, S.-H. Wei, and A. Zunger, Phys. Rev. Lett. **84**, 1232 (2000).
[400] T. Minami, H. Sato, H. Nanto, and S. Takata, Jpn. J. Appl. Phys., Part 2 **24**, L781 (1985).
[401] S. B. Zhang, S.-H. Wei, and A. Zunger, J. Appl. Phys. **83**, 3192 (1998).
[402] D. B. Laks, C. G. Van de Walle, G. F. Neumark, and S. T. Pantelides, Appl. Phys. Lett. **63**, 1375 (1993).
[403] S. F. J. Cox *et al.*, Phys. Rev. Lett. **86**, 2601 (2001).
[404] Y. M. Strzhemechny *et al.*, Appl. Phys. Lett. **84**, 2545 (2004).
[405] H. Kato, M. Sano, K. Miyamoto, and T. Yao, J. Cryst. Growth **237–239**, 538 (2002).
[406] S. Y. Myong, S. J. Baik, C. H. Lee, W. Y. Cho, and K. S. Lim, Jpn. J. Appl. Phys., Part 2 **36**, L1078 (1997).
[407] B. M. Ataev, A. M. Bagamadova, A. M. Djabrailov, V. V. Mamedo, and R. A. Rabadanov, Thin Solid Films **260**, 19 (1995).
[408] V. Assuncao, E. Fortunato, A. Marques, H. Aguas, I. Ferreira, M. E. V. Costa, and R. Martins, Thin Solid Films **427**, 401 (2003).
[409] Z. F. Liu, F. K. Shan, Y. X. Li, B. C. Shin, and Y. S. Yu, J. Cryst. Growth **259**, 130 (2003).
[410] M. Chen, Z. Pei, W. Xi, C. Sun, and L. Wen, Mater. Res. Soc. Symp. Proc. **666**, F.1.2. (2001).
[411] H. J. Ko, Y. F. Chen, S. K. Hong, H. Wenisch, T. Yao, and D. C. Look, Appl. Phys. Lett. **77**, 3761 (2000).
[412] T. Minami, H. Nanto, and S. Takata, Jpn. J. Appl. Phys., Part 2 **23**, L280 (1984).
[413] W. Walukiewicz, Phys. Rev. B **50**, 5221 (1994).
[414] C. G. Van de Walle, D. B. Laks, G. F. Neumark, and S. T. Pantelides, Phys. Rev. B **47**, 9425 (1993).
[415] O. F. Schirmer, J. Phys. Chem. Solids **29**, 1407 (1968).
[416] A. Valentini, F. Quaranta, M. Rossi, and G. Battaglin, J. Vac. Sci. Technol. A **9**, 286 (1991).
[417] Y. Kanai, Jpn. J. Appl. Phys., Part 1 **30**, 703 (1991).
[418] Y. Kanai, Jpn. J. Appl. Phys., Part 1 **30**, 2021 (1991).
[419] C. H. Park, S. B. Zhang, and S.-H. Wei, Phys. Rev. B **66**, 073202 (2002).
[420] C. G. Van de Walle, D. B. Laks, G. F. Neumark, and S. T. Pantelides, Phys. Rev. B **47**, 9425 (1993).
[421] D. B. Laks, C. G. Van de Walle, G. F. Neumark, and S. T. Pantelides, Phys. Rev. Lett. **66**, 648 (1991).
[422] A. Garcia and J. E. Northrup, Phys. Rev. Lett. **74**, 1131 (1995).
[423] M. L. Cohen, Phys. Scr., T **T1**, 5 (1982).
[424] J. Ihm, A. Zunger, and M. L. Cohen, J. Phys. C **12**, 4409 (1979).
[425] D. C. Look, R. L. Jones, J. R. Sizelove, N. Y. Garces, N. C. Giles, and L. E. Halliburton, Phys. Status Solidi A **195**, 171 (2004).
[426] A. Kobayashi, O. F. Sankey, and J. D. Dow, Phys. Rev. B **28**, 946 (1983).
[427] Z. L. Wu, J. L. Merz, C. J. Werkhoven, B. J. Fitzpatrick, and R. N. Bhargava, Appl. Phys. Lett. **40**, 345 (1982).
[428] H. Morkoç, S. Strite, G. B. Gao, M. E. Lin, B. Sverdlov, and M. Burns, J. Appl. Phys. **76**, 1363 (1994).
[429] E.-C. Lee, Y.-S. Kim, Y.-G. Jin, and K. J. Chang, Phys. Rev. B 64, 85120 (2001).
[430] R. M. Park, M. B. Troffer, C. M. Rouleau, J. M. DePuydt, and M. A. Hasse, Appl. Phys. Lett. **57**, 2127 (1990).
[431] L. Svob, C. Thiandoume, A. Lusson, M. Bouanani, Y. Marfaing, and O. Gorochov, Appl. Phys. Lett. **76**, 1695 (2000).
[432] H. D. Jung, C. D. Song, S. Q. Wang, K. Arai, Y. H. Wu, Z. Zhu, T. Yao, and H. Katayama-Yoshida, Appl. Phys. Lett. **70**, 1143 (1997).
[433] K. Iwata, P. Fons, A. Yamada, K. Matsubara, and S. Niki, J. Cryst. Growth **209**, 526 (2000).
[434] A. B. M. A. Ashrafi, I. Suemune, H. Kumano, and S. Tanaka, Jpn. J. Appl. Phys., Part 2 **41**, L1281 (2002).
[435] K. Minegishi, Y. Koiwai, Y. Kikuchi, K. Yano, M. Kasuga, and A. Shimizu, Jpn. J. Appl. Phys., Part 2 **36**, L1453 (1997).
[436] Z.-Z. Ye, J.-G. Lu, H.-H. Chen, Y.-Z. Zhang, L. Wang, B.-H. Zhao, and J.-Y. Huang, J. Cryst. Growth **253**, 258 (2003).
[437] J. Wang *et al.*, J. Cryst. Growth **255**, 293 (2003).
[438] J. Lu, Y. Zhang, Z. Ye, L. Wang, B. Zhao, and J. Huang, Mater. Lett. **57**, 3311 (2003).
[439] Y. Sato and S. Sato, Thin Solid Films **281–282**, 445 (1996).
[440] X.-L. Guo, H. Tabata, and T. Kawai, J. Cryst. Growth **237–239**, 544 (2002).
[441] Y. Yan, S. B. Zhang, and S. T. Pantelides, Phys. Rev. Lett. **86**, 5723 (2001).
[442] X. Wang, S. Yang, J. Wang, M. Li, X. Jiang, G. Du, X. Liu, and R. P. H. Chang, J. Cryst. Growth **226**, 123 (2001).
[443] X. Li, Y. Yan, T. A. Gessert, C. L. Perkins, D. Young, C. DeHart, M. Young, and T. J. Coutts, J. Vac. Sci. Technol. A **21**, 1342 (2003).
[444] X. Li, Y. Yan, T. A. Gessert, C. DeHart, C. L. Perkins, D. Young, and T. J. Coutts, Electrochem. Solid-State Lett. **6**, C56 (2003).
[445] J. G. Ma, Y. C. Liu, R. Mu, J. Y. Zhang, Y. M. Lu, D. Z. Shen, and X. W. Fan, J. Vac. Sci. Technol. B **22**, 94 (2004).
[446] C.-C. Lin, S.-Y. Chen, S.-Y. Cheng, and H.-Y. Lee, Appl. Phys. Lett. **84**, 5040 (2004).
[447] C. Wang, Z. Ji, K. Liu, Y. Xiang, and Z. Ye, J. Cryst. Growth **259**, 279 (2003).
[448] N. Y. Garces, N. C. Giles, L. E. Halliburton, G. Cantwell, D. B. Eason, D. C. Reynolds, and D. C. Look, Appl. Phys. Lett. **80**, 1334 (2002).
[449] N. Y. Garces, L. Wang, N. C. Giles, L. E. Halliburton, G. Cantwell, and D. B. Eason, J. Appl. Phys. **94**, 519 (2003).
[450] J. Lu, Z. Ye, L. Wang, J. Huang, and B. Zhao, Mater. Sci. Semicond. Process. **5**, 491 (2003).
[451] K. Iwata, P. Fons, A. Yamada, K. Matsubara, and S. Niki, J. Cryst. Growth **209**, 526 (2000).
[452] A. Zeuner *et al.*, Phys. Status Solidi C **1**, 731 (2004).
[453] S. Yamauchi, Y. Goto, and T. Hariu, J. Cryst. Growth **260**, 1 (2004).
[454] T. Yamamoto and H. Katayama-Yoshida, J. Cryst. Growth **214/215**, 552 (2000); , Jpn. J. Appl. Phys., Part 2 **38**, L166 (1999).
[455] T. Yamamoto, Thin Solid Films **420–421**, 100 (2002).
[456] A. Tsukazaki *et al.*, Appl. Phys. Lett. **81**, 235 (2002).
[457] K. Nakahara, H. Takasu, P. Fons, A. Yamada, K. Iwata, K. Matsubara, R. Hunger, and S. Niki, Appl. Phys. Lett. **79**, 4139 (2001).
[458] K. Nakahara, H. Takasu, P. Fons, A. Yamada, K. Iwata, K. Matsubara, R. Hunger, and S. Niki, J. Cryst. Growth **237–239**, 503 (2002).
[459] T. Ohshima, T. Ikegami, K. Ebihara, J. Asmussen, and R. Thareja, Thin Solid Films **435**, 49 (2003).
[460] M. Sumiya, A. Tsukazaki, S. Fuke, A. Ohtomo, H. Koinuma, and M. Kawasaki, Appl. Surf. Sci. **223**, 206 (2004).
[461] Ya. I. Alivov, D. C. Look, B. M. Ataev, M. V. Chukichev, V. V. Mamedov, V. I. Zinenko, Yu. A. Agafonov, and A. N. Pustovit, Solid-State Electron. **48**, 2343 (2004).
[462] T. Ohshima, T. Ikegami, K. Ebihara, J. Asmussen, and R. Thareja, Thin Solid Films **435**, 49 (2003).
[463] M. Joseph, H. Tabata, and T. Kawai, Jpn. J. Appl. Phys., Part 2 **38**, L1205 (1999).
[464] A. V. Singh, R. M. Mehra, A. Wakahara, and A. Yoshida, J. Appl. Phys. **93**, 396 (2003).
[465] J. M. Bian, X. M. Li, X. D. Gao, W. D. Yu, and L. D. Chen, Appl. Phys. Lett. **84**, 541 (2004).
[466] Z.-Z. Ye, Z.-G. Fei, J.-G. Lu, Z.-H. Zhang, L.-P. Zhu, B.-H. Zhao, and J.-Y. Huang, J. Cryst. Growth **265**, 127 (2004).
[467] T. Aoki, Y. Hatanaka, and D. C. Look, Appl. Phys. Lett. **76**, 3257 (2000).
[468] K.-K. Kim, H.-S. Kim, D.-K. Hwang, J.-H. Lim, and S.-J. Park, Appl. Phys. Lett. **83**, 63 (2003).
[469] Y. R. Ryu, S. Zhu, D. C. Look, J. M. Wrobel, H. M. Jeong, and H. W. White, J. Cryst. Growth **216**, 330 (2000).
[470] M. K. Ryu, S. H. Lee, and M. S. Jang, J. Appl. Phys. **92**, 158 (2002).
[471] C. Morhain *et al.*, Phys. Status Solidi B **229**, 881 (2002).
[472] Y. W. Heo, S. J. Park, K. Ip, S. J. Pearton, and D. P. Norton, Appl. Phys. Lett. **83**, 1128 (2003).
[473] S. Y. Lee, E. S. Shim, H. S. Kang, S. S. Pang, and J. S. Kang, Thin Solid Films **473**, 31 (2005).
[474] S.-J. Park (private communication).
[475] Y. W. Heo, Y. W. Kwon, Y. Li, S. J. Pearton, and D. P. Norton, Appl. Phys. Lett. **84**, 3474 (2004).
[476] O. Lopatiuk *et al.*, Appl. Phys. Lett. **86**, 012105 (2005).
[477] K. Ip, Y. W. Heo, D. P. Norton, S. J. Pearton, J. R. LaRoche, and F. Ren,

[This article is copyrighted as indicated in the article. Reuse of AIP content is subject to the terms at: http://scitation.aip.org/termsconditions. Downloaded to] IP: 128.172.48.58 On: Mon, 19 Oct 2015 20:45:44

Appl. Phys. Lett. **85**, 1169 (2004).
[478] C. Weisbuch and B. Vinter, *Quantum Semiconductor Structures* (Academic, San Diego, 1991).
[479] J. K. Furdyna, J. Appl. Phys. **64**, R29 (1988).
[480] G. A. Prinz, Science **282**, 1660 (1998).
[481] N. Samarth and D. D. Awschalom, in *Quantum Circuits and Devices*, edited by K. Ismail, S. Bandyopadhyay, and J. P. Leburton (Imperial College Press, London, 1998), pp. 136–141.
[482] H. Ohno, Science **281**, 951 (1998).
[483] B. Beschoten, P. A. Crowell, I. Malajovich, D. D. Awschalom, F. Matsukura, A. Shen, and H. Ohno, Phys. Rev. Lett. **83**, 3073 (1999).
[484] I. Malajovich, J. J. Berry, N. Samarth, and D. D. Awschalom, Nature (London) **411**, 770 (2001).
[485] K. Ueda, H. Tabata, and T. Kawai, Appl. Phys. Lett. **79**, 988 (2001).
[486] H. Saeki, H. Tabata, and T. Kawai, Solid State Commun. **120**, 439 (2001).
[487] K. Rode, A. Anane, R. Mattana, J.-P. Contour, O. Durand, and R. LeBourgeois, J. Appl. Phys. **93**, 7676 (2003).
[488] P. Sharma *et al.*, Nat. Mater. **2**, 673 (2003).
[489] S. Ramachandran, A. Tiwari, and J. Narayan, Appl. Phys. Lett. **84**, 5255 (2004).
[490] H.-T. Lin, T.-S. Chin, J.-C. Shih, S.-H. Lin, T.-M. Hong, R.-T. Huang, F.-R. Chen, and J.-J. Kai, Appl. Phys. Lett. **85**, 621 (2004).
[491] M. L. Reed, N. A. El-Masry, H. H. Stadelmaier, M. K. Ritums, M. J. Reed, C. A. Parker, J. C. Roberts, and S. M. Bedair, Appl. Phys. Lett. **79**, 3473 (2001).
[492] M. Linnarsson, E. Janzén, B. Monemar, M. Kleverman, and A. Thilderkvist, Phys. Rev. B **55**, 6938 (1997).
[493] K. Ando, H. Saito, Z. Jin, T. Fukumura, M. Kawasaki, Y. Matsumoto, and H. Koinuma, J. Appl. Phys. **89**, 7284 (2001).
[494] Z. Jin *et al.*, Appl. Phys. Lett. **78**, 3824 (2001).
[495] T. Fukumura, Z. Jin, A. Ohtomo, H. Koinuma, and M. Kawasaki, Appl. Phys. Lett. **75**, 3366 (1999).
[496] T. Fukumura, Z. Jin, M. Kawasaki, T. Shono, T. Hasegawa, S. Koshihara, and H. Koinuma, Appl. Phys. Lett. **78**, 958 (2001).
[497] S. W. Jung, S.-J. An, G.-C. Yi, C. U. Jung, S.-I. Lee, and S. Cho, Appl. Phys. Lett. **80**, 4561 (2002).
[498] D. P. Norton, S. J. Pearton, A. F. Hebard, N. Theodoropoulou, L. A. Boatner, and R. G. Wilson, Appl. Phys. Lett. **82**, 239 (2003).
[499] Y. M. Kim, M. Yoon, I.-W. Park, Y. J. Park, and J. H. Lyou, Solid State Commun. **129**, 175 (2004).
[500] D. P. Norton *et al.*, Appl. Phys. Lett. **83**, 5488 (2003).
[501] T. Wakano, N. Fujimura, Y. Morinaga, N. Abe, A. Ashida, and T. Ito, Physica C **10**, 260 (2001).
[502] M. Berciu and R. N. Bhatt, Phys. Rev. Lett. **87**, 107203 (2001).
[503] A. Kaminski and S. Das Sarma, Phys. Rev. Lett. **88**, 247201 (2001).
[504] T. Dietl, F. Matsukura, and H. Ohno, Phys. Rev. B **66**, 033203 (2002).
[505] S. Das Sarma, E. H. Hwang, and A. Kaminski, Phys. Rev. B **67**, 155201 (2003).
[506] J. Warnock and P. A. Wolff, Phys. Rev. B **31**, 6579 (1985).
[507] M. Sawicki, T. Dietl, J. Kossut, J. Igalson, T. Wojtowicz, and W. Plesiewicz, Phys. Rev. Lett. **56**, 508 (1986).
[508] J. M. D. Coey, M. Venkatesan, and C. B. Fitzgerald, Nat. Mater. **4**, 73 (2005).
[509] T. Dietl and J. Spalek, Phys. Rev. Lett. **48**, 355 (1982).
[510] C. Zener, Phys. Rev. **81**, 440 (1950); **83**, 299 (1950).
[511] T. Dietl, Nat. Mater. **2**, 646 (2003).
[512] K. Sato and H. Katayama-Yoshida, Jpn. J. Appl. Phys., Part 2 **39**, L555 (2000).
[513] K. Sato and H. Katayama-Yoshida, Physica B **308–310**, 904 (2001).
[514] K. Sato and H. Katayama-Yoshida, Semicond. Sci. Technol. **17**, 367 (2002).
[515] K. Nishizawa and O. Sakai, Physica B **281–282**, 468 (2000).
[516] J. Schliemann, J. Konig, and A. H. MacDonald, Phys. Rev. B **64**, 165201 (2001).
[517] J. Konig, H. H. Lin, and A. H. MacDonald, Phys. Rev. Lett. **84**, 5628 (2000).
[518] T. Jungwirth, W. A. Atkinson, B. H. Lee, and A. H. MacDonald, Phys. Rev. B **59**, 9818 (1999).
[519] Q. Wang and P. Jena, Appl. Phys. Lett. **84**, 4170 (2004).
[520] S. W. Yoon, S.-B. Cho, S. C. We, S. Yoon, B. J. Suh, H. K. Song, and Y. J. Shin, J. Appl. Phys. **93**, 7879 (2003).
[521] T. Sekiguchi, K. Haga, and K. Inaba, J. Cryst. Growth **214**, 68 (2000).
[522] J. H. Kim, H. Kim, D. Kim, Y. E. Ihm, and W. K. Choo, J. Appl. Phys. **92**, 6066 (2002).
[523] S. J. Pearton *et al.*, J. Appl. Phys. **93**, 1 (2003).
[524] L. W. Guo, D. L. Peng, H. Makino, K. Inaba, H. J. Ko, K. Sumiyama, and T. Yao, J. Magn. Magn. Mater. **213**, 321 (2000).
[525] A. Tiwari, C. Jin, A. Kvit, D. Kumar, J. F. Muth, and J. Narayan, Solid State Commun. **121**, 371 (2002).
[526] X. M. Cheng and C. L. Chien, J. Appl. Phys. **93**, 7876 (2003).
[527] A. Ohtomo, M. Kawasaki, T. Koida, K. Masubuchi, and H. Koinuma, Appl. Phys. Lett. **72**, 2466 (1998).
[528] A. Ohtomo, R. Shiroki, I. Ohkubo, H. Koinuma, and M. Kawasaki, Appl. Phys. Lett. **75**, 4088 (1999).
[529] S. Choopun, R. D. Vispute, W. Yang, R. P. Sharma, T. Venkatesan, and H. Shen, Appl. Phys. Lett. **80**, 1529 (2002).
[530] T. Gruber, C. Kirchner, R. Kling, F. Reuss, and A. Waag, Appl. Phys. Lett. **84**, 5359 (2004).
[531] K. Ogata, K. Koike, T. Tanite, T. Komuro, F. Yan, S. Sasa, M. Inoue, and M. Yano, J. Cryst. Growth **251**, 623 (2003).
[532] T. Minemmoto, T. Negami, S. Nishiwaki, H. Takakura, and Y. Hamakawa, Thin Solid Films **372**, 173 (2000).
[533] S. Krishnamoorthy, A. A. Iliadis, A. Inumpudi, S. Choopun, R. D. Vispute, and T. Venkatesan, Solid-State Electron. **46**, 1633 (2002).
[534] T. Makino, A. Ohtomo, C. H. Chia, Y. Segawa, H. Koinuma, and M. Kawasaki, Physica E (Amsterdam) **21**, 671 (2004).
[535] F. K. Shan, B. I. Kim, G. X. Liu, Z. F. Liu, J. Y. Sohn, W. J. Lee, B. C. Shin, and Y. S. Yu, J. Appl. Phys. **95**, 4772 (2004).
[536] D. J. Cohen, K. C. Ruthe, and S. A. Barnett, J. Appl. Phys. **96**, 459 (2004).
[537] A. Ohtomo *et al.*, Appl. Phys. Lett. **77**, 2204 (2000).
[538] A. Ohtomo, M. Kawasaki, I. Ohkubo, H. Koinuma, T. Yasuda, and Y. Segawa, Appl. Phys. Lett. **75**, 980 (1999).
[539] H. D. Sun, T. Makino, Y. Segawa, M. Kawasaki, A. Ohtomo, K. Tamura, and H. Koinuma, J. Appl. Phys. **91**, 1993 (2002).
[540] T. Makino, Y. Segawa, M. Kawasaki, A. Ohtomo, R. Shiroki, K. Tamura, T. Yasuda, and H. Koinuma, Appl. Phys. Lett. **78**, 1237 (2001).
[541] T. Makino, C. H. Chia, N. T. Tuan, Y. Segawa, M. Kawasaki, A. Ohtomo, K. Tamura, and H. Koinuma, Appl. Phys. Lett. **77**, 1632 (2000).
[542] D. W. Ma, Z. Z. Ye, and L. L. Chen, Phys. Status Solidi A **201**, 2929 (2004).
[543] K. Sakurai, T. Takagi, T. Kubo, D. Kajita, T. Tanabe, H. Takasu, S. Fujita, and S. Fujita, J. Cryst. Growth **237–239**, 514 (2002).
[544] T. Gruber *et al.*, Appl. Phys. Lett. **83**, 3290 (2003).
[545] T. Tanabe, H. Takasu, S. Fujita, and S. Fujita, J. Cryst. Growth **237–239**, 514 (2002).
[546] O. Vigil, L. Vaillant, F. Cruz, G. Santana, A. Morales-Acevedo, and G. Contreras-Puente, Thin Solid Films **361–362**, 53 (2000).
[547] Y.-S. Choi, C.-C. Lee, and S. M. Cho, Thin Solid Films **289**, 153 (1996).
[548] J. A. Van Vechten and T. K. Bergstresser, Phys. Rev. B **1**, 3351 (1970).
[549] E. R. Segnit and A. E. Holland, J. Am. Ceram. Soc. **48**, 412 (1965).
[550] R. P. Koffyberg, Phys. Rev. B **13**, 4470 (1976).
[551] M. E. Lin, Z. Ma, F. Y. Huang, Z. F. Fan, L. H. Allen, and H. Morkoç, Appl. Phys. Lett. **64**, 1003 (1994).
[552] V. Hoppe, D. Stachel, and D. Beyer, Phys. Scr., T **T57**, 122 (1994).
[553] A. A. Iliadis, R. D. Vispute, T. Venkatesan, and K. A. Jones, Thin Solid Films **420–421**, 478 (2002).
[554] H. Ishikawa, K. Tsukui, Y. Koide, N. Teraguchi, Y. Tomomura, A. Suzuki, and M. Murakami, J. Vac. Sci. Technol. B **14**, 1812 (1996).
[555] H. Sheng, N. W. Emanetoglu, S. Muthukumar, S. Feng, and Y. Lu, J. Electron. Mater. **31**, 811 (2002).
[556] H. K. Kim, S. H. Han, T. Y. Seong, and W. K. Choi, Appl. Phys. Lett. **77**, 1647 (2000).
[557] H. K. Kim, S. H. Han, T. Y. Seong, and W. K. Choi, J. Electrochem. Soc. **148**, G114 (2001).
[558] Y. J. Lin and C. T. Lee, Appl. Phys. Lett. **77**, 3986 (2000).
[559] H. K. Kim, K. K. Kim, S. J. Park, T. Y. Seong, and I. Adesida, J. Appl. Phys. **94**, 4225 (2003).
[560] T. Akane, K. Sugioka, and K. Midorikawa, J. Vac. Sci. Technol. B **18**, 1406 (2000).
[561] J. M. Lee, K. K. Kim, S. J. Park, and W. K. Choi, Appl. Phys. Lett. **78**, 3842 (2001).
[562] G. S. Marlow and M. B. Das, Solid-State Electron. **25**, 91 (1982).
[563] H. K. Kim, K. K. Kim, S. J. Park, T. Y. Seong, and Y. S. Yoon, Jpn. J. Appl. Phys., Part 2 **41**, L546 (2002).
[564] A. Inumpudi, A. A. Iliadis, S. Krishnamoorthy, S. Choopun, R. D. Vispute, and T. Venkatesan, Solid-State Electron. **46**, 1665 (2002).

[This article is copyrighted as indicated in the article. Reuse of AIP content is subject to the terms at: http://scitation.aip.org/termsconditions. Downloaded to] IP: 128.172.48.58 On: Mon, 19 Oct 2015 20:45:44

[565] L. J. Brillson, J. Vac. Sci. Technol. **15**, 1378 (1978).
[566] K. Ip *et al.*, J. Vac. Sci. Technol. B **21**, 2378 (2003).
[567] K. Ip, Y. Heo, K. Baik, D. P. Norton, S. J. Pearton, and F. Ren, Appl. Phys. Lett. **84**, 544 (2004).
[568] K. Ip, Y. Heo, K. Baik, D. P. Norton, S. J. Pearton, and F. Ren, J. Vac. Sci. Technol. B **22**, 171 (2004).
[569] S. Liang, H. Sheng, Y. Liu, Z. Huo, Y. Lu, and H. Shen, J. Cryst. Growth **225**, 110 (2001).
[570] H. Sheng, S. Muthukumar, N. W. Emanetoglu, and Y. Lu, Appl. Phys. Lett. **80**, 2132 (2002).
[571] J. C. Simpson and J. F. Cordora, J. Appl. Phys. **63**, 1781 (1988).
[572] G. Xiong, J. Wilkinson, M. Mischuck, S. Tuzemen, K. B. Ucer, and R. T. Williams, Appl. Phys. Lett. **80**, 1195 (2002).
[573] B. J. Koppa, R. F. Davis, and R. J. Nemanich, Appl. Phys. Lett. **82**, 400 (2003).
[574] N. Ohashi, J. Tanaka, T. Ohgaki, H. Haneda, M. Ozawa, and T. Tsurumi, J. Mater. Res. **17**, 1529 (2002).
[575] F. D. Auret, S. A. Goodman, M. Hayes, M. J. Legodi, H. A. van Laarhoven, and D. C. Look, Appl. Phys. Lett. **79**, 3074 (2001).
[576] S. Kim, B. Kang, F. Ren, Y. Heo, K. Ip, D. P. Norton, and S. J. Pearton, Appl. Phys. Lett. **84**, 1904 (2004).
[577] J. H. Lim, K. K. Kim, D. K. Hwang, H. K. Kim, J. H. Oh, and S. J. Park, J. Electrochem. Soc. **152**, G179 (2005).
[578] A. Y. Polyakov, N. B. Smirnov, E. A. Kozhukhova, V. I. Vdodin, K. Ip, Y. W. Heo, D. P. Norton, and S. J. Pearton, Appl. Phys. Lett. **83**, 1575 (2003).
[579] C. A. Mead, Phys. Lett. **18**, 218 (1965).
[580] R. C. Neville and C. A. Mead, J. Appl. Phys. **41**, 3795 (1970).
[581] S. V. Slobodchikov, Kh. M. Salikhov, E. V. Russu, and Yu. G. Malinin, Semiconductors **35**, 464 (2001).
[582] S.-H. Kim, H.-K. Kim, and T.-Y. Seong, Appl. Phys. Lett. **86**, 112101 (2005).
[583] K. Ip *et al.*, Appl. Phys. Lett. **84**, 5133 (2004).
[584] K. Ip *et al.*, Appl. Surf. Sci. **236**, 387 (2004).
[585] K. Ip, Y. W. Heo, K. H. Baik, D. P. Norton, S. J. Pearton, S. Kim, J. R. LaRoche, and F. Ren, Appl. Phys. Lett. **84**, 2835 (2004).
[586] S. M. Sze, *Physics of Semiconductor Devices* (Wiley, New York, 1981).
[587] G. Xiong, J. Wilkinson, S. Tüzemen, K. B. Ucer, and R. T. Williams, Proc. SPIE **256**, 4644 (2002).
[588] I.-S. Jeong, J.-H. Kim, and S. Im, Appl. Phys. Lett. **83**, 2946 (2003).
[589] S. E. Nikitin, Yu. A. Nikolaev, I. K. Polushina, V. Yu. Rud, Yu. V. Rud, and E. I. Terukov, Semiconductors **37**, 1329 (2003).
[590] Y. I. Alivov, J. E. Van Nostrand, D. C. Look, M. V. Chukichev, and B. M. Ataev, Appl. Phys. Lett. **83**, 2943 (2003).
[591] Q.-X. Yu, B. Xu, Q.-H. Wu, Y. Liao, G.-Z. Wang, R.-C. Fang, H.-Y. Lee, and C.-T. Lee, Appl. Phys. Lett. **83**, 4713 (2003).
[592] Ya. I. Alivov, E. V. Kalinina, A. E. Cherenkov, D. C. Look, B. M. Ataev, A. K. Omaev, M. V. Chukichev, and D. M. Bagnall, Appl. Phys. Lett. **83**, 4719 (2003).
[593] H. Ohta, K. Kawamura, M. Orita, M. Hirano, N. Sarukura, and H. Hosono, Appl. Phys. Lett. **77**, 475 (2000).
[594] A. Kudo, H. Yanagi, K. Ueda, H. Hosono, K. Kawazoe, and Y. Yano, Appl. Phys. Lett. **75**, 2851 (1999).
[595] H. Ohta, M. Hirano, K. Nakahara, H. Maruta, T. Tanabe, M. Kamiya, T. Kamiya, and H. Hosono, Appl. Phys. Lett. **83**, 1029 (2003).
[596] A. E. Tsurkan, N. D. Fedotova, L. V. Kicherman, and P. G. Pas'ko, Semicond. Semimetals **6**, 1183 (1975).
[597] I. T. Drapak, Semiconductors 2, 624 (1968).
[598] S. Ishizuka *et al.*, Phys. Status Solidi C **1**, 1067 (2004).
[599] J. A. Aranovich, D. Golmayo, A. L. Fahrenbruch, and R. H. Bube, J. Appl. Phys. **51**, 4260 (1980).
[600] Ya. I. Alivov, Ü. Özgür, S. Doğan, D. Johnstone, V. Avrutin, N. Onojima, C. Liu, J. Xie, Q. Fan, and H. Morkoç, Appl. Phys. Lett. **86**, 241108 (2005).
[601] Ya. I. Alivov, D. Johnstone, Ü. Özgür, V. Avrutin, Q. Fan, S. S. Akarca-Biyikli, and H. Morkoç, Jpn. J. Appl. Phys., Part 1 (to be published).
[602] C.-X. Wang, G.-W. Yang, H.-W. Liu, Y.-H. Han, J.-F. Luo, C.-X. Gao, and G.-T. Zou, Appl. Phys. Lett. **84**, 2427 (2004).
[603] H. Ohta, H. Mizoguchi, M. Hirano, S. Narushima, T. Kamiya, and H. Hosono, Appl. Phys. Lett. **82**, 823 (2003).
[604] S. E. Nikitin, Yu. A. Nikolaev, V. Yu. Rud, Yu. V. Rud, E. I. Terukov, N. Fernelius, and J. Goldstein, Semiconductors **38**, 393 (2004).
[605] A. G. Milnes and D. L. Feucht, *Heterojunctions and Metal-Semiconductor Junctions* (Academic, New York, 1972).
[606] A. Osinsky *et al.*, Appl. Phys. Lett. **85**, 4272 (2004).
[607] Y. I. Alivov, Ü. Özgür, S. Doğan, C. Liu, Y. Moon, X. Gu, V. Avrutin, and H. Morkoç, Solid-State Electron. (to be published).
[608] A. Shimizu, M. Kanbara, M. Hada, and M. Kasuga, Jpn. J. Appl. Phys. **17**, 1435 (1978).
[609] T. Minami, M. Tanigava, M. Yamanishi, and T. Kawamura, Jpn. J. Appl. Phys. **13**, 1475 (1974).
[610] H. Ohta and H. Hosono, Mater. Lett. **7**, 42 (2004).
[611] Y. Ohya, T. Niva, T. Ban, and Y. Takahashi, Jpn. J. Appl. Phys., Part 1 **40**, 297 (2001).
[612] S. Masuda, K. Kitamura, Y. Okumura, S. Miyatake, H. Tabata, and T. Kawai, J. Appl. Phys. **93**, 1624 (2003).
[613] R. L. Hoffman, B. J. Norris, and J. F. Wager, Appl. Phys. Lett. **82**, 733 (2003).
[614] R. L. Hoffman, J. Appl. Phys. **95**, 5813 (2004).
[615] F. M. Hossain *et al.*, J. Appl. Phys. **94**, 7768 (2003).
[616] P. F. Carcia, R. S. McLean, M. H. Reilly, and G. Nunes, Jr., Appl. Phys. Lett. **82**, 1117 (2003).
[617] Z. L. Wang, Mater. Today **7**, 26 (2004).
[618] Z. W. Pan, Z. R. Dai, and Z. L. Wang, Science **291**, 1947 (2001).
[619] Z. L. Wang, J. Phys.: Condens. Matter **16**, R829 (2004).
[620] Y. W. Heo, D. P. Norton, L. C. Tien, Y. Kwon, B. S. Kang, F. Ren, S. J. Pearton, and J. R. LaRoche, Mater. Sci. Eng., R. **47**, 1 (2004).
[621] X. Duan, Y. Huang, Y. Cui, J. Wang, and C. M. Lieber, Nature (London) **409**, 66 (2001).
[622] M. H. Huang *et al.*, Science **292**, 1897 (2001).
[623] X. Y. Kong, Y. Ding, R. Yang, and Z. L. Wang, Science **303**, 1348 (2004).
[624] X. D. Bai, P. X. Gao, Z. L. Wang, and E. G. Wang, Appl. Phys. Lett. **82**, 4806 (2003).
[625] V. A. L. Roy, A. B. Djurisic, W. K. Chan, J. Gao, H. F. Lui, and C. Surya, Appl. Phys. Lett. **83**, 141 (2003).
[626] S. F. Yu, C. Yuen, S. P. Lau, W. I. Park, and G.-C. Yi, Appl. Phys. Lett. **84**, 3241 (2004).
[627] T. Yatsui, T. Kawazoe, M. Ueda, Y. Yamamoto, M. Kourogi, and M. Ohtsu, Appl. Phys. Lett. **81**, 3651 (2001).
[628] Z. Qiu, K. S. Wong, M. Wu, W. Lin, and H. Xu, Appl. Phys. Lett. **84**, 2739 (2004).
[629] H. Chik, J. Liang, S. G. Cloutier, N. Kouklin, and J. M. Xu, Appl. Phys. Lett. **84**, 3376 (2004).
[630] Q. X. Zhao, M. Willander, R. E. Morjan, Q.-H. Hu, and E. E. B. Campbell, Appl. Phys. Lett. **83**, 165 (2003).
[631] W. I. Park, D. H. Kim, S.-W. Jung, and G.-C. Yi, Appl. Phys. Lett. **80**, 4232 (2002).
[632] X. Liu, X. Wu, H. Cao, and R. P. H. Chang, J. Appl. Phys. **96**, 3141 (2004).
[633] Y. B. Li, Y. Bando, and D. Golberg, Appl. Phys. Lett. **84**, 3603 (2004).
[634] P. X. Gao and Z. L. Wang, Appl. Phys. Lett. **84**, 2883 (2004).
[635] W. D. Yu, X. M. Li, and X. D. Gao, Appl. Phys. Lett. **84**, 2658 (2004).
[636] A. B. Djurišić, Y. H. Leung, W. C. H. Choy, K. W. Cheah, and W. K. Chan, Appl. Phys. Lett. **84**, 2635 (2004).
[637] Z. L. Wang, X. Y. Kong, and J. M. Zuo, Phys. Rev. Lett. **91**, 185502 (2003).
[638] B. P. Zhang, N. T. Binh, Y. Segawa, Y. Kashiwaba, and K. Haga, Appl. Phys. Lett. **84**, 586 (2004).
[639] M. Haupt *et al.*, J. Appl. Phys. **93**, 6252 (2003).
[640] A. Ladenburger, M. Haupt, R. Sauer, K. Thonke, H. Xu, and W. A. Goedel, Physica E (Amsterdam) **17**, 489 (2003).
[641] R. Könenkamp, R. C. Word, and C. Schlegel, Appl. Phys. Lett. **85**, 6004 (2004).
[642] Z. W. Pan, Z. R. Dai, and Z. L. Wang, Science **291**, 1947 (2001).
[643] X. D. Wang, Y. Ding, C. J. Summers, and Z. L. Wang, J. Phys. Chem. B **108**, 8773 (2004).
[644] X. Y. Kong and Z. L. Wang, Nano Lett. **3**, 1625 (2003).
[645] Y. W. Heo *et al.*, Appl. Phys. Lett. **85**, 2002 (2004).
[646] B. S. Kang, Y. W. Heo, L. C. Tien, D. P. Norton, F. Ren, B. P. Gila, and S. J. Pearton, Appl. Phys. A: Mater. Sci. Process. **80**, 1029 (2005).
[647] Y. W. Heo, L. C. Tien, Y. Kwon, S. J. Pearton, B. S. Kang, F. Ren, and J. R. LaRoche, Appl. Phys. Lett. **85**, 3107 (2004).
[648] M. S. Arnold, P. Avouris, Z. W. Pan, and Z. L. Wang, J. Phys. Chem. B **107**, 659 (2003).
[649] W. I. Park, J. S. Kim, G.-C. Yi, M. H. Bae, and H.-J. Lee, Appl. Phys. Lett. **85**, 5052 (2004).
[650] Z. Fan, D. Wang, P.-C. Chang, W.-Y. Tseng, and J. G. Lu, Appl. Phys.

[This article is copyrighted as indicated in the article. Reuse of AIP content is subject to the terms at: http://scitation.aip.org/termsconditions. Downloaded to] IP: 128.172.48.58 On: Mon, 19 Oct 2015 20:45:44

Lett. **85**, 5923 (2004).
[651] Z. Fan, P.-C. Chang, J. G. Lu, E. C. Walter, R. M. Penner, C.-H. Lin, and H. P. Lee, Appl. Phys. Lett. **85**, 6128 (2004).
[652] Y. W. Heo, L. C. Tien, Y. Kwon, D. P. Norton, S. J. Pearton, B. S. Kang, and F. Ren, Appl. Phys. Lett. **85**, 2274 (2004).
[653] H. S. Bae, M. H. Yoon, J. H. Kim, and S. Im, Appl. Phys. Lett. **82**, 733 (2003).
[654] M. Liu and H. K. Kim, Appl. Phys. Lett. **84**, 173 (2004).
[655] L. Lagowski, E. S. Sproles, Jr., and H. C. Gatos, J. Appl. Phys. **48**, 3566 (1977).
[656] J. Masum, P. Parmiter, T. J. Hall, and M. Crouch, IEE Proc.-G: Circuits, Devices Syst. **143**, 307 (1996).
[657] Y. Z. Xiong, G.-I. Ng, H. Wang, and J. S. Fu, IEEE Trans. Electron Devices **48**, 2192 (2001).
[658] M. H. Zhao, Z. L. Wang, and S. X. Mao, Nano Lett. **4**, 587 (2004).
[659] B. P. Zhang, N. T. Binh, K. Wakatsuki, Y. Segawa, Y. Yamada, N. Usami, M. Kawasaki, and H. Koinuma, Appl. Phys. Lett. **84**, 4098 (2004).
[660] M. Catti, Y. Noel, and R. Dovesi, J. Phys. Chem. Solids **64**, 2183 (2003).
[661] Y. Noel, C. M. Zicovich-Wilson, B. Civalleri, Ph. D'Arco, and R. Dovesi, Phys. Rev. B **65**, 014111 (2001).
[662] G. Carlotti, D. Fioretto, G. Socino, and E. Verona, J. Phys.: Condens. Matter **7**, 9147 (1995).
[663] G. Carlotti, G. Socino, A. Petri, and E. Verona, Appl. Phys. Lett. **51**, 1889 (1987).
[664] T. Azuhata *et al.*, J. Appl. Phys. **94**, 968 (2003).
[665] I. B. Kobiakov, Solid State Commun. **35**, 305 (1980).
[666] R. M. Martin, Phys. Rev. B **5**, 1607 (1972).
[667] M. Koyano, P. QuocBao, L. T. ThanhBinh, L. HongHa, N. NgocLong, and S. Katayama, Phys. Status Solidi A **193**, 125 (2002).
[668] E. F. Venger, A. V. Melnichuk, L. Lu. Melnichuk, and Yu. A. Pasechnik, Phys. Status Solidi B **188**, 823 (1995).
[669] J. Nause and B. Nemeth, Semicond. Sci. Technol. **20**, S45 (2005).
[670] K. Maeda, M. Sato, I. Niikura, and T. Fukuda, Semicond. Sci. Technol. **20**, S49 (2005).
[671] M. V. Cho, A. Setiawan, K. J. Ko, S. K. Hong, and T. Yao, Semicond. Sci. Technol. **20**, S13 (2005).
[672] A. Ohmoto and A. Tsukazaki, Semicond. Sci. Technol. **20**, S1 (2005).

[This article is copyrighted as indicated in the article. Reuse of AIP content is subject to the terms at: http://scitation.aip.org/termsconditions. Downloaded to] IP: 128.172.48.58 On: Mon, 19 Oct 2015 20:45:44